Copyright

by

Miri Choi

2014

The Dissertation Committee for Miri Choi Certifies that this is the approved version of the following dissertation :

Monolithic Integration of Functional Perovskite Structures on Si

Committee:

Alexander A. Demkov, Supervisor

Chih-Kang Shih, Co-Supervisor

Edward Yu

John Markert

Zhen Yao

Monolithic Integration of Functional Perovskite Structures on Si

by

Miri Choi, B.S.; M.S.

Dissertation

Presented to the Faculty of the Graduate School of

The University of Texas at Austin

in Partial Fulfillment

of the Requirements

for the Degree of

Doctor of Philosophy

The University of Texas at Austin

August, 2014

Dedication

To my parents, Jin Hwan Choi and Haeng Ae Suh,

to my sister, Nuri Choi,

and to my husband, Insun Jo.

Acknowledgements

I would like to express my sincere gratitude to my co-advisors, Dr. Demkov and Dr. Shih. Dr. Demkov has provided me an opportunity to work as a group member and has given me research insight and enthusiasm for my work. He has given me his ungrudging encouragement and advice whenever I felt that I was doing nothing and had trouble in research or difficulties studying physics. I am grateful to him for arranging for me to work as a summer intern at IBM, so that I could have a chance to experience the industry working environment. Without his caring, research guidance, and support, I would never have finished my dissertation. I want to thank Dr. Shih, as well, for supporting me, and for his willingness to share his numerous experimental ideas. Their experience and research enthusiasm drove me to explore my research with joy. I also would like to thank my dissertation committee—Professors John Markert, Zhen Yao and Edward Yu—for their time and valuable feedback on my final defense. In addition, I have been very grateful to work with collaborators: Dr. S. Zollner at New Mexico State University, Dr. C. Dubourdieu, Dr. M. Frank, Dr. J. Jordan-Sweat and Dr. V. Narayanan at IBM, Dr. M. Tsoi and H. Seinige at the University of Texas at Austin Physics Department, Dr. D. Triyoso at Freescale, Dr. Q. He, and Dr. Albina Y. Borisevich at the Oak Ridge National Laboratory.

I have been very grateful to get to know my colleagues in the Demkov research group. Dr. Agham Posadas is the best research scientist I have known so far. Agham, Rytis Dargis and I were the first members of the lab in its early stages. We had heavy tasks assembling the MBE chamber and setting up the experimental environment. For a long time, we had no crystalline STO films on Si. At the tough moments, Agham never lost his smile, and his research enthusiasm never stopped. Every time I asked him any

question, he let me know his deepest knowledge of solid state physics and offered me insights gained from his experimental experience. I am grateful, too, to Dr. Richard Hatch, for sharing his best expertise about ARPES and XPS. He explained very well about analysis of data and tried to help me in many ways. I still feel sorry that I broke the capillary of the UPS, through my own fault, and delayed his work for several months. Additionally, I would like to thank Chungwei Lin, Andy O'Hara, and Hosung Seo in Dr. Demkov's group, for theoretical calculations that contributed to my dissertation. They are kind and great to share their knowledge. When I was not familiar with theoretical details, they tried to explain very carefully, and made me understand. I am also grateful to Demkov group members Kurt Fredericksen, Gao Lingyuan, Donghan Shin, Patrick Ponath, Kristy Kormondy, and Tobias Hadamek, for their help.

I would like to thank to Dr. Shih's group members, especially Charlotte Sanders and Jisun Kim. We had a very hard time setting up the connection chamber and MBE-STM system. Charlotte and I had big troubles with the STM head, all the wiring, and the connection chamber. Whenever a wiring connection was dead or something was wrong, we shout, drank lots of coffee in the Java coffee shop, and were back to work. Now I miss the rocky time because I learned many things and accumulated the friendship. And also I would like to thank Thong Ngo and Martin McDaniel in Dr. Eckert's group. They were always friendly and kind in discussion and in the sharing of their knowledge and experimental experience.

I am deeply thankful to my close friends for giving me support and a state of balence: Eun Kyo Cho, SooHyun Cho, Hyunkyung Cho, Hyeran Yoon, Yoon Joo Lee, Jung won Lee, Woosuk Bang and Sujung Han.

Finally, I owe a great debt of gratitude to my parents, Jin Hwan Choi and Haeng Ae Suh, and to my younger sister Nuri Choi, for their love, support and sacrifice along

this long journey. My husband, Insun Jo, has always cheered me up, and has been there for me through thick and thin. He is the greatest reward of my Ph.D.

Monolithic Integration of Functional Perovskite Structures on Si

Miri Choi, Ph.D.

The University of Texas at Austin, 2014

Supervisors: Alexander A. Demkov and Chih-Kang Shih

Functional crystalline oxides with perovskite structure have a wide range of electrical properties such as ferroelectric, ferromagnetic, and superconductive, as well as unique properties that make them suited for a wide variety of applications including electro-optics, high-k dielectrics, and catalysis. Therefore, in order to realize the potential of perovskite oxides it is desirable to integrate them with semiconductors. Due to the high surface energy of oxides compared to that of semiconductors and the low number of oxides that are thermodynamically stable against SiO_2 formation, it has been extremely difficult to integrate epitaxial oxides with Si directly. However, in 1998, McKee and co-workers finally succeeded in depositing $SrTiO_3$ on Si directly using a Sr template via molecular beam epitaxy. This breakthrough opened the possibility of integrating the perovskite oxides with Si to realize potential device applications.

In this dissertation, alkaline earth metal (Sr and Ba) templates on semiconductors, which enable epitaxial growth of complex oxides on semiconductors, are investigated using molecular beam epitaxy (MBE) for growth and *in-situ* X-ray/ultraviolet photoemission spectroscopy (XPS/UPS) for the electronic structure analysis. An epitaxial layer of $SrTiO_3$ on Si using such alkaline earth templates is used as a pseudo-substrate for the integration of perovskite oxides on Si. Through the use of post-deposition annealing

as a function of oxygen pressure and annealing time, the strain relaxation behavior of epitaxial $SrTiO_3$ films grown on Si is also investigated to determine how the SiO_2 interlayer thickness affects the $SrTiO_3$ lattice constant. This ability to control strain relaxation can be used as a way to manipulate the properties of other perovskite oxides grown on $SrTiO_3$/Si. Additionally, $SrTiO_3$ can be made conductive by doping with La. Conductive $SrTiO_3$ can be used as a thermoelectric, a transparent conductive layer, and a quantum metal layer in a quantum metal field-effect transistor (QMFET). The structural, electrical, and optical properties of strained conductive La-doped $SrTiO_3$ are studied in order to understand the relation between elastic strain and electrical properties for electronic device applications.

Oxide quantum well systems based on $LaAlO_3$/$SrTiO_3$ are also investigated using spectroscopic ellipsometry to understand how the quantum well layer structure affects the electronic structure. Such quantum well systems are good candidates for the monolithic integration of functional perovskites on semiconductors. Oxides quantum wells can be used in various device applications such as in quantum well cascade lasers, laser diodes and high performance transistors.

As part of the growth optimization for high quality complex oxide heterostructures, the surface preparation of $SrTiO_3$ substrates using several different methods was also extensively studied using angle-resolved photoemission spectroscopy (ARPES). We found that acid-free water-based surface preparation is actually more effective at removing SrO_x crystallites and leaving the surface TiO_2-terminated compared to the more commonly used acid-based methods.

Table of Contents

List of Tables xiii

List of Figures xiv

Chapter 1. Introduction 1

Chapter 2. Molecular beam epitaxy and in-situ RHEED 8

2.1 Historical overview 8

2.2 Molecular Beams Epitaxy – Principle 9

2.2.1 Kinetic theory of gases 9

2.2.2 Vapor Pressure of materials 13

2.2.3 Effusion - Geometry 15

2.3 Molecular Beam Epitaxy (MBE) – Equipment 17

2.3.1 The component descriptions of Molecular Beam Epitaxy (MBE) 19

2.4 Reflection High Energy Electron Diffraction (RHEED) 24

2.4.1 Technical Description 24

2.4.2 The principle of electron diffraction 25

Chapter 3. Experimental Techniques 31

3.1 Introduction 31

3.1.1 θ-2θ diffraction 33

3.1.2 2θ-ω scan 35

3.1.3 Rocking curve (ω-scans) 37

3.2 X-ray reflectivity 38

3.2.1 X-ray reflectivity – film thickness 39

3.3 X-ray photoelectron spectroscopy 41

3.3.1 The principle of X-ray photoelectron spectroscopy 41

3.3.2 Sampling Depth 43

3.3.3 Spin-Orbit splitting 45

3.3.4 Quantification of sample stoichiometry 45

3.3.5 Experimental details 48

3.4 Ultra-violet photoelectron spectroscopy (UPS) 50

3.5 Atomic force microscopy (AFM) 51
3.5.1 Atomic force microscopy (AFM) – principle 51

Chapter 4. Alkanline earth metal Sr on Si (001) : Charge transfer in Sr Zintl template on Si (001)..54
4.1 Introduction...54
4.2 Experiment and theoretical calculations 56
4.3 Results and Discussion 58
4.4 Summary...64

Chapter 5. Alkanline earth metal Ba on Si (001) : Charge transfer in Sr Zintl template on Si (001)..65
5.1 Introduction...65
5.2 Experiment and theoretical calculations 69
5.3 Results and Discussion 71
5.4 Summary...82

Chapter 6. Strain relaxation in single crystal $SrTiO_3$ grown on Si (001) by molecular beam epitaxy 84
6.1 Introduction...84
6.2 Experiments 87
6.3 Results...89
6.4 Conclusion 98

Chapter 7. Surface electronic structure for various surface preparations of Nb-doped $SrTiO_3$ (001)...100
7.1 Introduction...101
7.2 Various surface preparations of Nb-doped $SrTiO_3$ (001) – Buffered HF, HCl/HNO_3/Vacuum annealing..103
7.2.1 Experiment – sample preparation 103
7.2.2 Experiment - measurement 105
7.2.3 Results...109
7.3 Various surface preparations of Nb-doped $SrTiO_3$ (001) – Water Boiling127
7.3.1 Experiment..127
7.3.2 Results...128

7.4 Surface characterization - AFM 134
7.5 Conclusion 138

Chapter 8. Structural, optical and electrical properties of strained La-doped $SrTiO_3$ films 140
8.1 Introduction 141
8.2 Experiment and theoretical calculation 144
8.2.1 Electrode test 146
8.3 Results and Discussion 148
8.3.1 Surface morphology 148
8.3.2. Stoichiometry and crystallinity 150
8.3.3. Electrical and optical properties 155
8.3.4. Theoretical calculations 161
8.4 Summary 165

Chapter 9. Transition metal oxide quantum wells 167
9.1 Introduction 167
9.2 Experiment 171
9.3 Results 172
9.3.1 Crystallinity, stoichiometry and surface morphology 172
9.3.2 Band alignment of the STO QW 176
9.3.3 Optical properties of STO QW 178
9.4 Conclusions 182

Chapter 10. Conclusions and outlook 184
10.1 Zintl templates on Si (001) 184
10.2 Epitaxial growth and the relaxation behavior of $SrTiO_3$ films on Si (001) 185
10.3 Structural, optical and electrical properties of strained La-doped $SrTiO_3$ films 185
10.4 Optical properties of transition metal oxide quantum wells 186

References 188

List of Tables

Table 2.1 Crucible selection depending on the materials to be evaporated. 23

Table 3.1 The quantitation results of the La doped STO sample. 48

Table 7.1 The ionic motion (Å) of hydrogenated surfaces with respect to the clean TiO_2 surface. A positive number means the ion is moving towards vacuum, and a negative number means the ion is moving towards the bulk. *O a corresponds to the O that is bonded to the first H. O b corresponds to the O bound to the second H (2 O-H, Ti-H surface only). 122

Table 8.1 The optical properties of 5 % and 15 % doped LSTO films on STO at room temperature. Plasma frequency, broadening, and calculated carrier concentrations from plasma frequency are presented. 159

Table 8.2 Summary of properties used to calculate the density of states effective mass and conductivity within relaxation time approximation. 163

Table 8.3 Summary of the transport related properties found using interpolation for comparison to the experimentally measured conductivity.............165

List of Figures

Figure 1.1 (a) Z-contrast cross-section STEM image and (b) capacitance as a function of voltage[14] of a $SrTiO_3$ film on Si (001). 2

Figure 1.2 (a) Asymmetric tilted dimer of clean Si (001) and (b) flattened dimer of Si (001) with 1/2 ML Sr. 4

Figure 1.3 Magnetic properties changes as a function of strain in (a) $LaCoO_3$ and (b) $EuTiO_3$. (c) A variety of oxide substrates with different lattice constants that can be used to impose strain in oxide thin films. 5

Figure 2.1 Molecules evaporate from the hole of a crucible. Molecules move a distance vdt through unit area, dA, with speed v and at angle θ from the normal to dA. This crucible is from DCA. 11

Figure 2.2 The vapor pressure as a function of temperature from Veeco. 14

Figure 2.3 Schematic view of the angular distribution of flux of molecules over the solid angle dΩ on a sphere of radius r between the angle θ and θ+ dθ. The molecules are condensed on the surface S. 15

Figure 2.4 DCA 600 oxide MBE deposition system which is connected to the transfer chamber equipped with another growth chamber and the XPS/UPS analysis system. The image comes from the group home page[47]. 18

Figure 2.5 Schematic view of the oxide MBE system. 19

Figure 2.6 The cryopanel inside the main MBE chamber. 21

Figure 2.7 The effusion cell used in MBE system. 22

Figure 2.8 The experimental set up of the reflection geometry for RHEED. 24

Figure 2.9 Schematic view of Ewald sphere constructions. (a) Side view of the Ewald sphere with the reciprocal lattice rods with indexes. (b) Top view of the Ewald sphere and the Laue zone labeled 0th, 1st, and 2nd. ...27

Figure 2.10 (a) The intersection of the Ewald sphere with reciprocal rods forms spots aligned along the semi-circular arc. The RHEED patterns from (b) the perfectly flat surface, (c) the surface with monolayer roughness, (d) the surface with large roughness, and (d) amorphous or polycrystalline film. (The RHEED images are from (b) STO substrate, (c-e) STO films on Si, taken by Miri Choi in UT Materials Physics Lab.)..........................28

Figure 2.11 The mechanism for RHEED intensity oscillations from specular spot during the growth of one ML. The original caption is from[57], copyright 2002..30

Figure 3.1 Bragg diffraction in (a) real space and (b) reciprocal space. 33

Figure 3.2 The diffraction peak of STO (002) film on Si (001). 35

Figure 3.3 The schematic of the scattering geometry of 2θ-ω scan. 36

Figure 3.4 (a) Several sets of planes satisfying with Bragg's Law at slightly different ω positions. ω-scans of (b) the La doped $SrTiO_3$ film on Si and (c) the La doped $SrTiO_3$ film on $LaAlO_3$. 38

Figure 3.5 Reflectivity curve of $SrTiO_3$ film with 78 Å thickness on Si (001). 39

Figure 3.6 Reflection of X-rays at material surface and at the interface. The material has the index of reflection n_2 40

Figure 3.7 The chamber of X-ray photoemission spectroscopy in UT Materials Physics Lab. 42

Figure 3.8 The schematic diagram of the photoemission spectroscopy. 43

Figure 3.9 Representative core level spectra of Sr 3d, La 3d, Ti 2p, and O 1s from a La doped STO film using *in situ* XPS. 47

Figure 3.10 (a) survey scan and (b) high resolution scan of Ti 2p component.....49

Figure 3.11 Schematic view of (a) the photoexcitation of electrons from the valence band by photons energy of hν and (b) the measured spectrum of 0.3 ML Sr on Si (001). 51

Figure 3.12 Feedback loop of the tapping mode AFM. Image taken from reference[81]. 53

Figure 4.1 RHEED patterns of the Si (001) surface as a function of Sr coverage for (a) 0, (b) 1/6, (c) 1/3, and (d) 1/2 ML Sr coverage on 2×1 Si (001) deposited at 600 °C. All patterns are viewed along the Si<110> azimuth. 58

Figure 4.2 Si 2p core-level spectra of (a) clean 2×1 Si (001), and (b) 1/2 ML Sr deposition on clean 2×1 Si (001) by *in situ* XPS at room temperature. Insets are theoretical structures of clean 2×1 Si (001) and 1/2 ML Sr on Si (001) obtained from the DFT calculations. 59

Figure 4.3 Valence band edge of the clean 2×1 Si (001) and 1/2 ML Sr on Si (001) measured using XPS. The zero of energy is set at the Fermi level...61

Figure 4.4 Work function variation as a function of Sr coverage on 2×1 Si (001) from experiment (filled squares) and theory (open circles). For the work function calculation for the Sr coverage of 1/6 ML, 1/4 ML, and 1/3 ML, we use the structural model proposed in Ref.[124]and Ref.[83], respectively. 63

Figure 5.1 RHEED patterns of the Si (001) surface as a function of Ba coverage for (a) 0, (b) 1/4, (c) 1/3, and (d) 1/2 ML Ba coverage on 2×1 Si (001) deposited at 600 °C. All patterns are viewed along the Si <110> azimuth...72

Figure 5.2 (a) Ball-and-stick models of the p(2×2) surface reconstruction of Si (001) (left) and the 2×1 reconstruction of Si (001) induced by 1/2-ML Sr or Ba deposition (right). (b) Si 2p core-level spectrum of 1/2-ML Ba/Si (001) by in-situ XPS at room temperature. The detailed description of the sub-peak structures and the analysis procedure are explained elsewhere[122,142]. (c) Schematic to show the 2p bulk peak shifts of clean 2×1 Si (001) (bottom) induced by 1/2-ML Ba (middle), and 1/2-ML Sr (top) depositions...74

Figure 5.3 One dimensional screening electron density for a bulk 2p core-hole in the 24-layer-thick pure Si (001) slab (black straight line in (a)) and in the 1/2-ML Ba/Si (001) slab (green straight line in (c)) compared to that of the 1/2-ML Sr/Si (001) slab (red dashed lines in (a) and (c)). Three dimensional screening electron density for the bulk 2p core-hole near the surface of the 24-layer-thick pure Si (001) (b) and the 1/2-ML Ba/Si (001)..75

Figure 5.4 Layer-by-layer projected density of states (pDOS) of pure Si (001) (a), 1/2-ML Ba/Si (001) (b), and 1/2-ML Sr/Si (001) (c). The Fermi levels are set to be 0 eV. For each panel, the upper three plots are the pDOSs of the surface atoms whose names are shown on the right upper corner of each plot. The surface gaps are calculated to be 0.05 eV, 0.19 eV, and 0.45 eV for Si (001), 1/2-ML Ba/Si (001), and half-monoalyer Sr/Si (001), respectively. The bottom plot is the pDOS calculated for one of the bulk Si atom with the bulk gap of 0.5 eV represented by two dashed lines. 77

Figure 5.5 (a) Density of states (DOS) of bulk 2p core-hole excited Si (001) projected on the bulk 2p core hole site. The Fermi levels are set to be 0 eV. (b) Layer-by-layer projected density of states (pDOS) of pure Si (001) (b), 1/2-ML Ba/Si (001) (c), and 1/2-ML Sr/Si (001) (d) in the presence of the bulk 2p core hole. 78

Figure 5.6 Valence band edge of the clean 2×1 Si (001) and 1/2 ML Br on Si (001) measured using XPS. The zero of energy is set at the Fermi level...80

Figure 5.7 Work function variation as a function of Ba coverage on 2×1 Si (001) from experiment. 81

Figure 6.1 2×1 RHEED pattern of Si (001) covered by Sr to form a template viewed from the Si <110> azimuth 89

Figure 6.2 RHEED patterns of the STO films on Si after each growth step along <010> (b,d,f, h) and <110> (c, d, g, i) directions. (a) and (b) are RHEED patterns after the initial 3 ML of amorphous STO are crystallized. (c) and (d) are RHEED patterns after the main 13 ML STO growth at 565 °C. (e) and (f) are RHEED patterns after a post-deposition oxygen anneal at 650 °C. 90

Figure 6.3 Typical x-ray diffraction and RHEED data used to determine STO lattice constants. (a) X-ray diffraction L scan about STO 002 peak; (b) H scan about STO 200 peak; (c) RHEED profile of STO film on Si. The data shown are for an unannealed film. 91

Figure 6.4 Cross sectional TEM images of STO films grown on Si. (a) High-resolution image of an unannealed film; (b) typical low-resolution image of an STO film annealed in oxygen. The specific image is for a sample annealed under 5×10^{-7} Torr of oxygen at 650 °C for 10 min. 93

Figure 6.5 (a) In-plane lattice constants and (b) SiO_2 thickness as a function of oxygen partial pressure. All films were annealed at 650 °C for 30 min in different oxygen environments. 95

Figure 6.6 (a) In-plane lattice constants and (b) SiO_2 thickness as a function of annealing duration. All films were annealed in oxygen environment of 5×10^{-7} Torr at 650 °C...97

Figure 6.7 RHEED patterns along <110> direction of a film which was (a) post-annealed at 650 °C in an oxygen environment of 5×10^{-7} Torr for 90 min, and of film which was (b) post-annealed at 650 °C in an oxygen environment of 1×10^{-5} Torr for 10 min. 98

Figure 7.1 Annealing condition of Nb-$SrTiO_3$ substrate. 104

Figure 7.2 (a) The bulk and surface Brillouin zones for $SrTiO_3$ with labeled symmetry directions and points. (b) Paths in the bulk Brillouin zone corresponding to ARPES measurements for two different photon energies, hν. (c, d) RHEED images for the vacuum annealed sample and a sample etched in buffered HF, respectively, with the images taken just off the [110] azimuth due to geometric constraints. 108

Figure 7.3 (a) The surface projected band structure of bulk STO along the [110] direction for a fine grid of kz values that spans the bulk Brillouin zone as calculated using DFT. (b) For ease of comparison to ARPES data, each line in (a) is broadened using a Lorentzian function with a FWHM of 0.3 eV. (c) Same as (b), but calculated using a tight-binding (TB) model.110

Figure 7.4 ARPES data along the [110] direction for STO samples prepared in a variety of ways for a photon energy of hν = 21.22 eV unless otherwise stated. (a) Raw data for vacuum-annealed STO, with the 2nd derivative (in the Energy direction) shown in (b) in order to better visualize dispersing bands. (c-d) After water-leaching the STO surface quality is greatly improved and the ARPES data reveals dispersing bands after a simple background removal. (e-h) Photoemission spectra (with background removal) for STO samples etched in BHF (e,f) and those etched using the Arkansas method (g,h). (i) The 2nd derivative of ARPES data for MBE-grown, undoped STO. 113

Figure 7.5 Normal emission XPS spectra of the Sr 3d core level for a STO(001) sample having undergone a vacuum-anneal (a) as well as a sample etched in BHF (b). The primary STO lattice peaks (more intense) are accompanied by lower intensity peaks (green) which are attributed to the presence of strontium oxide crystallites on the surface which are removed, to some extent, after etching with BHF. 115

Figure 7.6 (a) Angle-integrated photoemission data of the primarily O 2p-derived valence band states for a variety of STO preparations with a close-up of the gap region shown in (b). Data for the BHF-etched STO is omitted from (a) and (b) since it is very nearly indistinguishable from the Arkansas-prepared STO. The photoemission data reveals at least two gap-states: an oxygen-vacancy state at a binding energy of $E-E_F \approx -1$ eV and another gap state about 800 meV above the top of the valence band located at $E-E_F \approx -2.75$ eV. 116

Figure 7.7 ARPES data for emission angles, θ, along the [110] direction for an STO sample prepared using the Arkansas method that correspond to the O 2p-derived valence band and the gap region. The pronounced shoulder for larger emission angles (at an energy of $E-E_F \approx -3.75$ eV) corresponds to the top of the valence band at the R point of the Brillouin zone. A close-up of the shaded region is shown in the inset and shows a mid-gap state about 800 meV above the top of the valence band that hardly disperses. 117

Figure 7.8 Sections of $SrTiO_3$ slabs corresponding to several of the systems studied using DFT calculations of the surface electronic structure. All slabs are (1×1). (a) A TiO_2-terminated slab with one O replaced by F. (b) Same as (a) with the addition of a H bonded to Ti. (c) A TiO_2-terminated slab with a single hydroxyl group. (d) Same as (c) with a H bonded to Ti. (e) A fully hydrogenated slab with two hydroxyl groups, and a H bonded to Ti. 118

Figure 7.9 (a-g) DFT calculations of the surface electronic structure for SrO-and TiO_2-terminated slabs as well as slabs shown in Figure 7.8(a-e) respectively. DFT calculations predict a pronounced, dispersing surface state about 980 meV above the valence band states that roughly follows the dispersion of the STO bulk bands which is not present in the case of an SrO-terminated slab. Because of the dispersing nature of the surface state in (b), it is unlikely the origin of the mid-gap state discussed in Figure 7.7, despite the TiO_2-termination that results from the Arkansas preparation. As seen in (d) and (f), a likely explanation for this mid-gap state is the termination of the Ti dangling bond with H. As discussed in the text, for this termination to occur, it must be preceded by either a substitution of a surface O with F, or the formation of a hydroxyl group. 124

Figure 7.10 Normal emission XPS survey spectrum for a STO (001) sample prepared by BHF etching. The F 1s core level has a binding energy of ~685 eV, and, if present, should be located in the region highlighted with a red circle. Despite etching with BHF, the concentration of F on the surface is negligible (we estimate ≤ 1 % of all anions within the probe depth). Other sample preparations yield equally low concentrations of F (see inset)..125
Figure 7.11 (a) The charge density of the non-dispersing band for the F-substituted slab with H on Ti. There is no charge density on the F (not shown). (b) The charge density of the nondispersing band for the H on O, H on Ti slab. 126
Figure 7.12 Comparison of theoretical calculations for various STO systems with ARPES data for the BHF-prepared sample. (a) The calculation for bulk STO band structure (see also Figure 7.3(a-b)), where prominent features are highlighted with white open circles. For ease of comparison, these same open circles are overlaid on the data in (b-h) which corresponds to data in Figure 7.3(c), Figure 7.7(a-g) and Figure 7.4(e-f) respectively. It is apparent that the different STO terminations hardly affect band structure predicted by DFT bulk calculations, but can give rise to surface states both above and below the valence band as seen in (d-h). 127

Figure 7.13 ARPES data along the [110] direction for STO samples prepared in a variety of ways for a photon energy of hν = 21.22 eV unless otherwise stated. (a) Raw data for vacuum-annealed STO, with the 2nd derivative (in the Energy direction) shown in (b) in order to better visualize dispersing features. After etching the surface using the Arkansas method (c-d) and BHF (e-f) the surface quality is much improved and the ARPES data reveal dispersing bands after a simple background removal. As was the case for the acid-based techniques, simply boiling STO in water followed by a furnace anneal also produces a high-quality surface and ARPES data shows the dispersing bands (g-h). 130

Figure 7.14 XPS spectra of the Sr 3d core level for different surface preparations. Data was fit using two spin-orbit split doublets, one (blue) corresponding to the primary STO lattice, and the other (green) to SrO_x crystallites on the surface of STO. 132

Figure 7.15 The relative Sr and Ti concentration of the near surface region of STO (001) as determined by XPS measurements for samples prepared using a variety of methods. As expected, methods reported to leave the surface TiO_2-terminated have a higher Ti concentration in the surface region.134

Figure 7.16 (a) RHEED image and (b) STM image of STO surface etched by buffered by HF. STM image taken by Jisun Kim in the Dr. Shih group. 135

Figure 7.17 AFM image of the STO surface 10 days after the etching. 136

Figure 7.18 AFM image of the STO surface etched by HCl/HNO_3. 137

Figure 7.19 (a) AFM image for the STO surface boiled in DI water and (b) one day after boiling water preparation. 138

Figure 8.1 I-V curve of (a) Pt/Au, (b) In/Au, and (c) Ti/Au electrodes...........147

Figure 8.2 (a)The schematic view of measurement and (b) the system for electrical measurement of LSTO 148

Figure 8.3 The RHEED patterns of 25 % LSTO on LSAT along <100> direction (a) after growth, (b) after vacuum annealing, and (c) after air annealing. 149

Figure 8.4 The AFM images of 25 % LSTO on LSAT (a) after vacuum annealing and (c) after air annealing. 149

Figure 8.5 Representative core level spectra of (a) Sr 3d, (b) La 3d, (c) Ti 2p, and (d) O 1s from LSTO films using *in situ* XPS.................................150

Figure 8.6 (a) The ratio of [Ti] / [La+Sr+Ti] determined by XPS (open triangles) and RBS (filled squares) and (b) measured La dopant concentration (RBS and XPS) compared to the target concentration...................151

Figure 8.7 (a) X-ray diffraction pattern of (002) LSTO peaks and substrate peaks. Inset shows the rocking curve of 5 % doped LSTO films on LAO. (b) Measured out-of-plane lattice constants and expected out-of-plane lattice constants as a function of La concentration. (c) Reciprocal space map of (103) Bragg peak for an LSTO film on DSO substrate with 25 % La concentration. The in-plane lattice constant of the film is the same as that of DSO substrate. (d) Unit cell volume changes as a function of La concentration for the different substrates.......................................153

Figure 8.8 Carrier concentrations of 5, 15, and 25 % doped LSTO films with 20 nm thickness on four different substrates obtained from Hall Effect measurements (a) and the ratio $[Ti^{3+}]/([Ti^{4+}]+[Ti^{3+}])$ using *in-situ* XPS. The dashed lines indicate the theoretical values of carrier concentration assuming that each La atom donates one electron to the conduction band of STO. 156

Figure 8.9 Dielectric function of 20 nm thick LSTO films on STO with 5 % and 15 % La. Data for a bulk (undoped) STO substrate are shown for comparison. 158

Figure 8.10 (a) Mobility and (b) resistivity of 5, 15, and 25 % doped LSTO films grown under four different strain configurations. 160

Figure 8.11 (a) The calculated density of states effective mass is plotted as diamonds with interpolation (solid line) and the occupied conduction band width is plotted as squares with interpolation (dashed line), as a function of carrier concentration. (b) Plot of the constant relaxation time conductivity as a function of carriers using a supercell approach with interpolation. 164

Figure 9.1 The quantum well structure consisting of $LaAlO_3$ and $SrTiO_3$ 168

Figure 9.2 The RHEED patterns of 7 uc LAO/10 uc STO on LAO along (a) <100>, and (b) <110> directions. 172

Figure 9.3 (a) Survey scan and representative core level spectra of (b) Al 2p, (c) La 3d, (d) Sr 3d, and (e) Ti 2p from 7 uc LAO/10 uc STO on LAO using *in situ* XPS. 173

Figure 9.4 (a-b) Z-contrast STEM image of a 7 uc LAO/10 uc STO structure on LAO, (c) the spacing of the A-site atoms (Sr or La) and (d) Z-contrast STEM image of a 7 uc LAO/5 uc STO structure on LAO 175

Figure 9.5 AFM images of 7 uc LAO/5 uc STO on LAO (a) 5 µm × 5 µm, and (b) 10 µm × 10 µm..176

Figure 9.6 (a) XPS valance band spectrum of the STO substrate. The red line indicates the linear extrapolation to determine the VBM energy. (b) The energy band diagram of bulk STO and bulk LAO, and a thin LAO film on Nb-STO, as determined using XPS. (c) The calculated energy band alignment across the LAO/STO/LAO quantum structure. 177

Figure 9.7 Schematic diagram of the principle of ellpsometry[337]...................179

Figure 9.8 (a) Square of the absorption coefficient of 10 uc QW STO plotted as a function of photon energy. The red line is the linear extrapolation to determine the onset of the absorption coefficient. (b)Square of the absorption coefficient of STO vs photon energy for bulk STO and for STO QW structures...181

Figure 9.9 Quantized states of a two unit cell thick STO QW (Poisson-Schrödinger modeling by Matthew Bucher in the Demkov group). 182

Chapter 1. Introduction

The first integrated metal-oxide-semiconductor (MOS) capacitors and transistors utilized an SiO_2 layer as the gate dielectric. However, the scaling down of device dimensions has reached a practical limitation that the gate dielectric thickness is now only about 1.2 nm thick or less, resulting in substantial gate tunneling currents that can cause problems with proper device operation[1]. Therefore, alternative high-k dielectric materials are needed that can allow for larger physical thickness while maintaining high gate capacitance. One class of promising alternative materials is the family of perovskite oxides.

These functional complex oxides with perovskite structure exhibit a wide range of electronic behavior such as having high dielectric constant[2], multiferroicity[3], ferroelectricity[4], ferromagnetism[5], superconductivity[6], colossal magnetoresistivity[7], and Mott insulating[8] behavior. Because many perovskite oxides have a high dielectric constant, as well as some functional (magnetic/ferroelectric) properties useful for novel devices, researchers have exerted considerable effort in integrating them with semiconductors. However, there were several challenging issues to overcome. In the early stage of epitaxial growth of thin film oxides on Si, attempts at depositing the high Tc superconducting oxide $YBa_2Cu_3O_{7-\delta}$ on Si (001) were reported[9,10]. However, without proper buffer layers, the elements in the oxide film diffused into and reacted with Si, resulting in interdiffusion or an interfacial compound. Such degraded oxides on Si gave poor properties compared to the original oxide properties. As a result of the necessity of growing an oxide in the presence of oxygen and the high affinity of silicon for oxygen, unwanted by-products such as SiO_2, metal silicides, and silicates readily form. In 1996, K. J. Hubbard and D. G. Schlom published a summary of the thermodynamic stability of

binary metal oxides against SiO_2 formation[11]. According to this paper, binary oxides of alkaline earth and rare earth metals on Si are stable against SiO_2 formation. However, most transition metal oxides such as TiO_2 are thermodynamically unstable on Si, so proper buffer layers for growing materials such as $SrTiO_3$ would be needed.

The first attempt at depositing $SrTiO_3$ on Si was accomplished by the use of thick SrO buffer layers[12,13]. In 1998, McKee *et al.* demonstrated crystalline $SrTiO_3$ films without amorphous SiO_2 on Si (001) using a buffer consisting of submonolayer of Sr (reported to be 1/4 monolayer (ML)) on Si (001) using molecular beam epitaxy[14]. By showing the direct growth of $SrTiO_3$ films on Si and measuring the capacitance of the system, a new opportunity for the integration of functional perovksite oxides on Si (001) opened up (Figure 1.1).

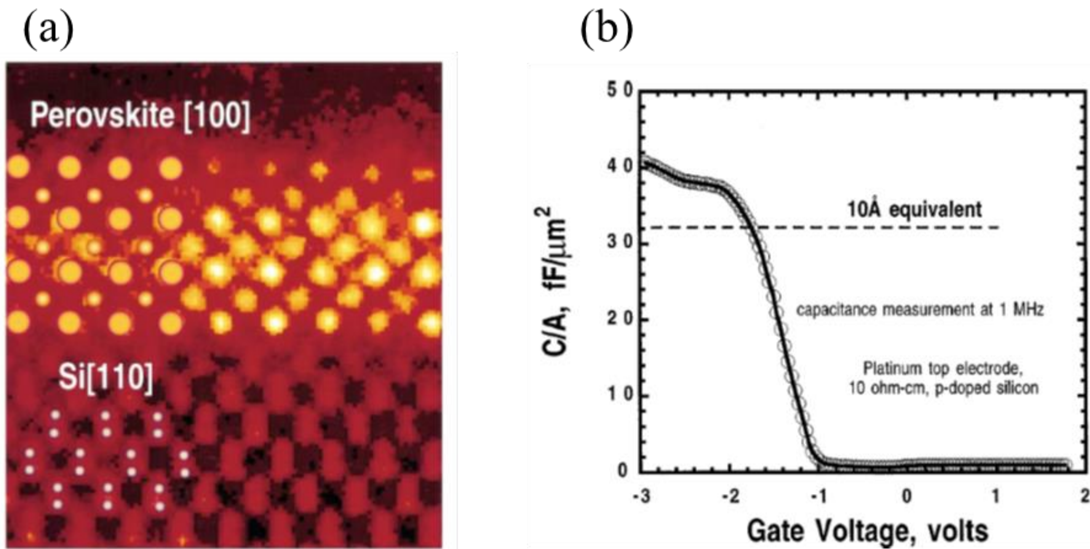

Figure 1.1 (a) Z-contrast cross-section STEM image and (b) capacitance as a function of voltage[14] of a $SrTiO_3$ film on Si (001).

After this pioneering work, much research effort (both theoretical and experimental) was directed to studying the physical and electronic structure of the interface between $SrTiO_3$ and Si, as well as on studies of the growth evolution and electrical properties of the $SrTiO_3$/Si system[15-18]. Because relatively high quality crystalline $SrTiO_3$ films could now be grown on Si (001), this materials system was also widely utilized as a peudo-substrate for the integration with Si of other functional perovskite oxides such as $LaCoO_3$[19], $Pb(Zr_{0.2}Ti_{0.8})O_3$[20], $BaTiO_3$[21-23], and $La_{0.7}Sr_{0.3}MnO_3$[24]. The key reason for the successful integration of perovskites on Si is the 1/2 ML Sr template. Each Si atom on the topmost layer of bulk Si has two dangling bonds. These two surface atoms of Si (001) undergo the so-called 2×1 dimer reconstruction, bonding together and reducing the number of dangling bonds to one per Si atom[25,26]. Further gain in energy of the surface is achieved through a rehybridization producing a tilted, asymmetric dimer with an up dimer atom (s-like orbital, occupied) and a down dimer atom (p-like orbital, empty), as shown in Figure 1.2(a). When 1/2 ML Sr is deposited on a clean, reconstructed Si (001) surface, Sr atoms occupy the trough sites between the dimer rows. As each Sr atom donates its two electrons to one dimer, the asymmetric dimer is un-tilted as in Figure 1.2(b). This 1/2 ML Sr template on Si has been studied intensely both theoretically and experimentally. However, the mechanism of how the Sr template facilitates perovskite epitaxy is not yet clear. In this dissertation, I focused on the surface reconstructions of the Sr template as a function of Sr coverage and investigated its effects on the electronic structure of the surface. In addition to Sr on Si (001), Ba templates on Si were also studied in this work.

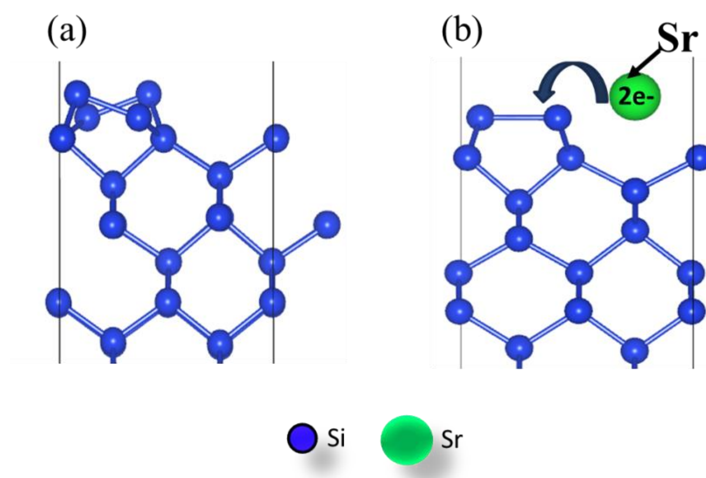

Figure 1.2 (a) Asymmetric tilted dimer of clean Si (001) and (b) flattened dimer of Si (001) with 1/2 ML Sr.

Other topics that were investigated in this dissertation are the strain relaxation behavior of epitaxial $SrTiO_3$ films on Si using *in situ* oxygen annealing, and the structural and electrical properties of conductive La-doped $SrTiO_3$ films that were grown under different biaxial strains (tensile and compressive). Perovskite oxides can accommodate an imposed strain via structural distortions such as a change in crystal lattice symmetry (cubic to tetragonal or orthorhombic), which is accompanied by tilting and/or rotation of BO_6 octahedra in the ABO_3 perovskite structure[27-29]. The resulting structural changes due to the strain can give rise to exotic properties that are not found in bulk oxides. For example, $LaCoO_3$ films with biaxial tensile strain in-plane shows insulating ferromagnetic behavior, which is not observed in unstrained $LaCoO_3$ as shown in Figure 1.3(a)[19,30]. Another interesting example is that of tensile strained $EuTiO_3$, which becomes ferromagnetic from its normally antiferromagnetic state as seen in Figure 1.3(b)[31]. These transitions from non-ferromagnetic to ferromagnetic behavior are obtained solely by an external epitaxial strain.

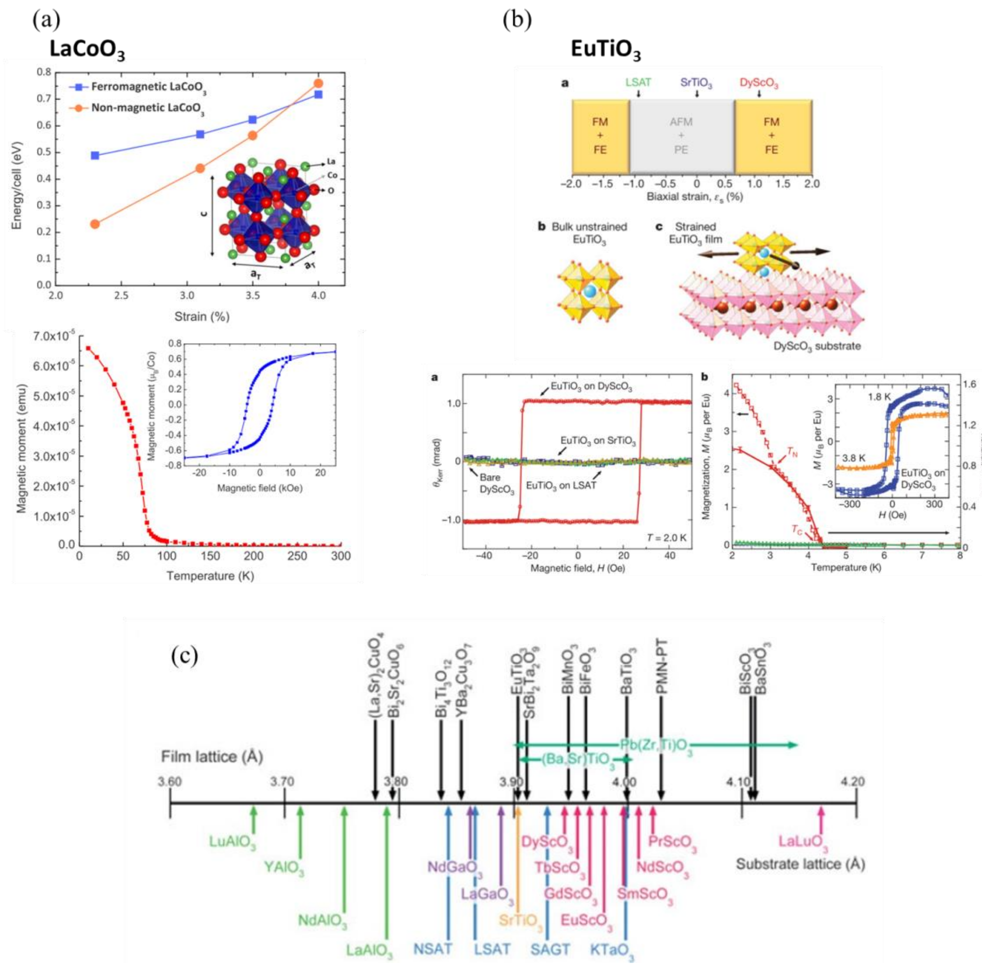

Figure 1.3 Magnetic properties changes as a function of strain in (a) $LaCoO_3$ and (b) $EuTiO_3$. (c) A variety of oxide substrates with different lattice constants that can be used to impose strain in oxide thin films.

Strain is a powerful tool to control the properties of a material and offers great promise for device applications. To utilize the emergent properties from the strained films, strained $SrTiO_3$ films on Si or on oxide substrates with various lattice constants can be utilized (Figure 1.3(c))[32].

In Chapter 2, I review the technique of molecular beam epitaxy (MBE) and *in situ* reflection high electron energy diffraction (RHEED). These two techniques are used heavily and in conjunction with each other during my research to grow high quality oxide thin films

In Chapter 3, the characterization methods I used in my work are presented and described in some detail. These include X-ray/Ultraviolet photoemission spectroscopy (XPS/UPS), X-ray diffraction (XRD), and atomic force microscopy (AFM).

In Chapters 4 and 5, I present the results of the study of atomic reconstruction of Sr on Si (001) as a function of Sr coverage, and the corresponding surface core-level shifts of Si (001) with Sr and without Sr using XPS. I also studied the behavior of another alkaline earth metal Ba on Si, and compared its behavior with Sr on Si. This work is supported by theoretical calculations done by Hosung Seo in the Demkov research group. These theoretical results will also be discussed in this dissertation.

In Chapter 6, I show the results of the study of the strain relaxation behavior of $SrTiO_3$ on Si (001). As a result of oxygen annealing, an SiO_2 layer is formed at the interface between $SrTiO_3$ and Si (001). The strain relaxation behavior due to the post-deposition annealing as a function of oxygen pressure and annealing time were investigated. The effect of the SiO_2 interlayer thickness on the strain relaxation behavior is discussed.

In Chapter 7, I prepared the surface of bulk $SrTiO_3$ substrates using three different methods to obtain a clean surface. The surfaces were prepared by: (1) etching in a buffered solution of HF (BHF), (2) etching with Arkansas method, (3) water leaching and (4) water boiling. Using high-resolution angle-resolved photoemission spectroscopy (ARPES), the electronic structures of the surfaces were studied. The measurements were

done by Dr. Richard C. Hatch, and accompanying theoretical calculations were done by Kurt D. Fredrickson in the Demkov group.

In Chapter 8, I present the structural and electrical properties of La-doped $SrTiO_3$ films grown on four different substrates that impose various levels of strain: $LaAlO_3$, LSAT, $SrTiO_3$, and $DyScO_3$. I measure the carrier density, resistivity and mobility as a function of strain, and also investigated the structural changes as a function of doping concentration. This work was done in collaboration with Dr. Stefan Zollner at New Mexico State University for optical measurements, and with Andy O'Hara in the Demkov group for theoretical calculations to explain the transport measurements.

In Chapter 9, I investigated the optical properties (complex dielectric function) of $SrTiO_3$ quantum wells (QW) grown by MBE. The QW is composed of $LaAlO_3$ (LAO)/STO on LAO substrate with different STO thicknesses. Optical properties were measured using spectroscopic ellipsometry (SE) in the range of 1.0 eV to 6.0 eV at room temperature. This work was done in collaboration with Dr. Stefan Zollner at New Mexico State University for optical measurements to explain the absorption edge shift as a function of QW thickness. The Z-contrast cross-section STEM images were taken by Dr. Qian He and Dr. Albina Borisevich at Oak Ridge Ntional Laboratory.

In Chapter 10, a summary of the entire work and future outlook will be presented.

Chapter 2. Molecular beam epitaxy and in-situ RHEED

2.1 Historical overview

Molecular beam epitaxy (MBE) is a powerful thin film deposition method that is capable of controlling the growth process at the atomic-level. The term "Epitaxy" is derived from Greek word, "epi" meaning "on" and "taxis" meaning "arrangement". This refers to the growing of a single crystalline film which has a particular orientation on top of another single crystal substrate. The substrate serves as a "seed" crystal whose structure the crystalline film follows.

The early "molecular beam epitaxy" concept was developed by Günther in 1958 [33]. For the growth of III-V compound semiconductors (GaAs), Günther had controlled three different temperatures, i.e., the temperatures of the group V and the group III element sources, and the growth temperature. The sample was not grown on a substrate epitaxially. However, his growth concept later evolved into molecular beam epitaxy.

The beginning of MBE in earnest was a result of the highly demanding nature of the epitaxial growth of III-V compound semiconductors. Researchers had the challenge to make thin crystalline semiconductor materials having a direct band gap along with their high electron mobility for their potential use in electronic and photonic devices as well as their lattice match to other III-V compounds. These significant advances between 1968 and 1973 were brought from Bell Laboratories in Murray Hill, NJ, with John Arthur, Jr., examining the mechanisms of GaAs growth[34] and Alfred Cho ('father of MBE'[35]), developing the instrument technology and optimized growth conditions for device quality material. This new technique was first named "molecular beam epitaxy" by Cho *et al.* in

1970[36]. This method allowed one to control the growth as a sequenced layer by layer deposition. In addition, another driving force of modern MBE systems was caused by the parallel developments in vacuum technology[37].

Based on the fundamental research of MBE, epitaxial growth of crystalline oxides using MBE started in the 1980s spurred by the discovery of the high-temperature superconductor, $YBa_2Cu_3O_{7-\delta}$ [38]. Later on, researchers focused on functional oxides with perovskite structure that possess other novel properties like colossal magnetoresistance ($Re_{1-x}A_xMnO_3$, where Re is a rare earth metal and A is a divalent alkali)[7], ferro-, pyro-, piezoelectricity[39], and multiferroicity[40].

2.2 Molecular Beams Epitaxy – Principle

2.2.1 Kinetic theory of gases

In MBE, elemental sources are evaporated from effusion cells that are focused onto the substrate, which is at an elevated temperature under ultra-high vacuum (UHV) conditions (10^{-9}-10^{-10} Torr). The arriving atoms then combine to form the epitaxial film on the substrate. Under UHV, the mean free path of atoms is much larger than the distance between the substrate and the source. Therefore, the word “beam” used in MBE means that atoms or molecules are travelling to the substrates without collisions or interactions with other atoms or molecules until they reach the substrate as a result of the large mean free path. Molecular beam epitaxy has been described as “spray painting a surface slowly with atoms or molecules”[41].

In a solid source MBE system, materials (Sr, Ba, Al, La, etc) are heated in Knudsen effusion cells until they start to evaporate into the vacuum chamber. The Knudsen effusion cell or K-cell is composed of a crucible, heating filaments, water

cooling, and heat shields. Each material to be evaporated is inside a Knudsen effusion cell, which has an enclosure with a small hole. Because the evaporating surface is much larger than the area of the small hole within enclosure, the molecules maintain the equilibrium vapor pressure p_{eq} inside the effusion cell. To understand how molecules spread out from the effusion cells, we need to consider the kinetic theory of gases. In the kinetic theory of gases, the assumptions are that the gas molecules do not interact with each other and the momentum is unchanged after their collisions. Under these assumptions, the velocity distribution of the molecules is calculated in accordance with the Maxwell-Boltzmann distribution. The Maxwell distribution law gives the velocity distribution as:

$$f(\vec{v})d^3\vec{v} = n[\frac{m}{2\pi kT}]^{3/2}e^{-mv^2/2kT}d^3\vec{v}. \quad (2.1)$$

where $n \equiv N/V$, n is the number of molecules per unit volume, m and v are the mass and velocity of a molecule, $f(\vec{v})d^3\vec{v}$ is the mean number of molecules per unit volume with velocity in the range between $\vec{v}$ and $\vec{v}$+d$\vec{v}$. Usually, it is more convenient to convert the velocity distribution to the speed distribution of the molecules because the energy of the molecule depends on its speed, not on its velocity.

The Maxwell distribution for the speeds is:

$$f(v)dv = 4\pi nv^2[\frac{m}{2\pi kT}]^{3/2}e^{-mv^2/2kT}d^3\vec{v}. \quad (2.2)$$

The mean speed is calculated as

$$\bar{v} = \frac{1}{n}\int_0^\infty v\, \mathrm{f}(v) d^3\vec{v} = \frac{1}{n}\int_0^\infty v\, \mathrm{f}(v) 4\pi v^2 dv = \sqrt{\frac{8kT}{\pi m}}. \tag{2.3}$$

Let us figure out how many molecules of a gas strike a unit area in unit time. If we consider that dA is a unit area of the wall where the hole is, and molecules move in the z-direction normal to the unit area in Figure 2.1, we can calculate how many molecules pass through the unit area.

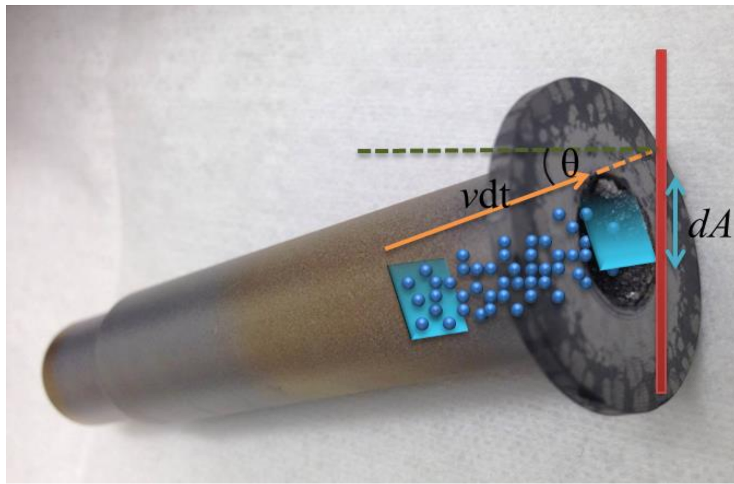

Figure 2.1 Molecules evaporate from the hole of a crucible. Molecules move a distance vdt through unit area, dA, with speed v and at angle θ from the normal to dA. This crucible is from DCA.

Consider the molecules with speed $|\vec{v}|$ that move a distance $|\vec{v}|dt$ in time interval dt. All the molecules within area dA and height $|\vec{v}|dtcos\theta$ will strike the wall. The number of molecules of the gas which strike the wall is equal to the number of molecules of the gas which leave the hole. Therefore, the number of molecules which will pass through dA in dt is $\mathrm{f}(\vec{v})d^3\vec{v}\, dA|\vec{v}|dtcos\theta$. When molecules are evaporated through the small hole, they create a flux defined as the number of molecules per unit area per unit time that leave the hole. Thus, the flux of molecules is $\Phi(\vec{v})d^3\vec{v} =$

$f(\vec{v})|\vec{v}|cos\theta d^3\vec{v}$. If we consider Φ_0 as the total flux of molecules per unit area per unit time, we can obtain

$$\Phi_0 = \int_{v_z>0} f(\vec{v})|\vec{v}|cos\theta d^3\vec{v}\,. \tag{2.4}$$

Because there are no collisions when the molecules pass through the hole, we only focus on $v_z > 0$. By converting to spherical coordinates, the total flux of molecules is[42]

$$\begin{aligned}\Phi_0 &= \int_{v_z>0} v^2 \mathrm{dv}\, \sin\theta f(v) v cos\theta d\theta \int_0^{2\pi} d\phi \\ &= \int_0^{\infty} f(v) v^3 dv \int_0^{\frac{\pi}{2}} sin\theta cos\theta \int_0^{2\pi} d\phi \\ &= \pi \int_0^{\infty} f(v) v^3 dv \\ &= \frac{1}{4} n\bar{v} = \frac{p}{\sqrt{2\pi mkT}}\end{aligned} \tag{2.5}$$

since n=p/kT.

Equation 2.5[42] was derived by Hertz[43] in 1882, using the kinetic theory of gases and the Maxwell distribution of velocities of gases. Additionally, he found experimentally that vaporization flux was proportional to $(p_{eq} - p)$, where peq is the equilibrium vapor pressure and p is the hydrostatic pressure acting on the evaporant in the gas phase in the vacuum chamber. Since effusion occurs in an UHV chamber, p can be practically set to zero. Later, in 1915, Knudsen[44] found that vapor molecules impinging on the condensed phase were reflected back. So, he introduced the sticking coefficient, α_v, for vapor molecules on the surface. This value is between 0 and 1. Hence, we can write vaporization flux, Jv as:

$$J_v = \alpha_v p_{ev}\sqrt{\frac{1}{2\pi m k_B T}}\ \ [\mathrm{m}^{-2}s^{-1}]. \tag{2.6}$$

The Equation 2.6 is the Hertz-Knudsen equation. This equation describes the case of an ideal Knudsen cell which has a thin walled orifice. However, in practice, the orifice of a Knudsen cell has a finite wall thickness, so we need to modify Equation 2.6[45]. The total effusion rate, which is the total number of molecules effusing from the Knudsen cell into the vacuum through A (hole area) per unit time is given by

$$\frac{dN}{dt} = J_v A = \alpha_v A p_{eq}\sqrt{\frac{1}{2\pi m k_B T}}\ . \tag{2.7}$$

2.2.2 Vapor Pressure of materials

As shown in Equation 2.5, the total effusion rate/total flux of molecules is related to the vapor pressure of a material at a certain material temperature. In an MBE system, the vapor pressure is controlled by the effusion cell temperature. Figure 2.2 shows the vapor pressure as a function of the material temperature for various elements. To achieve a flux of about 1 monolayer (ML) per min, the vapor pressure should be around the 10^{-3}~10^{-4} Torr region because the total flux is ~P (Torr, vapor pressure) $\times\ 0.5\times10^{21}$ /cm^2 sec as derived from Equation 2.5. Therefore, it is possible to find the expected effusion cell temperature that corresponds to the flux of 1 ML/min by looking at vapor pressure charts such as Figure. 2.2.

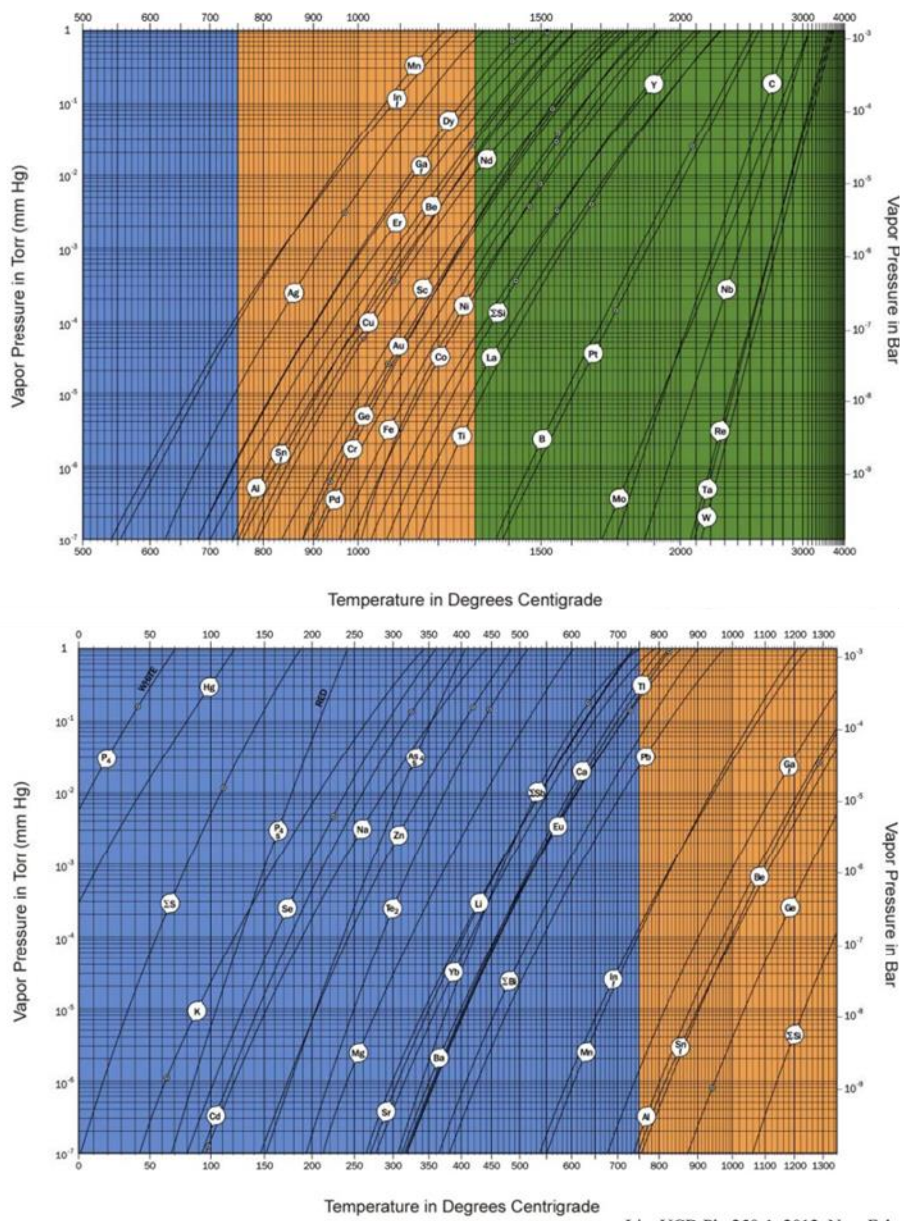

Figure 2.2 The vapor pressure as a function of temperature from Veeco.

2.2.3 Effusion - Geometry

The process by which evaporation occurs through a small hole is referred to as "effusion". Since evaporating molecules are emitted from a small hole, effusion has a dependence on the direction and is not isotropic. Hence, we need to investigate the geometry of the evaporation and the relative position of the substrate when deposition occurs.

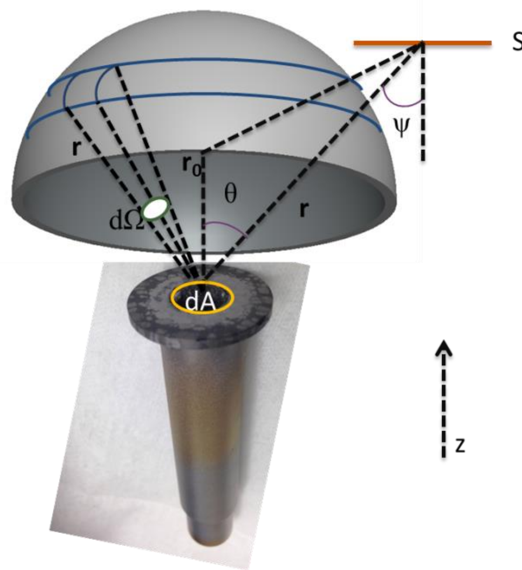

Figure 2.3 Schematic view of the angular distribution of flux of molecules over the solid angle dΩ on a sphere of radius r between the angle θ and θ+ dθ. The molecules are condensed on the surface S.

Consider the molecules within a volume V with an exit angle of θ distributed at a temperature T. We assume a molecule of gas moves though the small hole with velocity in the z-direction. To find the flux of molecules over the solid angle, dΩ, we need to modify the flux of molecules that pass through dA in time dt with a velocity between v and v+dv using Equation 2.5 since the molecules with velocity in the z-direction can leave the effusion cell:

$$dJ = \int_0^{\infty} n\left(\frac{m}{2\pi k_B T}\right)^{\frac{3}{2}} e^{-\frac{mv^2}{2k_B T}} v cos\theta\, v^2 sin\theta d\theta d\phi dv$$
$$= \frac{1}{4\pi} n\bar{v} cos\theta d\Omega \quad (2.8)$$

where $d\Omega = \sin\theta d\theta d\varphi$ and $v_z = v\cos\theta$.

Therefore, the total flux J is

$$dJ = J\cos\theta\, \frac{d\Omega}{\pi} \quad (2.9)$$

Equation 2.9 is called the cosine law of vapor emission[45]. This means that the flux of molecules through the effusion cell has a directional dependence. Let us consider S to be an area which the molecules are condensed in Figure 2.3. The area S is given by

$$dS = \frac{r^2 d\Omega}{cos\psi} \quad (2.10)$$

Using Equation 2.10 and 2.11, the flux of the molecules per unit area where condensation occurs is given by

$$\frac{dJ}{dS} = J\frac{d\Omega}{\pi} cos\theta \frac{1}{dS} = J\frac{cos\theta cos\psi}{\pi^2} \quad (2.11)$$

If the deposition area is on a spherical surface, θ is equal to ψ and r_0 is equal to r in Figure 2.3. Therefore,

$$\frac{dJ}{dS} = \frac{J}{4\pi r^2}. \quad (2.12)$$

From Equation 2.12, spherical geometry guarantees that the flux of molecules is uniform, compared to infinite plane substrate geometry and hemispherical geometry[46].

2.3 Molecular Beam Epitaxy (MBE) – Equipment

I used the DCA 600 oxide MBE deposition system for my experiments. The MBE chamber is connected to a transfer tube, which enables the movement of samples to the analyzer chamber and the atomic layer deposition (ALD) growth chamber *in situ*. The schematic view of the system is shown in Figure 2.4. The total pressure of the residual gas in the chamber is maintained around 3×10^{-10} Torr. To maintain the ultra-high vacuum (UHV), which is defined as the pressure regime below $\sim10^{-9}$ Torr[45], we need to consider several things, such as baking the chamber, low outgassing materials, high speed pumps, cooling systems and a chiller.

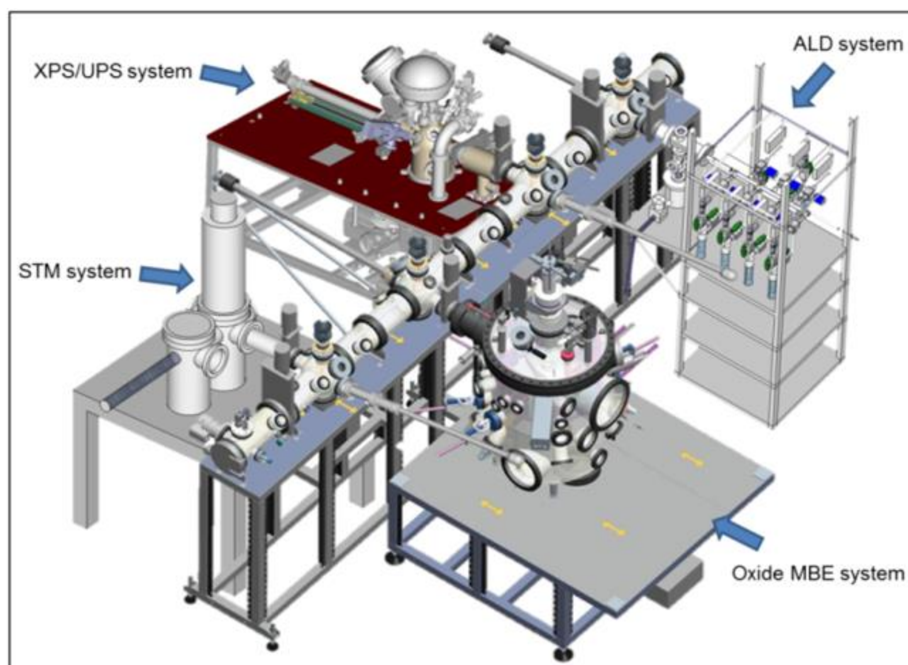

Figure 2.4 DCA 600 oxide MBE deposition system which is connected to the transfer chamber equipped with another growth chamber and the XPS/UPS analysis system. The image comes from the group home page[47].

2.3.1 The component descriptions of Molecular Beam Epitaxy (MBE)

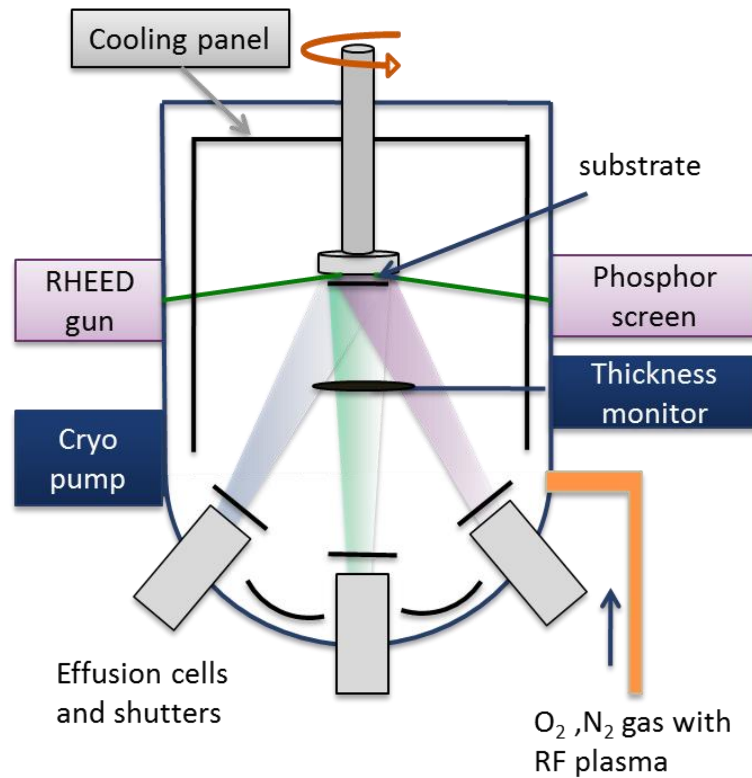

Figure 2.5 Schematic view of the oxide MBE system.

- Chamber : The chamber is made from stainless steel, which is not oxidized and outgasses less compared to other structural metals. When the chamber is exposed to the air, water molecules and other gases are adsorbed on the chamber walls. The vacuum pumps by themselves are not enough to remove all the adsorbed gases especially water vapor, so heating of the chamber to over 200 °C for sufficiently long time (around 72 hours) is required.
- Pumps : A combination of a scroll pump and a turbomolecular pump allows the chamber pressure to be pumped down from atmosphere down to ~10^{-6} Torr (high vacuum region). To achieve UHV, an ion pump or cryopump has to be used. Both

of these are oil-free vacuum pumps, so that the chamber is not contaminated by oil back streaming. The transfer chamber in the lab is pumped with three ion pumps from the Gamma Vacuum company. In contrast to ion pumps, cryopumps are much less susceptible to damage if the pressure goes up high all of a sudden due to their capability of handling higher gas loads. Also, when Sr, Ba or Eu is outgassed (these materials are so reactive that they are easily combined with O_2 and H_2O vapor in the atmosphere), the partial pressures of water vapor and oxygen are extremely high. Due to their higher pumping speeds, the growth chamber is equipped with CTI On-Board cryogenic vacuum pump (model 8). This cryopump has high pumping speed, especially for water vapor (7500 liters/sec).

- Heating system for the sample : Direct heating method (Joule heating) is not compatible with an oxygen environment. If the wires are connected to the sample for heating in oxygen, the wires are easily burned. So, the sample is indirectly heated by heat radiating from a silicon carbide heating block behind the sample. For growth uniformity, the sample stage is rotated during the growth.
- Cryopanels : An alcohol cooled cryopanel surrounds the upper half of the main chamber wall. This prevents re-evaporation from the chamber walls when effusion cells are hot. In addition, a water cooled cryopanel is also placed in the horizontal plane of the effusion cell apertures in the lower part of the main chamber. Water cooling provides the thermal isolation between the hot effusion cells and the rest of the chamber. The Figure 2.6 shows the alcohol-filled upper cryopanel inside the MBE chamber.

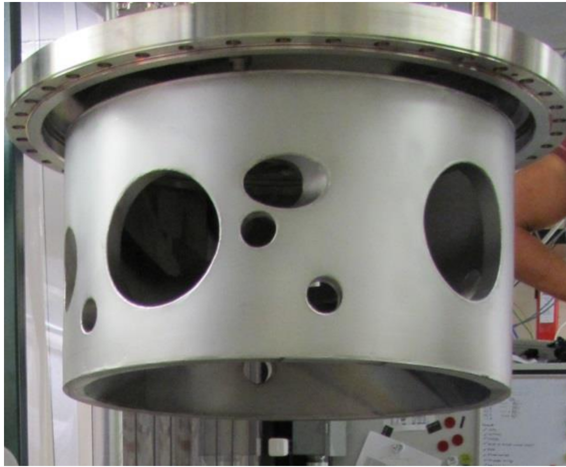

Figure 2.6 The cryopanel inside the main MBE chamber.

- Quartz crystal microbalance (QCM) or thickness monitor : A QCM is an instrument that measures the mass accumulation or deposition rate of a material. The QCM consists of a thin and round slice of crystalline quartz with gold electrodes on each side. When an electric field is applied to the quartz, it oscillates at its resonant frequency. When a mass is deposited on the quartz, the resonant frequency of the QCM decreases. Equation 2.13[48-50], which is called the "Sauerbrey equation", shows that the resonant frequency change is proportional to the mass change. The QCM instrument displays amounts of deposited material as an average thickness. When I check the flux of a certain material, the shutter of that source is opened for over 10 min prior to recording the deposition rate (Å/min) over a 5 min interval. This measurement is repeated several times. The average rate value is then used as the rate of deposition.

$$\Delta \mathrm{f} = -C_f \times \Delta m \tag{2.13}$$

where Δf = the observed frequency change in Hz

Cf = the sensitivity factor of the crystal in Hz/ng/cm^2

Δm = the change in mass per unit area in g/cm^2

- Effusion cell : The effusion cell is a crucial component to produce a molecular beam in MBE. The effusion cell has a source material in condensed phase inside an inert crucible. The source in the crucible is heated using a resistance heated filament. The filament is coiled up around the crucible and supported by Pyrolytic Boron Nitride (PBN) which prevents the filament from moving. The cell temperature is carefully controlled to maintain a reproducible flux of the material source. Both the filament and the crucible are surrounded by a radiation shield to minimize heating of areas outside the effusion cell. The cell temperature is monitored using a thermocouple that is attached to the bottom of the crucible supporter in the DCA 600 MBE system. Figure 2.7 shows the effusion cell used in my group.

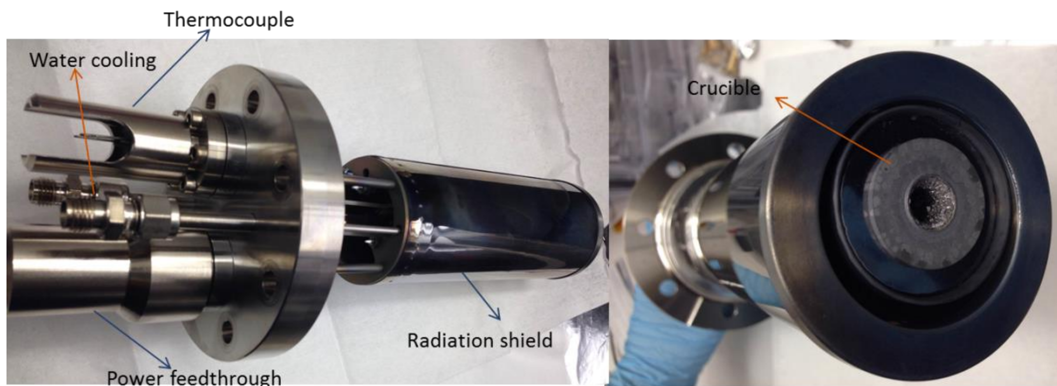

Figure 2.7 The effusion cell used in MBE system.

Depending on the material sources, we need to think about several important considerations when selecting crucibles to use. The crucible has to be chemically and

thermally compatible with the material source. Further, outgassing impurity levels should be very low when the crucible is heated up. In the MBE system in my group, there are six effusion cells that are placed around the chamber and all directed towards the substrate. Low temperature effusion cells are operated up to 1300 °C, while high temperature effusion cells are operated up to 1900 °C. Table 2.1 shows the crucibles which are currently used in DCA 600 MBE system.

Low temperature effusion cell				High temperature effusion cell	
Sr	Eu	Ba	Al	Ti	La
PBN	PBN	PBN	PBN	TiC	W

Table 2.1 Crucible selection depending on the materials to be evaporated.

- E-beam evaporator : The electron beam evaporator is an alternative tool to evaporate materials that have a very high melting point. The electron beam is generated by a thermionic emission from a heated filament (cathode). The emitted electron beam is then directed and accelerated toward the crucible (anode) by applying a large voltage (~8 kV). The emitted electron beam is focused on the material by magnetic and electrostatic fields which allows the beam to be bent as well as rastered. The electron beam makes the material heat up and evaporate.
- RF plasma source : A 13.56 MHz RF discharge is used to generate reactive oxygen species, atomic oxygen O and metastable excited molecular oxygen O_2[51]. Many transition metals exhibit several oxidation states. The low oxidation states are obtained very easily using molecular oxygen, but the higher oxidation states

may not be obtained easily. As a result, to get the fully oxidized states for some materials, we usually use the RF plasma source.

2.4 Reflection High Energy Electron Diffraction (RHEED)

2.4.1 Technical Description

RHEED is a very popular technique for monitoring the crystalline surface and morphology of the sample in-situ during sample growth. An electron beam of high energy (10-30 keV) hits the sample surface at a grazing angle of a few degrees (typically 0°~5°). The low grazing angle keeps the electron beam penetration depth small and provides high surface sensitivity (a few atomic layers). The schematic view of the basic set up of RHEED is shown in Figure 2.8.

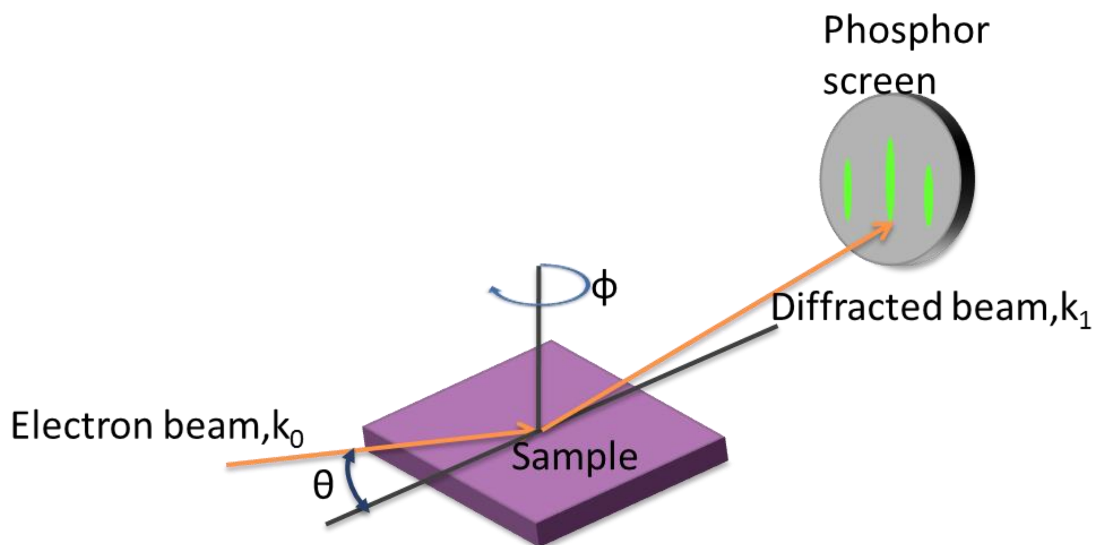

Figure 2.8 The experimental set up of the reflection geometry for RHEED.

The diffracted electron beam is directed to the phosphor-coated viewport equipped with a charge-coupled device (CCD) camera. The diffracted electron beam is

detected by the emission of visible light due to the fluorescence effect. As a result, we can observe and capture the diffraction patterns on the computer to which CCD camera is connected. The electron gun and the phosphor screen are aligned perpendicularly to the growth direction in an MBE chamber. As a consequence of this condition, RHEED allows us to monitor the sample surface structure or surface reconstruction *in situ* without any interruption of the growth. In addition, when the sample is rotated by φ as shown in Figure 2.8, we can observe the diffraction patterns in all azimuthal directions. The small grazing angle of incidence makes the penetration depth limited to a few atomic layers. For this reason, the RHEED is highly sensitive to the surface.

2.4.2 The principle of electron diffraction

To interpret the diffraction pattern of RHEED, we need to recall some basic solid state physics. The analysis of electron diffraction is usually based on the kinematic theory of diffraction[52]. The basic assumptions are as follows: elastic scattering occurs so that there is no energy transfer from electrons to the sample. This implies that since the intensity of the scattered beam at the scattering sites is much smaller than that of the incident beam, it is possible to ignore the energy loss of the incident beam after the scattering occurs at the scattering sites. The kinematic theory also assumes that the scattered beam does not act as a new incident beam. As a result, we can write $|\overrightarrow{k_0}| = |\overrightarrow{k_1}| = k$, where $\overrightarrow{k_0}$ and $\overrightarrow{k_1}$ are the incident and diffracted wave vectors, respectively. The geometrical construction of diffraction can be visualized by the Ewald sphere construction in reciprocal space. The Ewald sphere construction is combined with energy, $|\overrightarrow{k_0}| = |\overrightarrow{k_1}| = k$, and momentum conservation, $\vec{k}_1 = \vec{k}_0 + \vec{G}$ where G is a reciprocal lattice vector.

The Ewald sphere can be constructed with a radius $2\pi/\lambda$. The wavelength λ corresponding to the electron energy E is given by the Equation 2.14[53] , where m_0 is the electron mass.

$$\lambda = \left[\frac{2m_0E}{h^2}(1+\frac{E}{2m_0c^2})\right]^{-1/2} \approx \frac{12.247}{\sqrt{E(1+10^{-6}E)}}\ [\text{Å}] \quad (2.14)$$

Generally, I used 21 keV for generating electrons in my lab. By plugging the electron energy into the Equation 2.14, the wavelength is 0.0836 Å. The radius of the Ewald sphere construction is 75.2 $Å^{-1}$. In comparison, the reciprocal lattice spacing of $SrTiO_3$ [100] is 1.6 $Å^{-1}$ (the lattice constant of $SrTiO_3$ is 3.905 Å). The wave vector of the incident beam is much larger than the distance between the adjacent points of reciprocal lattice of the crystal. Here, since we are dealing with surface diffraction, we need to consider that reciprocal lattice points are replaced by infinite reciprocal lattice rods perpendicular to the surface as shown in the side view of Figure 2.9(a). The rods are labeled using two Miller indices (hk) where h represents the Laue zone, k means rods which can be negative (denoted with a bar on top of the number) or positive, depending on which side of the axis defined by the incident beam in Figure 2.9(b) they are on. The intersection between the reciprocal rods and the Ewald sphere gives rise to the diffraction spots on a semi-circular arc of diffraction patterns on the RHEED screen, as shown in Figure 2.9(b). The diffraction spots satisfy Bragg's law and the Laue condition which determine the constructive interference for electrons. The rings are called "Laue zones or Laue rings" and are labeled 0th, 1st, 2nd etc. Figure 2.9(b) shows the Laue zones, 0th in cyan, 1st in orange, and 2nd in purple.

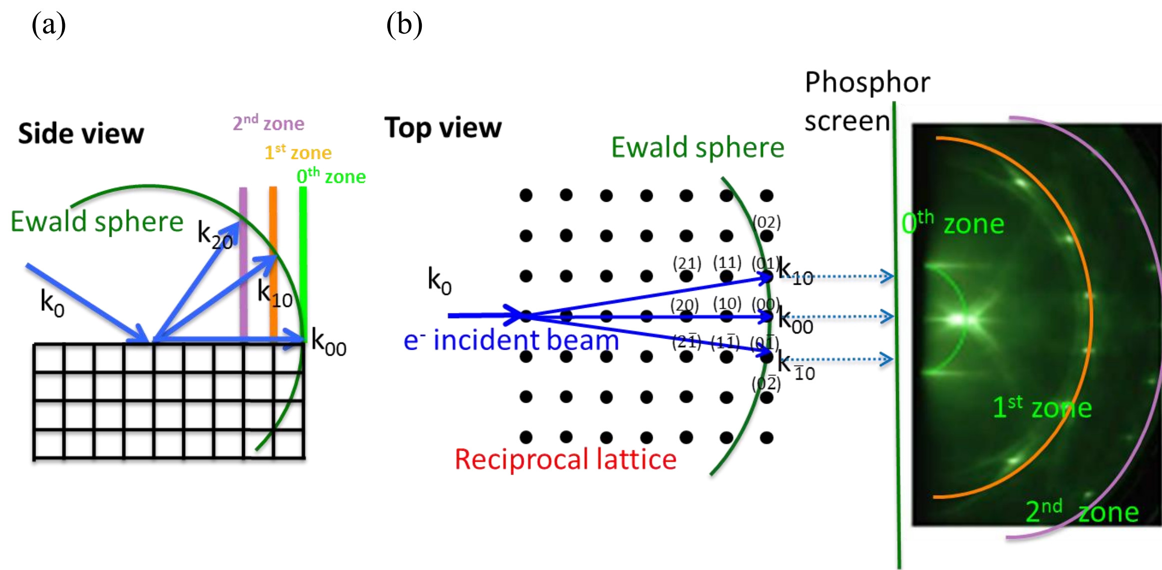

Figure 2.9 Schematic view of Ewald sphere constructions. (a) Side view of the Ewald sphere with the reciprocal lattice rods with indexes. (b) Top view of the Ewald sphere and the Laue zone labeled 0th, 1st, and 2nd.

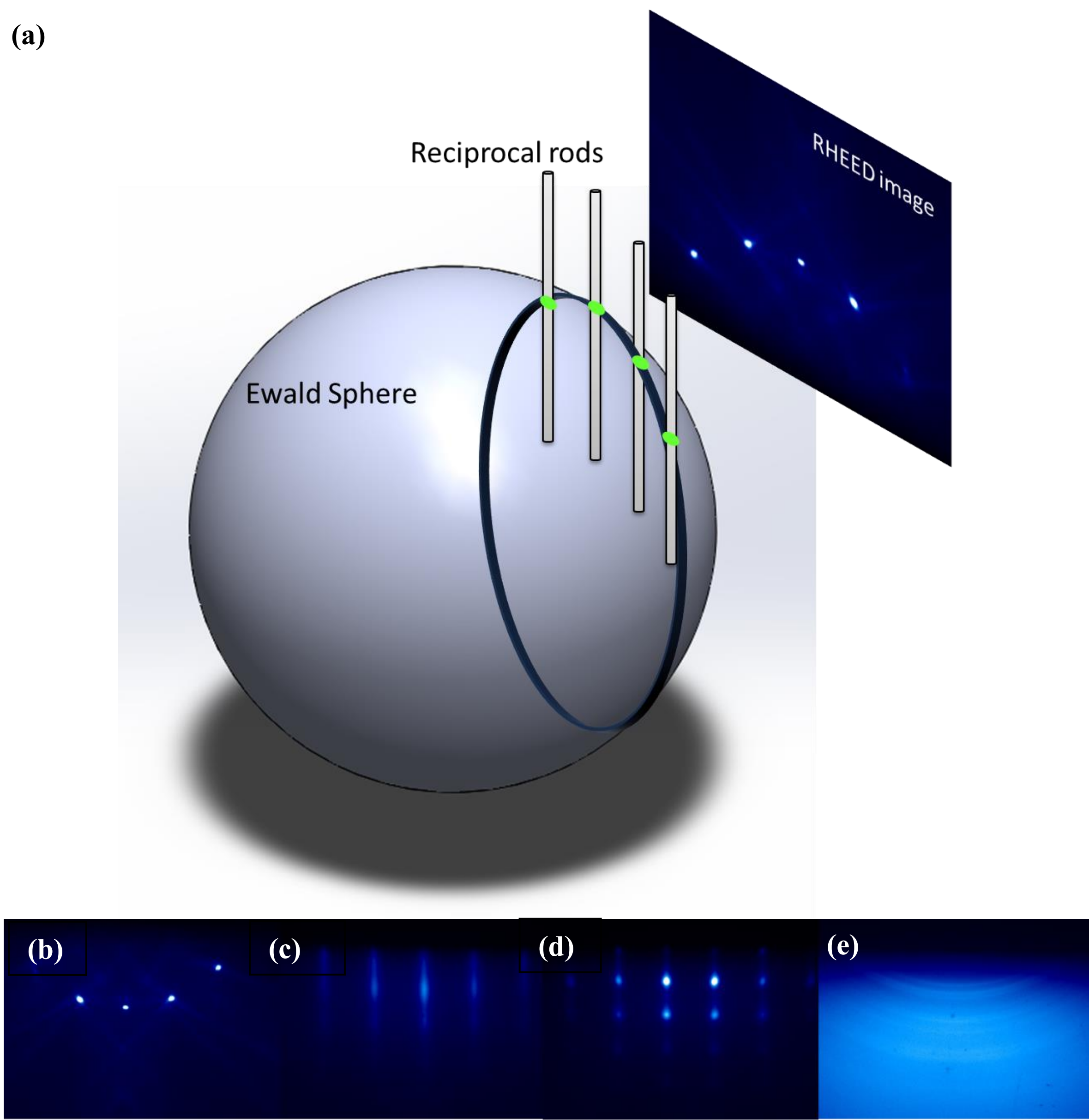

Figure 2.10 (a) The intersection of the Ewald sphere with reciprocal rods forms spots aligned along the semi-circular arc. The RHEED patterns from (b) the perfectly flat surface, (c) the surface with monolayer roughness, (d) the surface with large roughness, and (d) amorphous or polycrystalline film. (The RHEED images are from (b) STO substrate, (c-e) STO films on Si, taken by Miri Choi in UT Materials Physics Lab.)

From the RHEED patterns, we can evaluate the surface structures or the surface roughness of a sample. If a crystalline surface is perfectly ordered, we can observe a series of clear diffraction spots on the Laue rings as shown in Figure 2.10(a,b). However, if the surface has imperfections such as roughness or steps, the rods broaden to have a finite width. Therefore, we can observe "streak" diffractions as shown in Figure 2.10(c). If a surface is very rough or has islands from 3D growth (Volmer-Weber growth [54]), the reciprocal rods are replaced by bulk reciprocal lattices due to the surface asperities. Since the diffraction pattern is produced in transmission through the surface asperities, the RHEED patterns show many spots which are different from the spots which are produced on the Laue rings, as shown in Figure 2.10(b) and (d). For a polycrystalline surface, a polycrystalline ring pattern occurs in the RHEED image (Figure 2.10(e)). Besides being able to qualitatively know the surface structures of the film using RHEED, the growth rate can be also determined by RHEED beam intensity oscillations [55,56]. The intensity of the primary RHEED spot (the 00 rod -- even though the sample is rotated, one can definitely see the bright spot that doesn't change its position) depends on the overall surface roughness, with a smooth surface producing an intense spot, while a rough surface producing a weak spot. The beam intensity can be used to track the fraction of a monolayer (ML) growth of the material. When the atoms are deposited below 0.5 ML, the reflected beam become scattered due to the several growth centers and the destructive scattering. At 1 ML coverage, the beam intensity becomes bright again. At 0.5 ML, the minimum intensity is observed, while the maximum intensity is observed at 1 ML in Figure 2.11. One single oscillation means the completion of 1 ML of growth of the material. From the period of one oscillation, we can estimate the growth rate of the material and then calibrate the beam fluxes accordingly.

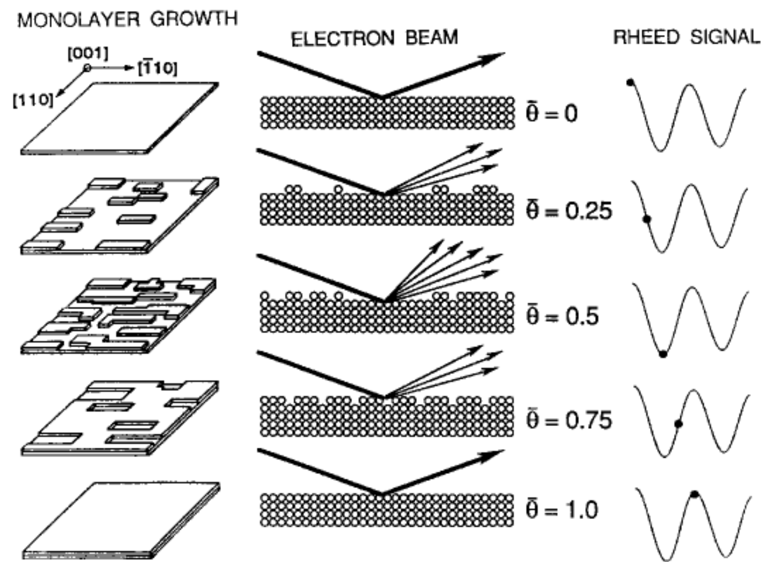

Figure 2.11 The mechanism for RHEED intensity oscillations from specular spot during the growth of one ML. The original caption is from[57], copyright 2002.

If we know the number of oscillations, we can also determine the thickness of the film. However, if the film becomes very rough or when the surface is sufficiently disordered (either thermally or structurally), the total intensity of the primary RHEED spot becomes smaller as the deposition progresses. In summary, *in situ* RHEED is a very powerful tool to monitor the growth of film deposition in real time and to calibrate the fluxes.

Chapter 3. Experimental Techniques

Experimental techniques commonly used for sample characterization are described in detail in this chapter. X-ray diffraction (XRD), X-ray reflectivity (XRR), X-ray photoelectron spectroscopy (XPS), Ultraviolet photoelectron spectroscopy (UPS) and atomic force microscopy (AFM) are employed to characterize the morphological, structural, chemical and electrical properties of oxide films and the Sr and Ba templates on Si (001).

3.1 INTRODUCTION

X-ray diffraction (XRD) is a characterization technique used to determine the degree of crystallinity, crystal orientation, and lattice spacing of the films. A crystal is composed of arrays of planes in which atoms are positioned periodically. When an X-ray beam is incident onto the lattice planes of a crystal, the X-rays are scattered by the electrons of the constituent atoms (scattering centers) without a change in wavelength. Because the wavelength is not changed after scattering, this process is called "elastic scattering"[58,59]. At specific directions, the amplitude of the scattered x-ray beam is enhanced as a result of constructive interference between x-rays scattered from different lattice planes.

When Bragg's law is satisfied, diffraction patterns can be observed. The condition is summarized in Equation 3.1[59,60], where the integer n is the order of the diffracted beam, λ is the wavelength of the incident X-ray, d is the distance between parallel planes of atoms in real space, and θ is the angle of the incident X-ray beam, as shown in Figure 3.1(a). For diffraction to take place, the scattered X-ray beams must be in phase and the difference in path length can be expressed as an integer multiple of wavelengths.

$$n\lambda = 2d_{hkl} sin\theta \tag{3.1}$$

Because the incident and the diffracted X-rays can be represented by its wavevector, diffraction can also be explained using the Ewald sphere construction in reciprocal space. The incident X-rays have wavevector k_i, while the diffracted X-rays have wavevector k_f. Because elastic scattering occurs during the diffraction, the length of the wavevector is $|k_i| = |k_f| = 2\pi/\lambda$. The difference between the wavevectors of incident and diffracted X-rays is expressed by $\vec{q}_{hkl}$, which is perpendicular to the lattice planes (hkl) in real space. The Laue condition for constructive interference will occur if the difference between incident and diffracted wavevectors, $\vec{q}_{hkl=} \vec{k}_f - \vec{k}_i$ is equal to a reciprocal lattice vector. Using trigonometry, $|\vec{q}_{hkl}|$ can be expressed by $|\vec{q}_{hkl}|$ $=2\pi/d_{hkl}=2|k_i|\sin\theta$ as shown in Figure 3.1(b). The amplitude of $|\vec{q}_{hkl}|$ is equal to $4\pi\sin\theta/\lambda$. Therefore, we can conclude that the Laue condition is equivalent to Bragg's law.

My XRD measurements were performed on a Philips X'pert commercial diffractometer with Cu Kα radiation (λ=1.5406 Å). For selected films, in-plane and out-of-plane XRD measurements were carried out at the National Synchrotron Light Source (λ = 1.5407 Å) in Brookhaven National Laboratory (BNL).

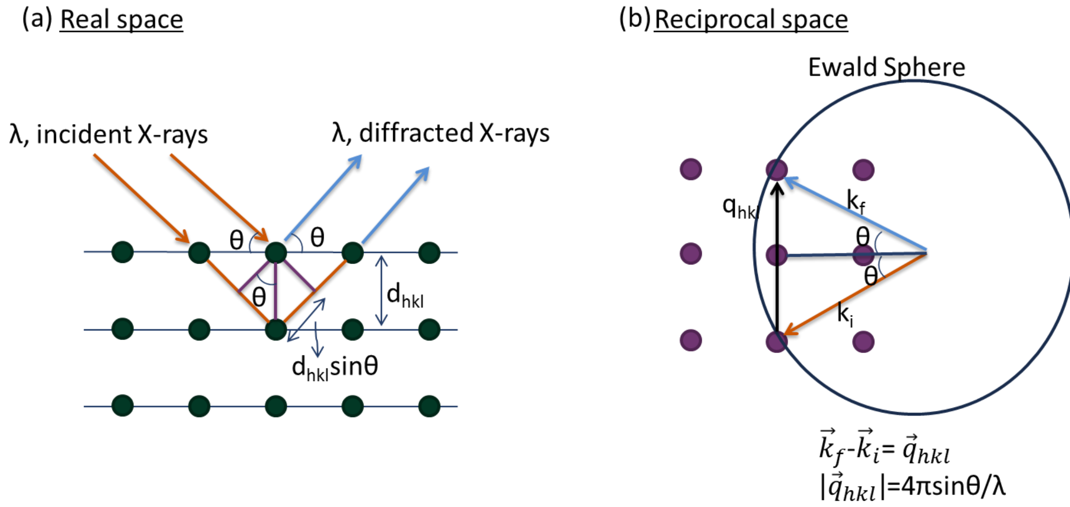

Figure 3.1 Bragg diffraction in (a) real space and (b) reciprocal space.

3.1.1 θ-2θ diffraction

In the symmetric θ-2θ measurement, θ is the angle of the incident X-rays, as well as the angle of the diffracted X-rays with respect to lattice planes. The angle between the incident and diffracted X-ray beam is equal to 2θ. From a θ-2θ diffraction scan, one is able to determine the interatomic spacing d perpendicular to the lattice planes. The d-spacing can be labeled by the Miller indices h, k, l according to the unit cell of the material.

STO has a perovskite structure, which is a simple cubic crystal with lattice constant a=b=c. As a result, the d-spacing can be expressed in terms of Miller indices in Equation 3.2.

$$\frac{1}{d^2} = \frac{h^2 + k^2 + l^2}{a^2}$$
$$d_{hkl} = \frac{a}{\sqrt{h^2 + k^2 + l^2}} \qquad (3.2)$$

Combining Equation 3.1 and 3.2, we obtain:

$$sin^2\theta = \frac{\lambda^2}{4a^2}\,(h^2 + k^2 + l^2) \tag{3.3}$$

Once the STO (00l) diffraction pattern is obtained, the lattice constants can be calculated using Equation 3.3. In this case, a is equal to the out-of-plane lattice constant (a=c for the cubic structure), h and k are equal to 0, l is an integer, and θ is determined from the peak positions in the diffraction pattern. The θ-2θ diffraction scan can also be used to determine whether the film is strained or not. Figure 3.2 shows the (002) diffraction peak of an STO epitaxial film on Si (001). When the STO is not strained, the peak position of the STO (002) is located at 46.5° (2θ), indicated as a green line in Figure 3.2. However, the (002) peak position of a tensile strained STO epitaxial film is positioned to the right hand side of the unstrained STO (002) peak. This diffraction scan in Figure 3.2 indicates that the STO film on Si (001) is tensile-strained. If the film is under compressive strain, the peak position of the film will be on the left side of the unstrained STO (002) peak. This basic diffraction scan has been employed to investigate the strain as discussed in Chapter 6 and 8.

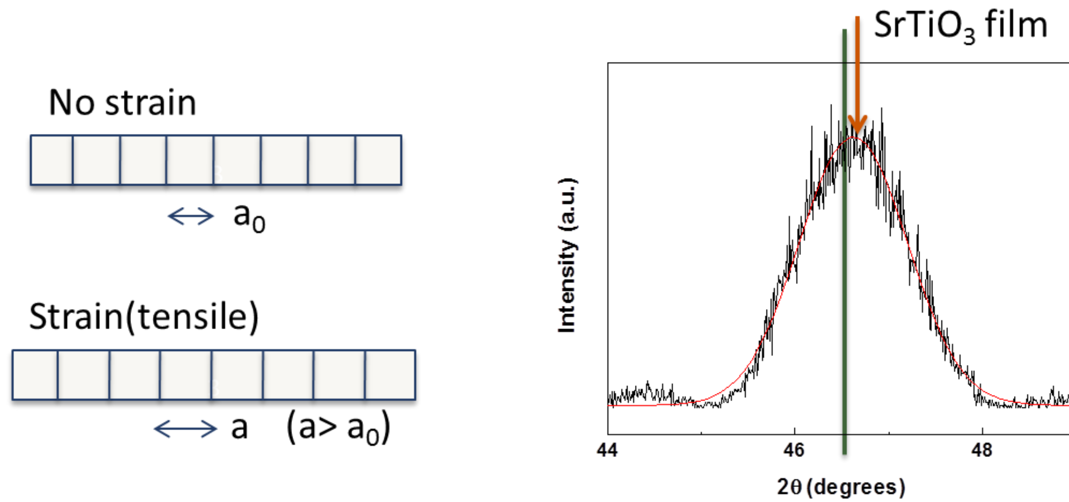

Figure 3.2 The diffraction peak of STO (002) film on Si (001).

3.1.2 2θ-ω scan

From a reciprocal space map of a two-dimensional region of reciprocal space, both in-plane and out of plane lattice constants can be obtained at the same time. This reciprocal space map can be accomplished by combining a series of asymmetric ω scans at different values of the sample tilt ψ, as shown in Figure 3.3. To determine the in-plane lattice constant of STO, a reciprocal space map should be acquired around the (103) Bragg reflection. The tilt angle ψ is defined as the angle between [001] and [103] directions and 2θ can be calculated from the relation, $\lambda=2d_{103}\sin\theta$. The angle ω is then defined as $\omega = 2\theta/2 + \psi$ according to the scattering geometry.

First of all, at a given tilt angle ψ (2θ-ω scan) to the $q_{\perp}$ of the crystal, an ω-scan is performed by rotating the sample around the ω-axis. Then, the tilt angle ψ is changed to $\psi+\delta\psi$ so that scattering vector has a small amount of δq. At $\psi+\delta\psi$, another ω-scan is performed, and so on. These series of ω scans with varying ψ is done until the reciprocal map around (103) Bragg reflection is obtained.

The ω-scan samples reciprocal space along the circumference of the scattering vector with fixed magnitude at a given tilt angle, and the 2θ-ω scan samples a portion of the radial direction of the scattering vector from the origin. Therefore, through the combination of the two scans, the reciprocal space map around the (103) Bragg reflection (the outlined area in Figure 3.3) can be accomplished. Due to geometric constraints, there is a forbidden scattering area indicated by a shaded area in Figure 3.3. In this forbidden region, the detector and x-ray source are on opposite sides of the sample. This type of diffraction scan has been employed to investigate the in-plane lattice constants of La-$SrTiO_3$ films in Chapter 8.

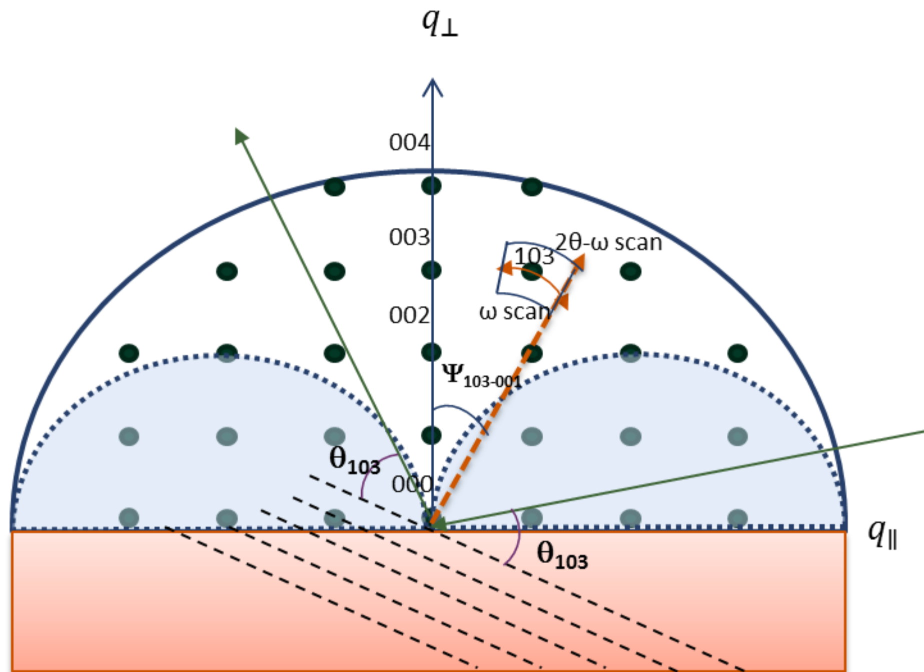

Figure 3.3 The schematic of the scattering geometry of 2θ-ω scan.

3.1.3 Rocking curve (ω-scans)

The θ-2θ diffraction scan only gives the out-of-plane lattice constants of the film, not the crystalline quality. On the other hand, rocking curve or ω-scans can be used to determine the degree of disorder of a particular orientation in epitaxial films

During an ω-scan, the X-ray source and the detector are fixed at a specific Bragg peak, but the sample is rocked around the Bragg peak slightly. Strong diffraction comes only from an aligned plane which satisfies with Bragg's Law. If a relatively wide profile in the ω-scan is observed, this means that there are several sets of planes satisfying with Bragg's Law at slightly different ω positions, as shown in Figure 3.4(a). The more aligned the planes, the narrower the full width at half maximum (FWHM) becomes, therefore, the peak width from the ω -scan provides a way to quantify the crystal quality of the epitaxial films. In Figure 3.4(b) and (c), ω-scans of a La doped $SrTiO_3$ film on Si and a La doped $SrTiO_3$ film on $LaAlO_3$ are shown. The FWHM of (b) and (c) is 0.286° and 0.633°. From this figure, we can determine that La doped $SrTiO_3$ film on $LaAlO_3$ has better crystalline quality.

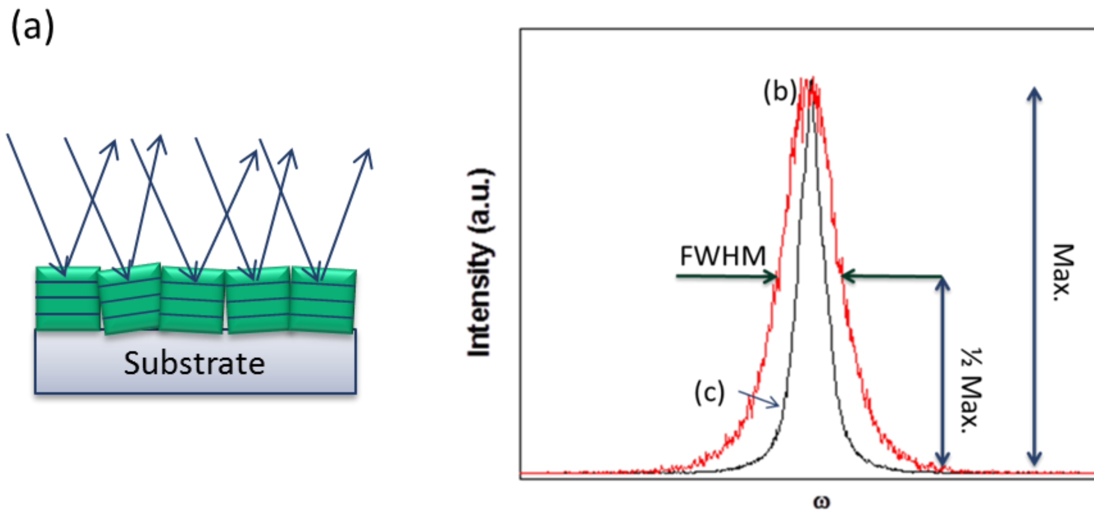

Figure 3.4 (a) Several sets of planes satisfying with Bragg's Law at slightly different ω positions. ω-scans of (b) the La doped $SrTiO_3$ film on Si and (c) the La doped $SrTiO_3$ film on $LaAlO_3$.

3.2 X-RAY REFLECTIVITY

X-ray reflectivity is a useful technique to determine the thickness of a film. In addition to the determination of the thickness, the density and roughness of a film can also be obtained. A monochromatic X-ray beam with a wavelength λ irradiates a sample at a grazing angle, ω = 2θ/2. When the incident angle is below the critical angle, θc, total external reflection occurs. However, beyond the critical angle θc, the incident X-ray beam can penetrate into the sample. The incident X-ray beams are reflected at the surface of the film and also at the interface between the film and the substrate. Reflected beams interfere with each other. Depending on the phases of the reflected beams, the total reflected intensity shows maxima and minima, which are called interference fringes or Kiessig fringes[61]. As shown in Figure 3.5, the periods of the interference fringes are

related to the thickness and the change in the intensity of the overall baseline is related to the film roughness. The critical angle and the oscillation amplitude depends on the density difference between the film and substrate[62]. Figure 3.5 shows the reflectivity curve of a $SrTiO_3$ film with 78 Å thickness on Si (001). For the data analysis, a simulation program was used[63]. This tool was utilized to figure out the film thicknesses in chapter 6 and 9.

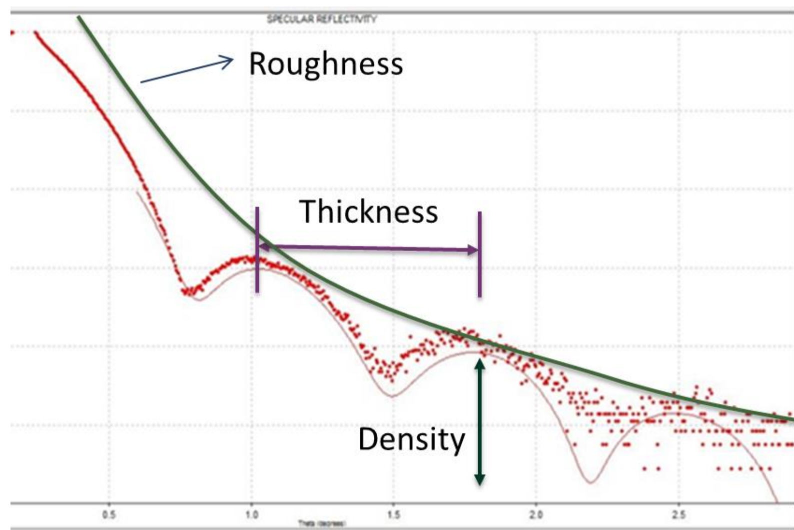

Figure 3.5 Reflectivity curve of $SrTiO_3$ film with 78 Å thickness on Si (001).

3.2.1 X-ray reflectivity – film thickness

As shown in Figure 3.6, the path difference mλ between the reflected and refracted beam can be described by the Equation 3.4, where m is an integer and λ is the wavelength of the X-ray. Equation 3.4 is analogous to Bragg's Law, however, we need to consider the Snell-Descartes's Law due to the different index of refraction of air and the film. The critical angle in Equation 3.5 is expressed by $\cos\theta_c = n = 1 - \delta$ ($\beta \sim 0$) where n is the index of refraction, δ is the dispersion (β is the absorption) of the X-ray in the

medium, with $\cos\theta_c$ approximated as $1-\frac{\theta_c^2}{2}$ at small angles. Using Equations 3.4 and 3.5, the expression for the film thickness can be written as Equation 3.6. From the X-ray reflectivity curve, incident angles for the mth interference can be plugged into the Equation 3.6. By plotting θ_m^2 as a function of m^2 from XRR data, the linear slope, $\left(\frac{\lambda}{2t}\right)^2$ can be used to determine the film thickness. Moreover, the y-intercept, δ_c, is related to the density of the film and the critical angle.

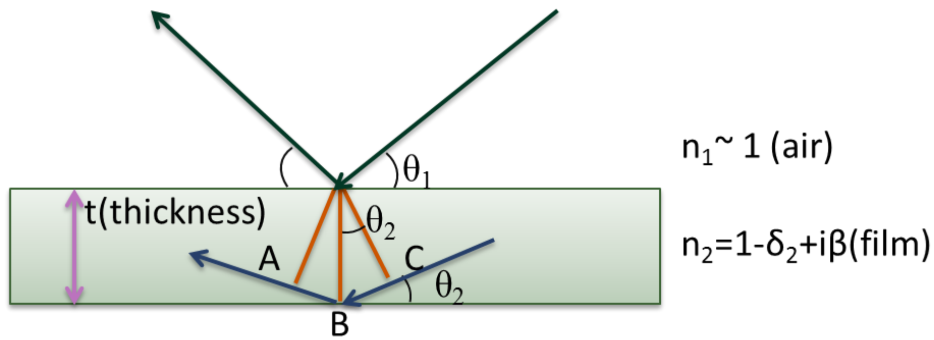

Figure 3.6 Reflection of X-rays at material surface and at the interface. The material has the index of reflection n_2

$$m\lambda = AB + BC \tag{3.4}$$

$$= 2t\sin\theta_2$$

Using Snell's Law of reflection (n1~1),

$$\cos\theta_m = n_1\cos\theta_c \tag{3.5}$$

$$\cos\theta_m = (1-\delta_c)\cos\theta_c$$

$$m\lambda = 2t\sqrt{\theta_m^2 - 2\delta_c}$$

$$\theta_m^2 - 2\delta_c{}^2 = m^2\left(\frac{\lambda}{2t}\right)^2 \tag{3.6}$$

3.3 X-RAY PHOTOELECTRON SPECTROSCOPY

X-ray photoelectron spectroscopy (XPS) is a powerful and widely used surface analytical tool. Using XPS, we can determine the element identity, atomic compositions of all the elements in the sample, chemical oxidation states and even electronic structures [64]. The basic principle of XPS is the photoelectric effect[65,66]. Based on this effect, Dr. K. Siegbahn and his research group at the University of Uppsala (Sweden) developed XPS in the mid-1960s. In 1981, he was awarded the Nobel Prize for physics for his work using XPS[67]. For my experiments, I utilize an x-ray photoelectron spectroscopy (XPS) analysis chamber (VG Scienta R3000) that allows for *in situ* transfer with the MBE chamber. The analyzer is calibrated using a two-point measurement of the Ag $3d_{5/2}$ core level at 368.28 eV and the Fermi edge of Ag at 0.00 eV. The resolution of the XPS spectra is limited by the x-ray source line width, which is approximately 300 meV. The beam spot size I used is 3 mm × 1 mm.

3.3.1 The principle of X-ray photoelectron spectroscopy

XPS is carried out under ultra-high vacuum (UHV) conditions to reduce the electron scattering from gas molecules and to maintain the surface cleanness of the samples. The X-rays are generated by an anode made of aluminum (Al) (or magnesium (Mg)). The generated X-rays contain several components including the Al Kα (electron transitions from a 2p orbital (L shell) to the K shell) line, bremsstrahlung continuous background, and other satellite lines. For high resolution measurements, all the components except for the Al Kα line must be removed using a monochromator. A set of 7 quartz crystals is placed at the end of the monochromator chamber (Figure 3.7). The aligned quartz crystals create a concave X-ray grating. The generated X-ray beams are directed onto the quartz crystals, and then the X-ray beams that satisfy Bragg's law are reflected, with the focus of the concave grating being governed by the Rowland circle

condition[68]. Therefore, only intense monochromatic Al Kα radiation with energy of 1486.7 eV is emitted from the monochromator. When the monochromatic X-rays hits the sample surface, electrons in solid sample are excited and are emitted from the surface. The kinetic energy of the emitted electrons is analyzed by the hemispherical energy analyzer.

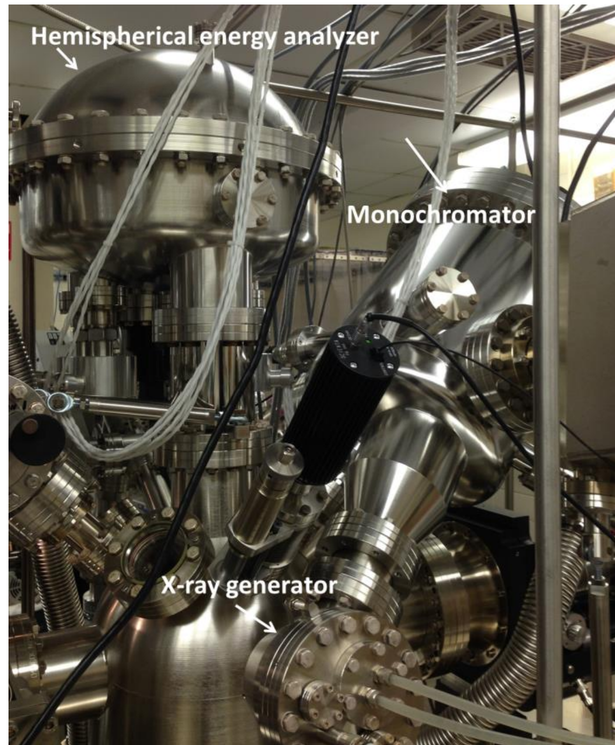

Figure 3.7 The chamber of X-ray photoemission spectroscopy in UT Materials Physics Lab.

As shown in Figure 3.8, X-ray photons have sufficient energy hν to excite not only the outer valence shells but also the core levels of all elements causing them to be ejected as photoelectrons. From energy conservation, the kinetic energy E_{kin} of a photoelectron is written as $E_{kin}=h\nu - \varphi_{sp} - E_b$ where E_{kin} is the kinetic energy of the emitted electron, φ_{sp} is the work function of spectrometer, and E_b is the binding energy.

The sample stage is connected electrically to the spectrometer, so the Fermi levels of the sample and the spectrometer are aligned. The value of φ_{sp} is compensated automatically using SES software program (from VG Scienta) and the kinetic energy E_{kin} is measured by the energy analyzer. Therefore, the binding energy E_b is easily converted from E_{kin} and hν. E_b is element specific, so that we can determine the composition of the sample from the various lines present in the collected spectrum. Specific values of E_b and relative intensities give composition information of the sample.

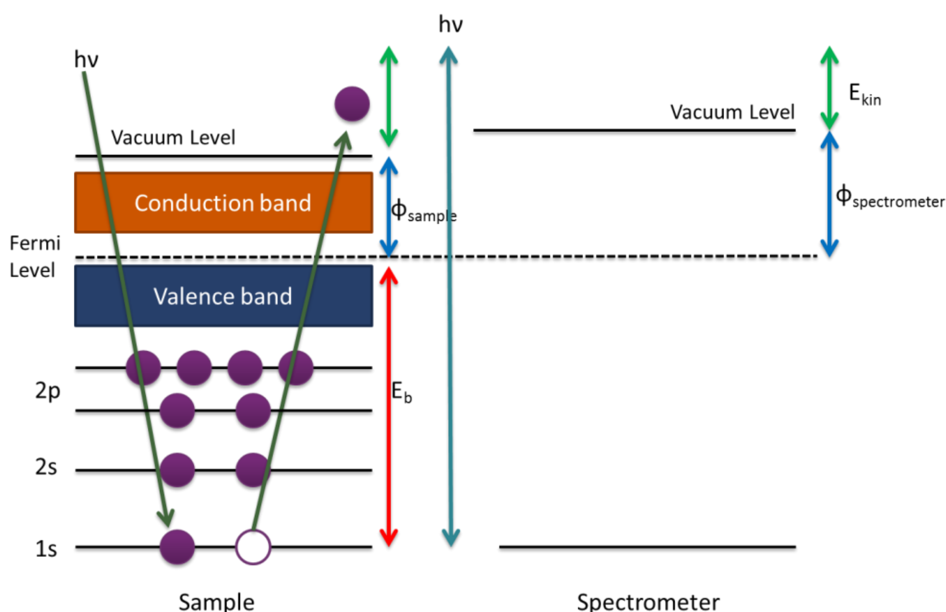

Figure 3.8 The schematic diagram of the photoemission spectroscopy.

3.3.2 Sampling Depth

When X-rays are irradiated onto the sample surface, X-rays penetrate a substantial distance into the sample in a range of 1~10 μm. However, only electrons that are a few tens of Å below the surface can escape and reach the analyzer due to the electron-electron and electron-phonon scatterings during the escape to the surface. Here we need to

introduce the term of "electron inelastic mean free path (IMFP), λ". IMFP can be defined as "the distance over which the probability of an electron escaping without significant energy loss due to inelastic processes drops to e^{-1} of its original value"[64]. The probability can be expressed by

$$P(z) = \exp(-\frac{z}{\lambda\cos\theta}) \tag{3.6}$$

where z is the length of travel without experiencing inelastic scattering, and the angle θ is measured with respect to the surface normal. At normal angle, one has z=λ=IMFP. If there is an overlayer through which the electrons have to go through, the intensity I0 will be attenuated. The intensity I emitted from the sample with thickness z is given by, $I = I_0 \exp(-\frac{z}{\lambda\cos\theta})$. For normal angle, with z equal to 3λ, $-\ln(I/I_0)=0.050$ or 95 % of electrons come from the sample thickness z=3λ. The sampling depth is defined as the depth from which 95 % of electrons that reach the surface come from.

IMFP can be calculated various methods. First of all, an article related to IMFP has been published by Tanuma *et al.*[69] in 1993. The equation is shown in Equation 3.7.

$$\lambda = E/\left\{E_P^2[\beta \ln(\gamma E) - \left(\frac{C}{E}\right) + \left(\frac{D}{E^2}\right)]\right\} \tag{3.7}$$

where E=electron kinetic energy in eV

$E_p=28.8\ (N v\rho/M)^{1/2}$ is the electron plasmon energy

ρ=density in g cm^{-3}

Nv=number of valence electron per atom or molecule

M=atomic or molecular weight

$\beta=-0.0216+0.944/(Ep^2+ Eg^2)1/2+0.738e^{-4}\ \rho$

$\gamma=0.191\ \rho^{-0.5}$

$C=1.97-0.91U$

$D=53.4-20.8U$

$U=N_v\ \rho/M= E_p^2/829.4$

The other method to calculate IMFP was presented by Seah and Dench[70]. According to their calculation, the IMFP is proportional to (kinetic energy, KE)^n. The exponent n is related to the materials, and is usually between 0.5 and 0.9. Several other methods to calculate IMFP have also been reported[71-73].

3.3.3 Spin-Orbit splitting

Due to the interaction between the electron spin angular momentum and the orbital angular momentum, all orbital levels except the s levels (l = 0) shows a doublet with two possible states that have different binding energies in XPS. This binding energy separation is known as spin-orbit splitting or j-j coupling. For p, d and f peaks, two peaks are observed. For 2p, two states arise from the quantum numbers n=2, L=1, and S=1/2, with the total angular momentum J values give rise to, J=1/2 and 3/2. The degeneracy g_J can be written as $g_J=2J+1$. The relative peak intensities of doublet (branching ratio) are given by the ratio of 1:2 which are from degeneracy, J=1/2 (g_J=2) and J=3/2 (g_J=4). The binding energy of the lower J member of the doublet is higher.

3.3.4 Quantification of sample stoichiometry

To quantify the amount of each element present in a sample, we need the integrated area of a specific peak and also the corresponding relative sensitivity factor (RSF)[74]. RSF is the relative intensity ratio of a pure element sample A to a standard pure element as indicated in Equation 3.8, where I_A^∞ is the intensity of element A at depth from 0 to ∞. Wagner *et al.*[75] used the fluorine (F) compounds as a standard, and derived

RSF values compared to $I_{F,1s}^{\infty}$. The empirical RSF values from Wagner were applied to my data analysis.

$$\text{RSF} = \frac{{I_A}^{\infty}}{I_{F,1s}} \tag{3.8}$$

For H or He, RSF values are too small to be useful. These RSF values can be used to determine the relative composition of each element in the sample. The relative concentrations can be determined by Equation 3.9 where R_i is the relative atomic concentration of element i in the sample and index j refers to the number of elements in the sample.

$$\text{R}_i(atomic\ \%) = \frac{I_i/RSF_i}{\sum_j I_j/RSF_j} \times 100(\%) \tag{3.9}$$

For example, core level spectra of Sr 3d, La 3d, Ti 2p, and O 1s from the La doped $SrTiO_3$ sample by *in situ* XPS at room temperature are shown in Figure 3.9. From these spectra, we can estimate the composition of the sample as relative ratios between the different elements present.

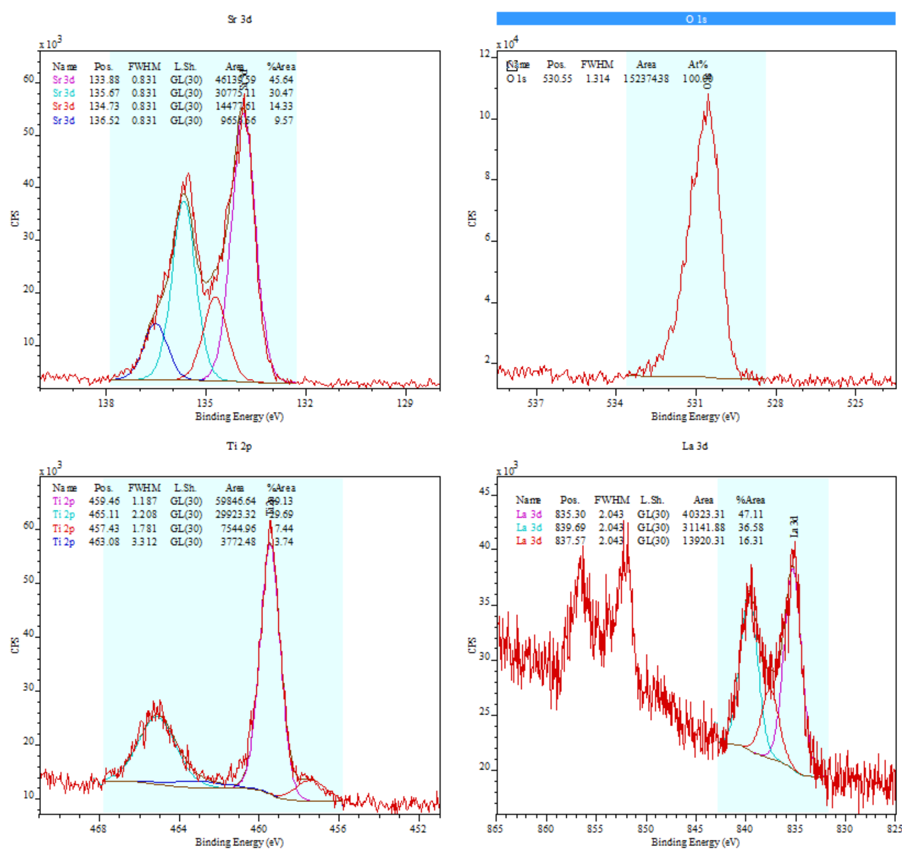

Figure 3.9 Representative core level spectra of Sr 3d, La 3d, Ti 2p, and O 1s from a La doped STO film using *in situ* XPS.

Once we obtain core level spectra, the total area can be determined using the CasaXPS program and hence, the composition of the film can be derived using Equation 3.9. The quantitation results for this sample are shown in Table 3.1. The composition of this sample from the relative concentrations is found to be $(La_{0.17}Sr_{0.83})TiO_{3.25}$. Depending on the thickness of the sample, the total intensity of each element should be adjusted due to the different IMFP for different binding energies. This intensity calibration can also be easily implemented with the CasaXPS program.

	Sensit -ive factor	Total area (Intensity)	Concentration	Relative concentration
Sr	1.843	91644.9	91644.0/1.843 = 4.973×104	$\frac{4.973 \times 10^4}{(4.973 + 6.010 + 6.010 + 19.54) \times 10^4}$
La	13.6	137627.5	137627.5/13.6 = 6.010×104	$\frac{6.010 \times 10^4}{(4.973 + 6.010 + 6.010 + 19.54) \times 10^4}$
Ti	2.001	120254.0	120254.0/2.001 = 1.012×104	$\frac{1.012 \times 10^4}{(4.973 + 6.010 + 6.010 + 19.54) \times 10^4}$
O	0.78	152374.4	152374.4/0.78= 1.954×105	$\frac{1.954 \times 10^5}{(4.973 + 6.010 + 6.010 + 19.54) \times 10^4}$

Table 3.1 The quantitation results of the La doped STO sample.

3.3.5 Experimental details

From the survey scan, we can confirm the presence and rough amount of each element of which the sample is composed of in Figure 3.10(a). After this survey scan, high resolution scans as shown in Figure 3.10(b) are carried out to determine the compositions of the sample, chemical shift or oxidation state, etc. Figure 3.10(a) shows that the XPS spectrum has a stepped background where the intensity of background at higher binding energy is greater than that at lower binding energy. This is due to the inelastic process from the photoelectrons which have kinetic energy between 100 and

1500 eV[76]. The details of the background shape depend on the material. During the electrons escape to the surface, some of them lose part of their initial energy. These electrons which lost some of their initial energy contribute to the background of the spectrum. To account for the background, a Shirley background shape[77] (see Figure 3.10(b)) was subtracted for the data analysis in my experiments. Using the CasaXPS program, the spectrum can be analyzed, using a constrained peak fitting model (area, peak positions, and FWHM). For example, the Ti 2p component includes a spin-orbit split pair located 5.6 eV higher in binding energy with a branching ratio fixed at the theoretical value of 0.5 in Figure 3.10(b).

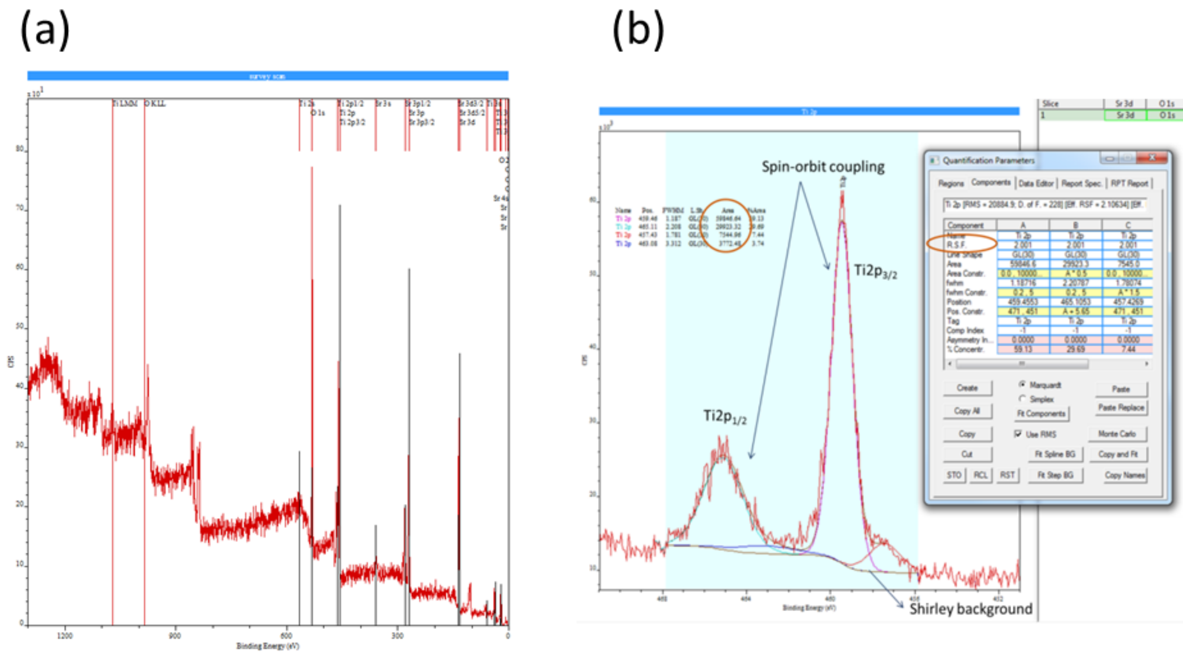

Figure 3.10 (a) survey scan and (b) high resolution scan of Ti 2p component.

The peak shape is determined by both the lifetime of the core-hole (Lorentzian), and instrument effects (Gaussian) such as resolution of the analyzer, energy spread of the X-rays. Therefore, the peak is fitted with a Voigt function.

3.4 ULTRA-VIOLET PHOTOELECTRON SPECTROSCOPY (UPS)

UPS was used to determine the work function (ionization energy) in my experiments in chapter x. Light based on helium (He) I (hν =21.22 eV) is used for the UV radiation source. This light comes from the transition, He ($^1P_1$) → He ($^1S_0$) + 21.22 eV. The plasma-based UV source has more photons (flux) with a narrower line width (~10 meV) compare to a laboratory x-ray source and it is suitable for measuring the valence band structure and work function of samples.

A schematic view of the photoexcitation of electrons from the valence band of a material by photons with energy hν is shown in Figure 3.11(a)[78], and the measured spectrum of 0.3 ML Sr on Si (001) is shown in Figure 3.11(b). The background of the spectrum is due to the secondary electrons as a result of inelastic scattering. These electrons still have enough energy to escape into vacuum, so that they are detected as secondary electrons and form the background of the spectrum. The work function of a sample can be determined by subtracting the width of the spectrum from the energy of the incident UV light source. This width is the energy separation between the onset of the secondary electrons to the Fermi edge. UPS measurement has been employed to investigate the work function change of Si (001) as a function of Sr and Ba coverage, as will be discussed in Chapters 4 and 5.

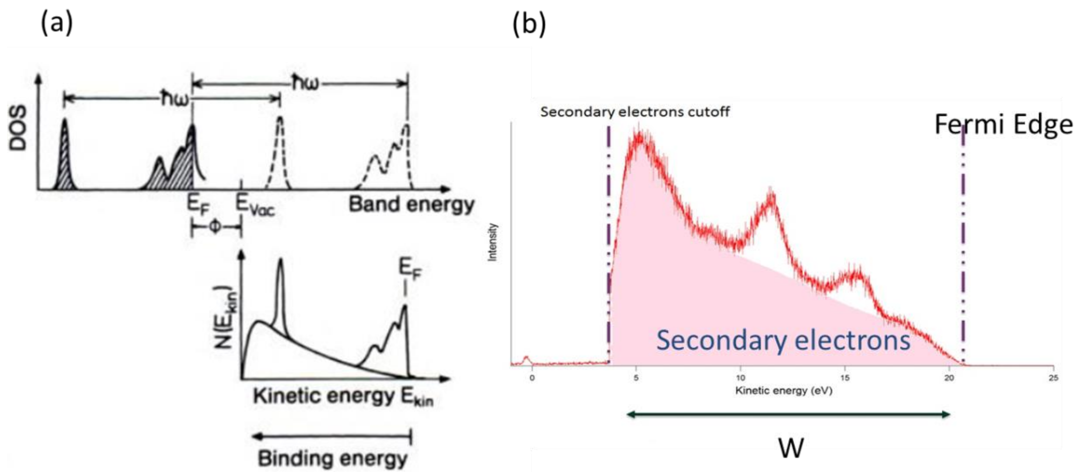

Figure 3.11 Schematic view of (a) the photoexcitation of electrons from the valence band by photons energy of hν and (b) the measured spectrum of 0.3 ML Sr on Si (001).

3.5 ATOMIC FORCE MICROSCOPY (AFM)

Atomic force microscopy (AFM) was used to investigate the roughness of the sample surface in Chapter 7, 8 and 9. The AFM measurements were performed in ambient using a commercial Veeco Multi-mode V commercial AFM. Tips were model TESP from Bruker, with specified resonant frequency between 306 and 350 kHz and spring constant k=20~80 N/m.

3.5.1 Atomic force microscopy (AFM) – principle

AFM is widely used as a non-destructive tool to investigate the morphology of sample surfaces. AFM was invented and demonstrated by Gerd Binnig, Calvein Quate and Christoph Gerber in 1986[79] to remedy the limitation of the technique of scanning tunneling microscopy (STM), which was not suited for measuring non-conductive

samples. The basic idea of AFM is that a sharpened tip on a spring cantilever is brought very close to the sample surface. The forces between the sharpened tip and the sample surface affect the deflection of the cantilever. The deflection of the cantilever is a direct measure of the topography of the surface. In the initial prototype of AFM, cantilever deflection was measured by the tunneling current between a tip and the backside of the cantilever. However, these days, the cantilever deflection is measured by the change in position of a laser beam reflected from the backside of the cantilever[80].

AFM uses the repulsive or attractive forces between a tip and a sample. There are three different modes of operation; contact mode, non-contact mode, and tapping mode. These modes are related to the distance and the force between the tip and the sample surface. Tapping mode will be described here because I used this mode for measuring the roughness of the surface.

In tapping mode, the tip has a large spring constant (20~50 N/m) with a resonance frequency of 100~400 kHz. The tip is forced to be oscillated with a certain oscillation amplitude at the resonance frequency. Because the tip keeps oscillating, the oscillated laser beam is detected in a photodiode detector, and then the laser beam signal is converted to a root mean square (RMS) amplitude value (DC voltage). When the tip is engaged to the surface and is then moved along the sample surface, the cantilever's oscillation amplitude is changed depending on the sample surface height. The changed oscillation amplitude is measured by the photodiode detector, which has four elements arranged as a quadrant photodiode as seen in Figure 3.12. The surface height difference is detected by the vertical beam difference (A+B)-(C+D)/sum where the sum is equal to A+B+C+D. Through the feedback loop, the oscillation amplitude maintains the RMS value. If the reflected beam has the higher set point value (RMS), the z motion piezo moves down to match the values between RMS and the reflected beam. The z-motion

piezo change is recorded in the computer and then the program converts that information to a topography image.

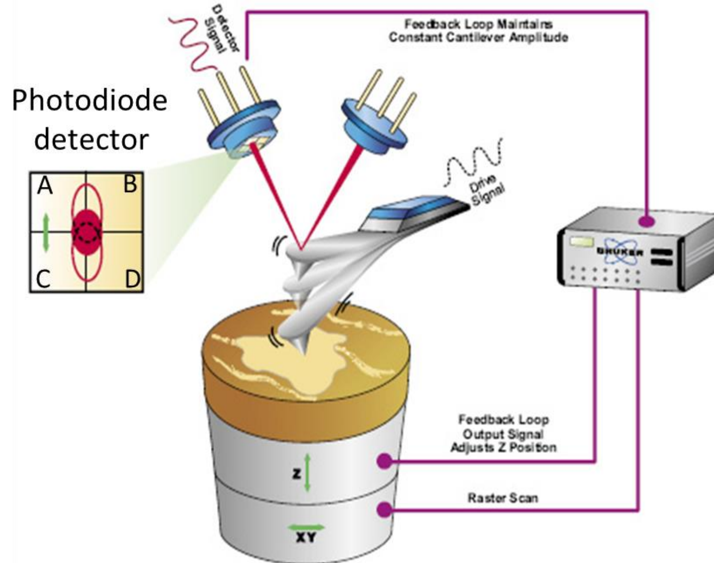

Figure 3.12 Feedback loop of the tapping mode AFM. Image taken from reference[81].

The roughness of the sample is expressed as root mean square (RMS) roughness within a given area. The RMS roughness is the standard deviation of the z values. The profile of the image shows the relative height difference compared to the surrounding area.

Chapter 4. Alkanline earth metal Sr on Si (001) : Charge transfer in Sr Zintl template on Si (001)

The Sr Zintl template on Semiconductors is necessary to deposit the $SrTiO_3$ films on Si (001) directly. The formation of the half monolayer (ML) Sr Zintl template layer on Si (001) is investigated using *in situ* reflection high energy electron diffraction, *in situ* x-ray photoelectron spectroscopy (XPS), and density functional theory. To compare the Sr template on Si (001), the same periodic table group, Ba on Si (001) also investigated. This work is accompanied with theoretical calculation using density functional theory (DFT). Therefore, the theoretical work also described in this chapter. Theoretical calculations were done by Hosung Seo. This work was published in : (1) M. Choi, A. B. Posadas, H. Seo, R. C. Hatch and A. A. Demkov, "Charge transfer in Sr Zintl templates for epitaxial oxide growth on Si (001)." Appl. Phys. Lett. **102**, 031604 (2013) photoemission experiment and density functional theory for the Sr Zintl template for oxide heteroepitaxy on Si (001).", J. Vac. Sci. Technol. B **31**, 04D107 (2013)

4.1 INTRODUCTION

Over a decade ago, McKee and co-workers achieved a breakthrough in the epitaxial growth of single crystal perovskite $SrTiO_3$ on Si (001) using 1/2 monolayer (ML) of Sr on clean Si (001) 2×1 as a template[14]. At 1/2 ML coverage, Sr atoms assume positions between Si dimer rows, and inhibit formation of the amorphous SiO_2 layer during the subsequent $SrTiO_3$ deposition in a relatively wide range of temperatures and pressures[14,82-85]. Epitaxial growth of $SrTiO_3$ on Si (001) has enabled replacing the SiO_2 gate dielectric with an epitaxial oxide in a field effect transistor, and more importantly, the monolithic integration of functional perovskite oxides on Si[19,86-93]. To date, no other template layer has been reported that enables direct perovskite epitaxy on Si (001).

The composition of 1/2 ML Sr on Si is expressed by $SrSi_2$, which is similar to a bulk $SrSi_2$ Zintl-Klemm intermetallic compound. 'Zintle phase' which was named after German Chemist, Eduard Zintl is compounds which comprise electropositive elements such as alkali or alkaline earth metals with the electronegative elements in the periodic group between 13 and 16. In Zintl phase followed by the Zintl-Klemm formalism, valence electrons transfer from electropositive to electronegative atoms and "covalent interaction" happens after transferring electrons. In the system of MSi_2 (M=Sr, and Ba in this dissertation) which is one of the Zintl phase, M metal donates its electrons to Si, and Si^{-1} and M^{+2} form covalent bonds which is fulfilled by octet rule. By using Zintl phase, $SrSi_2$, $SrTiO_3$ films were directly deposited on Si (001) without any buffer layers. Therefore, the understanding of the Sr template formation on Si (001) is crucial to controlling the growth of epitaxial oxides on silicon and possibly extending this mechanism to other semiconductors[94-98].

X-ray photoemission has been extensively used to study Si (001), and ample literature exists describing the bulk and surface core-level states both experimentally and theoretically[99-107]. At room temperature in vacuum, a clean Si (001) surface exhibits 2×1 reconstruction with buckled asymmetric dimers[108], giving rise to two surface states of which one is filled (the so-called "up atom" of a dimer) and the other is empty (the "down atom"). Experimentally, the Si 2p core level spectrum of 2×1 Si (001) can be described (fitted) with seven spin-orbit split pairs of surface core-level components. Specifically, the spectrum is decomposed into one bulk component (B), and six surface components (S_u, C, S_d, SS, D and L) including the up (S_u) and down (S_d) surface states[106]. The C component is positioned in energy between the bulk and S_d components and originates from one half of the third layer atoms[102]. The SS component has been associated with either the second layer of Si atoms or with one half of the third layer plus

the fourth layer of Si atoms[101]. The D and L components are observed on the higher binding energy side of the spectrum with their origin debated in the literature. However, the D component is likely due to surface defects[101,109], while the L component is related to a surface loss process via interband transitions in surface bands[106].

The detailed changes in the Si 2p core level spectrum depend on the specific adsorbing atom and show a unique trend since core level shifts are related to the electronic structure of the system[110-112]. For example, when Mg and Ca are adsorbed on Si (001) to form $MgSi_2$ and $CaSi_2$, the Si 2p core-level shifts observed as a function of Ca and Mg coverage indicate charge transfer from alkaline-earth metals to Si (001)[112]. Using density functional theory (DFT), we recently proposed that at sub-monolayer coverage, Sr on Si (001) results in un-tilting of the dimers due to Zintl charge transfer from the electropositive metal to Si[113]. This structural change is an essential factor in creating the template for the subsequent $SrTiO_3$ growth[114]. Though the electronic structure of Sr on Si (001) has been studied using x-ray standing wave[115] and x-ray photoemission techniques[115,116], our understanding of the relationship between the surface reconstruction and the electronic structure changes induced by Sr deposition is still incomplete.

4.2 EXPERIMENT AND THEORETICAL CALCULATIONS

B-doped ($\sim10^{16}$ cm^{-3}) prime Si wafers were cut into 20 mm×20 mm pieces and ultrasonically cleaned in acetone, deionized water and isopropanol for 5 minutes each, then exposed to ultraviolet (UV)-ozone lamp to remove carbon impurities at the surface. The Si substrates were then introduced into a customized DCA 600 molecular beam epitaxy (MBE) system with a base pressure of 3×10^{-10} Torr. To remove the native SiO_2 layer, the substrates were heated up to 875 ^oC and annealed for three hours under ultrahigh vacuum. After annealing, a sharp 2×1 reconstruction pattern is observed by *in*

situ RHEED. The samples are then transferred *in situ* to the x-ray and ultraviolet photoelectron spectroscopy (XPS/UPS) analysis chamber (VG Scienta R3000). The C 1s and O 1s core level spectra are measured to verify the cleanness of the Si (001) surface. After confirming that there is no detectable SiO_2 layer at the surface, the sample is moved to the MBE chamber for subsequent Sr deposition. The Sr flux is calibrated using a quartz crystal monitor and fine tuned using RHEED oscillations to yield a rate of 1 ML per minute, where we define 1 ML as the atomic surface density of an ideal unreconstructed Si (001) surface (1 ML = 6.78×10^{14} atoms/cm^2). Measurements of the surface core level shifts and work function as a function of Sr coverage at room temperature are performed with *in situ* XPS using monochromatic Al Kα radiation (hυ = 1486.6 eV) and *in situ* UPS using a bright monochromatic He plasma light source (He I radiation hυ = 21.22 eV). The analyzer is calibrated using a two-point measurement of the Ag $3d_{5/2}$ core level at 368.28 eV and the Fermi edge of Ag at 0.00 eV. The resolution of the XPS spectra is limited by the x-ray source line width, which is approximately 300 meV, while that of UPS is analyzer-limited and is <30 meV.

To assist with the interpretation of the XPS spectra, we perform DFT calculations of SCLS within the local density approximation[117], along with the projector augmented wave pseudopotentials[118] to describe Si and Sr. The valence electron configurations for the elements are $3s^2 3p^2$ and $4s^2 4p^6 5s^2$ for Si and Sr, respectively. We model the Si surface using a 16-layer thick slab with a surface cell (dimension = 10.81 Å × 10.81 Å), which is separated from its periodic images along the c-direction by 15 Å of vacuum. Both surfaces of the slab are treated as active surfaces and no hydrogen passivation is used. A cutoff energy of 500 eV is used for the plane-wave expansion along with a 4×4×2 Monkhorst-Pack k-point grid for the Brillouin zone integration.

4.3 RESULTS AND DISCUSSION

Figure 4.1 shows the RHEED patterns for clean 2×1 Si (001) and Si with various coverage of Sr. As the Sr coverage increases, the RHEED pattern evolves from a 2×3 reconstruction between 1/6 and 1/4 ML of Sr into a 2×1 structure between 1/3 and 1/2 ML of Sr coverage. At 1/2 ML Sr coverage the RHEED pattern is identical to that of clean 2×1 Si (001). After Sr deposition and RHEED imaging, the samples were transferred *in situ* to the photoemission analysis chamber.

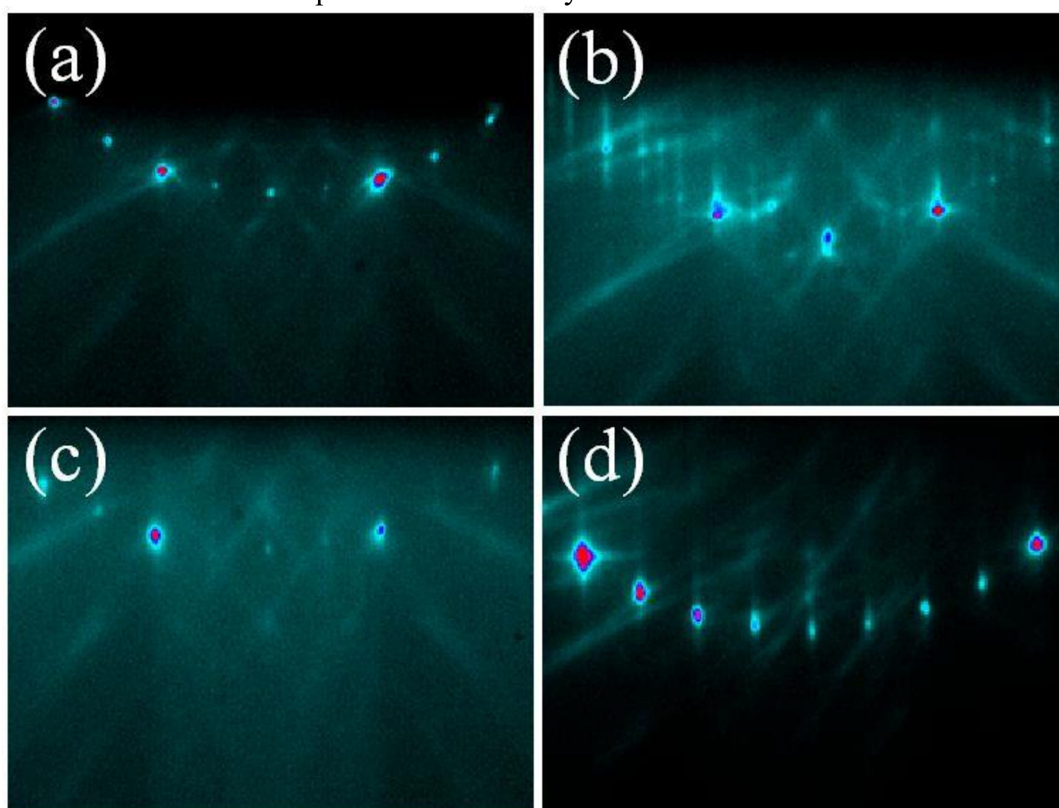

Figure 4.1 RHEED patterns of the Si (001) surface as a function of Sr coverage for (a) 0, (b) 1/6, (c) 1/3, and (d) 1/2 ML Sr coverage on 2×1 Si (001) deposited at 600 °C. All patterns are viewed along the Si<110> azimuth.

Si 2p core-level photoemission spectra of 2×1 reconstructed Si (001) and 1/2 ML Sr-induced 2×1 reconstruction on Si (001) are taken at normal emission at room temperature and analyzed as shown in Figure 4.2. We model the Si 2p core-level spectra using six components labeled S_u, S_d, C, SS, L, and B (for bulk). For buckled asymmetric Si dimers, the S_u and S_d components represent up and down dimer atoms, respectively.

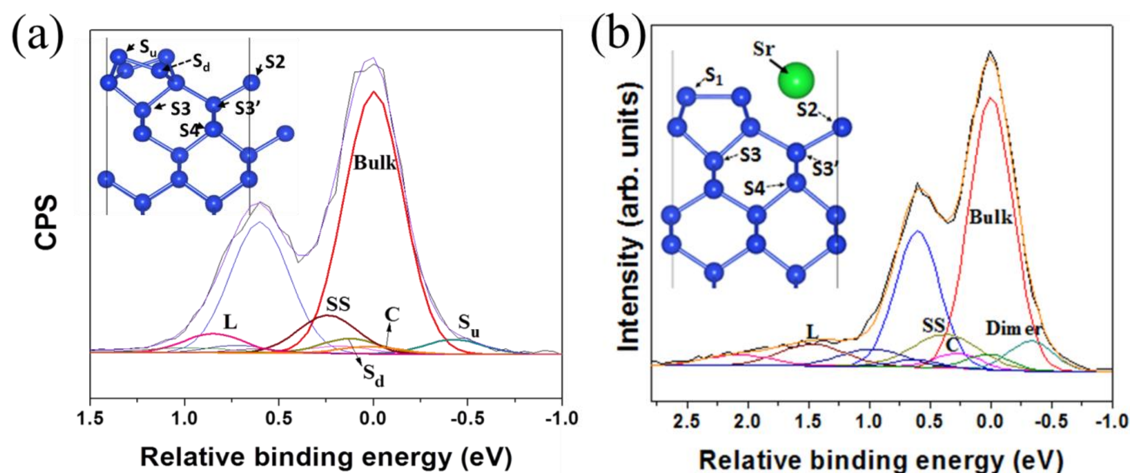

Figure 4.2 Si 2p core-level spectra of (a) clean 2×1 Si (001), and (b) 1/2 ML Sr deposition on clean 2×1 Si (001) by *in situ* XPS at room temperature. Insets are theoretical structures of clean 2×1 Si (001) and 1/2 ML Sr on Si (001) obtained from the DFT calculations.

The intensity and full width at half maximum (FWHM) of the two dimer components are constrained to be equal to each other, in accordance with the known structure of a clean Si (001) surface. The C component, which can be readily resolved in Si 2p core-level synchrotron measurements, is reported to be from the 3rd layer beneath the troughs formed by the dimer rows (S3' in Figure 4.2(a))[102]. In the present study, the C components in Figure 4.2 are somewhat difficult to assign precisely due to the resolution limit. The SS component is assigned to sub-surface components of the 3rd and 4th layers

(S3 and S4 in Figure 4.2(a)). The L component is needed to fit the tail of the spectrum on the higher binding energy side[106]. All components include a spin-orbit split pair located 0.605 eV higher in binding energy with a branching ratio fixed at the theoretical value of 0.5. The energy positions of all components are expressed in terms of the binding energy relative to binding energy of the well-resolved bulk component. The peaks are fit with the Voigt function that is 90 % Gaussian and 10 % Lorentzian using Casa XPS software[119]. The value of the FWHM from the bulk component is constrained to be the same as that of S_u, C, and S_d components. For SS and L, FWHM is constrained to be 1.5 times wider than that of bulk because the SS component is a combination of two very closely spaced features (3rd and 4th layers) that cannot be effectively resolved, while the L component has a broad tail in the higher binding region.

For clean 2×1 reconstructed Si (001), the surface core-level shifts (SCLS) of the S_u, S_d, and SS components are -0.43 eV, 0.12 eV, and 0.22 eV, respectively and are shown in Figure 4.2(a). These values are in good agreement with recent synchrotron-based measurements.[101,105] After 1/2 ML Sr deposition on clean 2×1 Si (001), the asymmetric tilt of the dimer is eliminated as a result of Sr atoms donating their two electrons to the Si (001) surface, giving rise to a single merged peak in place of previously separate S_u and S_d components. The SCLS of the merged dimer peak is -0.33 eV as shown in Figure 4.2(b).

An unexpected result in the Si 2p core-level spectra of the 1/2 ML Sr on Si (001) is that the bulk component shifts toward higher binding energy by 0.49 eV even though two electrons are donated to the Si (001) surface. From a purely electrostatic point of view, when electrons are donated to a system, the bulk core-level is expected to move to lower binding energy because the extra charge raises the electric potential. However, in the case of 1/2 ML Sr on Si, an opposite shift towards higher binding energy is observed.

In addition, we observe that the shape of Si 2p spectra broadens in the higher binding region after 1/2 ML Sr deposition.

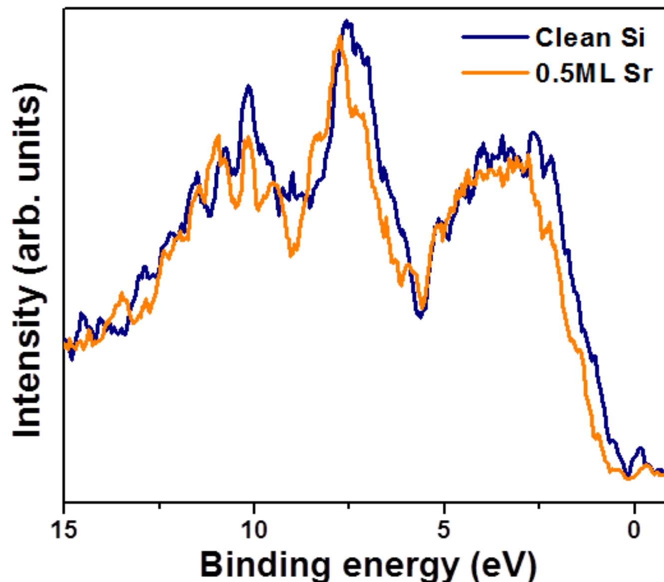

Figure 4.3 Valence band edge of the clean 2×1 Si (001) and 1/2 ML Sr on Si (001) measured using XPS. The zero of energy is set at the Fermi level.

To verify the charge transfer, the location of the valence band edge was measured for both clean Si (001) and 1/2 ML Sr on Si (001) as shown in Figure 4.3. The valence band edge positions are determined using the linear extrapolation method[120]. The energy shift of the valence band for 1/2 ML Sr on Si is approximately 0.42 eV toward higher binding energy when compared to that of clean Si (001). This value of the valence band shift confirms that it is the entire spectrum that shifted, supporting the presence of charge transfer from the Sr atoms.

To identify the possible origin of core level shift to higher binding energy induced by the Sr deposition, we calculated the 2p SCLS's at the Si (001) p(2×2) and 1/2 ML Sr-adsorbed 2×1 Si (001) surfaces. In the initial state approximation, the 2p core level

binding energy is calculated from the difference between the 2p energy level ε_{2p} and the Fermi level ε_F. However, when a core hole is created at a Si atom, the system is excited and electrons tend to screen the core hole positive charge[121]. This relaxation energy gain is included on top of the initial state effect in the final state calculations. Therefore, the difference between the initial and final state calculations could be used as a measure of the screening ability of the system[101,107]. The larger relaxation effect tends to push the 2p peak toward the lower binding energy.

The 2p core level binding energy in the final state theory is calculated as where $E(n_c)$ is the ground state energy and $E'(n_c - 1)$ is the system's energy with a screened core hole. In order to ensure the overall charge neutrality of the system, one electron is added to the system (complete screening picture). First, we calculate the SCLS at the Si (001) p(2×2) surface and the positions of the S_u and S_d components are -0.53 eV and -0.12 eV, respectively, in good agreement with our experimental results in Figure 4.2 (a) as well as existing theoretical work[100,101,107]. For Sr on Si (001), we find that the tilted dimer rows of the Si (001) p(2×2) surface are flattened due to the charge transfer[113]. As a result, there is only one dimer peak remaining at -0.35 eV in good agreement with the -0.33 eV found in the experiment as shown in Figure 4.2(b). (See supplementary information for the detailed theoretical calculation[122]).

Considering the bulk $SrSi_2$[123], we calculate the 2p chemical shift induced by the charge transfer from Sr to Si to be -0.35 eV. Strikingly, however, our experiment on 1/2 ML Sr on Si shows that the bulk 2p peak and all other surface 2p peaks shift in an opposite way compared to the bulk case. Using the initial state theory, we calculate the bulk 2p binding energy shift to be almost zero. This can be explained by the bulk 2p level rising up due to the surface dipole layer induced by the charge transfer, simultaneously with the Fermi level rising upward due to the change of the surface electronic structure.

On the other hand, using the final state theory we calculate the bulk 2p binding energy to be increased by 0.42 eV in excellent agreement with experiment. Since there is a negligible shift in the initial state calculation, we note that the shift of 0.42 eV originates from the reduced relaxation energy gain (screening effect) when the 1/2 ML Sr is deposited.

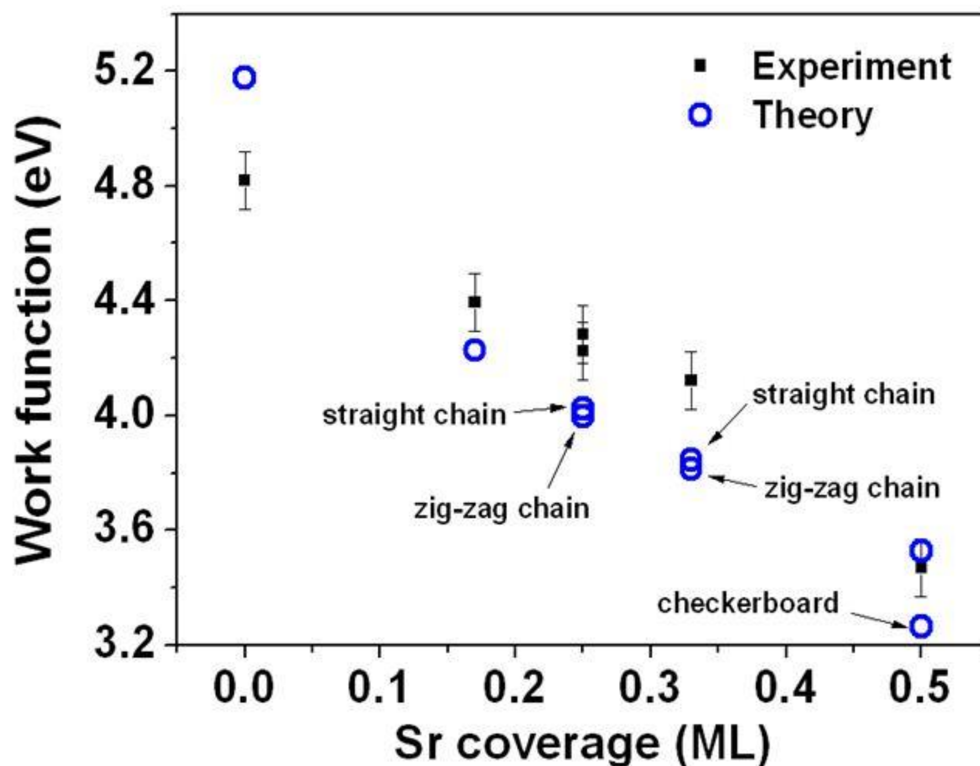

Figure 4.4 Work function variation as a function of Sr coverage on 2×1 Si (001) from experiment (filled squares) and theory (open circles). For the work function calculation for the Sr coverage of 1/6 ML, 1/4 ML, and 1/3 ML, we use the structural model proposed in Ref.[124] and Ref.[83], respectively.

Figure 4.4 shows the work function of Si (001) as a function of Sr coverage from experiment and theory[122]. We measure the work function of clean 2×1 Si (001) to be 4.82 eV using *in situ* UPS[124,125]. The change in the work function with Sr coverage is determined by the onset of the secondary electron cutoff. The work function decreases with increasing Sr coverage. The deposition of 1/2 ML of Sr causes a change of electronic structure of Si (001), which leads to a decrease in the work function by 1.35 eV and, considering experimental uncertainty, is in excellent agreement with theory. Similar work function changes caused by the interface electronic properties were also observed when organic molecules were deposited on metals or oxides[126,127].

4.4 Summary

In conclusion, we establish the key features of the Sr-based Zintl template on Si (001) by investigating the change in the electronic structure of 1/2 ML Sr-induced 2×1 reconstruction on Si (001) from that of clean 2×1 Si (001) using XPS, UPS and DFT. As a strong evidence of the charge transfer from 1/2 ML of Sr into the 2×1 Si (001) substrate, the bulk component of the Si 2p spectrum shifts toward higher binding energy by 0.49 eV and the previously separate Su and Sd dimer components merge into a single surface component at -0.33 eV with respect to the bulk This indicates that, though intact, Si dimers of the Zintl template are un-tilted, in agreement with density functional theory predictions. Theoretical calculations using the final state theory are quantitatively consistent with the experimental results for the shift of the Si 2p spectrum and the decrease of the work function of the system upon Sr deposition.

Chapter 5. Alkanline earth metal Ba on Si (001) : Charge transfer in Sr Zintl template on Si (001)

We report a study of the x-ray surface core level shifts in the Ba/Si (001) and Sr/Si (001) Zintl templates using density functional theory and in-situ x-ray photoemission spectroscopy. We demonstrate that charge transfer from a half-monolayer of Ba or Sr to the silicon surface leads to a single dimer related peak in the surface core level spectra. We find that the use of the final state theory is necessary to describe the evolution of the dimer peak. Most interestingly, we observe that the Si 2p bulk peak is sensitive to the surface structure and is shifted by 0.39 and 0.49 eV toward higher binding energy as a half-monolayer of Ba and Sr are deposited, respectively. Final state calculations show that this shift of the bulk peak results because the Si (001) surface state in the bulk band gap is destroyed after Ba or Sr deposition. Theoretical calculation is done by Hosung Seo. This work was published in : H. Seo, M. Choi, A. B. Posadas, R. C. Hatch, and A. A. Demkov, "Origin of anomalous Si 2p core level shifts of Zintl templates on Si (001) from ab-initio final state theory and in-situ X-ray phoemission experiment", submitted to *PRB*.

5.1 Introduction

As mentioned in Chapter 4, sub-monolayer coverages of alkaline earth metals (AEM), such as Sr or Ba, on semiconductor surfaces, such as Si (001) or Ge (001), have been identified as Zintl templates enabling epitaxial growth of complex oxides on semiconductors. Early theoretical calculations of half-monolayer (1/2-ML) Ba on Si (001) revealed that the charge transfer from AEM to Si (001) passivates the dangling bonds on the surface and leads to the 2×1 surface reconstruction observed in experiment[128-130]. And, Ba Zintl template also contributes to integrate the functional

perovskite with Si (001) such as $BaTiO_3$ on Si[131]. However, there are a number of important issues that remain unresolved. The Zintl templates are known to protect against oxidation of Si (001) substrates[14,132], while the mechanism that protects the substrates is largely unknown[115,133]. A detailed understanding of the evolution of the atomic and electronic structures of Si (001) induced by sub-monolayer AEMs would be invaluable for advancing the epitaxial growth of crystalline oxides on semiconductors.

Core-level x-ray photoemission spectroscopy (CXPS), combined with first-principles calculations are ideal tools for providing such understanding[64,134]. While maintaining the atomic character, core-levels are highly sensitive to the local electronic environment through electrostatic effects, resulting in core-level shifts (CLS) for different physical environments. To trace the origin of the CLS, theoretical modeling is crucial and various theoretical methods have been developed[64]. When a core electron is excited by a photon with an energy of hν and emitted from a sample with a kinetic energy, Ekin, then the binding energy, EB of the electron is defined by

$$E_B = h\nu - E_{kin} - \varphi = E'(n_c - 1) - E(n_c) \tag{5.1}$$

where φ is the work function, $E(n_c)$ and $E'(n_c-1)$ are the system's ground and excited state energies, respectively, with nc being the number of the core electrons. The quantities on the left-hand side can be determined in experiment, and the total energies on the right-hand side are the subject of theoretical calculations. A simple theory to calculate the CLS is based on the Koopmans' theorem in the Hartree-Fock theory, stating that the binding energy is the same as the orbital energy under the frozen orbital approximation [135]. Thus, in this theory, the CLS are the same as the shifts of the orbital energy in the

ground state due to the change of the local electrostatic potential. This contribution to the CLS is called the initial state effect.

When a core hole is created, the system tends to screen it (final state effect) as much as possible, providing a relaxation energy gain for the emitted electron and pushing the core level binding energy toward lower binding energy from the initial state result. The final state theory has been largely developed for understanding the chemical shifts in metallic alloys using the so-called Z+1 approximation[136]. The change in the final state effect between different chemical environments could be small, especially for metallic systems, due to the short metallic screening length[137]. However, the final state relaxation at the surface of even metallic systems can be noticeably different to those in the bulk, playing an important role in the SCLS[138-140].

The proper account of the final state effect becomes even more critical when it comes to the SCLS of semiconductor surfaces, which may undergo drastic surface reconstructions[99-101,106,107,141]. Pehlke and Scheffler have suggested that the surface electronic structure and site-sensitive screening of core holes play important roles in the determination of the SCLS of Si (001) and Ge (001) [107]. They found a large relaxation energy gain for the peak derived from the down atom of a surface dimer at Si (001). It has been explained that the potential induced by a core hole at the “down atom” places the empty dangling-bond state below the Fermi level. Subsequently, the lowered localized state is occupied by an electron from the Fermi level, leading to effective screening of the core hole.

Using combined in-situ x-ray photoemission spectroscopy and density functional theory, we have recently investigated the change in the SCLS of Si (001) induced by 1/2-ML Sr deposition[122,142]. We have shown that charge transfer flattens the tilted dimers, resulting in a single dimer-related peak in the photoemission spectrum, compared to two

dimer-related peaks for pure Si (001). Additionally, we have found that the final state theory is necessary to describe the evolution of the Si 2p dimer peaks, with respect to the 2p bulk peak, as a function of Sr coverage.

Additionally, we observed that the 2p bulk peak of Si (001) is shifted toward higher binding energies by 0.49 eV upon 1/2-ML Sr deposition, but the origin of this effect was unclear [122,142]. Based on the simple charge transfer picture, the extra electrons transferred to Si (001) should push the Si 2p levels toward lower binding energy, but the opposite shift was observed experimentally. We note that similar observations have been reported for other sub-monolayer metal/Si (001) systems[110,112,143,144], and the origin of these shifts remains unknown. The case of Ba on Si (001)[110] is of particular interest because of its similarity to that of Sr/Si (001), in terms of the charge transfer and 2×1 surface reconstruction. However, from the data reported in Ref. [110] for a Ba coverage of 0.6 ML, the bulk 2p shift is less than 0.3 eV, which is a factor of two smaller than for that of 1/2-ML Sr/Si (001). The main question is what makes the bulk peak so sensitive to the surface structure. Answering this question may provide valuable insight in the surface electronic structure of Zintl templates on Si (001) and will advance the oxide heteroepitaxy on semiconductors.

In this chapter, we discuss the evolution of the electronic structure of Si (001) induced by 1/2-ML Sr or Ba deposition using in-situ x-ray photoemission spectroscopy combined with the first-principles final state calculations. We find that the bulk Si 2p peak of Si (001) is shifted by 0.49 eV and 0.39 eV toward higher binding energies as 1/2-ML of Sr and Ba are deposited, respectively. Theoretical calculations reveal that the shift originates from the elimination of the surface states in the energy gap of Si due to the presence of AEM. We explain the difference in the bulk 2p peak shifts between the Sr and Ba in terms of the surface electronic structure near the Fermi level.

5.2 EXPERIMENT AND THEORETICAL CALCULATIONS

B-doped (~10^{16} cm^{-3}) prime Si wafers were cut into 20 mm×20 mm pieces and ultrasonically cleaned in acetone, deionized water and isopropanol for 5 minutes each, then exposed to ultraviolet (UV)-ozone lamp to remove carbon impurities at the surface. The Si substrates were then introduced into a customized DCA 600 molecular beam epitaxy (MBE) system with a base pressure of 3×10^{-10} Torr. To remove the native SiO_2 layer, the substrates were heated up to 875 ^{o}C and annealed for three hours under ultrahigh vacuum. After annealing, a sharp 2×1 reconstruction pattern is observed by *in situ* RHEED. The samples are then transferred *in situ* to the x-ray and ultraviolet photoelectron spectroscopy (XPS/UPS) analysis chamber (VG Scienta R3000). The C 1s and O 1s core level spectra are measured to verify the cleanness of the Si (001) surface. After confirming that there is no detectable SiO_2 layer at the surface, the sample is moved to the MBE chamber for subsequent Ba deposition. The Ba flux is calibrated using a quartz crystal monitor and fine tuned using RHEED oscillations to yield a rate of 1 ML per minute, where we define 1 ML as the atomic surface density of an ideal unreconstructed Si (001) surface (1 ML = 6.78×10^{14} atoms/cm^2). Measurements of the surface core level shifts and work function as a function of Ba coverage at room temperature are performed with *in situ* XPS using monochromatic Al Kα radiation (hυ = 1486.6 eV) and *in situ* UPS using a bright monochromatic He plasma light source (He I radiation hυ = 21.22 eV). The analyzer is calibrated using a two-point measurement of the Ag $3d_{5/2}$ core level at 368.28 eV and the Fermi edge of Ag at 0.00 eV. The resolution of the XPS spectra is limited by the x-ray source line width, which is approximately 300 meV, while that of UPS is analyzer-limited and is <30 meV.

We use density functional theory (DFT) as implemented in the VASP code[117]. The exchange-correlation energy is approximated within the local density approximation (LDA), using the Ceperley-Alder data parameterized by Perdew and Zunger[145]. We employ projector augmented wave (PAW) pseudopotentials[118] to describe Si, Sr and Ba, for which $3s^2 3p^2$, $4s^2 4p^6 5s^2$, and $5s^2 5p^6 6s^2$ electrons are treated as valence, respectively. The electronic total energy is converged to 10^{-6} eV/cell for each electronic self-consistent calculation. Using a plane-wave cutoff energy of 500 eV along with a 8×8×8 Monkhorst-Pack k-point grid, we calculate the lattice constant and the band gap of Si to be 5.403 Å and 0.47 eV, respectively, which are underestimated compared to the experimental lattice constant of 5.431 Å and 1.12 eV for the band gap in Si[146,147]. Higher cutoff energies and denser k-point meshes have been tested for convergence.

We model Si (001) using slab geometry. For structural optimization, we use a 12-layer thick Si slab with 15 Å of vacuum to separate the slab from its periodic images along the (001) direction. The in-plane cell size is 2×2 with dimensions of 7.64 Å × 7.64 Å. We treat both surfaces of the slab as active surfaces to satisfy the periodic boundary condition along the (001) direction with no hydrogen passivation. We fix the middle 4 bulk layers, while both surfaces are relaxed until the Hellmann-Feynman forces are less than 10 meV/Å using 500 eV cutoff energy and 6×6×2 k-point grid.

To calculate the Si 2p core level binding energies, we consider slab thicknesses from 16 to 32 layers. We increase the bulk region of the 12-layer thick relaxed slab by increment of 4 Si layers. The initial state calculations are done by calculating the core-level eigenvalues with respect to the Fermi level. In the PAW formalism, the information of the core-levels can be recovered by a linear transformation. For the final state calculations, we use the PAW method in the frozen core approximation[121], in which a 2p core hole is generated at an atomic site of interest followed by full relaxation of the

valence band. To consider the completely screened final state, which sets the lower bound of the binding energy, we add one electron to the system. This extra electron also ensures the charge neutrality of the system in the presence of the core hole. In order to minimize the interaction between a core hole in the slab and its periodic images on the same Si layer, we increase the surface cell size to (dimension = 10.81 Å × 10.81 Å). For the total energy calculations in the final state theory, a cutoff energy of 600 eV is used along with 6×6×2 (6×6×1) k-point meshes for 16 and 20 layer-thick (24 to 32 layer-thick) slabs.

5.3 RESULTS AND DISCUSSION

Figure 5.1 shows the RHEED patterns for clean 2×1 Si (001) and Si with various coverage of Ba. RHEED patterns of sub-monolayers of Ba on Si (001) shows the same as the those of Sr on Si (001). As the Ba coverage increases, the RHEED pattern evolves from a 2×3 reconstruction between 1/4 and 1/3 ML of Ba into a 2×1 structure between 1/3 and 1/2 ML of Ba coverage. At 1/2 ML Ba coverage the RHEED pattern is identical to that of clean 2×1 Si (001). After Ba deposition and RHEED imaging, the samples were transferred *in situ* to the photoemission analysis chamber.

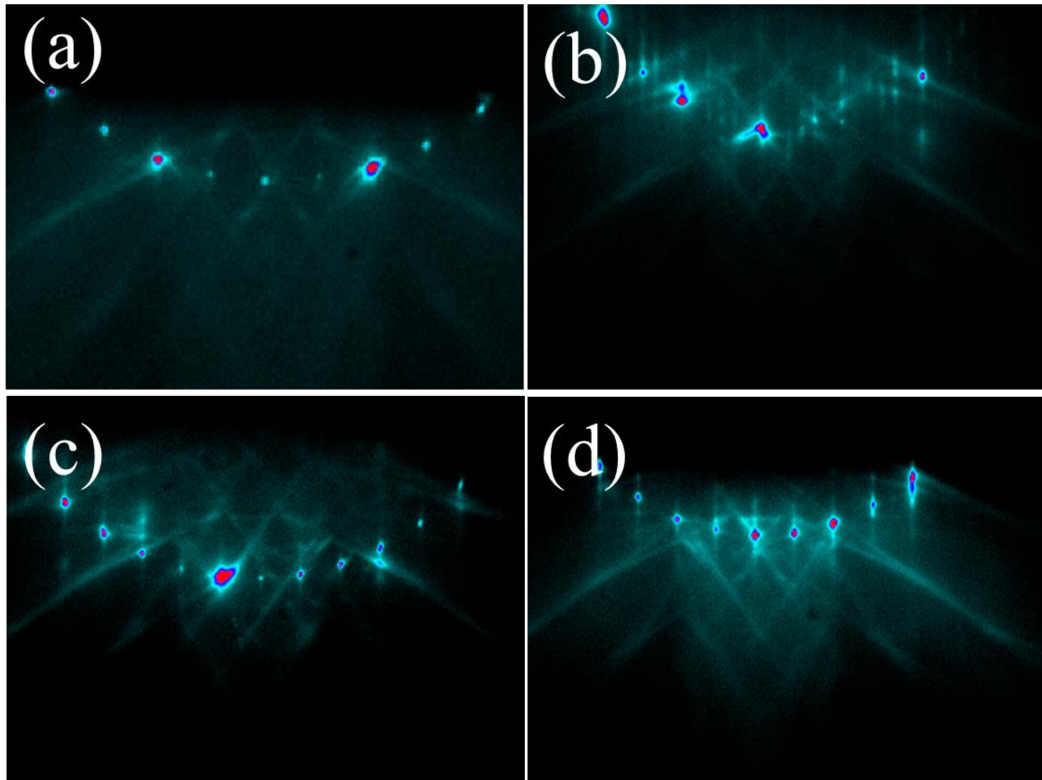

Figure 5.1 RHEED patterns of the Si (001) surface as a function of Ba coverage for (a) 0, (b) 1/4, (c) 1/3, and (d) 1/2 ML Ba coverage on 2×1 Si (001) deposited at 600 °C. All patterns are viewed along the Si <110> azimuth.

In Figure 5.2(a), we show the surface structures of Si (001) and 1/2-ML Sr or 1/2-ML Ba on Si (001) obtained from first-principles calculations. The Si (001) surface, with the asymmetric dimers, is insulating with empty p_z-like dangling bond states at the down atom sites and fully occupied s-like dangling bond states at the up atom sites[148]. When 1/2-ML Sr is deposited, all trough sites on the Si (001) surface are occupied and the passivated dimers recover the symmetric un-tilted geometry, leading to the 2×1 symmetry as shown in Figure 5.2(a). The surface passivation mechanism works with 1/2-ML Ba in the same way[114]. However, we note that the position of Ba from the Si (001) surface is

calculated to be higher than that of Sr by 0.167 Å due to its larger ionic radius. The theory value is in good agreement with an experimental value of 0.14 Å[114] and the difference of 0.17 Å between the ionic radii of Ba^{2+} and Sr^{2+} [149].

In Figure 5.2(b), we show the SCLS of the 1/2-ML Ba on the Si (001) surface. The data fitting and analysis of the Si 2p peak structures are explained in detail in previous papers[122,142], in which we also reported the SCLS spectra of the pure Si (001) surface and the surface with 1/2-ML Sr. For pure Si (001), there are two dimer-related peaks at -0.43 eV (S_u) and 0.12 eV (S_d) with respect to the 2p bulk peak[122,142]. For the 2×1 surface with 1/2-ML Ba, all the surface Si atoms are symmetrically equivalent, yielding a single dimer-related peak (S1 in Figure 5.2(b)), measured to be at -0.33 eV with respect to the 2p bulk peak. Using the final state theory, we calculate the position of S1 for the Ba/Si (001) surface to be -0.50 eV, which is in reasonable agreement with experiment. Interestingly, we also observe a shift of the 2p bulk peak toward higher binding energies by 0.39 and 0.49 eV, respectively, as we deposit 1/2-ML Ba and 1/2-ML Sr on the pure Si (001) surfaces. This is shown schematically in Figure 5.2(c). We note that all bulk peaks are very sharp in experiment and their positions are insensitive to the fitting process of the surface-related peaks.

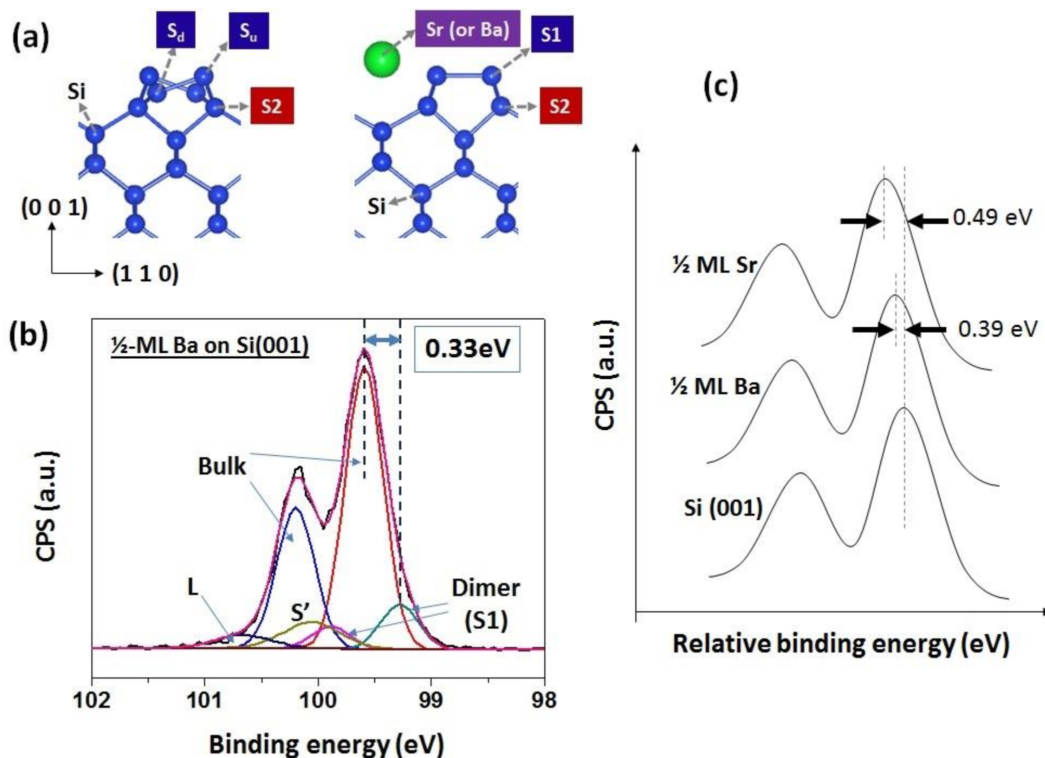

Figure 5.2 (a) Ball-and-stick models of the p(2×2) surface reconstruction of Si (001) (left) and the 2×1 reconstruction of Si (001) induced by 1/2-ML Sr or Ba deposition (right). (b) Si 2p core-level spectrum of 1/2-ML Ba/Si (001) by in-situ XPS at room temperature. The detailed description of the sub-peak structures and the analysis procedure are explained elsewhere[122,142]. (c) Schematic to show the 2p bulk peak shifts of clean 2×1 Si (001) (bottom) induced by 1/2-ML Ba (middle), and 1/2-ML Sr (top) depositions.

To understand the dependence of the bulk peak shift on the surface structure and composition, we take a 24-layer thick Si (001) slab and perform the initial and final state calculations of the bulk 2p binding energy. The initial state effect (ground state property) for the bulk 2p states is provided by the dipole layer formed at the surface due to the charge transfer from 1/2-ML Sr (or Ba) to the Si dimers. However, the initial state result is calculated to be basically zero, meaning that the increase in the Si 2p energy by the initial state surface dipole is compensated by the simultaneous increase in the Fermi level of the system by the 2×1 surface reconstruction induced by 1/2-ML Sr or 1/2-ML Ba. On

the other hand, using the final state calculations with equation (1), we calculate the bulk 2p binding energy to be shifted by 0.18 and 0.30 eV for Ba and Sr, respectively, with respect to that of pure Si (001). We first note that the theoretical results qualitatively agree with experiment. We remark, however, that a direct quantitative comparison with the experimental values is not possible because in theory we only consider a single core hole at a particular bulk region, while in experiment a multiple number of core holes from various locations are present.

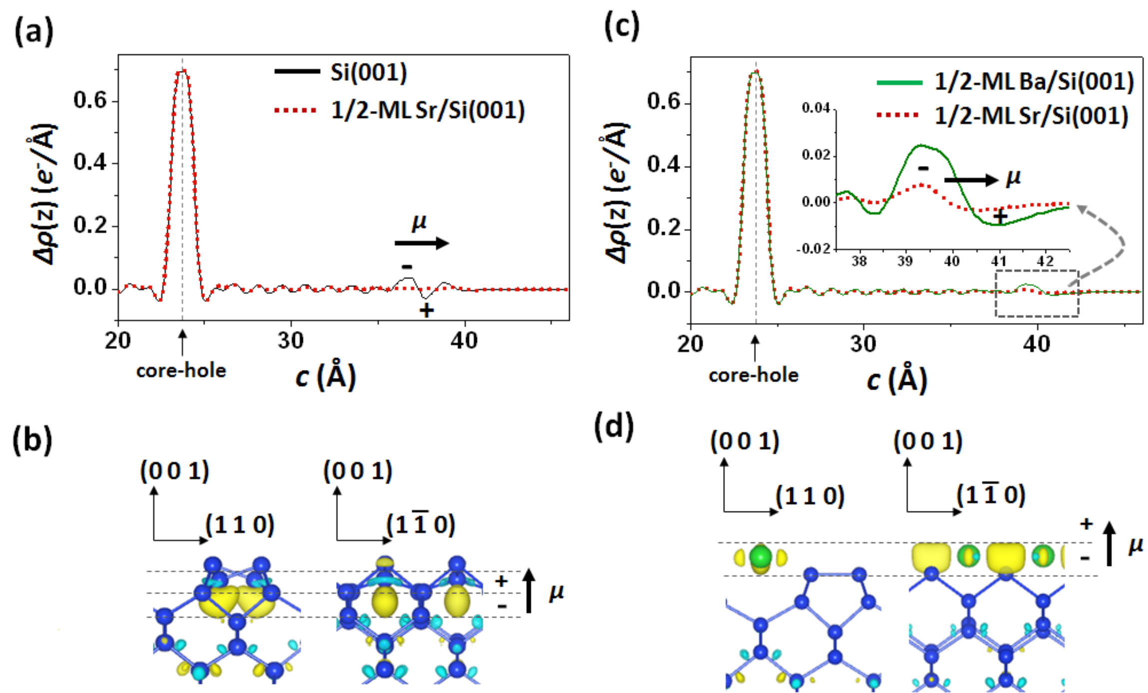

Figure 5.3 One dimensional screening electron density for a bulk 2p core-hole in the 24-layer-thick pure Si (001) slab (black straight line in (a)) and in the 1/2-ML Ba/Si (001) slab (green straight line in (c)) compared to that of the 1/2-ML Sr/Si (001) slab (red dashed lines in (a) and (c)). Three dimensional screening electron density for the bulk 2p core-hole near the surface of the 24-layer-thick pure Si (001) (b) and the 1/2-ML Ba/Si (001).

To shed more light on the dependence of the final state effect on the surface structure of Si (001), we compare the screening electron density for a bulk 2p core hole created in the 24 layer-thick Si (001) and Sr/Si (001) slabs in Figure 5.3(a), which is defined as

$$\Delta\rho(x,y,z) = \rho'_{N+1}(x,y,z) - \rho_N(x,y,z) \tag{5.2}$$

where ρ'N+1 and ρN are the charge densities of the excited and ground states, respectively. In addition, a one dimensional profile as a function of distance normal to the surface can be calculated as

$$\Delta\rho(z) = \int_0^L \int_0^L \Delta\rho(x,y,z)\,dxdy \tag{5.3}$$

where L is the dimension of the surface cell. As expected, most of the screening electron density is strongly localized around the core hole site. The rest of the screening electron density decays outward with Friedel-like oscillations and shows a rather noticeable difference at the surface. Notably, for pure Si (001), we observe that the final state effect for the bulk 2p core hole involves the formation of a dipole layer at the surface, which vanishes when 1/2-ML Sr is deposited. We call this a final-state surface-dipole (FSSD) to distinguish it from the initial-state surface-dipole formed by the charge transfer from 1/2-ML Sr to Si (001). From the three dimensional plot of the FSSD of the Si (001) surface in Figure 5.3(b), we find that the p_z-like state at the down atom plays an important role. Interestingly, as seen in Figure 5.3(c), the p_z-related FSSD of pure Si (001) also disappears when 1/2-ML of Ba is deposited, but another FSSD is visible around the Ba layer. Figure 5.3(d) also shows that the FSSD at the 1/2-ML Ba/Si (001) surface is associated with the Ba states.

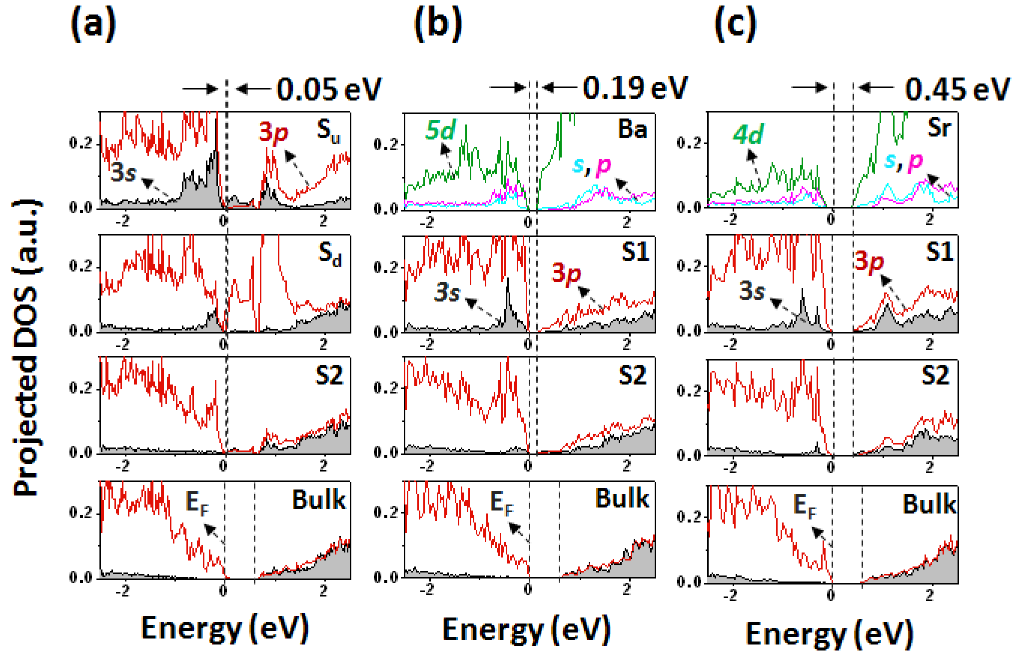

Figure 5.4 Layer-by-layer projected density of states (pDOS) of pure Si (001) (a), 1/2-ML Ba/Si (001) (b), and 1/2-ML Sr/Si (001) (c). The Fermi levels are set to be 0 eV. For each panel, the upper three plots are the pDOSs of the surface atoms whose names are shown on the right upper corner of each plot. The surface gaps are calculated to be 0.05 eV, 0.19 eV, and 0.45 eV for Si (001), 1/2-ML Ba/Si (001), and half-monoalyer Sr/Si (001), respectively. The bottom plot is the pDOS calculated for one of the bulk Si atom with the bulk gap of 0.5 eV represented by two dashed lines.

In Figure 5.4(a), we show the layer-by-layer projected density of states (pDOS) of the Si (001) surface, showing an empty p_z surface state inside the bulk gap, which is about 0.5 eV in our LDA calculations. Considering the electronic structure of the corresponding excited state with the bulk 2p core hole, we find that a strong s-like bound state forms at the core hole site and is 13.0 eV below the Fermi level as shown in Figure 5.5(a). As discussed previously, using the screening electron density profile in Figure 5.3(b), we also find in Figure 5.5(b) that the empty p_z surface state is partially occupied

by the screening electron, contributing to the formation of the FSSD on Si (001). On the other hand, when 1/2-ML Sr is deposited, the surface gap increases to 0.45 eV, which is close to the bulk gap of 0.5 eV as shown in Figure 5.4(c). The increased surface gap for 1/2-ML Sr/Si (001) leads to a negligible FSSD as shown in Figure 5.3(a) and Figure 5.5(d) since there is no surface state for the screening charge to occupy. Figure 5.4(b) shows the surface electronic structure of 1/2-ML Ba/Si (001). We note that the increased surface gap of 0.19 eV for 1/2-ML Ba/Si (001) compared to that of pure Si (001) is still smaller than that of 1/2-ML Sr/Si (001) by a factor of two. The smaller surface gap of Ba/Si (001) leads to relatively larger FSSD, induced by screening charge accumulated at the empty Ba state below the bulk Si conduction band edge as shown in Figure 5.5(c).

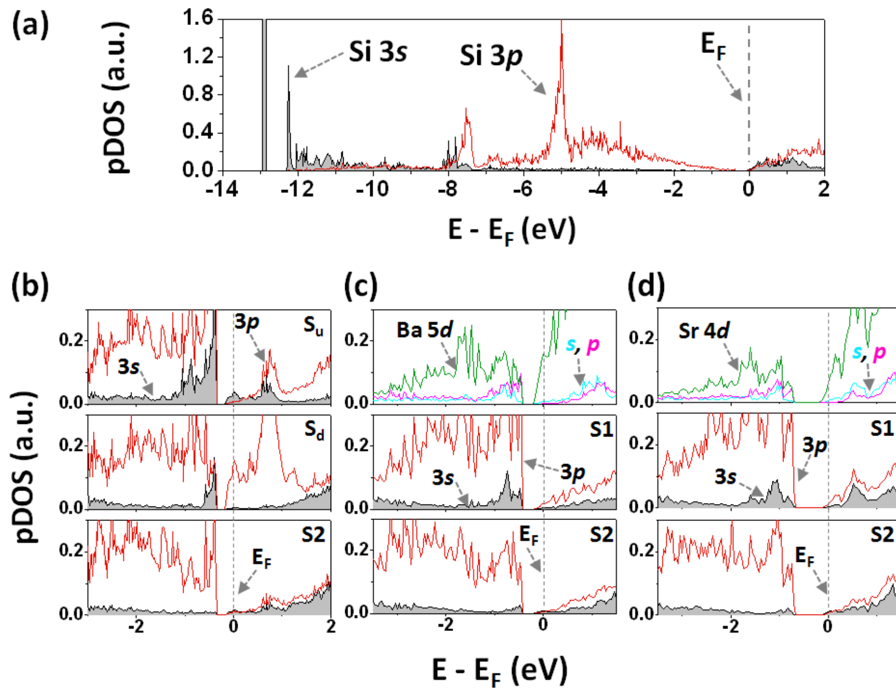

Figure 5.5 (a) Density of states (DOS) of bulk 2p core-hole excited Si (001) projected on the bulk 2p core hole site. The Fermi levels are set to be 0 eV. (b) Layer-by-layer projected density of states (pDOS) of pure Si (001) (b), 1/2-ML Ba/Si (001) (c), and 1/2-ML Sr/Si (001) (d) in the presence of the bulk 2p core hole.

These results inspire a number of questions. The first one is what could be sources of the screening electron or the electron accumulated in the empty surface state contributing to the formation of a FSSD on the Si (001) surface? Once a 2p core hole is generated, a strong positive potential is induced at the core hole site, and the empty conduction band states are pulled down in energy. If the empty states are pulled down below the Fermi level, the screening electron could be provided by the system. We also speculate that there could be electron accumulation in the empty surface states during the photoemission experiment due to relaxation of photo-excited electrons, thus contributing to the formation of a FSSD. In the three-step model of photoemission process, photo-excited electrons travel to the surface and escape from the surface[64]. However, there would be a certain number of electrons which do not escape from the surface due to the kinetic energy loss. In the presence of the surface states below the bulk conduction band edge, the photo-excited electrons would relax into the empty surface states[150,151].

The last questions are why there is a significant amount of Sr 4d (Ba 5d) states near the Fermi level for 1/2-ML Sr (Ba)/Si (001) and why the surface gap differs for the Sr and Ba adsorption (Figure 5.4). Using separate atom-in-a-box calculations, we check that the Sr 4d states are placed higher in energy by 2.2 eV than the Sr 5s states. For 1/2-ML Sr/Si (001), we calculate the center of the Sr 4d band to be about 5 eV above the Fermi level. However, the width of the Sr 4d band is calculated to be greater than 9 eV due to a strong interaction between 1/2-ML Sr and Si (001), giving rise to the finite density of Sr 4d states near the Fermi level. On top of the band broadening, the importance of covalent interaction between AEMs and Si (001) has been previously pointed out[128,152]. Using a Wannier function method, Garrity and co-workers suggested that the surface gap is related to a covalent interaction between the Si dangling bonds and Sr orbitals. In our calculations, the dominant interaction occurs between the Sr $4d_{xy}$ and

Si $3sp_z$ states. On the Si (001) surface, Ba sits 0.167 Å higher than Sr, which results in less hybridization and subsequently a smaller surface gap opening for the 1/2-ML Ba/Si (001) template. Experimentally, there is not yet a direct observation of the empty Sr 4d (Ba 5d) states of 1/2-ML Sr (Ba)/Si (001) system. However, empty Sr 4d states near the Fermi level have been observed for a Sr/Si (001) 2×3 surface using scanning tunneling spectroscopy[153,154]. By considering a possible structural model of the Sr/Si (001) 2×3 surface[152], we also checked that the surface electronic structure of the 2×3 surface shows a similar interaction between Sr $4d_{xy}$ and Si $3p_z$ states near the Fermi level.

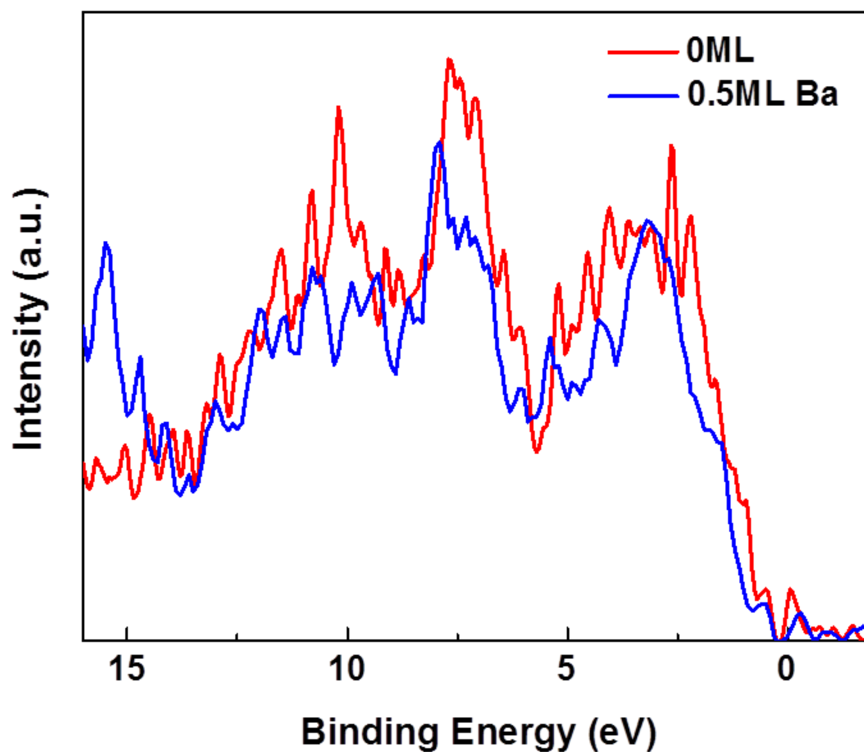

Figure 5.6 Valence band edge of the clean 2×1 Si (001) and 1/2 ML Br on Si (001) measured using XPS. The zero of energy is set at the Fermi level.

To verify the charge transfer, the location of the valence band edge was measured for both clean Si (001) and 1/2 ML Ba on Si (001) as shown in Figure 5.6. The valence band edge positions are determined using the linear extrapolation method[120]. The energy shift of the valence band for 1/2 ML Ba on Si is approximately 0.238 eV toward higher binding energy when compared to that of clean Si (001). This value of the valence band shift confirms that it is the entire spectrum that shifted, supporting the presence of charge transfer from the Ba atoms.

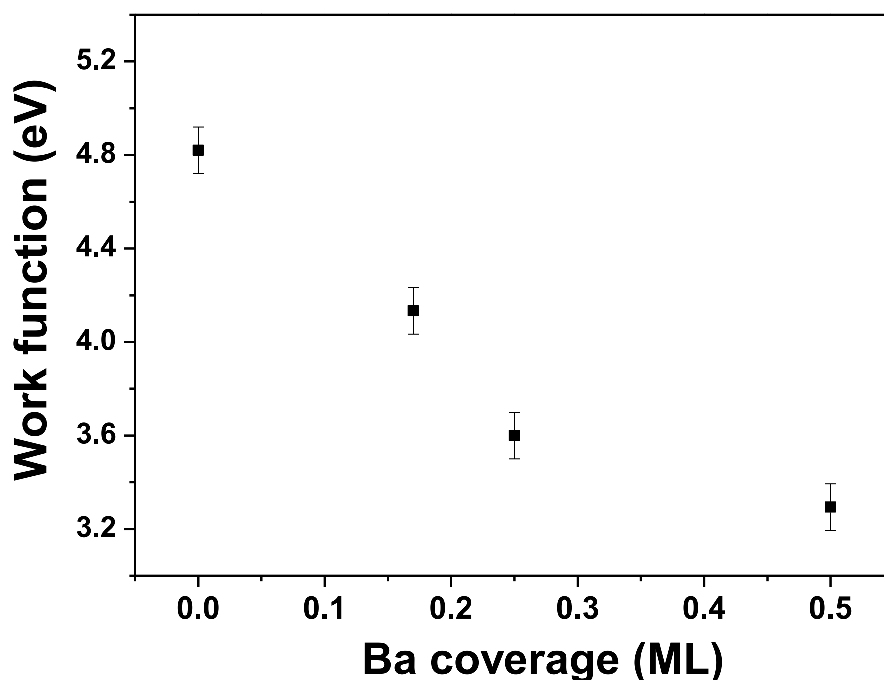

Figure 5.7 Work function variation as a function of Ba coverage on 2×1 Si (001) from experiment.

Figure 5.7 shows the work function of Si (001) as a function of Sr coverage from experiment. We measure the work function of clean 2×1 Si (001) to be 4.82 eV using *in situ* UPS[124,125]. The change in the work function with Ba coverage is determined by the onset of the secondary electron cutoff. The work function decreases with increasing Ba

coverage. The deposition of 1/2 ML of Ba causes a change of electronic structure of Si (001), which leads to a decrease in the work function by 1.53 eV.

Similar work function changes caused by the interface electronic properties were also observed when organic molecules were deposited on metals or oxides[126,127].

5.4 SUMMARY

To summarize, we investigate the surface 2p core level shifts of Si (001) induced by deposition of 1/2-ML of Sr and Ba using the density functional final state theory and in-situ x-ray photoemission spectroscopy. We find that, in terms of the initial state theory, the increase of the Si 2p orbital energy in the bulk, due to the surface dipole layer formed by the charge transfer from Sr (or Ba) to Si (001), is compensated by the Fermi level rising due to the 2×1 surface reconstruction and results in no net shift of the bulk 2p peaks due to initial state effects. However, we find that the bulk 2p peak shifts, induced by 1/2-ML Sr or 1/2-ML Ba deposition on Si (001), are derived from the final state effect induced by creation of core holes near the surface. For pure Si (001), we show that the creation of core holes within the critical distance from the surface (31 Å in our theory) induces a final-state surface-dipole (FSSD), giving rise to an additional potential energy shift toward lower binding energy for the bulk Si 2p peak. When 1/2-ML of Sr or 1/2-ML Ba is deposited, this pz-derived FSSD is reduced, which reduces the potential energy shift of the bulk 2p core level. As a result, the bulk 2p peak of Si (001) is shifted toward higher binding energy when 1/2-ML of Sr or Ba is deposited. Comparing the Sr and Ba cases in detail, we find that the FSSD depends on the surface gap; the greater the surface gap (0.05 eV for Si (001), 0.19 eV for 1/2-ML Ba/Si (001), and 0.45 eV for 1/2-ML Sr/Si (001)), the smaller the FSSD, and the more the 2p peak is shifted toward higher binding energy. We also find that the surface band gap is controlled by the interaction between

the AEM d states and the Si (001) surface dangling bonds. Because the larger ionic radius of Ba results in Ba located 0.17 Å higher above the Si (001) surface than Sr, the surface gap of 1/2-ML Ba/Si (001) is smaller than that of 1/2-ML Sr/Si (001), leading to a significant density of surface states within the Si bulk band gap.

Chapter 6. Strain relaxation in single crystal $SrTiO_3$ grown on Si (001) by molecular beam epitaxy

An epitaxial layer of $SrTiO_3$ grown directly on Si may be used as a pseudo-substrate for the integration of perovskite oxides onto silicon. When $SrTiO_3$ is initially grown on Si, it is nominally compressively strained. However, by subsequent annealing in oxygen at elevated temperature, an SiO_x interlayer can be formed which alters the strain state of the $SrTiO_3$. We report a study of strain relaxation in $SrTiO_3$ films grown on Si by molecular beam epitaxy as a function of annealing time and oxygen partial pressure. Using a combination of x-ray diffraction, reflection high energy electron diffraction, and transmission electron microscopy, we describe the process of interfacial oxidation and strain relaxation of $SrTiO_3$ on Si (001). Understanding the process of strain relaxation of $SrTiO_3$ on silicon will be useful for controlling the $SrTiO_3$ lattice constant for lattice matching with functional oxide overlayers. XRD data were taken by use of the National Synchrotron Light Source, Brookhaven National Laboratory. This work was published in : M. Choi, A. B. Posadas, R. Dargis, C. K. Shih and A. A. Demkov, D. H. Triyoso, N. David Theodore, C. Dubourdieu J. Bruley and J. Jordan-Sweet, J. Appl. Phys. **111**, 064112, (2012).

6.1 INTRODUCTION

In 1998 McKee and co-workers demonstrated epitaxial growth of $SrTiO_3$ (STO) films directly on Si (001) by molecular beam epitaxy (MBE)[14]. The structural and electronic properties of the interface between silicon and $SrTiO_3$ have been studied both theoretically and experimentally[23,82,155-160]. Initial interest in the system stemmed from its possible applications in complementary metal-oxide-semiconductor (CMOS) technology as a replacement for the SiO_2 gate dielectric. Unfortunately, the STO/Si conduction

band offset was found to be practically zero, making it unsuitable for gate dielectric applications[82,161]. More recently, $SrTiO_3$ on Si has been used as a buffer layer for integration with Si of many perovskite oxides. These include high-k dielectrics such as $SrHfO_3$ and $LaAlO_3$ for metal-oxide-semiconductor field effect transistors (MOSFETs) [86,87], ferroelectric $BaTiO_3$[88,89], ferromagnetic $La_{1-x}Sr_xMnO_3$[90], and multiferroic $BiFeO_3$[91]. Strain plays an important role in determining the properties of many perovskites, for example, in stabilizing a ferromagnetic state in non-magnetic $LaCoO_3$ when grown on STO/Si[19], and in the realization of a strong magnetic ferroelectric state in $EuTiO_3$[31]. Therefore, applications of STO/Si as a virtual substrate would benefit greatly from a thorough understanding of strain relaxation in STO films grown on Si. Controlling the strain of oxide materials also offers another route for monolithic integration and development of new device applications of epitaxial oxide films on Si.

STO can be grown epitaxially on Si without forming an interfacial SiO_2 layer by first depositing half a monolayer of Sr metal on Si, which partially protects the Si surface from rapid oxidation while essentially maintaining the underlying surface structure of Si [162]. If a thin amorphous STO layer is then grown on the Sr-passivated Si surface near room temperature and subsequently crystallized in vacuum, an epitaxial layer of STO can be formed directly on Si. Thin STO grown in this manner has a compressive strain of 1.7 % at room temperature, with the STO unit cell rotated by 45° relative to the Si conventional unit cell. Once the initial STO layer is crystallized, subsequent STO growth can be done in two ways. If one continues the STO deposition near room temperature and annealing in vacuum after each deposition step, a thicker STO layer with no interfacial SiO_2 can be obtained after repeating the process a sufficient number of times. Below the critical thickness, STO grows coherently strained to Si. Strained STO on Si is polar and has also been reported to be ferroelectric[163,164].

Another way of obtaining thicker STO is to simply treat the initial STO layer as if it were a regular STO substrate and deposit more STO under the usual high oxygen partial pressure at high substrate temperature. Using this method, however, results in the formation of a thin amorphous SiO_2 layer at the interface of STO and Si, since the excess oxygen is able to diffuse through the STO into the underlying silicon. STO films grown in this manner are found to have an in-plane lattice constant that is larger than that of bulk STO[116,165]. This in-plane expansion is attributed to the thermal expansion coefficient mismatch (the thermal expansion coefficient of STO is 8.8×10^{-6} K^{-1} which is four times bigger than that of Si)[166]. The presence of the SiO_2 interlayer itself has beneficial effects from the MOSFET point of view: sufficient conduction band offset and improved channel mobility, but at the price of a larger equivalent oxide thickness. Furthermore, post-deposition oxygen annealing of the STO/SiO_2/Si stack can provide a way of controlling the strain relaxation of the STO layer by controlling the thickness of the SiO_2 interlayer.

In this paper, we report on the investigation of residual strain control in STO films by post-deposition annealing in oxygen to adjust the thickness of the SiO_2 interlayer (IL). Specifically, we study the effect of oxygen partial pressure and annealing duration on the thickness of the amorphous interfacial SiO_2 layer, and how that in turn affects the lattice constant of STO films grown on Si (001). The epitaxial STO films are deposited on Si (001) using molecular beam epitaxy (MBE). The STO/SiO_2/Si samples are characterized by reflection high energy electron diffraction (RHEED), X-ray diffraction (XRD), and transmission electron microscopy (TEM).

6.2 EXPERIMENTS

A customized DCA 600 MBE system with a base pressure of 2×10^{-10} Torr is used to deposit STO films on Si (001). During growth, the films are monitored *in situ* by reflection high energy electron diffraction (RHEED) to ensure high crystalline quality. STO films on Si (001) are grown by co-deposition of Sr and Ti in the presence of oxygen. The Sr and Ti fluxes are calibrated to be the same by initial measurement of the fluxes using a quartz crystal monitor and subsequent fine tuning using the appearance of reconstruction spots in RHEED.

We use epi-grade prime Si (001) wafers cut into 20 mm × 20 mm pieces, which are cleaned ultrasonically with acetone, isopropanol, and deioinized water for 5 min each. The samples are then exposed to ultraviolet (UV)-ozone for 15 min to remove residual carbon contamination. After cleaning, the samples are introduced into the MBE growth chamber and outgassed at 675 °C for 15 min prior to growth. The native SiO_2 layer is desorbed using a variation of the Sr-assisted deoxidation process developed by Motorola, allowing the SiO_2 desorption to occur at a reduced temperature of 775 °C[167]. After removal of the native oxide as confirmed by a 2×1 RHEED pattern, the substrate temperature is reduced to 575 °C. During the cooling, the RHEED pattern changes to 3×2 indicating sub-monolayer Sr coverage[167]. Additional Sr is then deposited until the 2×1 pattern is recovered, which corresponds to a clean Si surface covered with 0.5 monolayer (ML) of Sr (Figure 6.1)[113,168]. At this point, the surface is ready for STO deposition.

STO growth via co-deposition of Sr and Ti is initiated on Si (001) at 200 °C in an oxygen environment of 8×10^{-8} Torr. After the growth of 1.5 unit cells of STO, the oxygen partial pressure is quickly increased from 8×10^{-8} Torr to 7×10^{-7} Torr and an additional 1.5 unit cells are deposited. The 3-unit cell film is then annealed at 525 °C without oxygen for 5 min to fully crystallize the thin STO layer. An additional thirteen

unit cells of STO are deposited at 565 °C in an oxygen atmosphere of 4×10^{-7} Torr, and the film is subsequently annealed in vacuum at 575 °C for 7 min. All films in this study are grown with the same recipe described above and have approximately 62 Å total STO thickness. This growth process also results in the formation of a ~20 Å SiO_2 interlayer prior to any post-deposition annealing under a controlled oxygen partial pressure. Aside from post-deposition annealing, all of the samples undergo the same substrate preparation and growth process.

For the post-deposition anneal, the oxygen partial pressure is varied from 2×10^{-7} Torr to 1×10^{-5} Torr using an annealing temperature of 650 °C. The annealing time is varied from 10 min to 90 min. The surface crystal structure of the films is monitored *in situ* by RHEED during the annealing process. After annealing, the samples are cooled down to room temperature without oxygen at a rate of 30 °C per minute and unloaded from the chamber. The lattice parameters of the STO films are measured at room temperature by RHEED and by x-ray diffraction (XRD) using a Philips X'Pert diffractometer. The layer thicknesses are measured by a combination of x-ray reflectivity (XRR) and transmission electron microscopy (TEM). For selected films, in-plane and out-of-plane XRD measurements were carried out at the National Synchrotron Light Source (λ = 1.5407 Å).

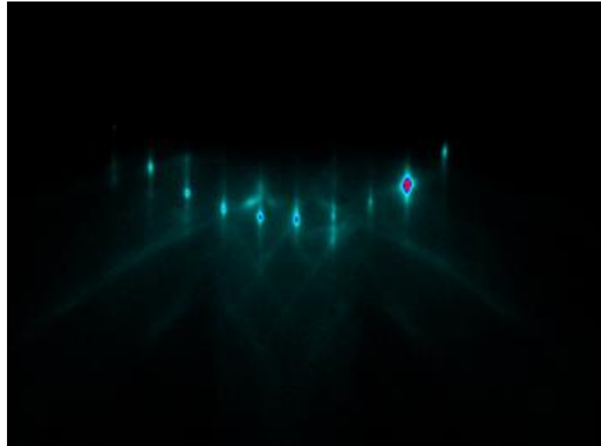

Figure 6.1 2×1 RHEED pattern of Si (001) covered by Sr to form a template viewed from the Si <110> azimuth .

6.3 RESULTS

Figure 6.2(a-d) shows the RHEED patterns along the <010> and <110> directions of STO after each growth step. All of the STO films show qualitatively the same RHEED patterns. The RHEED pattern shown in Figure 6.2(e, f) is for a sample annealed at 650 °C for 30 min in a 1×10^{-6} Torr oxygen environment. After post-deposition annealing, the streaks became sharper, indicating improvement in the crystallinity and flatness of the STO film.

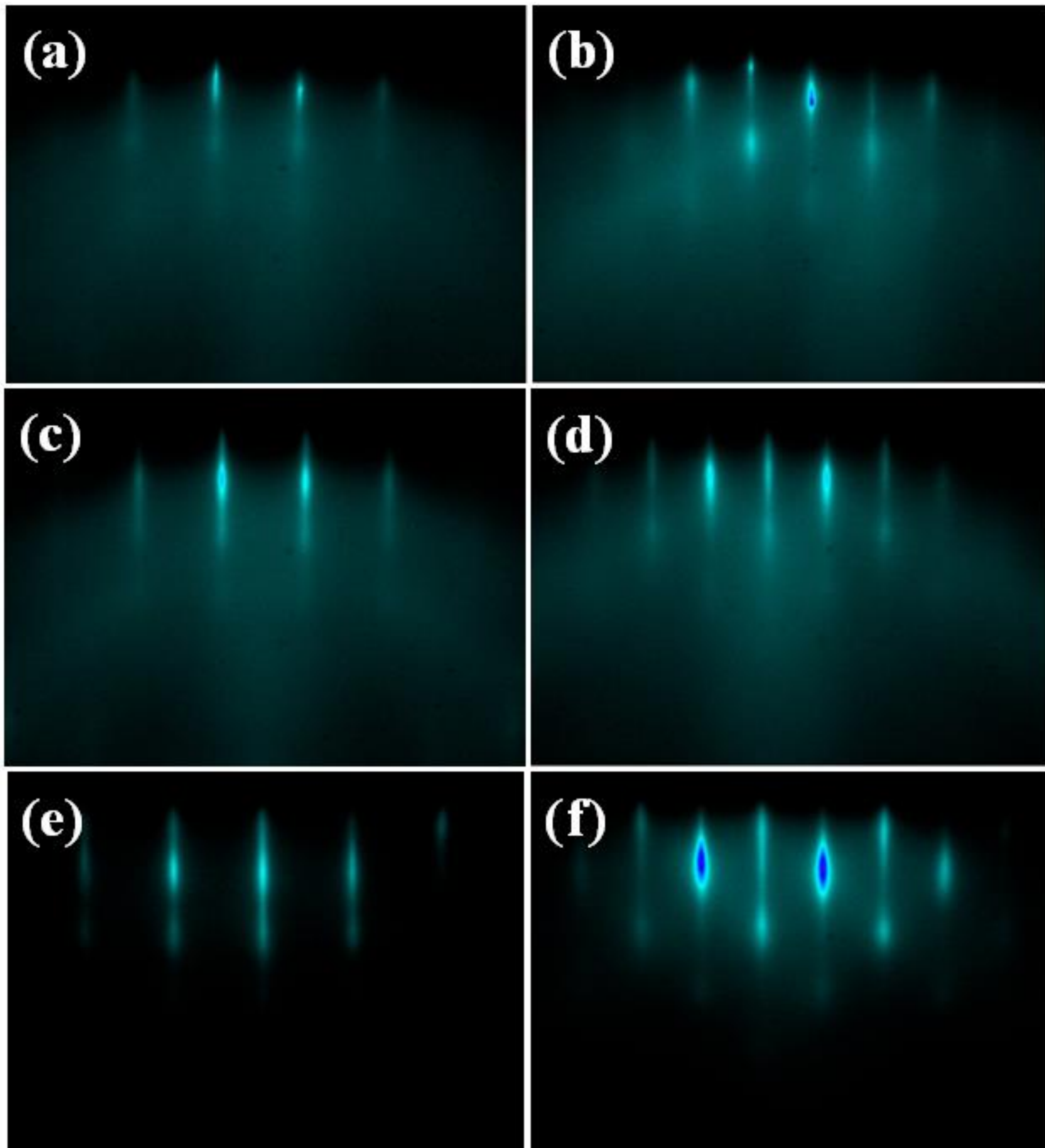

Figure 6.2 RHEED patterns of the STO films on Si after each growth step along <010> (b,d,f, h) and <110> (c, d, g, i) directions. (a) and (b) are RHEED patterns after the initial 3 ML of amorphous STO are crystallized. (c) and (d) are RHEED patterns after the main 13 ML STO growth at 565 °C. (e) and (f) are RHEED patterns after a post-deposition oxygen anneal at 650 °C.

An x-ray diffraction L scan around the 002 diffraction peak of an unannealed STO film on Si is shown in Figure 6.3(a).

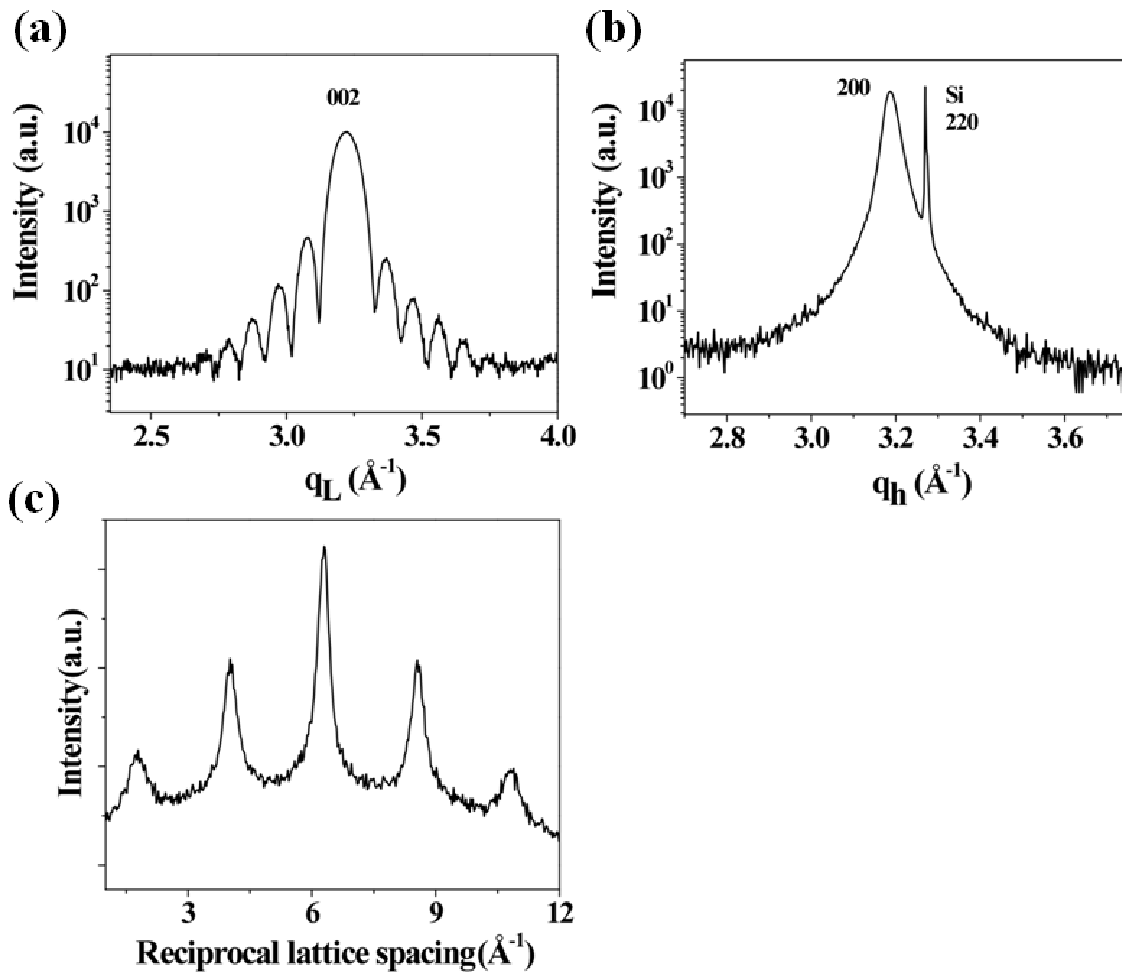

Figure 6.3 Typical x-ray diffraction and RHEED data used to determine STO lattice constants. (a) X-ray diffraction L scan about STO 002 peak; (b) H scan about STO 200 peak; (c) RHEED profile of STO film on Si. The data shown are for an unannealed film.

The 002 peak is used to obtain the out-of-plane lattice constant. The in-plane lattice constant is then calculated from the measured out-of-plane lattice constant using the bulk $SrTiO_3$ Poisson's ratio. The in-plane lattice parameter can be calculated following the equation, $a = a_{STO,bulk} + (c - a_{STO, bulk})\cdot((\nu-1) / 2\nu)$, where $a_{STO, bulk}$ is the bulk lattice parameter of STO; c is the experimental value obtained from the x-ray diffraction 002 peak of the STO films; and ν is the Poisson's ratio of $SrTiO_3$ (0.232)[169]. The unannealed film has lattice parameters a = 3.935 Å and c = 3.902 Å, indicating an in-plane expansion of STO on Si relative to bulk due to the thermal expansion coefficient mismatch during the cool down process[166]. During interlayer formation, the STO lattice assumes a size appropriate to the growth temperature because the exothermic oxidation process disrupts the epitaxy. The larger thermal expansion coefficient of STO compared to Si (four times larger) results in an in-plane expansion during cool down from the growth temperature because STO is clamped to the SiO_2 interlayer. We measured the in-plane lattice constant of an unannealed sample using grazing incidence x-ray diffraction at the National Synchrotron Light Source. High structural quality was confirmed from Kiessig fringes in Figure 6.3(a) and an in-plane lattice constant of 3.936 Å was obtained, confirming in-plane expansion of the unannealed STO film (Figure 6.3(b)). As a further check to confirm the observed trends in XRD lattice constants, in-plane lattice constants of the deposited film were also obtained from RHEED patterns at room temperature, with a typical measurement shown in Figure 6.3(c). RHEED confirms that the unannealed film has an expanded in-plane lattice constant and that the lattice constant trend observed in RHEED is the same as that in the values calculated using the Poisson's ratio.

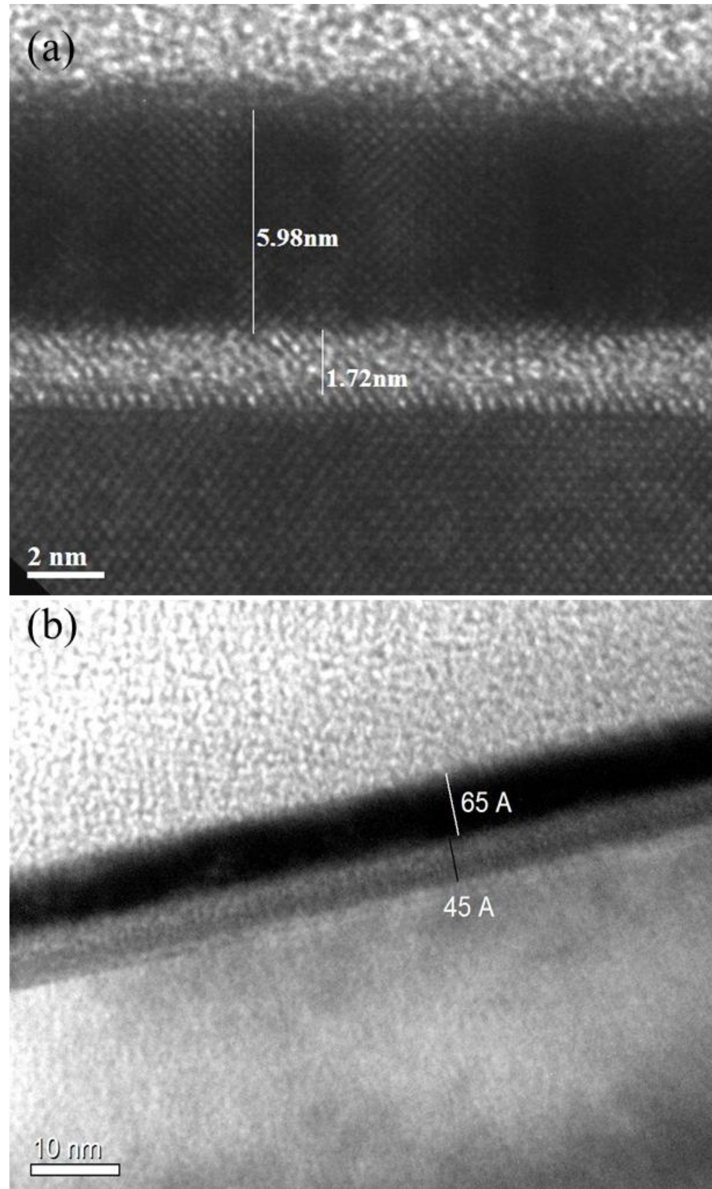

Figure 6.4 Cross sectional TEM images of STO films grown on Si. (a) High-resolution image of an unannealed film; (b) typical low-resolution image of an STO film annealed in oxygen. The specific image is for a sample annealed under 5×10^{-7} Torr of oxygen at 650 °C for 10 min.

To obtain the SiO_2 thickness, we used x-ray reflectivity (XRR) and analyzed the data with the simulation program SimulReflec[63]. Due to the multilayer system, various conditions such as density, roughness, and thickness have to be considered. The fitting

process was repeated with varying initial conditions to minimize error. We also performed cross-section TEM on the samples and measured the thickness of the amorphous interlayer. Figure 6.4(a) shows a high resolution image of an unannealed sample showing highly crystalline STO layers with an initial ~20 Å SiO_2 interlayer. Figure 6.4(b) shows a typical low resolution cross-sectional TEM image of an annealed STO film on Si (001). This particular film was subjected to post-annealing in 5×10^{-7} Torr oxygen pressure at 650 °C for 10 min. The annealing results in an SiO_2 thickness of 45 Å as measured by TEM. The SiO_2 thickness obtained from the TEM images agrees well (to within 10 %) with that from the x-ray reflectivity simulation program for all of the samples measured.

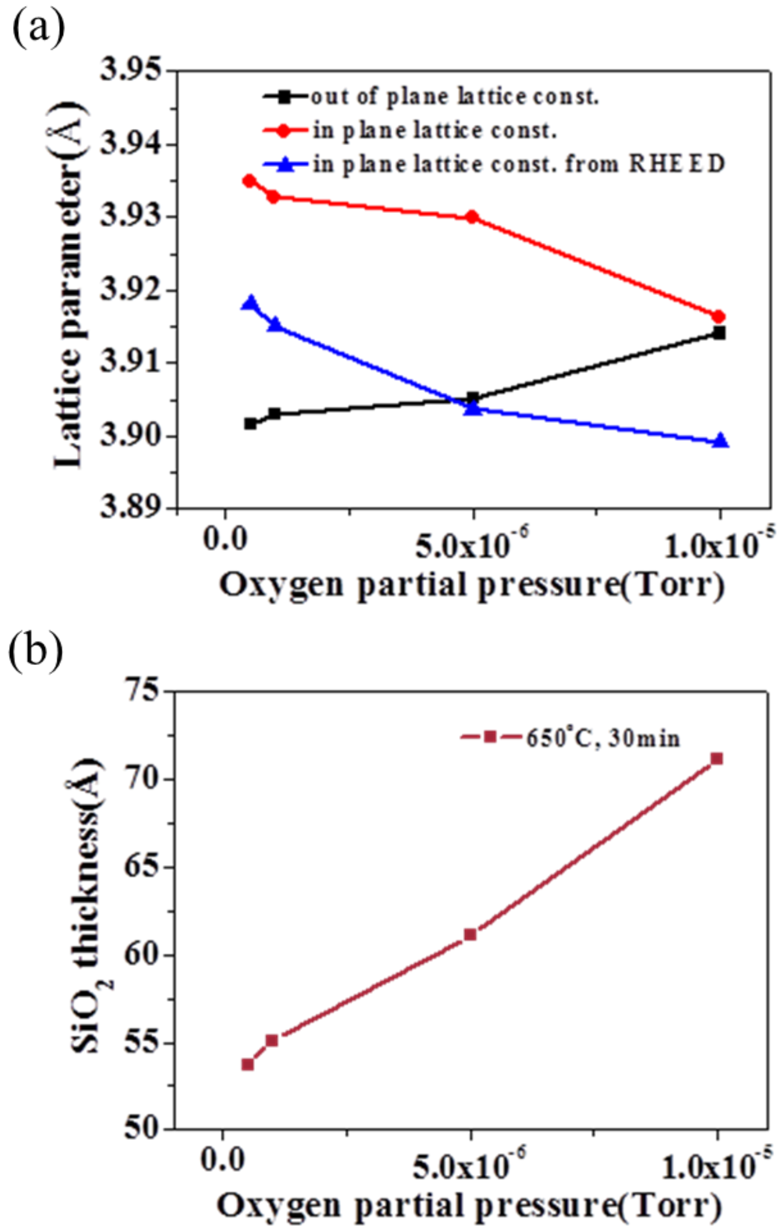

Figure 6.5 (a) In-plane lattice constants and (b) SiO_2 thickness as a function of oxygen partial pressure. All films were annealed at 650 °C for 30 min in different oxygen environments.

A summary of the effect of oxygen partial pressure on the SiO_2 thickness and the STO lattice constants is shown in Figure 6.5. All films shown in Figure 6.5 were annealed at 650 °C for 30 min under different oxygen partial pressures. In Figure 6.5(a), both the in-plane and out-of-plane lattice constants show a systematic variation as the oxygen partial pressure is increased. The in-plane lattice constant of the STO film is initially larger than that of bulk STO, due to the difference in thermal expansion between Si and STO film. However, as oxygen partial pressure is increased, the in-plane lattice constant of the STO films decreases while out-of-plane lattice constant increases. The STO films thus become more cubic, indicating that the STO films experience relaxation toward the bulk, stress-free lattice parameters. At the same time, the SiO_2 thickness increases with increasing oxygen partial pressure, as shown in Figure 6.5(b). This suggests that the relaxation of STO towards its bulk lattice constant is concurrent with the growth of the SiO_2 interlayer during the annealing process, with the STO becoming increasingly decoupled from Si as oxygen partial pressure is increased.

Figure 6.6 summarizes the effect of annealing time on SiO_2 thickness and lattice constants of STO. All films shown in Figure 6.6 were annealed at 650 °C for different lengths of time in an oxygen environment of 5×10^{-7} Torr. From 10 min to 60 min of annealing, the SiO_2 thickness and lattice constants were unchanged to within the limits of experimental error. However, annealing for 90 min results in an unexpected compression of the in-plane, and expansion of the out-of-plane lattice constants. This unusual behavior was found to be reproducible. It is not yet clear why the in-plane lattice constants decreased as SiO_2 thickness was increased for the longer annealing duration at this oxygen pressure. We also note that there is a marked difference in the evolution of the RHEED patterns for 90 min annealing duration and 10 min annealing duration.

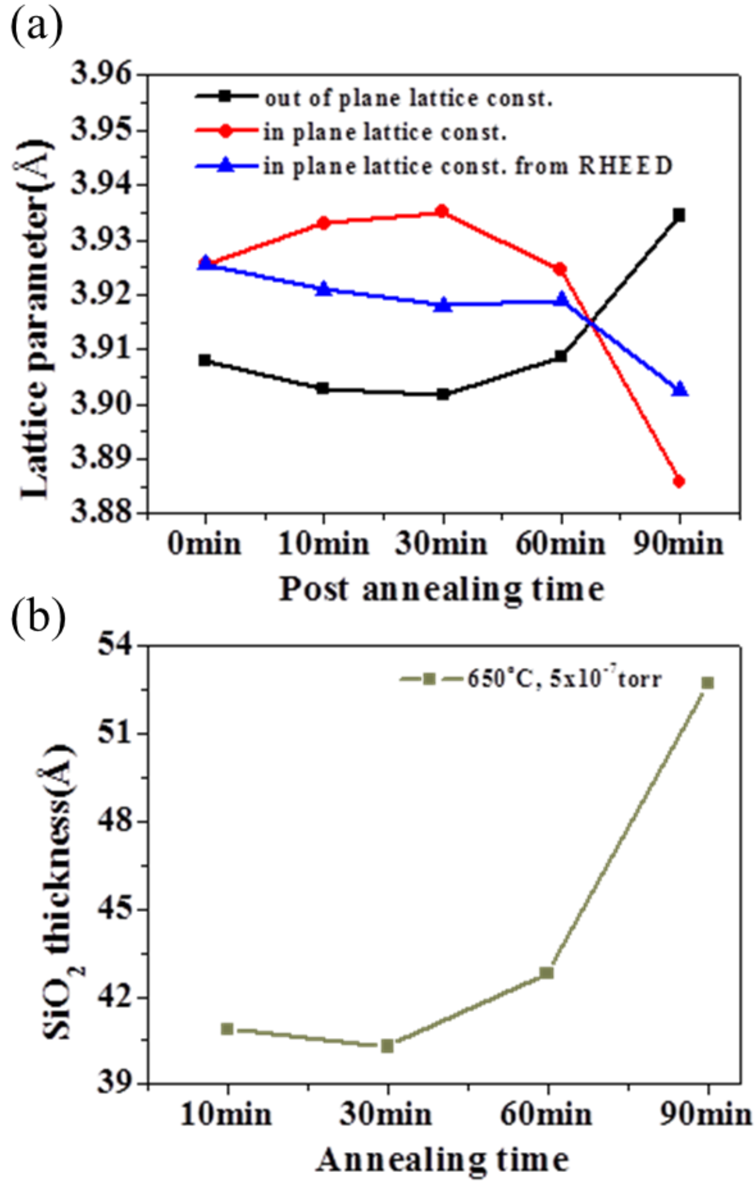

Figure 6.6 (a) In-plane lattice constants and (b) SiO_2 thickness as a function of annealing duration. All films were annealed in oxygen environment of 5×10^{-7} Torr at 650 °C

Figure 6.7(a) shows the RHEED pattern of the film which was annealed at 650 °C at 5×10^{-7} Torr for 90 min. This film had 53 Å SiO_2 thickness. During this longer annealing, the streaks became weaker and the background of the RHEED pattern became

brighter, indicating degradation of the STO crystallinity. However, for the film annealed at 650 °C in an oxygen environment of 1×10^{-5} Torr for 10 min (Figure 6.7(b)), the streaks remained very sharp, indicating that the STO crystallinity is still good even though the SiO_2 thickness has increased to 71 Å. One possible explanation is that the longer annealing duration could allow for Sr and/or Ti to diffuse down to the SiO_2 layer (or Si to diffuse upward) and react with Si to form a strontium silicate or titanium silicate[170-172]. This indicates that STO on Si may be a thermodynamically unstable but kinetically-limited state, which should be taken into consideration when using STO on Si as a virtual substrate.

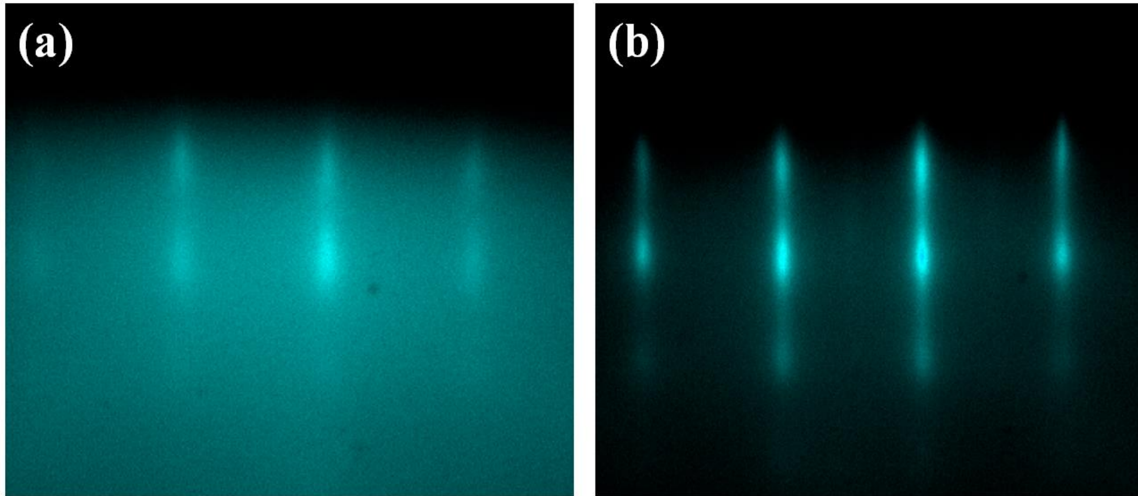

Figure 6.7 RHEED patterns along <110> direction of a film which was (a) post-annealed at 650 °C in an oxygen environment of 5×10^{-7} Torr for 90 min, and of film which was (b) post-annealed at 650 °C in an oxygen environment of 1×10^{-5} Torr for 10 min.

6.4 Conclusion

We have studied the strain relaxation behavior of STO films grown on Si through post-deposition annealing as a function of oxygen pressure and time. STO films grown at high temperature and high oxygen partial pressure develop a thin SiO_2 interlayer during

growth. During post-deposition annealing, the thickness of this SiO_2 interlayer increases, affecting the strain relaxation behavior of the STO layer. Prior to annealing, the STO layers are initially expanded in-plane as a result of thermal expansion mismatch. As oxygen partial pressure is increased, the STO lattice constants relax towards their bulk, cubic values, concurrent with an increase in the SiO_2 interlayer thickness. The use of post-deposition annealing can be used to tune the strain in STO films within a half a percent. However, for prolonged annealing times (over 90 min), we find that STO films showed evidence of decomposition as manifested by an unexpected decrease of the in-plane lattice constant as SiO_2 thickness was increased.

Chapter 7. Surface electronic structure for various surface preparations of Nb-doped $SrTiO_3$ (001)

High-resolution angle-resolved photoemission spectroscopy (ARPES) was used to study the surface electronic structure of Nb-doped $SrTiO_3$ (STO) prepared using a variety of surface preparations. ARPES measurements show that simple degreasing with subsequent anneal in vacuum is not an adequate surface preparation of STO, rather, preparations consisting of etching with buffered HF, or HCl/HNO_3, to a lesser extent, simple water leaching resulted in surfaces with much less disorder and boiling STO in deionized water. It was also found that ARPES was a more sensitive probe of surface disorder than basic reflection high-energy electron diffraction (RHEED). A non-dispersing, mid-gap state was found ~800 meV above the top of the valence band for samples which underwent etching. This mid-gap state is not present for vacuum-annealed and water-leached samples, as well as samples grown using molecular beam epitaxy (MBE). Theoretical modeling of STO slabs using density functional theory (DFT) suggests that this mid-gap state is not related to the SrO- and TiO_2-terminated surfaces, but rather, due to a partial hydrogenation of the STO surface that occurs during etching. I prepared the samples with different etchants and Richard Hatch measured the surface properties using ARPES. Theoretical calculation is mainly done by Kurt Fredrickson and Chungwei Lin. This chapter is published in : (1) R. C. Hatch, K. D. Fredrickson, M. Choi, C. Lin, H. Seo, A. B. Posadas and A. A. Demkov, J. Appl. Phys. **114**, 103710 (2014) and (2) R. C. Hatch, M. Choi, H. Seo, A. B. Posadas and A. A. Demkov in preparation.

7.1 Introduction

Complex oxide materials exhibit a wide range of phenomena such as magnetism, superconductivity, ionic conduction, ferroelectricity and multiferroicity, and have many promising applications[173-175]. Many of the more interesting oxides have perovskite structure[176], with $SrTiO_3$(STO), a cubic perovskite, being one of the most heavily studied examples. By itself, STO possesses many notable properties such as water photolysis [177], photovoltaic effect[178], blue-light emission[179] and superconductivity[180]. Furthermore, STO is favorably lattice-matched to many other complex oxides, and is a widely-used substrate for epitaxial oxide growth. The interfaces of STO with other oxides also display an array of interesting phenomena. Perhaps the most heavily studied of these interfaces is that of $LaAlO_3$/STO, motivated by the discovery of a two-dimensional electron gas (2DEG) at the interface[181-184]. This 2DEG is quite remarkable with interesting magnetic effects[185], superconductivity[186], and ferromagnetism[187,188]. Several other STO heterostructures have notable properties as well such as magnetic ordering in $LaMnO_3$/STO[189] superlattices and $LaCoO_3$/STO heterostructures[190,191], electronic reconstructions[192,193] and superconductivity[194-196] at $LaTiO_3$/STO and $LaVO_3$/STO interfaces. To understand these numerous properties, and maximize the functionality of STO-based devices it is important to gain a greater understanding of the surface electronic structure of STO, and prepare STO substrates with high surface quality.

Since many of the unique properties of oxide heterostructures require atomically abrupt interfaces, the preparation of atomically flat, defect-free substrates is of utmost importance. The surfaces of STO (001) crystals, as provided by the manufacturer, do not typically have a unique surface termination as a result of mechanical polishing. One of the most common methods of preparing atomically-smooth, uniquely-terminated STO surfaces is based on a process used heavily in the semiconductor industry for removal of

SiO_2 on Si, and consists of etching of the surface in a buffered solution of HF (BHF) followed by a high-temperature anneal in flowing O_2[197-200]. A similar process, often referred to as the "Arkansas" method, substitutes HCl/HNO_3 for HF, and reportedly minimizes surface defects resulting from the BHF etch[201,202]. Regardless of the method, the acid-based etching dissolves the SrO terraces more quickly than the TiO_2 terraces, leaving a rough surface comprised of TiO_2 islands. The subsequent anneal in O_2 results in large, atomically flat TiO_2 terraces as a consequence of mass transport[198,203,204]. More recently, in an effort to avoid the safety issues of acidic etchants which have served as an obstacle to researchers embarking on studies of interfacial properties of oxides, it has been shown that various forms of water-leaching are able to preferentially dissolve the SrO terraces, which, after a subsequent anneal, result in atomically flat, TiO_2-terminated STO[205-207]. While the water-leaching methods result in flat, TiO_2-terminated STO, a thorough study comparing the effectiveness of acid-based etching and water-leaching is not yet available.

In order to study the electronic properties of STO, a number of researchers have utilized angle-resolved photoemission spectroscopy (ARPES). These studies have employed a number of different surface preparations including sputtering and annealing [208], cleaving or scraping[209-212], vacuum-anneal[213], epitaxial thin film growth[214], and chemical etching with vacuum anneal[215-218]. It is unlikely that sputtering and annealing provides the desired, atomically flat surfaces because of the different sputtering cross sections of the STO constituents which will likely result in non-ideal surface stoichiometry. While cleaving is a moderately effective method of surface preparation for ARPES experiments, it is expected to give rise to a large number of oxygen vacancies at the surface, and likely contributes to the formation of a 2DEG at the surface of STO [209-212]. Furthermore, cleaving in ultra-high vacuum (UHV) is not a convenient method

of preparing substrates for heteroepitaxy and the creation of heterojunctions. Regardless of surface preparation, ARPES has been used to study a number of the electronic properties of STO. Using n-doped STO, such experiments have shed light on the nature of the bottom of the conduction band, or quantum-confined conduction band states and resulting 2DEGs[209-212,215-218] and have revealed the presence, and origin of mid-gap states[209-214,217,218]. Finally, a number of ARPES measurements have investigated the valence band dispersions, with an older work sampling at a few k-points using the so-called normal emission method[208], and, more recently, works providing detailed measurements by utilizing a range of emission angles[212,213,215].

Because of the sensitivity of ARPES to defects in materials, this work utilizes ARPES as a tool to compare the effectiveness of a number of different preparations of STO (001). The ARPES measurements show that the surface electronic structure depends heavily on the surface preparation. Finally, a comparison of ARPES to first-principles band structure calculations, for different STO terminations, sheds light on the origins of a number of electronic features in STO.

7.2 Various surface preparations of Nb-doped $SrTiO_3$ (001) – Buffered HF, HCl/HNO_3/Vacuum annealing

7.2.1 Experiment – sample preparation

A. Etching in Buffered HF

This sample preparation is based on the BHF preparation described in the literature[197-200]. In this case, the sample was degreased ultrasonically in acetone, IPA, and DI H_2O, with an electrical resistivity of 18 MΩ-cm for 20 minutes each. The sample was again sonicated in DI H_2O at 60 °C for 20 minutes. This was followed by a 1 minute etch in a 60 °C solution of 49 % HF and 40 % NH_4F (volume ratio of 1:20 and pH of

5.5). After a thorough rinse in DI water, the sample was annealed at 950 °C for 4 hours in a furnace with flowing O_2 shown in Figure 7.1. This relatively long, furnace anneal should result in larger terraces than in the case of a shorter 1 hour anneal, as reported previously[219]. The sample was then annealed at 725 °C for 1 hour in UHV.

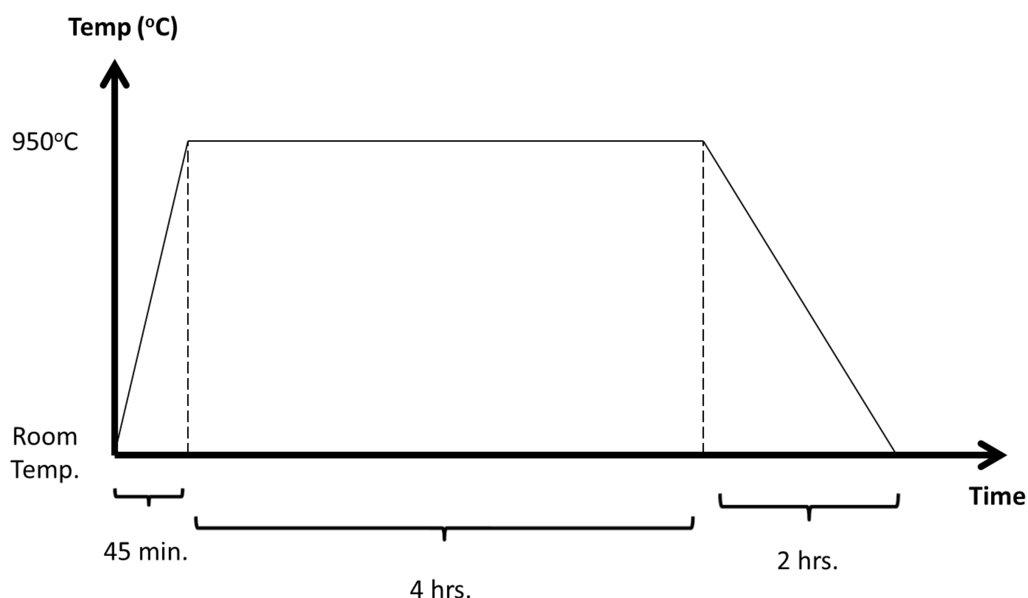

Figure 7.1 Annealing condition of Nb-$SrTiO_3$ substrate.

B. The "Arkansas" Etch

This sample preparation is based on the Arkansas method explained previously [201,202]. This particular preparation consisted of 12 minutes of ultrasonic etching in a solution of HCl (36.5 %) and HNO_3 (69.4 %) (volume ratio of 3:1 and pH of ~0), followed by a thorough rinse in DI water. This was followed by 10 minutes of ultrasonic cleaning in both acetone and IPA. The final annealing in the furnace and UHV are identical to samples prepared using BHF.

C. Thin Film Growth Using MBE

The fifth and final preparation method was the growth of an undoped, STO thin film (10 unit cells thick), using MBE, which was grown on an 700 °C Nb-doped STO substrate. The substrate was prepared using BHF, as explained above. The etched sample was then introduced into a customized DCA 600 molecular beam epitaxy (MBE) system with a base pressure of 3×10^{-10} Torr. The sample was annealed for 1hour in an O_2 environment of 5×10^{-8} Torr. The thin film was grown at a substrate temperature of 600 °C with a partial O_2 pressure of $P_{O_2} = 8\times10^{-8}$ Torr, and a total pressure of $P = 2.7\times10^{-7}$ Torr. Growth of alternating SrO and TiO_2 layers was facilitated by shuttering of the Sr, and Ti sources, and the thin film was terminated with a TiO_2 layer. After growth, the film was annealed at 650 °C for 10 minutes and was then cooled to room temperature with a partial O_2 pressure of $P_{O_2} = 5\times10^{-8}$ Torr.

7.2.2 Experiment - measurement

The surface electronic structure of (001)-oriented, Nb-doped STO ($SrNb_{0.01}Ti_{0.99}O_3$) single crystals was studied using ARPES for a variety of surface preparations. The ARPES system consists of an electrostatic, hemispherical, electron-energy analyzer (Scienta R3000) with a monochromated He discharge source. He Iα radiation (hν = 21.22 eV) was used in all experiments except for those where a photon energy of hν = 40.81 eV (He IIα) is explicitly indicated. The combined energy resolution was ΔE < 20 meV for hν = 21.22 eV and ΔE < 35 meV for hν = 40.81 eV and the angular resolution was Δθ ~ 1°. All measurements presented here were performed in the $\bar{\Gamma}\bar{M}$ direction (i.e. the [110] direction of the surface Brillouin zone) as shown in Figure 7.2(a), and the sample temperature was between 120 K and 150 K (well above the second-order phase transition from cubic to tetragonal structure which occurs at the critical temperature of Tc ≈ 105 K[220,221]). The approximate k-path probed in the bulk Brillouin zone, can be

determined using the free electron final state model[222,223], where the wave vector perpendicular to the sample is given by

$$k_z \approx \sqrt{\frac{2m_e}{\hbar^2}}\sqrt{V_0 + E_K \cos^2(\theta)} \qquad (7.1)$$

where me is the electron mass, V_0 is the inner potential, E_K is the kinetic energy of the photoelectron, and θ is the emission angle. Assuming an inner potential of V_0 = 14.5 eV, which is consistent with literature values[208,209,215] and expectations based on the depth of the oxygen valence band, as well as an STO lattice constant of a = 3.905 Å, we calculate the k-paths probed for the two photon energies and plot them in Figure 7.2(b). These k-paths are broadened due to the range of kinetic energies measured, and because of the finite escape depth of the photoelectrons. As seen in Figure 7.2(b), the measurements, roughly speaking, map the band structure along the XR and ΓM directions for photon energies of hν = 21.22 and 40.81 eV respectively.

Five different surface preparations were studied in this work. The first preparation, referred to as "vacuum anneal" consisted of ultrasonic degreasing of the sample in acetone and isopropanol (IPA) for 10 minutes each, followed by a 4 hour anneal in UHV at a temperature of 750 °C. The second preparation is based on the BHF etch[197,198], with further details found in part A of the Section 7.2.1. The third preparation is based on the "Arkansas" method[202] with complete details found in part B of the Section 7.2.1. The fourth sample preparation is based on water leaching[207], and consisted of the same ultrasonic degreasing as the vacuum annealed samples, followed by a 48 hour soak in deionized water (DI H_2O) at room temperature. The sample was then annealed at 775 °C for 2 hours. The fifth and final preparation method was the growth

of an undoped STO thin film (10 unit cells thick), using molecular beam epitaxy (MBE) with the complete growth details explained in part C of the Section 7.2.1.

All surface preparations were also studied using reflection highenergy electron diffraction (RHEED) and resulted in sharp diffraction patterns with no noticeable surface reconstructions. Representative RHEED images taken along the [110] azimuth of STO at an electron energy of 18 keV and glancing angle of 3° are shown in Figure 7.2(c-d). Somewhat surprisingly, there were no obvious differences in the diffraction features for the different surface preparations, but a more rigorous RHEED study, with a comprehensive, quantitative analysis may reveal differences[205].

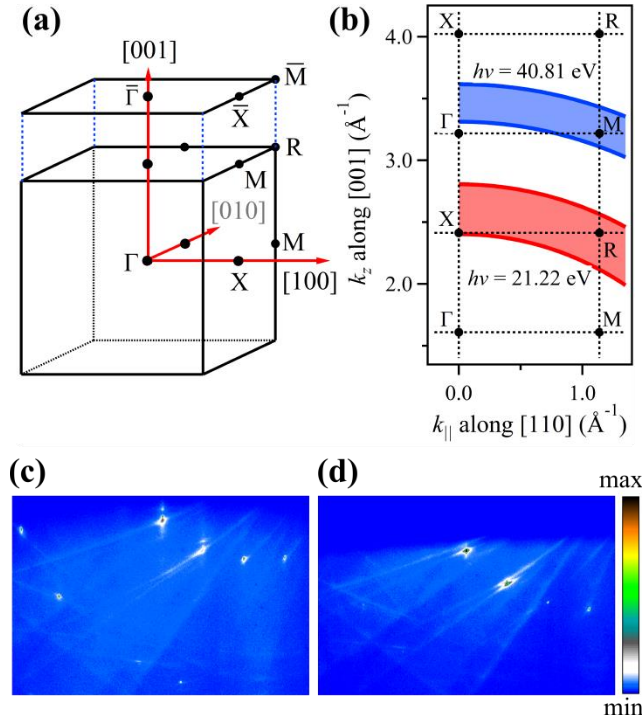

Figure 7.2 (a) The bulk and surface Brillouin zones for $SrTiO_3$ with labeled symmetry directions and points. (b) Paths in the bulk Brillouin zone corresponding to ARPES measurements for two different photon energies, hν. (c, d) RHEED images for the vacuum annealed sample and a sample etched in buffered HF, respectively, with the images taken just off the [110] azimuth due to geometric constraints.

Density functional theory was used to model the bulk and surface of STO. All calculations were done using the local density approximation and plane augmented-wave pseudopotentials as included in the VASP code[117,118,224-227]. We used the Perdew-Zunger form of the exchange-correlation potential [228]. The valence configuration of $3p^6 4s^2 3d^2$ was used for titanium, $4s^2 4p^6 5s^2$ for strontium, $2s^2 2p^4$ for oxygen, $1s^1$ for H and $2s^2 2p^5$ for F. A kinetic energy cutoff of E_{cutoff} = 650 eV was used. For the Brillouin zone integration, the following Monkhorst-Pack[229] k-point meshes were used: 6×6×6 for bulk STO, and 6×6×1 for the relaxation of surface structures, and 18×18×2 for the surface-band calculations. Bulk STO was optimized, and all structures were optimized with

respect to the ionic positions until the forces on all atoms were less than 10 meV/Å; for the STO slabs, optimization was performed until the forces were less than 50 meV/Å. The energy was converged to 10^{-3} meV per atom. The lattice constant of cubic STO was calculated to be 3.861 Å, in good agreement with an experimental value[230] of 3.905 Å and a previously reported theoretical value of 3.873 Å[231]. The small difference in lattice constant calculated in this work as opposed to that in Ref. 61 can be attributed to the 650 eV cutoff energy used here compared to 600 eV used previously. All slabs were symmetrically terminated (1×1), and were 8.5 unit cells thick, with a vacuum thickness of 15 Å.

7.2.3 Results

In order to better understand the differences between the surface and bulk electronic structure of STO, DFT calculations were performed for bulk STO. Figure 7.3(a) shows the results of these calculations, where the STO band structure in the [110] direction is projected onto the [001] surface. For convenience in comparison to ARPES measurements, the data in Figure 7.3(a) are broadened using a Lorentzian function with a full-width at half-maximum of FWHM = 0.3 eV with the results shown in Figure 7.3(b). While this process neglects all photoemission matrix element effects that are present in ARPES data, the regions of maximum amplitude correspond to bands that have less k_z-dependence, and should account for features in the experimental data. The large width of 0.3 eV is chosen to account for the strong electron-(optical) phonon coupling in STO, which causes a significant 0.4 eV broadening of the quasi-particle peak[210,215,232].

A similar analysis can be carried out using a tight-binding (TB) model for the band structure as seen in Figure 7.3(c). This tight binding model uses modified parameters from a previous work[215] which consist of the energy difference between the

Ti 3d and O 2p energy levels, the crystal-field splitting of the Ti 3d and O 2p orbitals, hopping parameters between nearest neighbor Ti 3d and O 2p orbitals, and second and third neighbor hoppings between O 2p orbitals[233]. While there are subtle differences between the DFT and tight binding calculations, it will be shown that both are in reasonable agreement with ARPES data.

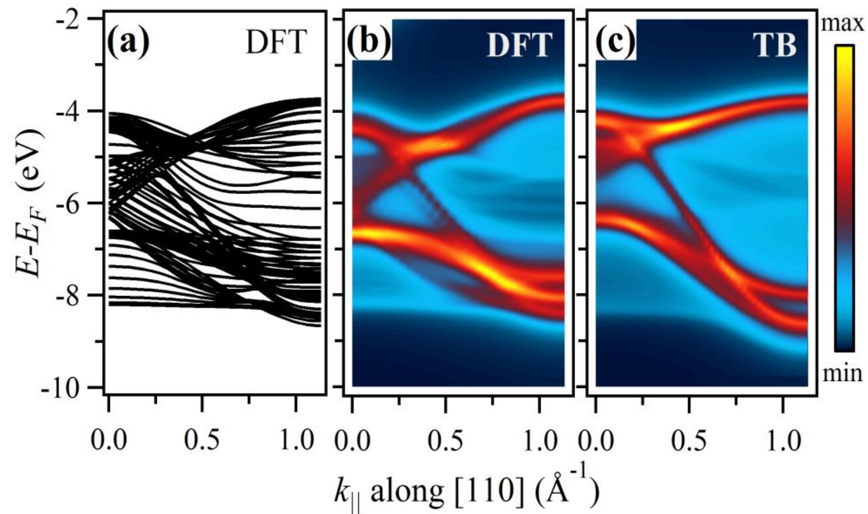

Figure 7.3 (a) The surface projected band structure of bulk STO along the [110] direction for a fine grid of kz values that spans the bulk Brillouin zone as calculated using DFT. (b) For ease of comparison to ARPES data, each line in (a) is broadened using a Lorentzian function with a FWHM of 0.3 eV. (c) Same as (b), but calculated using a tight-binding (TB) model.

Figure 7.4(a) shows the ARPES intensity map for the vacuum-annealed sample. As shown in the literature[207], a simple anneal results in large islands on the STO surface that are due to strontium oxide, or strontium hydroxide segregation[198]. These islands can serve as scattering centers for photoelectrons. Because photoelectrons can scatter off of these numerous islands, and lose their momentum signature, the ARPES data shows

two regions of high photoemission intensity located at energies of $E-E_F \approx -5$ and -7 eV which correspond to regions of high density of states for the primarily O 2p-derived valence band of STO. Captured in these measurements is some indication of the STO bandwidth, but because of the scattering, a study of the STO surface electron structure is problematic. There are, however very subtle features present in the ARPES data that correspond to photoelectrons which did not undergo scattering events. These features are only visible if one resorts to taking second derivatives of the photoemission spectra in the energy direction, as shown in Figure 7.4(b), which shows some indication of several dispersing bands. The most notable of these bands, with an energy of $E-E_F \approx -3.75$ and parallel wavevector of $k_{||} \sim 1$ Å^{-1}, corresponds to the top of the valence band near the bulk R point (labeled with a white arrow).

One way to remove the Sr-based islands is to dissolve them in DI water[206,207]. After water leaching, ARPES data reveals very apparent, dispersing features that correspond to the STO bulk band structure. These dispersing bands are even more obvious after removing a simple background from the ARPES data as shown in Figure 7.4(c). This background removal was accomplished by integrating the photoemission data over the entire angular range. The resulting angle-integrated spectrum was then scaled, and subtracted from each constant emission angle spectrum, or energy distribution curve (EDC). After this background removal, the top of the valence band is again visible, as well as a downward dispersing band (both marked with white arrows) despite the fact that no 2nd derivatives have been taken. Another interesting feature of the ARPES data is the fact that the uppermost valence bands disperse downward as one goes away from Γ, in exactly the same fashion predicted by DFT (see Figure 7.3(b)). It should be noted that this same background removal technique was not successful in the case of the vacuum-annealed sample because each EDC was very nearly identical due to the k-

smearing resulting from scattering of photoelectrons off of surface defects. Finally, one consequence of this technique is that if a state is non-dispersing, it may be somewhat suppressed in the presentation of the dataset.

Second derivatives of ARPES data for 10 unit cells of undoped STO grown on a Nb-doped STO substrate using MBE are shown in Figure 7.4(d). When compared to Figure 7.4(b), for the vacuum-annealed sample, it is obvious that the sample is of higher quality, with much more defined features. At this time, only a subset of data is available, but, as will be discussed later, there is some indication that the surfaces of MBE-grown films can be of equal quality to single crystals which underwent water leaching, or etching.

The surface preparations that yield the highest quality STO surfaces, and consequently give rise to the best ARPES data, are the preparations that etch the sample using either BHF, or the Arkansas preparation. The photoemission data for samples prepared using these two methods are shown in Figure 7.4(e-f). For comparison of data measured with a photon energy of $h\nu = 21.22$ eV refer to Figure 7.4(c), 4(e) and 4(g), for the water-leached, BHF-prepared, and Arkansas-prepared samples respectively. It is immediately apparent that the samples which underwent etching (Figure 7.4(e) and (g)) give rise to sharper photoemission features than the water-leached sample (Figure 7.4(c)). The presence of dispersing bands becomes much more apparent for a photon energy of $h\nu = 40.81$ eV, which, roughly speaking, maps the band structure from Γ to M, as shown in Figure 7.2(b). Any of the subtle differences in the photoemission data for the BHF- and Arkansas-prepared samples is more likely related to data processing (primarily background subtraction) than an actual difference in surface quality.

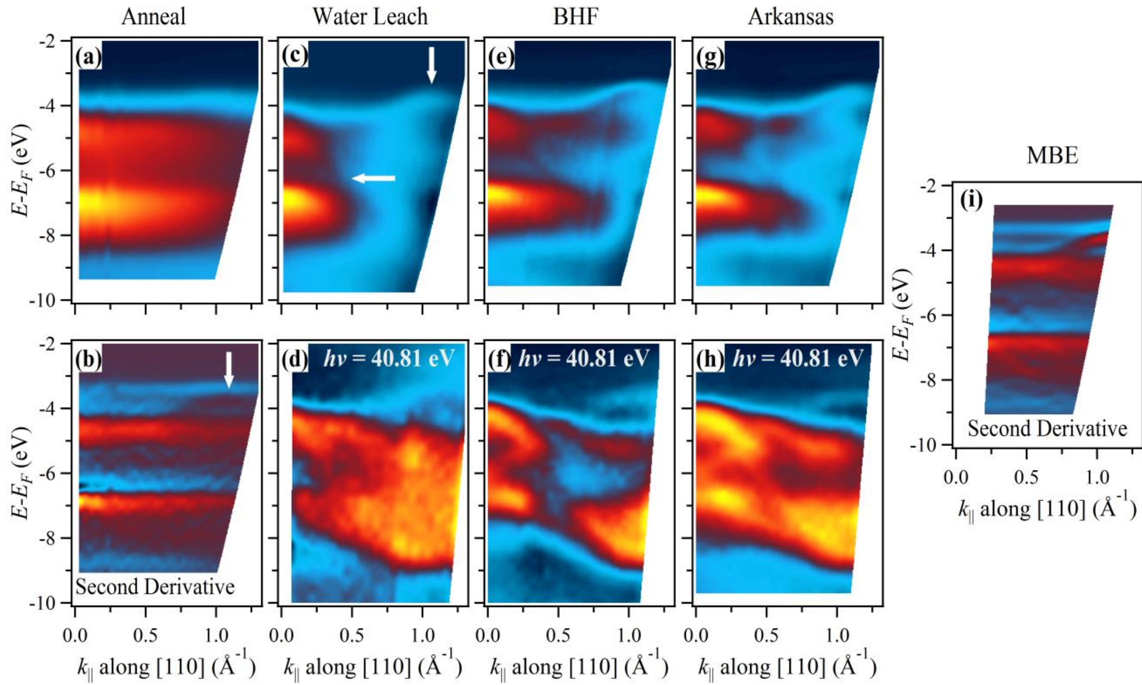

Figure 7.4 ARPES data along the [110] direction for STO samples prepared in a variety of ways for a photon energy of hν = 21.22 eV unless otherwise stated. (a) Raw data for vacuum-annealed STO, with the 2nd derivative (in the Energy direction) shown in (b) in order to better visualize dispersing bands. (c-d) After water-leaching the STO surface quality is greatly improved and the ARPES data reveals dispersing bands after a simple background removal. (e-h) Photoemission spectra (with background removal) for STO samples etched in BHF (e,f) and those etched using the Arkansas method (g,h). (i) The 2nd derivative of ARPES data for MBE-grown, undoped STO.

The most likely reason for the improvement in ARPES spectra for samples that underwent surface preparations beyond the simple vacuum anneal is the removal of the strontium oxide islands on the surface. Evidence of this occurring can be seen in x-ray photoemission spectroscopy (XPS) studies shown in Figure 7.5. Figure 7.5 shows XPS spectra of the Sr 3d core level for the vacuum-annealed sample (a) as well as for the sample etched in BHF (b). At least two spin-orbit split doublets are required to fit the

data with a structure-free residual. The more intense doublet corresponds to the primary STO lattice, and the less-intense doublet, with a slightly higher binding energy, has been attributed to strontium oxide crystallites, and the presence of F on the surface[206,234,235]. As seen in Figure 7.5(a-b), there is a noticeable decrease in intensity for the higher binding energy doublet after etching with BHF—a clear indication that the concentration of strontium oxide crystallites on the surface has been reduced by the etch. Water leaching yields similar results, but the reduction in intensity of the higher binding energy doublet is not quite as pronounced as for the case of BHF etching.

Second derivatives of ARPES data for 10 unit cells of undoped STO grown on a Nb-doped STO substrate using MBE are shown in Figure 7.4(i). When compared to Figure 7.4(b), for the vacuum-annealed sample, it is obvious that the sample is of higher quality, with much more defined features. At this time, only a subset of data is available, but, as will be discussed later, there is some indication that the surfaces of MBE-grown films can be of equal quality to single crystals which underwent water leaching, or etching.

There are a number of photoemission features that are not apparent in Figure 7.4(a-h), that are only apparent when looking at the energy distribution of the photoemission data. Figure 7.6(a) shows photoemission data for a variety of sample preparations that are integrated over a large emission angle of roughly 20°. The first obvious difference is the higher peak-to-valley ratio for the MBE-grown and Arkansas-prepared samples compared to the water-etched and vacuum-annealed samples. A second difference is the background level (i.e. the number of inelastically scattered photoelectrons) which is highest in the vacuum-annealed sample, then the water-leached sample, with the Arkansas-prepared and MBE-grown samples having the lowest, and very nearly identical backgrounds. These two photoemission characteristics are often

associated with sample quality and indicate that surface-quality is best for etched and MBE-grown samples, followed by water-leaching and finally vacuum-annealing. These conclusions are also in agreement with the quality of ARPES data shown in Figure 7.4(a-h).

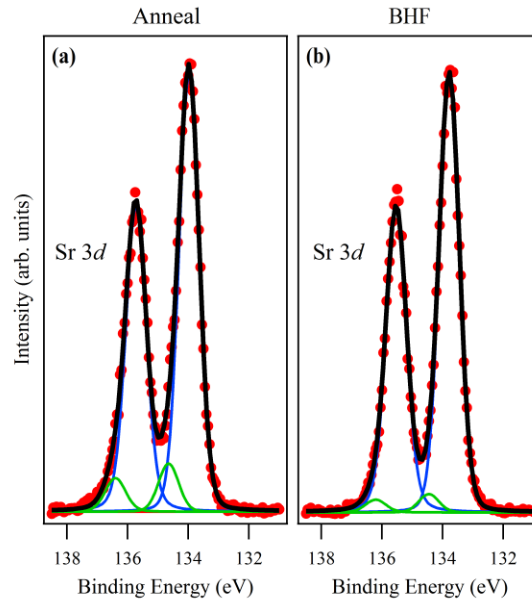

Figure 7.5 Normal emission XPS spectra of the Sr 3d core level for a STO(001) sample having undergone a vacuum-anneal (a) as well as a sample etched in BHF (b). The primary STO lattice peaks (more intense) are accompanied by lower intensity peaks (green) which are attributed to the presence of strontium oxide crystallites on the surface which are removed, to some extent, after etching with BHF.

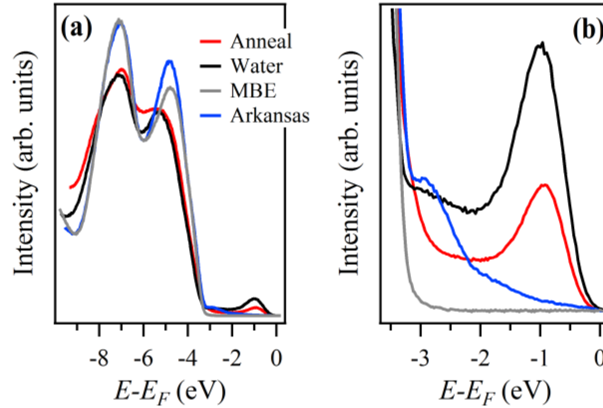

Figure 7.6 (a) Angle-integrated photoemission data of the primarily O 2p-derived valence band states for a variety of STO preparations with a close-up of the gap region shown in (b). Data for the BHF-etched STO is omitted from (a) and (b) since it is very nearly indistinguishable from the Arkansas-prepared STO. The photoemission data reveals at least two gap-states: an oxygen-vacancy state at a binding energy of $E-E_F \approx -1$ eV and another gap state about 800 meV above the top of the valence band located at $E-E_F \approx -2.75$ eV.

Different sample preparations also give rise to different gap states as shown in Figure 7.6(b). The most prominent gap state present in both the water-leached and vacuum-annealed samples is at an energy of $E-E_F \approx -1$ eV. This state has been studied both experimentally[179,208-212,236,237], and theoretically[238-246], and is likely due to oxygen vacancies in the STO crystal, although it may be caused by a local screening effect, chemical disorder or donor levels (see Ref.[214] and references therein). The oxygen vacancy state for the water-leached sample has a higher spectral intensity than that of the vacuum-annealed sample and may be due to the slightly higher annealing temperature (775 °C vs. 750 °C) resulting in a higher concentration of defects. For etched samples (both BHF and Arkansas) there is another gap state located about 800 meV above the top of the valence band at an energy of $E-E_F \approx -2.75$ eV. If this state is present for the

water-leached sample it is not clear due to the higher spectral intensity in this energy range. As seen in Figure 7.7, this state is located in the gap region, and has basically no angular dependence. While the origins of additional gap states have been studied in the literature[214,217,247-252] the origins of this particular gap state have not been discussed, and must be related to the preparation of surface using either of the two etching methods.

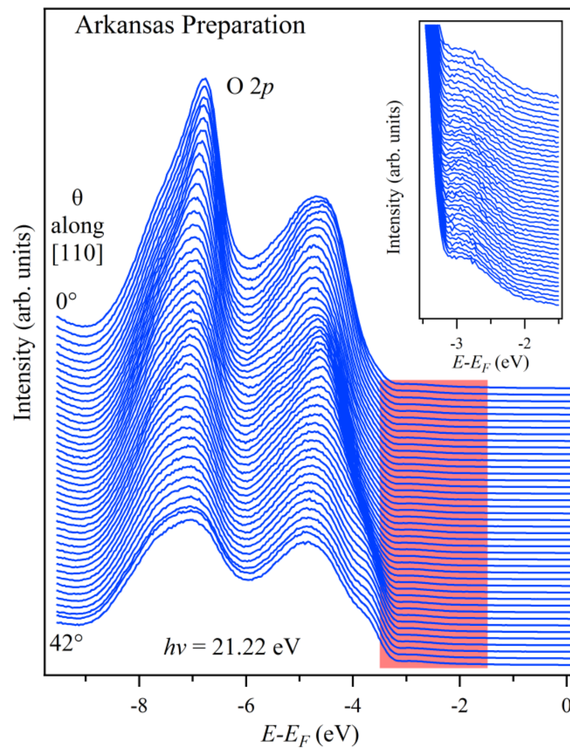

Figure 7.7 ARPES data for emission angles, θ, along the [110] direction for an STO sample prepared using the Arkansas method that correspond to the O 2p-derived valence band and the gap region. The pronounced shoulder for larger emission angles (at an energy of $E-E_F \approx -3.75$ eV) corresponds to the top of the valence band at the R point of the Brillouin zone. A close-up of the shaded region is shown in the inset and shows a mid-gap state about 800 meV above the top of the valence band that hardly disperses.

First-principles calculations of STO-based slabs can provide additional information about the electronic structure of prepared STO surfaces, and shed light on the origin of the gap state located at $E-E_F \approx -2.75$ eV. In addition to STO slabs with SrO- and TiO_2-terminations, a number of additional slabs are considered in this work, and are shown in Figure 7.8(a-e), with their corresponding surface electronic structures shown in Figure 7.9(a-g) respectively.

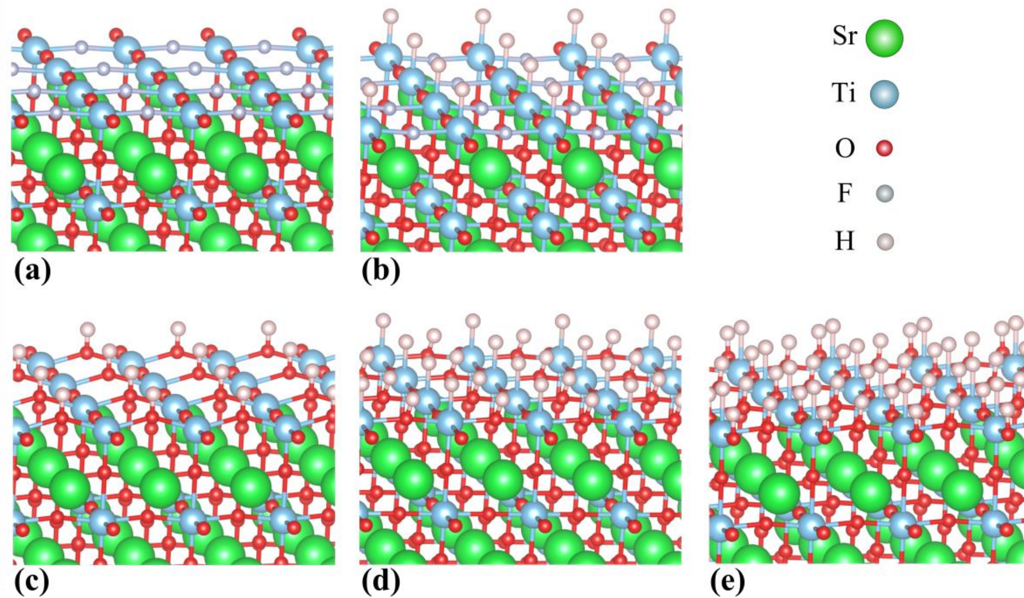

Figure 7.8 Sections of $SrTiO_3$ slabs corresponding to several of the systems studied using DFT calculations of the surface electronic structure. All slabs are (1×1). (a) A TiO_2-terminated slab with one O replaced by F. (b) Same as (a) with the addition of a H bonded to Ti. (c) A TiO_2-terminated slab with a single hydroxyl group. (d) Same as (c) with a H bonded to Ti. (e) A fully hydrogenated slab with two hydroxyl groups, and a H bonded to Ti.

The motivation of considering both F and H on the surface is the considerable experimental evidence that surprisingly high concentrations of these species can be found on the surface of STO[206,253,254]. The actual presence of F on the surface of our samples after various surface preparations was monitored using XPS. As seen in the XPS spectra of Figure 7.10, there is possibly a trace amount of F present for all samples, but the actual concentration is noticeably less than what has been previously reported for BHF-etched samples.[206] As seen in Figure 7.9, much of the bulk-related electronic structure is not affected by different surface terminations, and surface adsorbates. The different surface configurations, however, do give rise to surface-related electronic states. One such state is the surface state seen in Figure 7.9(b) (TiO_2-terminated slab) that resides in the bulk gap, is about 980 meV above the upper-most valence bands, and whose dispersion follows that of the valence band top. The dispersion of this state of roughly 950 meV in the [110] direction precludes this as an explanation for the gap state located at $E-E_F \approx -2.75$ eV in photoemission data. The reason this surface state is not present in the ARPES data for the TiO_2-terminated surfaces that result from various surface preparations is not immediately clear, but it is possible that, despite the care taken during surface preparation, there is simply too much surface disorder to support the development of surface states which can be notoriously sensitive to surface quality. It should also be noted that while our RHEED data does not indicate surface reconstructions, there have been numerous reports of reconstructed STO surfaces[255-260] which may or may not give rise to surface states similar to the one in Figure 7.9(b).

A more likely origin for the gap state at $E-E_F \approx -2.75$ eV can be explained by DFT calculations for the slabs shown in Figure 7.8(b) and (d). Calculations suggest that this non-dispersing state has its origin in the H-Ti bond present in both of these slabs, and that the H-Ti bond is unlikely to form without additional modifications to the surface. The

first scenario considered, that enables the H-Ti bond, is shown in Figure 7.8(b), where one surface O is substituted by F. Theory shows that, in the presence of this substituted F, the H will not remain at an O site and relaxes to the Ti site. Theoretical calculations for this slab are shown in Figure 7.9(d) and show the presence of states both above and below the STO valence band. The non-dispersing, localized state that is ~810 meV above the top of the valence band originates from the H-Ti bond which is consistent with previous findings [261]. The energy of this state, as well as its dispersive character, is virtually identical to the gap state seen in the photoemission data. The charge density of this non-dispersing state is shown in Figure 7.11(a). It is obvious that the surface state is highly localized on H and Ti, with some charge on the neighboring O. There is no charge density on the F substituted on the surface. The second scenario that enables this H-Ti bond is shown in Figure 7.8(d) where one H and one O form a hydroxyl group, and an additional H bonds to the Ti. For this system the same non-dispersing state is present (see Figure 7.9(f)) which has a very similar localized charge density (Figure 7.11(b)). Similar to the first scenario, the introduction of a single H to the surface will first form a hydroxyl group, but with the addition of a second H, the formation of the H-Ti bond is energetically more favorable than the creation of a second hydroxyl group. A further confirmation of this non-dispersing state having its origin at the Ti-H bond is the fact that neither a F-O substitution (first scenario and Figure 7.9(c)) nor the formation of a single hydroxyl group (second scenario and Figure 7.9(e)) alone give rise to this state—it only appears after the formation of a H-Ti bond (see Figure 7.9(d) and (f)). In light of DFT calculations, a more likely explanation for the absence of the dispersing surface state seen in Figure 7.9(b), is the presence of adsorbed H on the STO surface, which serves to kill this dispersing state. This state is comprised entirely of surface O p-states, and are destroyed by the presence of H, which lifts the bonding O out of the surface; the flat band

is still present, but it is pushed down in energy and is found now within the bulk valence band states. It should also be noted, that it is not necessary for every surface unit cell to have adsorbed H, in order for the non-dispersing state to be present. DFT calculations reveal the presence of this non-dispersing state for surfaces where only one in four surface unit cells has both a single hydroxyl group and a H-Ti bond (results not shown). There are also a number of surface modifications that result from H adsorption. The calculated ionic reconstruction due to different coverage of H is given in Table 7.1. An obvious trend is that when H bonds with either O or Ti, O or Ti rises out of the surface relative to the original clean surface of TiO_2. A surface-sensitive technique, such as surface X-ray diffraction could be sensitive to these ionic reconstructions, assuming a sufficient number of surface unit cells have the presence of adsorbed H. Furthermore, the presence of both hydroxyl groups, as well as H-Ti bonds on the surface could be verified by their vibrational signature, which could be studied with attenuated total reflection Fourier transform infrared spectroscopy. In light of these DFT calculations, a more likely explanation for the absence of the dispersing surface state seen in Figure 7.9(b), is the presence of adsorbed H on the STO surface, which serves to kill this dispersing state. This dispersing state is comprised entirely of surface O p-states, and is destroyed by the presence of H, which buries the energy levels of both surface O bands deep in the valence band. Similarly, fully hydrogenating the STO surface leads to an energy shift of the non-dispersing, flat band found in Figure 7.9(f); the flat band is actually still present, but it gets pushed down in energy and is found now within the bulk valence band states, and becomes difficult to observe with ARPES.

H present	Layer 1 Ti	Layer 1 O a*	Layer 1 O b*	Layer 2 Sr	Layer 2 O
O-H	0.02	0.48	0.03	-0.30	0.07
O-H, Ti-H	0.11	0.24	-0.15	-0.17	-0.02
2 O-H, Ti-H	0.11	0.24	0.24	-0.30	0.10

Table 7.1 The ionic motion (Å) of hydrogenated surfaces with respect to the clean TiO_2 surface. A positive number means the ion is moving towards vacuum, and a negative number means the ion is moving towards the bulk. *O a corresponds to the O that is bonded to the first H. O b corresponds to the O bound to the second H (2 O-H, Ti-H surface only).

In Figure 7.9(c) and (d), it is likely that the states below the valence band, with an energy of $E-E_F \approx -9$ to -12 eV, are related to the presence of fluorine on the surface. This assignment is also supported by XPS data from a previous work[206] which shows an increased spectral intensity below the valence band for samples etched in BHF, which have, on average, a ~13 % fluorine for oxygen substitution on the surface. Furthermore, recent photoemission data on STO exposed to a 4000 L H-dosage (1 L = 9.75×10^{-7} Torr s) also shows an increased spectral intensity below the valence band and suggests that the states below the valence band in Figure 7.9(e-g) are related to the adsorption of H[217,218]. DFT calculations show that these low bands belong to the O p-states of the hydroxyl group formed at the surface; note that in Figure 7.9(e-f) there is one low band present corresponding to the hydroxyl group, and in Figure 7.9(g), there are two low bands corresponding to the two hydroxyl groups present on the surface. The DFT calculations also verify that the low energy bands in Figure 7.9(d), originate from the F p-states.

What likely occurs during sample etching, with both BHF and the Arkansas method, is a partial hydrogenation of the STO surface, and the formation of a H-Ti bond, in much the same fashion that the dangling bonds on Si surfaces are passivated with H

when etched with BHF (see, for example Ref.[262] and references therein). This H-Ti bond on the STO surface then gives rise to this non-dispersing gap state present in the photoemission data. If this gap state is indeed related to the hydrogenation of the STO surface, as theory suggests, there are two consequences. First, the hydrogenation is surprisingly, thermally stable and the state remains unchanged even after a 4 hour anneal at 900 °C. This is in strong contrast to the case of Si, where all H is desorbed from Si surfaces with an anneal of less than 600 °C[263]. Second, because DFT does not predict a non-dispersing state in the gap for a fully hydrogenated surface (see Figure 7.9(g)), a third H approaching the surface must encounter a relatively large potential barrier, making the complete hydrogenation of the surface unlikely. To quantify these results, the energy of a slab shown in Figure 7.8(c) (the slab with one O-H group) with a H_2 molecule located far in vacuum, is compared with the slab in Figure 7.8(d) (which contains an O-H group and a H-Ti bond). The slab in Figure 7.8(d) is lower in energy by 0.152 eV per cell, suggesting that, in the presence of H_2, the surface will prefer to break the H_2 and have the H atoms attach to Ti sites. However, when one compares the slab in Figure 7.8(d) with a H_2 molecule located far in vacuum to the slab in Figure 7.8(e) (the fully hydrogenated surface), one sees that the H_2 molecule plus the slab in Figure 7.8(d) is lower in energy by 0.543 eV per slab indicating that the fully hydrogenated slab is not energetically favorable. Thus, it is expected that in the presence of sufficient H_2, the surface will hydrogenate until each TiO_2 surface unit has one O-H and one Ti-H bond, but will not fully hydrogenate, which explains why many of the ARPES images show this flat band that is not present in DFT calculations for the fully hydrogenated surface.

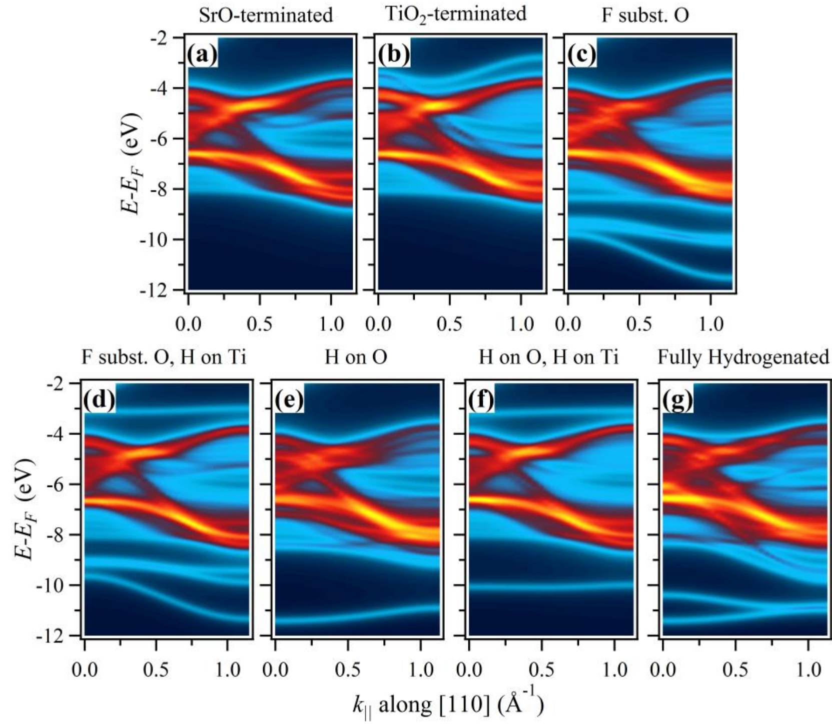

Figure 7.9 (a-g) DFT calculations of the surface electronic structure for SrO-and TiO_2-terminated slabs as well as slabs shown in Figure 7.8(a-e) respectively. DFT calculations predict a pronounced, dispersing surface state about 980 meV above the valence band states that roughly follows the dispersion of the STO bulk bands which is not present in the case of an SrO-terminated slab. Because of the dispersing nature of the surface state in (b), it is unlikely the origin of the mid-gap state discussed in Figure 7.7, despite the TiO_2-termination that results from the Arkansas preparation. As seen in (d) and (f), a likely explanation for this mid-gap state is the termination of the Ti dangling bond with H. As discussed in the text, for this termination to occur, it must be preceded by either a substitution of a surface O with F, or the formation of a hydroxyl group.

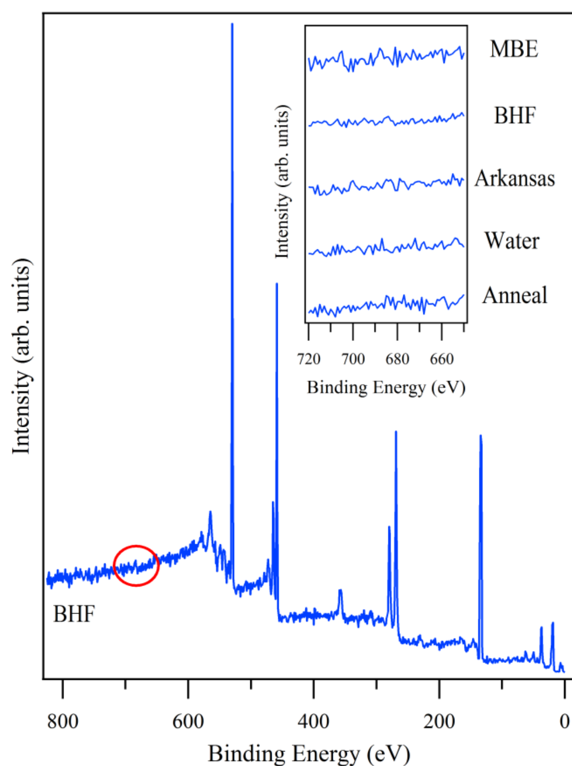

Figure 7.10 Normal emission XPS survey spectrum for a STO (001) sample prepared by BHF etching. The F 1s core level has a binding energy of ~685 eV, and, if present, should be located in the region highlighted with a red circle. Despite etching with BHF, the concentration of F on the surface is negligible (we estimate ≤ 1 % of all anions within the probe depth). Other sample preparations yield equally low concentrations of F (see inset).

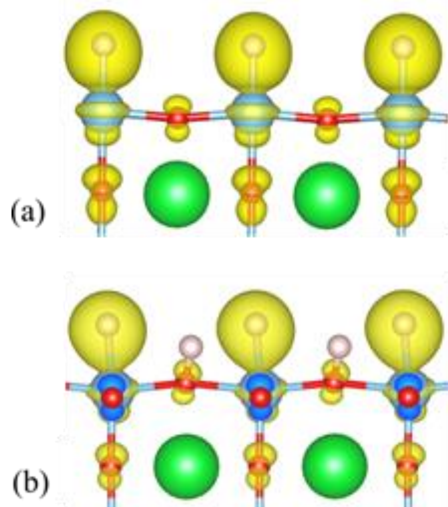

Figure 7.11 (a) The charge density of the non-dispersing band for the F-substituted slab with H on Ti. There is no charge density on the F (not shown). (b) The charge density of the nondispersing band for the H on O, H on Ti slab.

A thorough comparison of different theoretical calculations and ARPES data is shown in Figure 7.12. To facilitate the comparison, prominent features in the bulk calculations are highlighted with white circles in Figure 7.12(a). These same white circles are then overlaid on other calculations, and on the ARPES data. It is interesting to note that the theoretical calculations for bulk STO account for virtually all observed ARPES features corresponding to the STO valence band for photon energies of hν = 40.81 and 21.22 eV as seen in Figure 7.12 (i) and (j), even though all photoemission matrix elements effects have been ignored. Furthermore, the overall bandwidth, of ~4.8 eV is in perfect agreement with DFT calculations, and in reasonable agreement with tight-binding calculations.

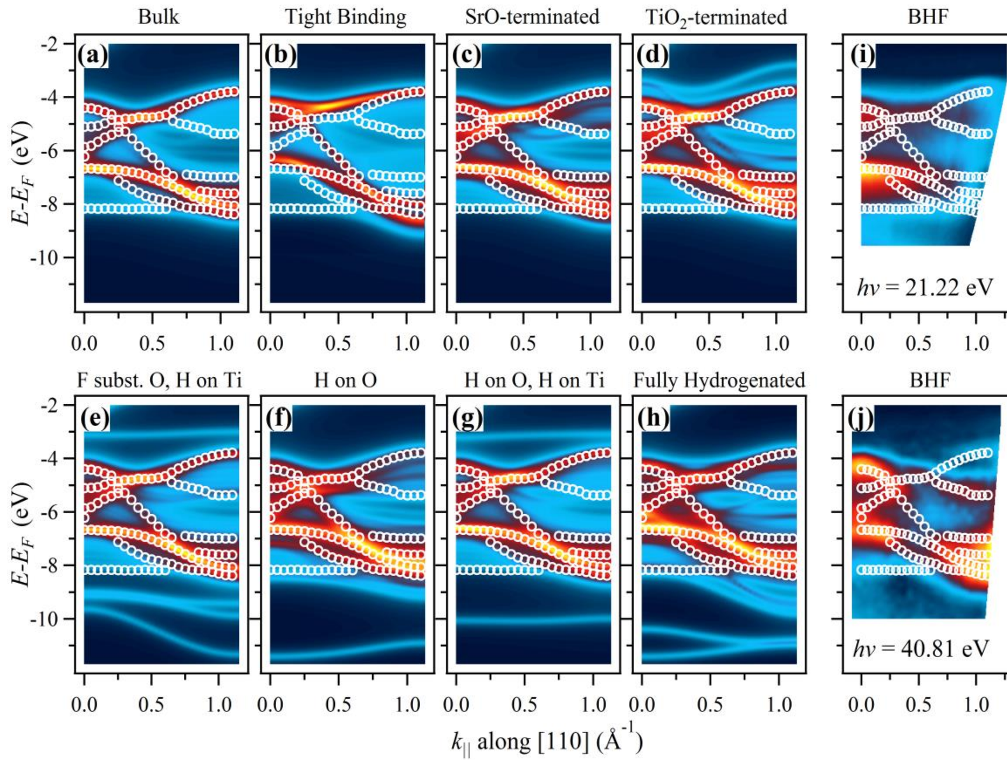

Figure 7.12 Comparison of theoretical calculations for various STO systems with ARPES data for the BHF-prepared sample. (a) The calculation for bulk STO band structure (see also Figure 7.3(a-b)), where prominent features are highlighted with white open circles. For ease of comparison, these same open circles are overlaid on the data in (b-h) which corresponds to data in Figure 7.3(c), Figure 7.7(a-g) and Figure 7.4(e-f) respectively. It is apparent that the different STO terminations hardly affect band structure predicted by DFT bulk calculations, but can give rise to surface states both above and below the valence band as seen in (d-h).

7.3 Various surface preparations of Nb-doped $SrTiO_3$ (001) – Water Boiling

7.3.1 Experiment

STO (001) samples prepared using the water-boiling method were first ultrasonically cleaned using acetone and isopropanol for 10 minutes each. After degreasing, the samples were boiled in DI H_2O with an electrical resistivity of 18 MΩ-cm

for 30 minutes. This was followed by a 4 hour anneal at 950 °C in a furnace with flowing O_2. At this point the sample was introduced to ultra-high vacuum (UHV) and annealed at 725 °C for 1 hour. Both the furnace- and vacuum-anneals were identical to those performed on samples prepared using BHF and the Arkansas method. All surface preparations were also studied using reflection high-energy electron diffraction (RHEED) and displayed sharp diffraction patterns consistent with an atomically flat surface with no noticeable surface reconstructions.

7.3.2 Results

Figure 7.13(a) shows the ARPES intensity map for an STO sample that was ultrasonically degreased in acetone and isopropanol followed by a 4 hour anneal at 750 °C in UHV. It has been shown[207] that a simple anneal results in large islands on the STO surface that are due to strontium oxide, or strontium hydroxide segregation.[198] As photoelectrons leave the sample they can scatter off these islands and lose their momentum signature and what is measured is a basically momentum-averaged spectrum. The ARPES data shows two regions of high photoemission intensity located at energies of E-EF ≈ -5 and -7 eV which correspond to regions of high density of states for the primarily O 2p-derived valence band of STO. Despite the noticeable momentum smearing, there is a subtle feature present in the ARPES data that corresponds to photoelectrons that were not scattered. This feature is only visible in the second derivatives of the photoemission spectra in the energy direction, as shown in Figure 7.13(b). This feature, with an energy of $E\text{-}E_F \approx -3.75$ and parallel wavevector of $k_{\parallel} \sim 1$ $Å^{-1}$, actually corresponds to the top of the valence band near the bulk R point. The fact that ARPES measures dispersing bands illustrates how this technique is sensitive to the long-range order required to develop a band structure.

As mentioned previously, the surface quality of STO can be greatly improved by using acid-based surface preparations to remove the Sr-based islands.[197-202] The ARPES data, after background subtraction, for samples prepared using these two methods are shown in Figure 7.13(c-f). This background subtraction was accomplished by integrating the photoemission data over the entire angular range, with the resulting angle-integrated spectrum then being scaled, and subtracted from each energy distribution curve (constant emission angle spectrum). After this background removal, the top of the valence band is again visible, as well as additional dispersing bands, despite the fact that no 2nd derivatives have been taken. It is immediately apparent that the samples which underwent etching give rise to sharper photoemission features than the vacuum annealed sample. The dispersing bands becomes much more apparent for a photon energy of $h\nu$ = 40.81 eV (Figure 7.13 (d), (f) and (h)), which, roughly speaking, maps the band structure from Γ to M. The band dispersions revealed with photon energies of $h\nu$ = 21.22 and 40.81 eV are in excellent agreement with ab-initio and tight-binding calculations of the bulk STO band structure[264]. We attribute the subtle differences in the ARPES data for the BHF- and Arkansas-prepared samples to data processing (primarily background subtraction) rather than an actual difference in surface quality.

Another way to remove the Sr-based islands is to dissolve them in DI water[206,207]. After boiling STO in DI water, ARPES data also reveal the dispersing bands, with the quality of ARPES spectra being on par with samples prepared with the acid-based techniques. We found that boiling STO, with subsequent anneal in flowing O_2, is a more effective surface preparation technique than the simple water-leaching reported previously[264]. Interestingly, there is some indication that the boiling aspect of this preparation seems to be the most critical step since ARPES spectra for boiled samples,

annealed in UHV seem to be of nearly the same quality as spectra for boiled samples annealed in flowing O_2 (data not shown).

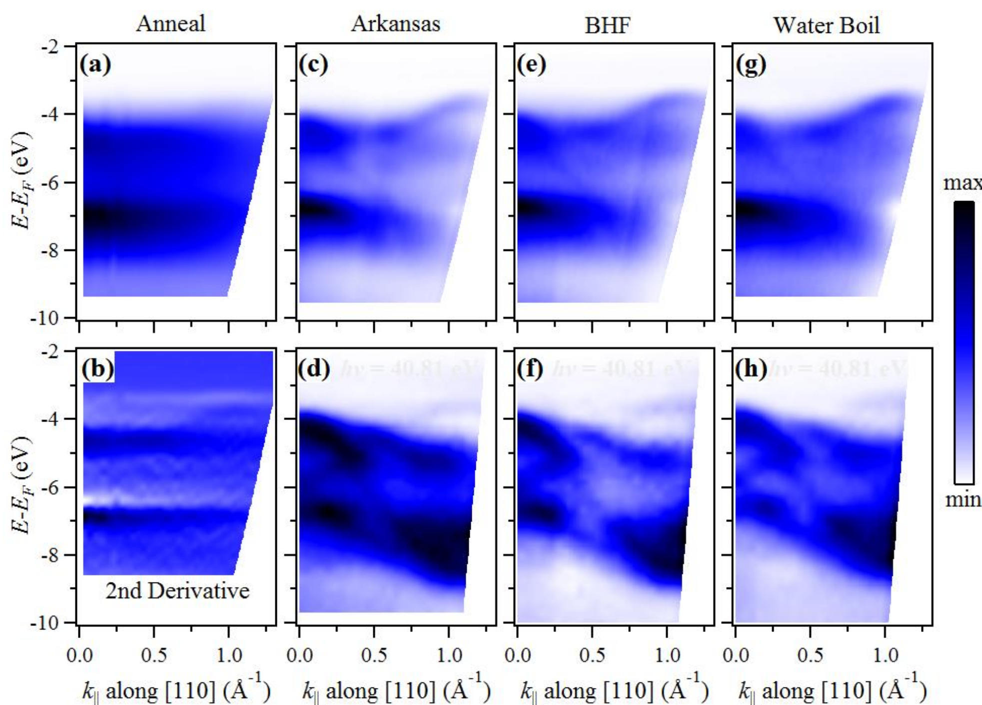

Figure 7.13 ARPES data along the [110] direction for STO samples prepared in a variety of ways for a photon energy of hν = 21.22 eV unless otherwise stated. (a) Raw data for vacuum-annealed STO, with the 2nd derivative (in the Energy direction) shown in (b) in order to better visualize dispersing features. After etching the surface using the Arkansas method (c-d) and BHF (e-f) the surface quality is much improved and the ARPES data reveal dispersing bands after a simple background removal. As was the case for the acid-based techniques, simply boiling STO in water followed by a furnace anneal also produces a high-quality surface and ARPES data shows the dispersing bands (g-h).

As alluded to previously, the most likely reason for the improvement in ARPES spectra for samples that underwent surface preparations, beyond the simple vacuum

anneal, is the removal of the strontium oxide islands on the surface. The removal of SrO_x from the surface region of the STO samples can be monitored using XPS. Figure 7.13 shows XPS spectra of the Sr 3d core level for STO samples prepared using a variety of methods. Fitting of the spectra with a structure-free residual requires at least two spin-orbit split doublets. The more intense doublet has its origin in the primary STO lattice. The less-intense doublet, with a slightly higher binding energy, has been attributed to strontium oxide crystallites[206,234,235]. For the analysis, a simple polynomial background was removed from all of the spectra and all of the spectra were then fit, simultaneously, with two spin-orbit split doublets. The Voigt lineshape was used for the doublets and the Gaussian and Lorentzian contributions to the Vogt peak width, the spin-orbit splitting, the branching ratio and the energy offset of the SrO_x doublet were determined from the simultaneous fit of all data. To be clear, all of the aforementioned fit parameters were considered to be the same for each spectrum, but were determined from the fitting, and the branching ratio and widths of the SrO_x doublet and the primary doublet were the same. The absolute position of the largest peak and its amplitude were allowed to vary for the individual spectra. Fitting the data in this fashion ensures that the relative contribution of the SrO_x doublet to the total photoemission intensity is accurately determined. As seen in Figure 7.14, there is a noticeable decrease in intensity for the higher binding energy doublet (the one corresponding to SrO_x) when using techniques to remove SrO_x crystallites. This is a clear indication that the concentration of strontium oxide crystallites on the surface has been reduced by the surface preparation. It is also comforting to see that the peak to valley ratio (as indicated by the horizontal dashed lines) is consistent with the data fitting, and is likely an accurate way to assess the effectiveness of different surface preparations at removing the surface SrO_x crystallites. It is interesting to note that the water boiling methods

appear to be more effective at removing SrO_x from the surface region of STO than the acid-based methods. We speculate that the acid-based processing may etch the surface too aggressively, attacking some of the TiO_2 surface and resulting in a mostly, but not entirely, TiO_2-terminated surface, which would be consistent with the data of Figure 7.14. Whether or not this is the case would be an excellent focus of a future study using scanning tunneling or atomic force microscopy techniques.

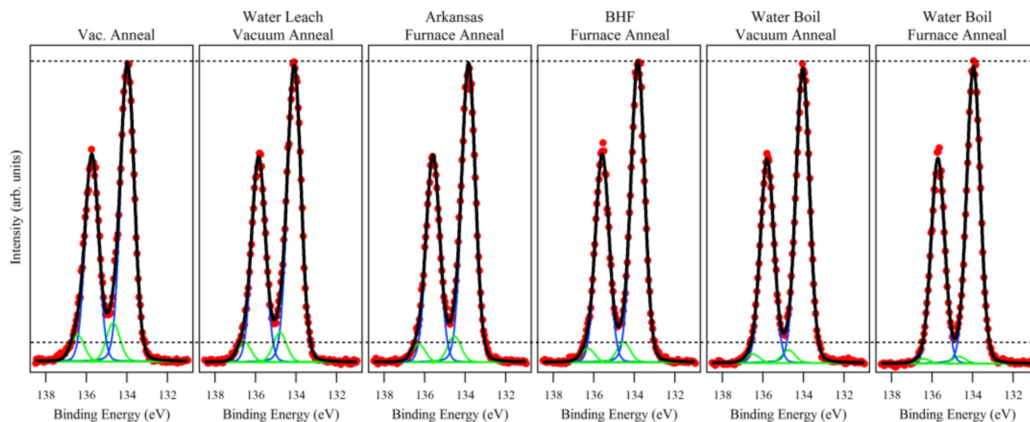

Figure 7.14 XPS spectra of the Sr 3d core level for different surface preparations. Data was fit using two spin-orbit split doublets, one (blue) corresponding to the primary STO lattice, and the other (green) to SrO_x crystallites on the surface of STO.

More can be learned about the relative effectiveness of different surface preparations by looking at the relative stoichiometry determined from XPS measurements. Figure 7.15 shows the relative concentration of Sr and Ti in the near surface region of STO. Because of the surface-sensitivity of XPS measurements one would expect to have a relative excess of Ti for samples that are TiO_2-terminated. For this analysis, a polynomial background was removed from the XPS spectra of the Sr 3d and the Ti 2p core levels and the spectra were then fit with 4 Voigt peaks (the minimum

number required to obtain a structure-free residual). The total photoemission intensity of the Sr 3d and the Ti 2p core levels was then used to determine the relative concentration, considering both escape depths and sensitivity factors. The error bars in Figure 7.15 represent variability between samples, analyzed in the identical fashion, and not the estimated uncertainty in the actual concentrations due to systematic errors in the analysis or experiment, which may be even larger. As expected, samples prepared using acid-based etching, or water treatments have a Ti rich surface region. The data indicate that the water-based methods are more effective at removing Sr from the surface region than the acid-based methods. Again, this could be related to the potentially aggressive etching of the surface, and subsequent surface roughening, caused by acid-based techniques. It is also interesting to note that for boiled samples, a simple vacuum anneal appears to remove more surface Sr than a furnace anneal followed by a gentler anneal in UHV. This may indicate that water boiling may even remove some sub-surface Sr, which is later "healed" during the furnace anneal due to mass transport[198,203,204].

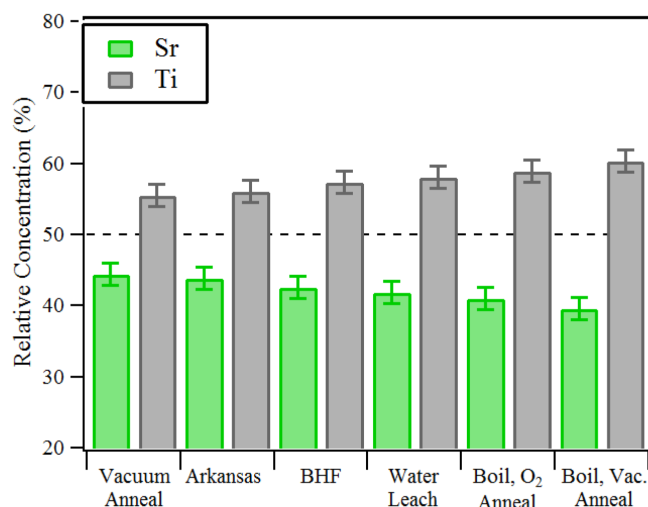

Figure 7.15 The relative Sr and Ti concentration of the near surface region of STO (001) as determined by XPS measurements for samples prepared using a variety of methods. As expected, methods reported to leave the surface TiO_2-terminated have a higher Ti concentration in the surface region.

7.4 SURFACE CHARACTERIZATION - AFM

Atomic force microscopy (AFM) is a valuable tool to investigate the quality of the sample surface. This section shows AFM images of sample surfaces prepared by several different ways. All the preparation methods that were previously described result in atomically flat surfaces with TiO_2 termination. Occasionally, however, some unwanted features do appear on the STO surface. I describe below several representative AFM images that highlight these features. All samples were annealed in oxygen as described in detail in Section 7.2.1.

Etching with buffered HF is one of the ways of obtaining a TiO_2-terminated surface of STO substrate. However, the etching rate is sufficiently fast to cause the STO surface to be overetched if not done carefully. The buffered HF etches the top layer of SrO quickly but etches the next topmost layer of TiO_2 as well. In Figure 7.16, the STO

surface etched with buffered HF (1: 20 diluted HF for 1 min) was imaged by RHEED and scanning tunneling microscopy (STM). The RHEED image showed sharp diffraction patterns but with additional features, as seen in Figure 7.16 (a). When the surface was scanned by STM, the several holes in the terraces were observed, as seen in Figure 7.16 (b). The additional features in the RHEED image are likely related to these holes. For HF etching, it is critical to find the proper time and concentration in order to etch the surface cleanly.

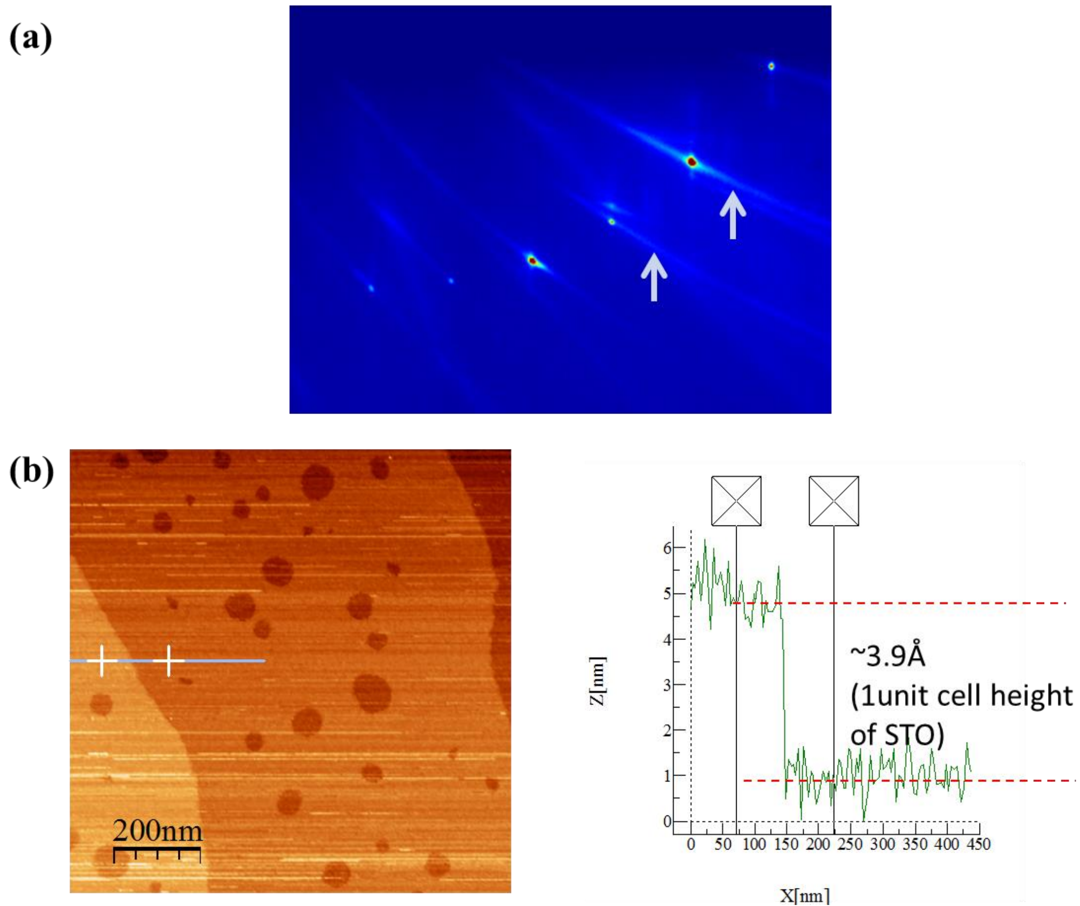

Figure 7.16 (a) RHEED image and (b) STM image of STO surface etched by buffered by HF. STM image taken by Jisun Kim in the Dr. Shih group.

With the proper etching time, etching with buffered HF is an effective way to obtain TiO_2-terminated surfaces. Figure 7.17 shows an AFM image of the surface ten days after the HF etching. The AFM image still shows the steps and terraces indicating that the surface is very stable.

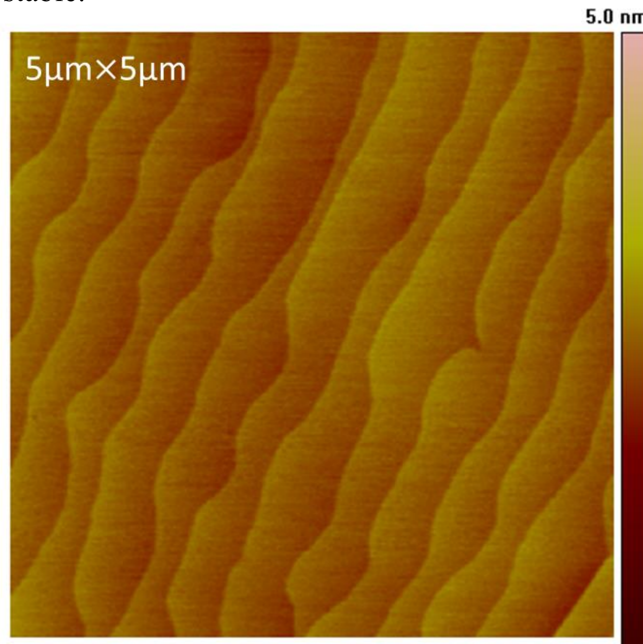

Figure 7.17 AFM image of the STO surface 10 days after the etching.

However, HF is a dangerous chemical compound that can cause fatal tissue damage. If we can use a safer method to etch the surface, that would be preferable. The somewhat safer etchant HCl/HNO_3 is also a good way to prepare atomically flat STO surfaces. After etching with HCl/HNO_3, RHEED and AFM show that the surface is atomically flat (images not shown here). However, when the surface is not etched well, the surface contains holes and SrO / $Sr(OH)_2$ islands[207] at the terrace edges, as shown in Figure 7.18. Before HCl/HNO_3 etching, water soaking for 20 min at 70 °C is done to create the soluble hydroxide complexes $Sr(OH)_x$. If the etching time is not long enough to

remove these hydroxide complexes, a surface similar to that in Figure 7.18 may be obtained.

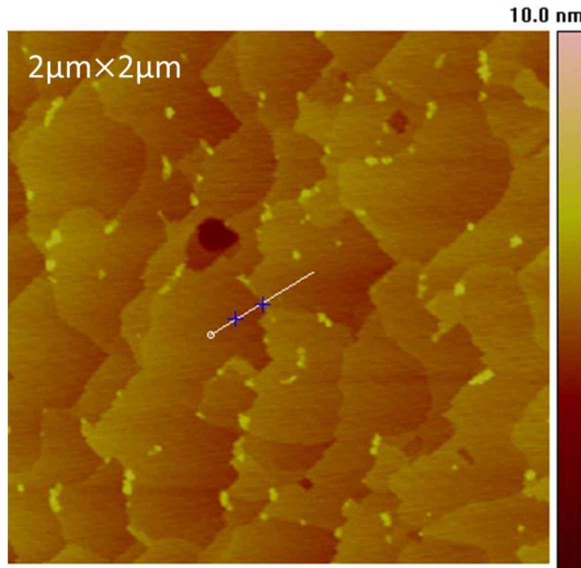

Figure 7.18 AFM image of the STO surface etched by HCl/HNO_3.

Water boiling is safest way to prepare the surface among the various surface preparations described. In Figure 7.19(a), AFM shows the TiO_2-terminated STO surface that is atomically flat. One day after water boiling, several SrO and $Sr(OH)_2$ islands are observed in the AFM image, as seen in Figure 7.19(b). According to Ref.[207], these islands can be removed by additional water boiling followed by annealing.

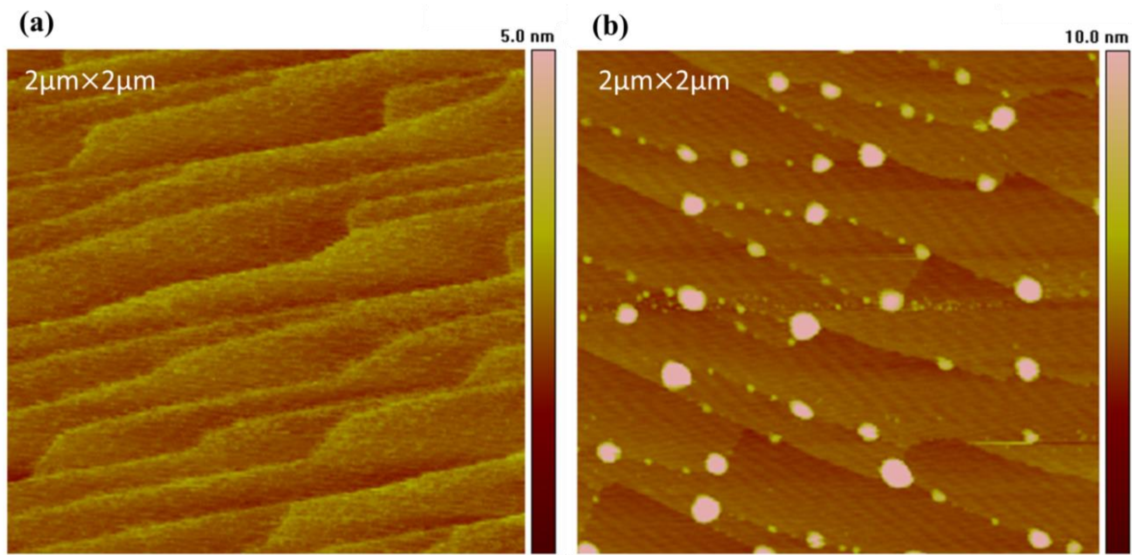

Figure 7.19 (a) AFM image for the STO surface boiled in DI water and (b) one day after boiling water preparation.

7.5 Conclusion

High-resolution ARPES measurements showed that a simple degreasing of STO single crystals, accompanied by a subsequent anneal in UHV is not an adequate surface preparation of STO. Other surface preparations such as MBE growth, the Arkansas method, or etching with BHF, and to a lesser extent, simply leaching the STO with water result in surfaces with much less disorder. It was also found that ARPES was an excellent probe of surface disorder.

Density functional theory calculations for bulk STO account for virtually all dispersing features in the ARPES data. A tight-binding model of the band structure, while in reasonable agreement with ARPES data, is not quite as successful as the DFT calculations. The agreement of tight-binding calculations with ARPES data may be improved with additional, fine tuning of the tight-binding parameters.

Using ARPES to study the gap region showed that gap states depend strongly on surface preparation methods. A non-dispersing oxygen vacancy state, located ~1 eV

below the Fermi level, is present in vacuum-annealed and water-leached samples, whereas a non-dispersing, mid-gap state was found ~800 meV above the top of the valence band for samples which underwent etching. In contrast, MBE-grown thin films show very little indication of any gap states. This suggests that it should be possible to use different surface preparations to tailor interface properties between STO and other complex metal oxides. Theoretical modeling of STO slabs using DFT within the LDA for the exchange correlation, indicate that the mid-gap state is not related to the SrO- and TiO_2-terminated surfaces, but rather, due to a partial hydrogenation of the STO surface that occurs during etching. A theoretical study of the charge density for this non-dispersing, mid-gap state shows that its origin lies in the formation of a H-Ti bond on the TiO_2-terminated STO surface. Further theoretical studies of surface properties show that for this H-Ti bond to form it must be preceded by either a F substitution of a surface O, or the formation of a single hydroxyl group on the 1×1 surface unit cell. These two surface-modifications that enable the H-Ti bond to form both give rise to electronic states just below the STO valence band. The H-Ti bond is very thermally stable, and is not broken even with an anneal of 900 °C. Furthermore, there is considerable evidence that boiling STO in water for 30 min., followed by an anneal in O_2, results in a surface as good, or better, than surfaces prepared using acid-based methods.

Chapter 8. Structural, optical and electrical properties of strained La-doped $SrTiO_3$ films

The structural, optical and room-temperature electrical properties of strained La-doped $SrTiO_3$ epitaxial thin films are investigated. Conductive La-doped $SrTiO_3$ thin films with concentration varying from 5 to 25 % are grown by molecular beam epitaxy on four different substrates: $LaAlO_3$, $(LaAlO_3)_{0.3}(Sr_2AlTaO_6)_{0.7}$, $SrTiO_3$ and $DyScO_3$, which result in lattice mismatch strain ranging from -2.9 % to +1.1 %. We compare the effect of La concentration and strain on the structural and optical properties, and measure their effect on the electrical resistivity and mobility at room temperature. Room temperature resistivities ranging from $\sim 10^{-2} \sim 10^{-5}$ Ω-cm are obtained depending on strain and La concentration. The room temperature mobility decreases with increasing strain regardless of the sign of the strain. The observed Drude peak and Burstein-Moss shift from spectroscopic ellipsometry clearly confirm that the La addition creates a high density of free carriers in $SrTiO_3$. First principles calculations were performed to help understand the effect of La-doping on the density of states effective mass as well as the conductivity and DC relaxation time. Theoretical calculation is done by Andrew O'Hara. And optical measurement and analysis are done by Dr. Stefan Zollner and Cesar Rodriguez at New Mexico State University (NMSU). This work was published in : M. Choi, A. B. Posadas, C. B. Rodriguez, A. O'Hara, H. Seinige, A. J. Kellock, M. M. Frank, M. Tsoi, S. Zollner, V. Narayanan and A. A. Demkov, "Structural, optical and electrical properties of strained La-doped $SrTiO_3$ films", J. Appl. Phys. **116**, 043705 (2014)

8.1 INTRODUCTION

Among the various perovskite oxide materials, $SrTiO_3$ (STO) has been extensively studied since the 1960s due to its large dielectric constant and non-linear dielectric properties[265-267]. Thanks to these unique properties, STO finds a wide range of applications such as a dielectric layer in capacitors[268,269], high frequency tunable devices[270,271], and in oxygen sensing[272]. Furthermore, heterostructures of STO with other perovskites give rise to emergent phenomena, such as a two dimensional electron gas (2DEG) at the interface between STO and $LaAlO_3$[273,274], two dimensional superconductivity at $LaTiO_3$/STO interfaces[194], and confinement effects in artificial quantum well structures[275,276].

STO is a wide band gap insulator (E_g ~3.2 eV) but can easily be made conductive through n-type doping using Nb[277,278], La[279], or oxygen vacancies[280]. The substitution of La^{3+} for Sr^{2+}, Nb^{5+} for Ti^{4+}, or electrons from ionized oxygen vacancies, render STO highly conductive. The electronic properties of doped STO attract significant attention due to its many potential applications. For example, both Nb-doped[279] or La-doped[281] STO have been considered as thermoelectric materials. Doping via cation substitution also modifies the electronic band structure of STO, resulting in changes in the band curvature and band degeneracy[282], which cause the electron effective mass (m*) of the material to change. This possibility of tuning the effective mass and carrier density is one reason why doped STO is a promising material for thermoelectric applications. In the case of La-doped STO, partial substitution of La^{3+} into Sr^{2+} sites should result in each La atom donating one electron to the conduction band of STO. Depending on the dopant concentration, the carrier concentration of La-doped STO (LSTO) can made to vary in a wide range from 10^{17} cm^{-3} to ~10^{21} cm^{-3} [273,283,284]. At 2 K, the electron mobility of dilute (8×10^{17} cm^{-3}) La-doped LSTO thick films grown by hybrid molecular beam epitaxy

(MBE) was reported to be over 50 000 $cm^2\ V^{-1}\ s^{-1}$ [284]. At room temperature, however, the electron mobility of bulk LSTO at room temperature has been reported to be between 0.13 and ~7 $cm^2\ V^{-1}\ s^{-1}$, depending on La concentration and microstructure[278,281,285]. In the $\sim10^{20}\ cm^{-3}$ concentration region, LSTO mobility was reported to be ~0.26 to 1 $cm^2\ V^{-1}\ s^{-1}$ for films grown by PLD[281,286], and ~7 $cm^2V^{-1}s^{-1}$ for films grown by MBE[284]. In the $\sim10^{21}\ cm^{-3}$ concentration region, a mobility of around 1 $cm^2V^{-1}s^{-1}$ was obtained for a PLD-grown film[281]. All previous reports measured the mobility using relatively thick (>100 nm) LSTO films. The resistivity of bulk LSTO is reported to range from 0.001 to 1 Ω-cm at room temperature, and from $1.3\sim1.6\times10^{-4}$ Ω-cm at 10 K, depending on La concentration[287,288]. These electrical properties of LSTO make it promising for use as a conductive layer in oxide electronic devices based on perovskite oxides[14]. For example, LSTO was used as an epitaxial conducting template to integrate epitaxial ferroelectric $Pb(Zr,Ti)O_3$ on Si (001)[289]. LSTO was also used as an n-type buried channel material in an all-oxide metal-insulator-semiconductor field-effect transistor[290]. Depending on the La concentration, LSTO shows a wide range of carrier density. Due to this tunable carrier density, LSTO is a promising candidate for the quantum metal layer in a quantum metal field-effect transistor (QMFET)[291]. It has been proposed that inserting a very thin metal between the ferroelectric and the semiconductor in a field-effect transistor and connecting this layer to the source could address the electrical mismatch in a negative capacitance FET[292].

LSTO is also a promising candidate for use as a transparent conducting oxide. By controlling the oxygen vacancies[286] and La concentration[286,288], LSTO is not only highly conductive, but is also transparent. STO is commonly used as a substrate or a template for the growth of other functional perovskite oxides. Therefore, LSTO would be useful for the fabrication of various optoelectronic devices. One obvious drawback of STO-

based conductive layers is their low room temperature mobility. One possible route to enhance the mobility is to use strain, which affects the electronic band structure[293]. The bottom of the STO conduction band is comprised of Ti 3d states forming a triply degenerate t_{2g} band. If spin-orbit coupling is accounted for, the conduction band bottom is split such that the conduction band minimum at the Γ point is formed by two-fold degenerate heavy electron and light electron bands. Tetragonal strain in a thin film can further split the heavy and light bands. Theoretically, for unstrained 12.5 at.% La doped into STO, the energy of the light and heavy electrons are still degenerate at the band minimum at Γ[282]. However, when pure STO is under in-plane tensile strain, the energy of the light electron band is lowered by ~40 meV[294]. Experimentally, by imposing a uniaxial 0.3 % compressive strain along <100> to lightly-doped (7.5×10^{17} cm^{-3}) LSTO epitaxial films, it was reported that the electron mobility could be enhanced by 300 % at 1.8K[295]. The band splitting in uniaxially strained STO was also observed using angle-resolved photoemission spectroscopy[296]. Therefore, applying strain may provide a way of enhancing the electrical properties of LSTO.

In this paper, we investigate the room temperature structural, optical and electrical properties of thin (20 nm) strained epitaxial LSTO films grown by molecular beam epitaxy (MBE) as a function of La concentration in the range 5 to 25 at.%. To achieve a range of epitaxial strain values, we grow LSTO on four different substrates: $LaAlO_3$, $(LaAlO_3)_{0.3}(Sr_2AlTaO_6)_{0.7}$, $SrTiO_3$ and $DyScO_3$, resulting in in-plane strain values ranging from -2.9 % to +1.1 %. We measure the changes in the unit cell volume, optical absorption, carrier concentration, resistivity and mobility as a function of La concentration and strain. Contrary to previous reports of mobility enhancement at low temperature in dilute LSTO films, we find that at the high La concentrations we studied

and at room temperature, less strained LSTO films had higher mobility compared to more strained films, regardless of the sign of the strain.

8.2 EXPERIMENT AND THEORETICAL CALCULATION

Four different substrates, $LaAlO_3$ (LAO) (100), $(LaAlO_3)_{0.3}(Sr_2AlTaO_6)_{0.7}$ (LSAT) (100), $SrTiO_3$ (STO) (100) and $DyScO_3$ (DSO) (110), were used in the study to impose a range of epitaxial strain values on the LSTO films. The substrates were introduced into a customized DCA 600 MBE system with a base pressure of 3×10^{-10} Torr. The substrates were outgassed at 800 ^{o}C for 30 min in an oxygen partial pressure of 3×10^{-7} Torr to remove surface impurities. The LSTO films were grown by MBE using effusion cells for the metal evaporation and molecular oxygen as the oxidant. The fluxes of Sr, Ti and La were calibrated to be 1 ML/min using a quartz crystal monitor with feedback from *in situ* x-ray photoelectron spectroscopy (XPS). LSTO films were deposited on four different substrates using a layer-by-layer alternating shuttering method of Sr, La and Ti. For each shuttering cycle, the Sr and La shutters were sequentially opened for an amount of time depending on the target La concentration, while the Ti shutter was opened for 1 min. The shuttering cycle was repeated until the desired thickness of 20 nm was reached. All the films grown were terminated with a TiO_2 monolayer.

For each substrate, films of three different La concentrations (5, 15, and 25 at. %) with 20 nm thickness were grown. All films were grown under identical conditions at 800 ^{o}C growth temperature with total oxygen pressure of 1×10^{-6} Torr. After LSTO film growth, annealing was performed *in situ* at 800°C in an oxygen partial pressure of 3×10^{-7} Torr for 10 mins. The samples were then cooled down in this atmosphere to 200 ^{o}C at a rate of 30 °C/min and then transferred *in situ* into another ultrahigh vacuum chamber for

additional vacuum annealing for 5 min at 750 ^{o}C. After vacuum annealing, the samples were further annealed ex situ at 350 ^{o}C for one hour in air to remove oxygen vacancies.

The film compositions were determined by XPS using a VG Scienta R3000 analyzer. Measurements at room temperature are performed using monochromatic Al Kα radiation (hυ = 1486.6 eV). The resolution of the XPS spectra is limited by the x-ray source line width, which is approximately 300 meV. Sensitivity factors for each element were calibrated with $SrTiO_3$ and $LaAlO_3$ substrates and verified using Rutherford backscattering spectroscopy (RBS). To independently confirm the XPS compositional analysis, RBS was performed on selected samples using an NEC 3UH Pelletron with 2.3 MeV He^+ ions with Si surface barrier detectors (19 keV FWHM). Out-of-plane and in-plane lattice constants of the LSTO films were measured by X-ray diffraction (XRD) on a Philips X'Pert diffractometer using Cu Kα radiation. The thicknesses of films were measured on the same instrument by X-ray reflectivity (XRR).

For electrical measurements, gold metal electrodes (Au) were sputtered onto the four corners of the 5 mm × 5 mm LSTO samples using a shadow mask. The resulting Au electrical pads were 100 nm thick with a lateral size of less than 1 mm × 1 mm each. Indium (In) was then soldered directly onto the Au pads and ohmic behavior of the contacts was confirmed at room temperature prior to transport measurements. We have performed electrical resistivity measurements in the van der Pauw geometry[297] and Hall Effect measurements to determine resistivity and carrier concentration of the LSTO thin films. The four-terminal resistances were measured at room temperature by the low-frequency (17 Hz) ac lock-in technique. The magnetic field used for Hall Effect measurements was ±0.135 T. To avoid the effect of sample geometry and to eliminate the longitudinal Hall voltages, we have averaged values from eight measurements for

Hall voltages (V_{13}, V_{24}, V_{42}, V_{31} at ±0.135 T) and eight measurements for the resistivity ($R_{12(21)}$, $R_{23(32)}$, $R_{34(43)}$, $R_{41(14)}$)[297].

The dielectric functions of LSTO films on single-side polished LAO and STO substrates were determined using spectroscopic ellipsometry from 1.0 to 6.5 eV at 300 K as described previously[16,298]. Due to the small (5 × 5 mm^2) sample size and the presence of Au contacts at the corners, data were taken with a rather shallow 60° angle of incidence. The Au contacts were covered with black paint to avoid reflections from the contacts. The depolarization spectra are small, indicating good uniformity of the samples. To model the ellipsometric angles of these samples[299,300], we used tabulated optical constants for the STO[16] and LAO[301] substrates. The optical constants of the LSTO films were described by a Drude term (to account for free carrier response) and several Gaussian and Tauc-Lorentz oscillators[300] to account for optical interband transitions. The parameters of these oscillators were fitted until good agreement between the measured ellipsometric angles and the model was achieved. We assumed that the film thickness of 20 nm (confirmed with x-ray reflectance) was accurate and we ignored surface roughness. Small errors in thickness will not affect our conclusions.

8.2.1 Electrode test

Prior to the transport measurements, the several combinations of electrode materials were tested to find proper electrodes for La doped $SrTiO_3$ film. Three different electrodes were tested here; Pt/Au, In/Au, and Au/Ti. Figure 8.1(a) shows the current-voltage (I-V) curve at room temperature using Au/Pt electrodes. Pt electrodes were prepared using a focused ion beam (FIB) and 100 nm thick Au pads were deposited on the Pt electrodes. The I-V characteristic is linear only within -2 V to 2 V voltage range at room temperature. The In/Au electrodes are shown in Figure 8.1 (b). Au electrodes with

100 nm thickness were deposited and In was then soldered directly onto the Au pads. The ohmic behavior of the contacts was confirmed at room temperature. The last combination of Ti/Au electrodes shows in Figure 8.1(c). The linear I-V curves indicate ohmic contacts. The measurements were accomplished from 2 K up to 300 K. For the transport measurements of La doped $SrTiO_3$ films, I used the In/Au electrodes.

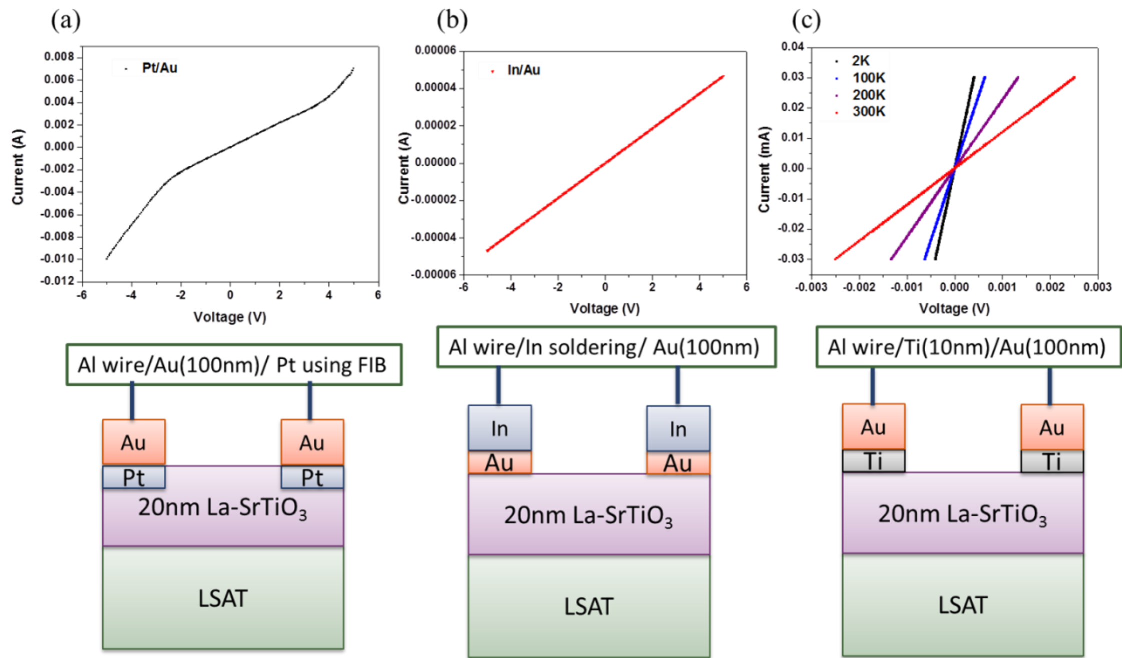

Figure 8.1 I-V curve of (a) Pt/Au, (b) In/Au, and (c) Ti/Au electrodes.

Transport measurement of the LSTO thin films were carried out using the van der Pauw geometry. The equivalent circuit diagram and pictures of the measurement setup are shown in Figure 8.2. The four-terminal resistances were measured at room temperature by the low-frequency (17 Hz) ac lock-in technique. The voltage V_0 across the reference resistance (10 Ω) was measured to determine the current through circuit, which is assumed to be the same as the current through the two current leads of the sample. The

sample voltages (V_S) between the two voltage leads of the sample were then measured directly.

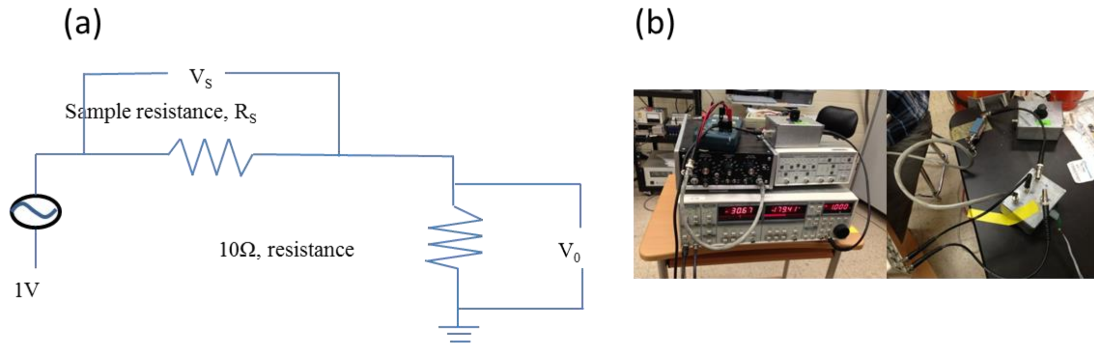

Figure 8.2 (a)The schematic view of measurement and (b) the system for electrical measurement of LSTO

8.3 Results and Discussion

8.3.1 Surface morphology

Figure 8.3(a) shows the reflection high energy electron diffraction (RHEED) pattern of as-grown LSTO film on LSAT which has 25 % La concentration. The RHEED pattern of the same sample after vacuum annealing is shown in Figure 8.3(b). To eliminate the oxygen vacancies that likely formed during vacuum annealing, LSTO films were further annealed at 350 °C in air[302]. Figure 8.3(c) shows the RHEED pattern of the same LSTO film after additional annealing in air. The initial high temperature growth gives rise to good crystallinity as seen in Figure 8.3(a). After additional annealing, RHEED patterns showed that film tends to become rougher. This roughening due to post-deposition annealing was also observed in atomic force microscopy (AFM) measurements. Figure 8.4(a) shows the AFM image of an as-grown LSTO film on LSAT (the same sample shown in Figure 8.3). The film surface has an RMS roughness around

0.39 nm measured by AFM. After annealing in air, the film surface shows an increased RMS roughness of around 1.39 nm.

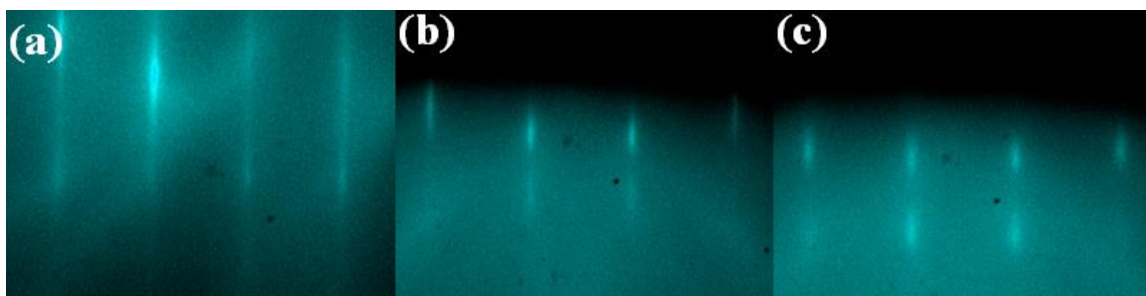

Figure 8.3 The RHEED patterns of 25 % LSTO on LSAT along <100> direction (a) after growth, (b) after vacuum annealing, and (c) after air annealing.

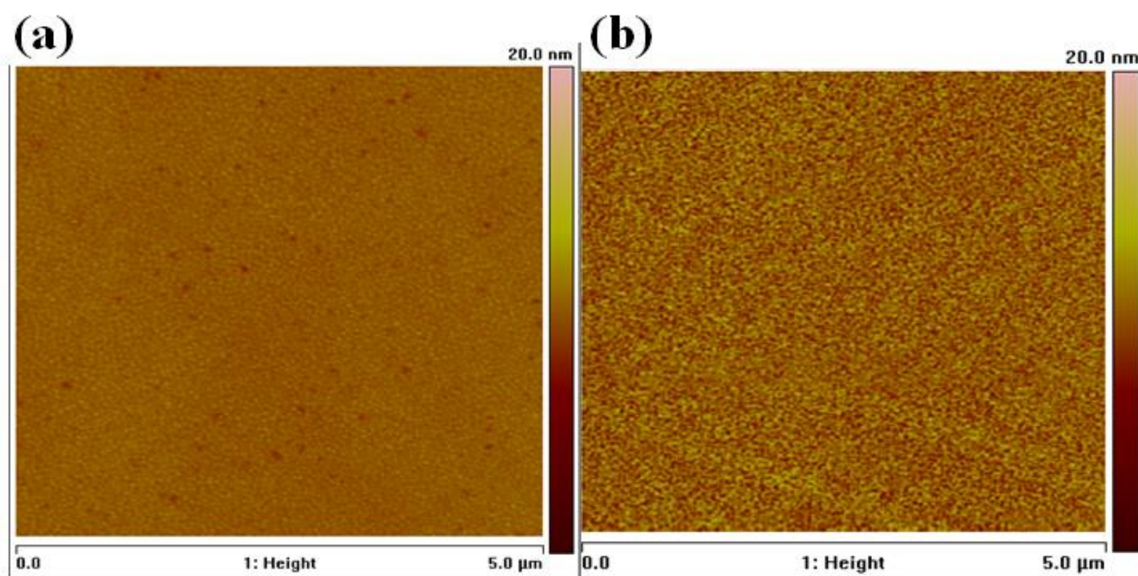

Figure 8.4 The AFM images of 25 % LSTO on LSAT (a) after vacuum annealing and (c) after air annealing.

8.3.2. Stoichiometry and crystallinity

After growth, the compositions of LSTO films were determined by *in situ* XPS. High resolution spectra of the Sr 3d, Ti 2p, O 1s, and La 3d core levels were measured for each sample. Typical XPS spectra are shown in Figure 8.5. After subtracting a Shirley background for each spectrum and determining the integrated intensity, the film stoichiometry was determined using the appropriate Wagner sensitivity factors for each core level[75].

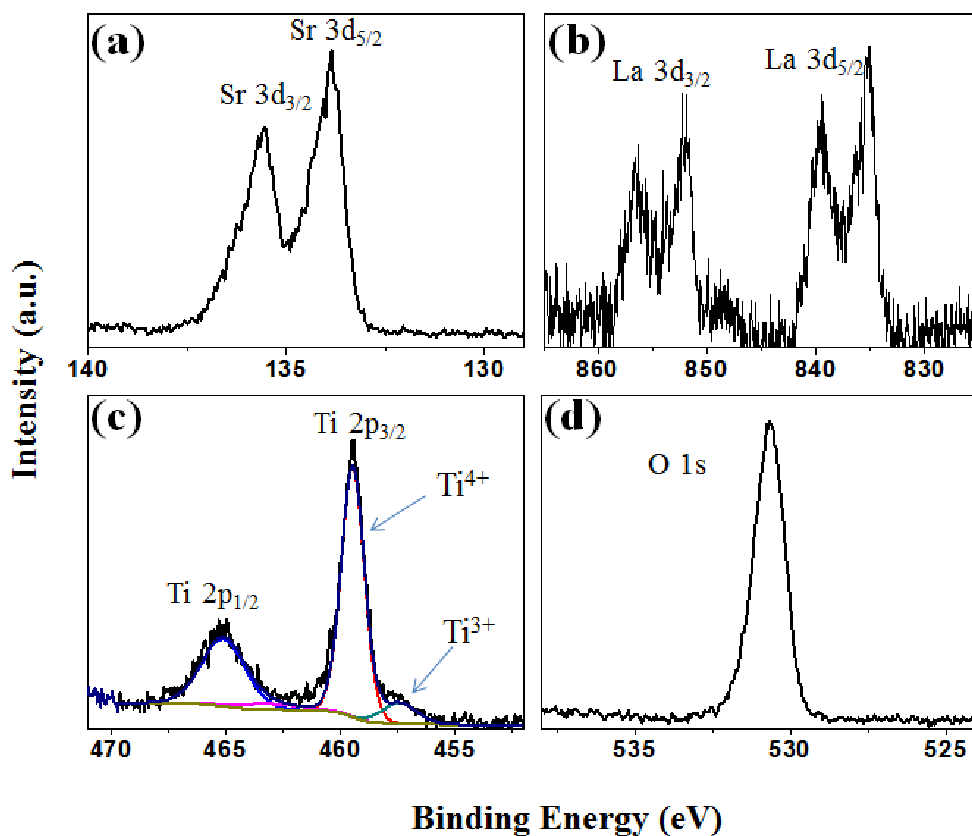

Figure 8.5 Representative core level spectra of (a) Sr 3d, (b) La 3d, (c) Ti 2p, and (d) O 1s from LSTO films using *in situ* XPS.

The overall composition as determined by XPS using the standard sensitivity factors is within 5 % of the target composition for all the metal elements but with systematically lower La and higher Ti than expected. Because La substitutes for Sr sites, La concentration is reported as the ratio of La concentration to the total of Sr and La concentrations.

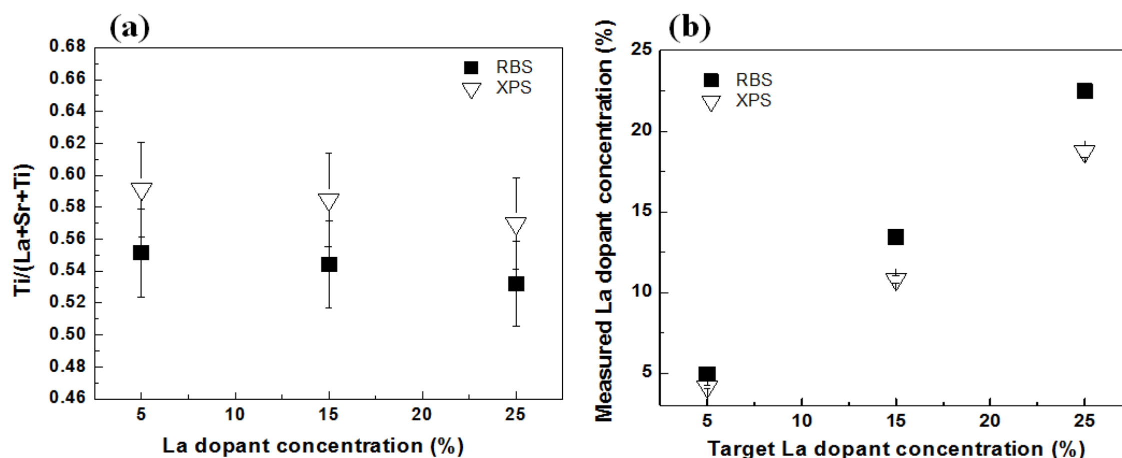

Figure 8.6 (a) The ratio of [Ti] / [La+Sr+Ti] determined by XPS (open triangles) and RBS (filled squares) and (b) measured La dopant concentration (RBS and XPS) compared to the target concentration.

As an independent check of the XPS results RBS measurements were performed on a control group of samples and compared to the results of XPS. Figure 8.6(a) shows the ratio of [Ti] to [La+Sr+Ti] for films containing three different La dopant concentrations determined from XPS and RBS. From Figure 8.6(a), there are two explanations about the film compositions: we underestimated Ti concentrations or overestimated La concentrations. In Figure 8.6(b), we plot the measured La dopant concentrations ([La]/[La+Sr]) using XPS and RBS vs. the target value. We estimate the relative experimental errors to be ±1 at.% for RBS and ±10 % for XPS for each La

concentration. From Figure 8.6(b), we note that La concentration is consistently underestimated by XPS by about 10 % of the RBS-measured value. Using the data obtained from RBS, the sensitivity factors used in XPS analysis were adjusted slightly and fluxes used during growth were modified accordingly for the subsequent LSTO epitaxial film growth.

Figure 8.7(a) shows typical symmetric $2\theta-\theta$ x-ray diffraction scans of 20 nm thick LSTO films on LAO, LSAT and DSO substrates. No secondary phases and other orientations are observed from the full range of the XRD pattern (not shown) and all LSTO films were confirmed to have a thickness of 20 nm ± 0.3 nm, as measured by XRR. The Bragg peak of LSTO films on STO substrate is buried under that of the STO substrate peak so the data for LSTO films on STO substrate is excluded from Figure 8.7(a). The lattice constant of bulk LSTO for 10 % La concentration is 3.906 Å[302] at room temperature, increasing to 3.908 Å at 30 %. The lattice constant of bulk LSTO is slightly larger than that of bulk STO (3.905 Å) due to a combination of dopant size and electronic effects[303]. The full width at half maximum (FWHM) of the rocking curve around the (002) film peak is measured to vary between 0.11 and 0.35° (Figure 8.7 (a), inset). The FWHM of the films with 25 % La concentration are generally broader than that of the films with 5 % La concentration. Figure 8.7(b) shows the measured out-of-plane lattice constants of 20 nm LSTO films as a function of La concentration. The out-of-plane lattice constants generally increase with increasing La concentration irrespective of the substrate used, although the rates of lattice constant increase with concentration are substrate-dependent.

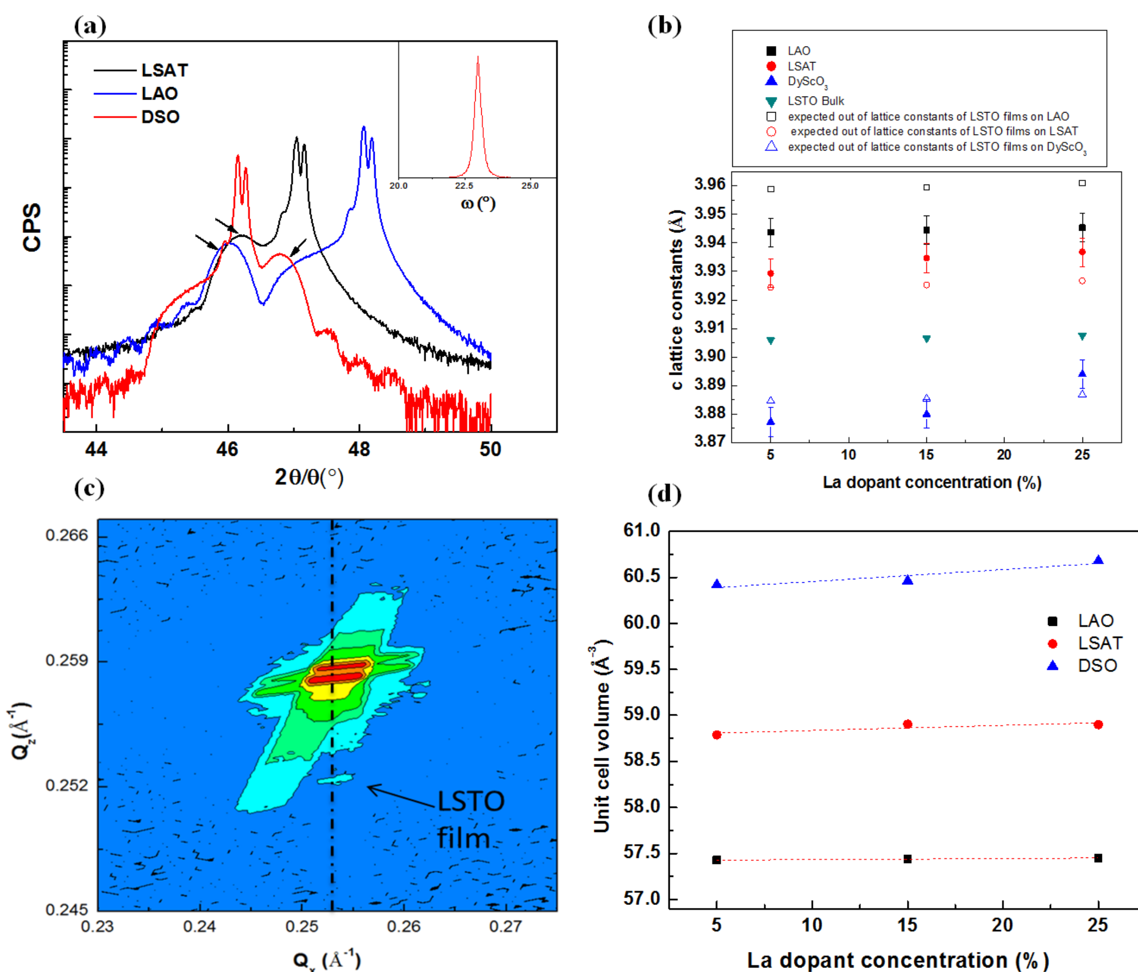

Figure 8.7 (a) X-ray diffraction pattern of (002) LSTO peaks and substrate peaks. Inset shows the rocking curve of 5 % doped LSTO films on LAO. (b) Measured out-of-plane lattice constants and expected out-of-plane lattice constants as a function of La concentration. (c) Reciprocal space map of (103) Bragg peak for an LSTO film on DSO substrate with 25 % La concentration. The in-plane lattice constant of the film is the same as that of DSO substrate. (d) Unit cell volume changes as a function of La concentration for the different substrates

Assuming that the films are commensurate to the substrates and that the elastic properties of LSTO are the same as undoped bulk STO, it is possible to determine the expected out-of-plane lattice constants. Using the Poisson's ratio of STO[304], the expected out-of plane lattice constants are indicated by the open symbols in Figure 8.7(b). For LSTO films on LSAT and DSO substrates, the measured out-of-plane lattice constants are reasonably similar to the expected out-of-plane lattice constants suggesting fully strained films. However, for LSTO films on LAO, the measured out-of-plane lattice constants are significantly less than the expected values, indicating that the LSTO films are partially relaxed. To verify that the LSTO films are commensurate to the substrates, a reciprocal space map of the (103) Bragg peak is performed. Figure 8.7(c) shows such a measurement for a 25 % LSTO film on DSO. The in-plane lattice constants of the film and substrate are identical. Such commensurate growth is observed for all samples grown on LSAT and DSO, with partial relaxation on films on LAO of about 22 %. The one interesting thing is that the measured out-of-plane lattice constants of thin LSTO films on DSO and on LSTO is a bit off from the expected out-of plane lattice constants determined using the undoped STO elastic constants. The possible explanations are that LSTO thin films become softer as La concentration is increased, or that our films are so thin compared to the references[281,303] that the La doping effect is not negligible.

From the measured out-of-plane and in-plane lattice constants, the variation in the unit cell volume of LSTO films as a function of La concentration for the different substrates is shown in Figure 8.7(d). The unit cell volumes generally increase with increasing La concentration, consistent with bulk LSTO regardless of the specific strain configuration.

8.3.3. Electrical and optical properties

Figure 8.8 shows the measured carrier concentrations of 5, 15 and 25 % doped LSTO films on LAO, LSAT, STO and DSO as a function of strain at room temperature. The dashed lines indicate the theoretical values of carrier concentration assuming that each La atom donates one electron to the conduction band of STO. Surprisingly, for all La concentrations studied, the measured carrier concentration is typically around 1/2 to 2/3 of the La concentration, with the largest discrepancy at the highest La concentration. Prior to Hall measurements, we determined the ratio $[Ti^{3+}]/([Ti^{4+}]+[Ti^{3+}])$ using *in situ* XPS to estimate the carrier concentration independently[305], as shown in Figure 8.5(c). As La^{3+} substitutes for the Sr site in STO, assuming the oxygen composition does not change, the valence of an equivalent concentration of Ti should change from Ti^{4+} to Ti^{3+}. From the ratio of Ti^{3+} to total Ti, we can therefore estimate how many dopants are "activated." From both the Hall measurement and *in situ* XPS measurement, the activated carrier concentration is always found to be less than the La concentrations.

For 25 % La-doped STO, the carrier concentration is well below the expected values. Typically, the measured carrier concentrations correspond to what is expected for 15 % La doping even though XPS confirms that 25 % La atoms are doped into STO. The reason for the lack of full activation at the higher doping concentration is presently unclear. Possible explanations for this phenomenon include charge self-compensation[306] or the presence of excess oxygen in the form of interstitials[307], which may form as a result of the final air annealing. Recently, we reported achieving 80 % activation from 15 % La doped LSTO with 20 nm thickness grown on Si by atomic layer deposition[308].

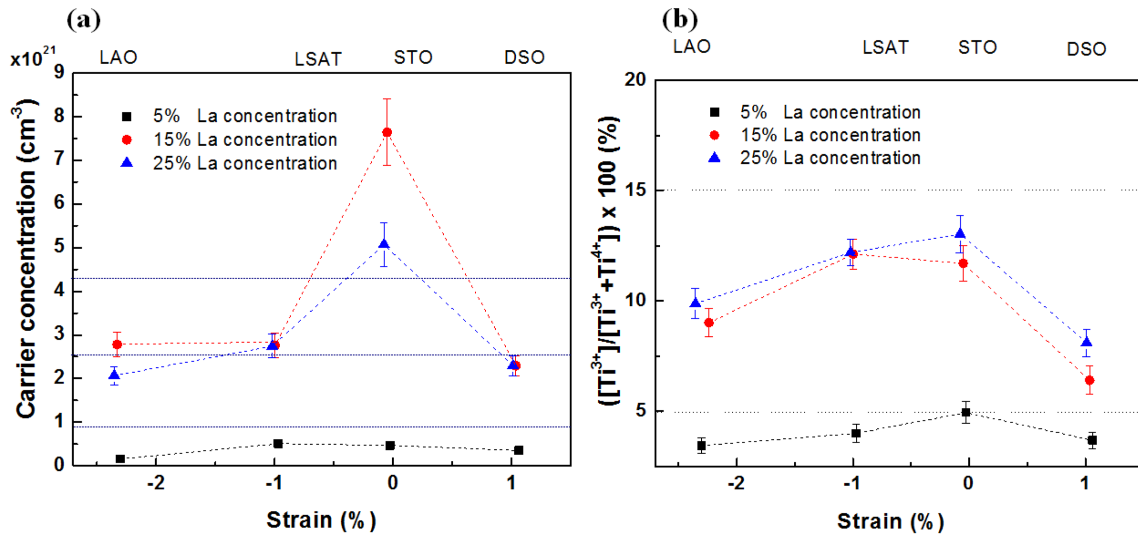

Figure 8.8 Carrier concentrations of 5, 15, and 25 % doped LSTO films with 20 nm thickness on four different substrates obtained from Hall Effect measurements (a) and the ratio $[Ti^{3+}]/([Ti^{4+}]+[Ti^{3+}])$ using *in-situ* XPS. The dashed lines indicate the theoretical values of carrier concentration assuming that each La atom donates one electron to the conduction band of STO.

In the case of LSTO films on STO, measured carrier densities are generally higher than the La concentration. This is most likely due to parasitic conduction from the STO substrate itself, which may become sufficiently conductive due to oxygen vacancies depending on the growth and annealing conditions[278,309]. With regards to the strain dependence of the carrier concentration, we observe that the larger the magnitude of the strain experienced by the LSTO films (either compressive or tensile), the lower the measured carrier concentration becomes for a given La doping concentration.

We also investigated how the optical properties of the LSTO films change with La concentration. Figure 8.9 shows the dielectric function of LSTO films on STO with 5 % and 15 % La. Data for a bulk (undoped) STO substrate are shown for comparison. As the La dopants are electrons donors, two effects are expected. First, a Drude peak at low

energy should emerge when the system becomes metallic. Indeed in Figure 8.9, we see that ε_1 decreases at lower energies and ε_2 increases, which is consistent with the free carrier response within the Drude model[310]. The Drude term becomes larger for the higher La concentration as expected. The Drude response causes a very sharp change in the ellipsometric angles below 2 eV, which cannot be mistaken. Second, the optical gap is expected to widen as the La concentration increases, because occupying states near the conduction band bottom blocks the low-energy optical transitions. This is known as the Burstein-Moss shift[311]. As seen from Figure 8.9, the band gap for LSTO is indeed significantly higher than for undoped STO, particularly for the 15 % sample. The observations of Drude peak and Burstein-Moss shift in our ellipsometry data clearly demonstrate that the La addition creates a high density of free carriers (doping) in STO. Such a clear free carrier response in optical spectra is difficult to achieve in silicon.

From the Drude response we can obtain a rough estimate of the carrier concentration of LSTO films on STO and LAO. We derived the plasma frequency and the broadening of the Drude peak from the ellipsometry spectra of LSTO films on STO and LAO. Table 8.1 shows Drude parameters (plasma frequency and broadening) for the 5 %, 15 % and 25 % doped LSTO films on STO and LAO. The carrier concentration is calculated using the equation $\omega^2 = ne^2/\varepsilon_0 m^*$, where ω is the plasma frequency, n is the carrier concentrations, e is the electron charge, ε_0 is the vacuum permittivity, and m* is the effective electron mass of LSTO films. Choosing the proper value for the effective mass in STO is not trivial. The effective mass of 5 % La doped STO is reported as 3.2~7.8 m_0[279,281,285,312], 5~7.8 m_0 for 15 %[281,285], and 4 m_0 for 25 %[279]. These effective masses are not applicable to our films. LSTO films[281] from which the effective mass was derived were grown under different conditions compared to our films and in many cases incorporate a large number of oxygen vacancies. In terms of calculated values of the

effective mass for heavy doping, these discrepancies will be addressed in the theoretical section.

Here we used the density of states effective masses of 1.124 m_0 for 5 % doped LSTO, 1.276 m_0 for 15 % and 1.329 m_0 for 25 % doped LSTO where m_0 is the free electron mass. The calculation of the effective mass is described below in section 8.3.4 of the paper. As the La doping concentration was increased, the carrier concentration from Drude parameters also were increased. The carrier concentration estimates from the Drude parameters shows qualitative agreement with those from the Hall measurements shown in Table 8.1.

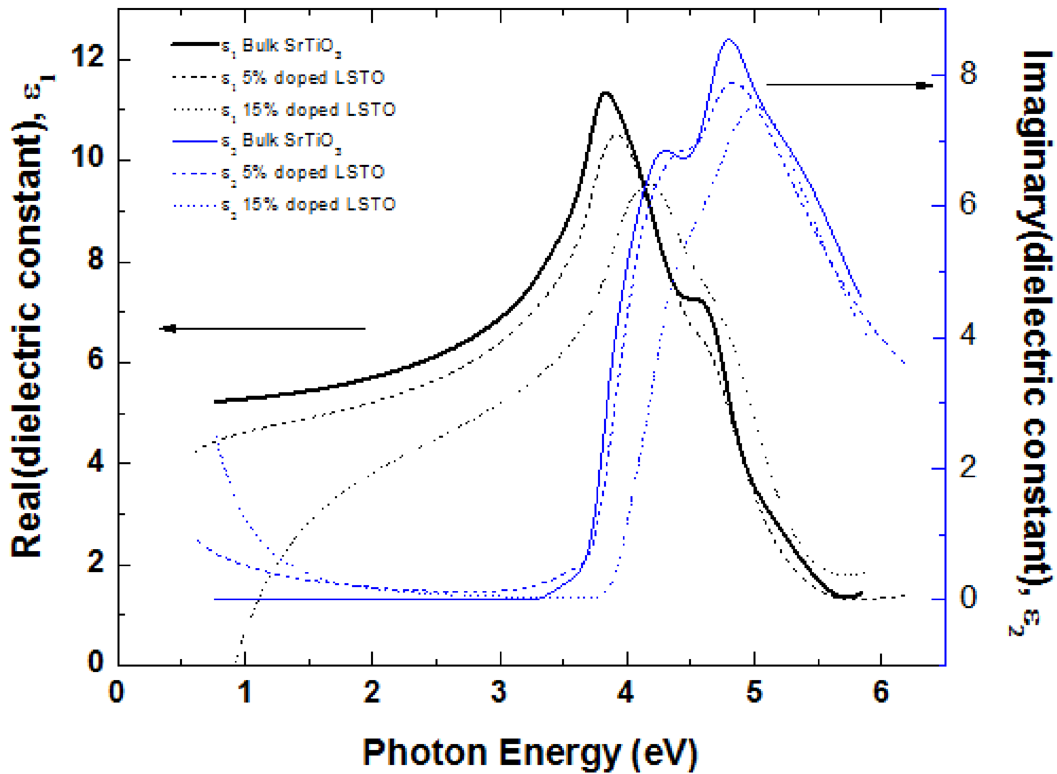

Figure 8.9 Dielectric function of 20 nm thick LSTO films on STO with 5 % and 15 % La. Data for a bulk (undoped) STO substrate are shown for comparison.

Substrate	La at.%	Plasma frequency (eV)	Plasma broadening (eV)	Carrier concentration from ellipsometry (cm^{-3})	Carrier concentration from electrical measurement (cm^{-3})
STO	5	1.26	2.67	1.29×10^{21}	4.650×10^{21}
	15	1.94	0.378	3.48×10^{21}	7.644×10^{21}
LAO	5	2.12	10	3.65×10^{21}	1.55×10^{21}
	15	1.90	0.297	3.34×10^{21}	2.779×10^{21}
	25	2.34	10	5.26×10^{21}	2.650×10^{21}

Table 8.1 The optical properties of 5 % and 15 % doped LSTO films on STO at room temperature. Plasma frequency, broadening, and calculated carrier concentrations from plasma frequency are presented.

Figure 8.10 shows the Hall mobility and resistivity of LSTO films determined from the same samples shown in Figure 8.8. The Hall mobility of the LSTO films was calculated from the equation $\mu=1/ne\rho$, where n is the measured carrier concentration, ρ is the measured resistivity, and e is the charge of the electron. It is noteworthy that the higher the absolute strain in the film, the lower the observed mobility at room temperature.

It is known that the band structure is altered in strained films, which may lead to a modification of the effective mass m*. LSTO films with tensile strain are predicted to have a lower effective mass than those with compressive strain[294,313]. Consistent with this prediction, we find that at low temperature (2 K), tensile-strained LSTO films on DSO do indeed have a slightly higher mobility than other films of the same doping concentration at low temperature. However, at room temperature, we observe that the higher the magnitude of the strain (either compressive or tensile), the lower the mobility. Hence, the mobility of more highly strained films on LAO and DSO were below that of less strained

films on LSAT. The mobility values of our thin films were found to be between 1 and 9 $cm^2V^{-1}s^{-1}$ at room temperature, depending on La concentration and strain.

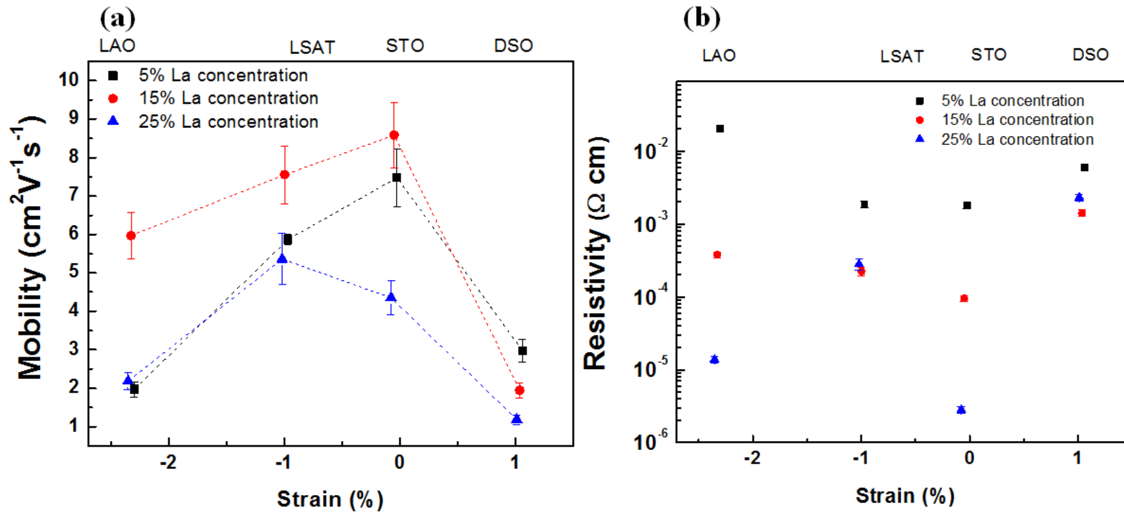

Figure 8.10 (a) Mobility and (b) resistivity of 5, 15, and 25 % doped LSTO films grown under four different strain configurations.

Figure 8.10(b) shows the resistivity of LSTO films on four substrates with values ranging from 10^{-5} to 10^{-2} Ω-cm. The resistivity of bulk LSTO was reported to range from 0.001 to 1 Ω-cm at room temperature, and that of thin LSTO films (~150 nm thickness) on LAO and STO substrates was reported from 7.7×10^{-2} to 1.7×10^{-3} Ω-cm, depending on La concentration[279,287,288]. However, the resistivity of LSTO films on STO in Figure 8.10(b) is lower than that of LSTO films on other substrates. Depending on the growth conditions, the STO substrate can become partly conductive by oxygen vacancies. Sculling *et al*. reported that the film with 2 % La doped STO grown at low growth pressure has lower resistivity than that grown at higher growth pressure[314]. In our work,

LSTO films with 20 nm thickness were grown at 10^{-6} Torr growth pressure. This growth pressure and relatively low thickness of films may affect the resistivity of LSTO films on STO substrate.

8.3.4. Theoretical calculations

To study the effects of doping on the effective mass, density functional theory (DFT) calculations were performed using the Vienna ab initio Simulation Package (VASP)[117] with the Perdew-Burke-Ernzerhof (PBE) version of the generalized gradient approximation to the exchange-correlation function[145]. Projector augmented wave pseudopotentials[118,227] were used to describe the atomic species with valence configurations of $4s^2 4p^6 5s^2$ for Sr, $4s^2 4p^6 5s^2 5d^1$ for La, $3p^6 3d^3 4s^1$ for Ti, and $2s^2 2p^4$ for O. A plane wave cutoff energy of 650 eV was found to ensure convergence to less than 1 meV per stoichiometric unit. For density of states calculations, the Brillouin zones were sampled using Gamma centered Monkhorst-Pack grids[229] scaled based on a 24×24×24 grid for the primitive $SrTiO_3$ cell (such dense grids were used since the systems are metallic under n-type doping). All atomic positions were fully relaxed and Brillouin zone integration was done using the tetrahedron method with Blöchl corrections[315].

To model heavily doped LSTO, supercells of the primitive STO were used with one Sr atom replaced by La. Cells were constructed to account for 1.56 % La (a 4×4×4 supercell), 3.7 % La (a 3×3×3 supercell), 4.17 % La (a 2×2×3 supercell of the 45° rotated $\sqrt{2}$ cell), 6.25 % La (a 2×2×2 supercell of the 45° rotated $\sqrt{2}$ cell), 12.5 % La (a supercell 2×2×2), and 25 % (the rhombohedral cell). For each cell, the lattice geometry was optimized and the expected number of carriers in the conduction band was determined assuming that La completely surrenders its electron to the Ti-states (shown in Table 8.2). In order to determine the chemical potential, at 300 K, we calculate the

number of carriers and self-consistently adjust μ until μ (n, T) the integrated number of carriers in the band matches the value of Table 8.2 using:

$$n_e = \int_{E_C}^{\infty} \rho(E) f(\mu, T) dE \tag{8.1}$$

where E_c is the conduction band minimum, ρ (E) is the density of states, and f (μ, T) is the Fermi function.

In the parabolic band approximation with degeneracy z, the density of states effective mass for degenerately-doped systems can be calculated as[316,317]:

$$\frac{m^*}{m_0} = \frac{h^2}{2k_B T m_0}\left(\frac{n}{2\pi z F_{\frac{1}{2}}(\eta^*)}\right)^{\frac{2}{3}} \tag{8.2}$$

where $F_{\frac{1}{2}}(\eta^*)$ is the un-normalized Fermi-Dirac integral of order $\frac{1}{2}$ and $\eta^* = \frac{\mu - E_C}{k_B T}$ is the temperature-reduced relative chemical potential. Numerical evaluation of the Fermi-Dirac integrals was performed using the code of X. Sun, *et al.*[318,319]. For STO, the spin orbit splitting is ΔE_{SO}=28 meV, approximately equal to the thermal energy at 300 K. Furthermore, the smallest occupied width of the conduction band (1.56 % La) was determined to be 61 meV. Therefore, we use z=6 as the band degeneracy factor. The results of this calculation are summarized in Table 8.2. Most importantly, we notice the trend that as the conduction band is filled, the effective mass increases from a low of 0.999 m_0 at 1.56 % La to 1.329 m_0 at 25 % Lanthanum. Compared to previous calculations of the density of states effect mass, our values are lower[282]. We attribute this discrepancy to our increased resolution of the occupied band width, which can be done by increasing the k-point grid and the number of pins used in calculating the density of states. Furthermore, it appears that the other authors used $F_0(\eta *)$ rather than $F_{\frac{1}{2}}(\eta *)$. While other transport properties calculated using Fermi-Dirac integral methods do use

different orders of the integral dependent upon the type of scattering mechanism assumed (e.g. r=0 for constant relaxation time approximation), $F_{\frac{1}{2}}(\eta *)$should be used for the density of states effective mass.

La at.%	n_e (cm^{-3})	$\mu(300\text{K}) - E_C$ (eV)	m_D/m_0	σ/τ (Ω-cm-s)$^{-1}$
1.56%	2.55×10^{20}	0.103	0.999	1.70×10^{15}
3.70%	6.04×10^{20}	0.112	1.071	2.44×10^{16}
4.17%	6.80×10^{20}	0.119	1.093	2.85×10^{16}
6.25%	1.02×10^{21}	0.149	1.162	9.91×10^{16}
12.50%	2.04×10^{21}	0.222	1.254	7.51×10^{17}
25.00%	4.07×10^{21}	0.334	1.329	1.11×10^{18}

Table 8.2 Summary of properties used to calculate the density of states effective mass and conductivity within relaxation time approximation.

For comparison with our 5 % and 15 % La samples, we use the theoretical equilibrium lattice constant for STO of a=3.94 Å to determine the expected number of carriers to be 8.17×10^{20} cm^{-3} and 2.45×10^{21} cm^{-3}, respectively. Using piecewise cubic Hermite interpolation (pchip), plotted in Figure 8.11(a), we determine that the effective masses are 1.124 m_0 and 1.276 m_0 at these concentrations.

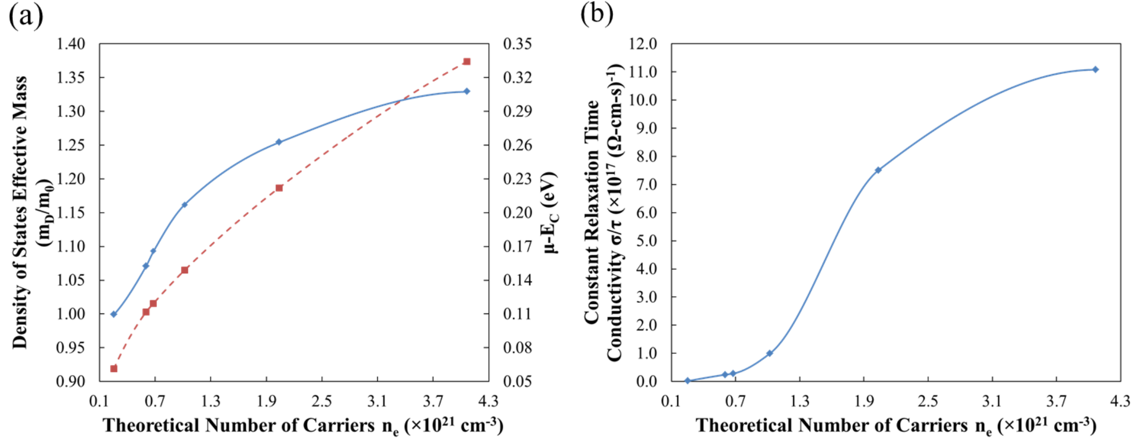

Figure 8.11 (a) The calculated density of states effective mass is plotted as diamonds with interpolation (solid line) and the occupied conduction band width is plotted as squares with interpolation (dashed line), as a function of carrier concentration. (b) Plot of the constant relaxation time conductivity as a function of carriers using a supercell approach with interpolation.

We calculate the Boltzmann conductivity in the constant relaxation time approximation:

$$\frac{\boldsymbol{\sigma}}{\tau} = e^2 \sum_n \int \frac{d\mathbf{k}}{4\pi^3} \mathbf{v}_n(\mathbf{k}) \mathbf{v}_n(\mathbf{k}) \left(-\frac{\partial f}{\partial E} \right)_{E=E_n(\mathbf{k})} \tag{8.3}$$

where n is the band index and the velocity is defined to be the $\mathbf{k}$ derivative of the band energy. We used the BoltzTraP[320] code, which allows for the use of DFT-based band velocities on a dense k-point grid. In order to provide a better density of eigenvalues for the Fourier interpolation used by BoltzTraP, they were recalculated non-self-consistently on k-point grids twice as dense as those originally used and the BoltzTraP interpolation parameter was taken to be at least 20 to ensure convergence. For comparison to measurements, we use the trace of the conductivity tensor. The results are summarized in Table 8.3. Again, by interpolating our calculated values (plotted in Figure

8.11(b)), we can obtain $\frac{\sigma}{\tau}$ at 5 % and 15 % La content which are 4.79×10^{16} (Ω-cm-s)$^{-1}$ and 8.67×10^{17}(Ω-cm-s)$^{-1}$. By using the measured conductivity for the unstrained samples, we can approximate the DC relaxation time τ. These results are summarized in Table 8.3 along with the other interpolated properties. These results show that between 5 % and 15 % La content the relaxation time varies very little and is approximately 1.2×10^{14} s. This value is between that of metals which are considered good conductors (free electron metals) and poor elemental metals of lower conductivity. However, we find an anomalously high value for τ in the case of 25 % La content. In our calculation, we assumed uniform La distribution and despite structural optimization, the cell remained in the cubic symmetry. Given that LSTO is known to undergo a structural phase transition from cubic to orthorhombic symmetry at over 20 % in the bulk[287], this result is indicative that either such a structural transition may occur in epitaxially grown thin films or that there is an onset of some kind of phase separation that affects the microstructure of the films.

La at.%	$\mu(300K)-E_C$ (eV)	m_D/m_0	σ/τ (Ω-cm-s)$^{-1}$	Exp. σ (Ω-cm)$^{-1}$	Relaxation Time τ (s)
5 %	0.132	1.124	4.79×10^{16}	5.56×10^{2}	1.16×10^{-14}
15 %	0.248	1.276	8.67×10^{17}	1.05×10^{4}	1.21×10^{-14}
25 %	0.334	1.329	1.11×10^{18}	3.53×10^{5}	3.19×10^{-13}

Table 8.3 Summary of the transport related properties found using interpolation for comparison to the experimentally measured conductivity.

8.4 SUMMARY

In summary, we have grown La-doped $SrTiO_3$ films with 5, 15 and 25 % dopant concentrations by molecular beam epitaxy. By utilizing four different substrates, $LaAlO_3$,

LSAT, $SrTiO_3$, $DyScO_3$, La-doped $SrTiO_3$ films with various degrees of compressive and tensile strain were synthesized. As La dopant concentration was increased, the unit cell volume of the film generally increased for all strain conditions. For all doping concentrations, the measured carrier concentration was less than the La dopant concentration, with the discrepancy becoming larger, the higher the La concentration. Room temperature resistivities ranging from 10^{-5} to 10^{-2} Ω-cm and Hall mobilities ranging from 1 to 9 $cm^2V^{-1}s^{-1}$ were measured, depending on La concentration and strain. The room temperature mobility of less strained La-doped $SrTiO_3$ was found to be higher than that of more strained La-doped $SrTiO_3$ regardless of the sign of the strain. This suggests that strain engineering may not be beneficial for enhancing the mobility of $SrTiO_3$-based conductive layers for practical, room temperature applications. Ellipsometry measurements confirm the presence of free electron-like carriers in the conduction band as a result of La doping without significant optical absorption in the visible light range and carrier density are derived from plasma frequency and effective mass from theoretical calculations. Theoretical calculations show that the density of states effective mass increases with band occupation, however approaching a plateau at very high concentrations. The theoretical calculations also place the room temperature DC relaxation time to be $\sim 1.2\times 10^{14}$ s. LSTO which is a candidate of transparent conductive oxide can be attractive for optoelectronic device applications. And, LSTO is promising as a quantum metal layer for negative capacitance FET owing to tunable carrier density.

Chapter 9. Transition metal oxide quantum wells

In this chapter, I report on the investigation of $SrTiO_3$ (STO) quantum wells (QWs) grown by molecular beam epitaxy (MBE). The QW structure consists of $LaAlO_3$ (LAO) and STO layers grown on LAO substrate. Structures with different QW thicknesses ranging from two to ten unit cells were grown. Optical properties (complex dielectric function) were measured by spectroscopic ellipsometry (SE) in the range of 1.0 eV to 6.0 eV at room temperature. We observed that the absorption edge was blue-shifted by approximately 0.39 eV as the STO quantum well thickness was reduced to two unit cells (uc). The optical measurements were performed in the group of Dr. Stefan Zollner at New Mexico State University. The high resolution scanning transmission electron microscope (STEM) images were taken by Dr. Qian He and Dr. Albina Y. Borisevich at the Oak Ridge National Laboratory.

9.1 INTRODUCTION

In recent years, owing to advances in layer-by-layer growth techniques, it has become possible to grow high quality transition metal oxide films with atomic-scale precision and to fabricate artificial structures based on these complex materials. This in turn enabled band engineering, interface manipulation and dimensional control in oxide heterostructures. By controlling the layer thickness and interface chemistry, unique phenomena with no bulk analogues have been demonstrated. For example, in $LaAlO_3$ (LAO)/$SrTiO_3$ (STO) heterostructures[181] a two dimensional electron gas (2DEG) was reported at the interface when the thickness of the LAO layer grown on the TiO_2-terminated STO substrate is more than 4 unit cells (uc) thick[321]. In $LaTiO_3$ (LTO)/STO heterostructures, two dimensional superconductivity[194] exists at the interface, in which Tc

can be tuned by electrostatic gating in the temperature range from 200 mK to 0 K[322]. Oxide heterostructures have properties that can be quite different from the parent bulk phases. In particular, oxide heterostructures have demonstrated conductivity enhancement[323], new optical absorption bands[324], interfacial magnetic ordering[189], and various forms of electronic reconstruction[192].

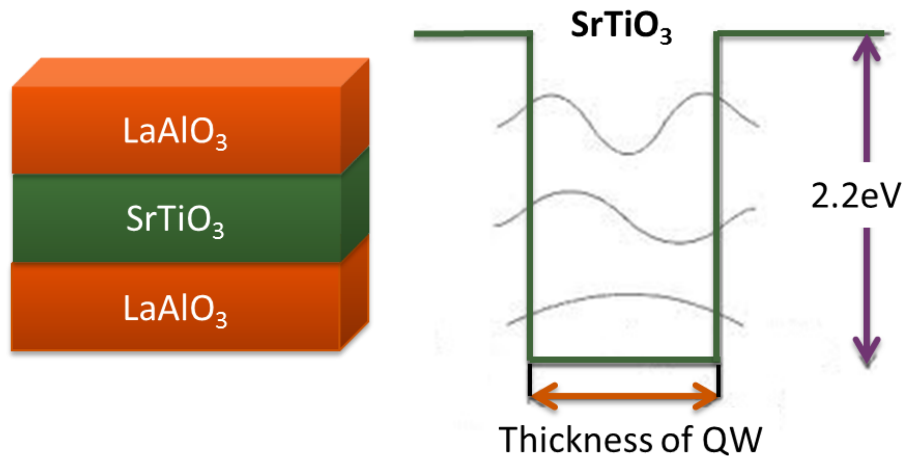

Figure 9.1 The quantum well structure consisting of $LaAlO_3$ and $SrTiO_3$

After a single heterointerface, the simplest heterostructure is a quantum well. In a one-dimensional QW, the electronic wave functions are confined along one of the three directions. Such confinement can be achieved by alternating layers of materials with a large band discontinuity. For example, this can be done for GaAs and AlAs or STO and LAO. One can then manipulate the degree of confinement of the electronic states by adjusting the well thickness. Semiconductor QW structures are widely used in multiple device applications such as quantum cascade lasers[325], laser diodes[326] and high-performance transistors[327]. The QWs of transition metal oxides are very attractive for two

reasons. First, the large band offsets on the order of several electron volts, offer an unprecedented degree of quantum confinement. Second, interesting and unusual phenomena are expected because of correlation effects of the d-electrons of transition metals. Figure 9.1 shows a schematic view of the QW system comprised of LAO and STO. In STO, the transition metal, titanium, is at the center of the oxygen octahedron. The conduction band bottom is formed by the Ti t_{2g} orbitals and in the bulk is triply degenerate. At the interface with LAO the degeneracy of Ti t_{2g} orbitals is lifted, with the d_{xy} band shifting to lower energy[328]. When the STO QW thickness is decreased, the entire conduction band starts feeling the effects of confinement. This confinement causes the band structure to develop sub-bands corresponding to the quantum well levels. By controlling the QW thickness, one can manipulate the number of quantized energy levels in the well and energy separation between them.

The interplay between the d-electron correlation and lowering of orbital symmetry due to confinement may give rise to unique quantum states not observed in the bulk. For example, a metal-to-insulator transition in $SrVO_3$ (SVO)/Nb:$SrTiO_3$ quantum wells was observed by Yoshimatsu *et al.* using photoemission spectroscopy when the SVO layer thickness was reduced to two uc[329]. In their later work, they also found evidence of metallic quantum well states that showed dispersion of subbands[276]. In the $LaTiO_3$ (LTO)/LAO system[330] quantum confinement was demonstrated by measuring interband transitions using optical absorption. Reducing the LTO layer thickness confines the electron motion along the z direction, making the band more anisotropic. As the LTO thickness is further decreased, the degeneracy of the Ti t_{2g} orbitals is lifted with a signature of that being observable in the interband transitions. The $GdTiO_3$ (GTO)/$SrTiO_3$/$GdTiO_3$ QW exhibits hysteresis in the magnetoresistance as a result of the

interfacial proximity effect due to the ferrimagnetic nature of GTO, even though STO does not have a magnetic moment[331].

In the present study, we investigated LAO/STO QW structures on LAO substrates. Compared to semiconductor-based QWs, where constituent materials have band gaps on the order of 1.0 eV thus limiting the band offset, transition metal oxide quantum wells can have rather large barriers. STO has a 3.2 eV band gap and LAO has a 5.6 eV band gap, and as the valence band maxima have similar energy levels (the valence band offset is only 0.2 eV[332]), the conduction band offset between the two materials is about 2.3 eV. For comparison, the conduction band offset between GaAs and AlAs is slightly under 1.0 eV[333].

When the thickness of a QW is reduced, only a limited number of the quantized energy levels can exist inside the QW. These quantized energy levels can be detected by optical measurements when they are unoccupied. Therefore, by controlling the thickness of the STO QW layer, we expect to observe modulation of the optical transition energies from the ellipsometric measurements. In order to perform this study, we grew STO layers with a thickness varying from two (approximately 8 Å) to ten (approximately 40 Å) unit cells on LAO substrate followed by a seven unit cell thick LAO capping layer to form a well. The structures are characterized by *in situ* reflection high-energy electron diffraction (RHEED), and *in situ* X-ray photoemission spectroscopy (XPS). The surface roughness of the grown QW structures was measured by *ex situ* atomic force microscopy (AFM). We investigated the changes in the complex dielectric function ε as a function of the $SrTiO_3$ layer thickness using spectroscopic ellipsometry (SE) at room temperature. The dielectric function ε was measured from 1.0 eV to 6.0 eV. We observed that the absorption edge of a two unit cells thick STO QW was shifted by 0.39 eV toward higher energy, compared to bulk STO.

9.2 EXPERIMENT

The LAO substrates were introduced into a customized DCA 600 MBE system with a base pressure of 3×10^{-10} Torr. The substrate was outgassed at 800 ^{o}C for 1 hour in an oxygen partial pressure of 3×10^{-7} Torr to remove surface contamination. The STO QW and LAO capping layers were grown by MBE using effusion cells for the metal evaporation and molecular oxygen as the oxidant. The fluxes of Sr, Ti, Al, and La were calibrated to be 1 ML/min using a quartz crystal monitor with feedback from *in situ* XPS. STO films were deposited on LAO (001) substrates using a layer-by-layer alternating shuttering method of Sr and Ti. The shuttering cycle was repeated until the desired thickness was reached. All the films grown were terminated with a TiO_2 monolayer. STO films were grown under identical conditions at 700 ^{o}C growth temperature with a total oxygen pressure of 1×10^{-6} Torr. The STO film thicknesses grown were 10 uc, 5 uc and 2 uc. Here, 1 uc of STO is 3.905 Å and 1 uc of LAO is 3.79 Å. In the case of 2 uc STO film, we grew a five-repeat superlattice, $[(LAO)_7(STO)_2]_5$, on the LAO substrate. After the STO film growth, an LAO film with a thickness of 7 uc was deposited using shuttering of the La and Al sources at 750 ^{o}C growth temperature under a total oxygen pressure of 1×10^{-6} Torr. This capping layer was terminated with an AlO_2 layer. After deposition, the film was left in the same oxygen pressure used for the growth and held for 10 minutes. The structure then was cooled down to room temperature at a rate of 30 ^{o}C/min in the same oxygen pressure. The film was monitored during growth by *in situ* RHEED and the surface roughness of the film was measured by *ex situ* AFM. An atomic resolution cross-section image was taken by a field emission STEM. The dielectric functions of STO QWs on LAO were determined using spectroscopic ellipsometry from 1.0 to 6.5 eV at 300 K. The depolarization spectra are small, indicating good uniformity

of the samples. To model the ellipsometric angles of these samples, tabulated optical constants for the LAO substrate were used.

9.3 RESULTS

9.3.1 Crystallinity, stoichiometry and surface morphology

Figure 9.2(a) shows RHEED patterns of a 7 uc LAO/10 uc STO structure on LAO. From the RHEED patterns, we see that the film exhibits excellent crystallinity.

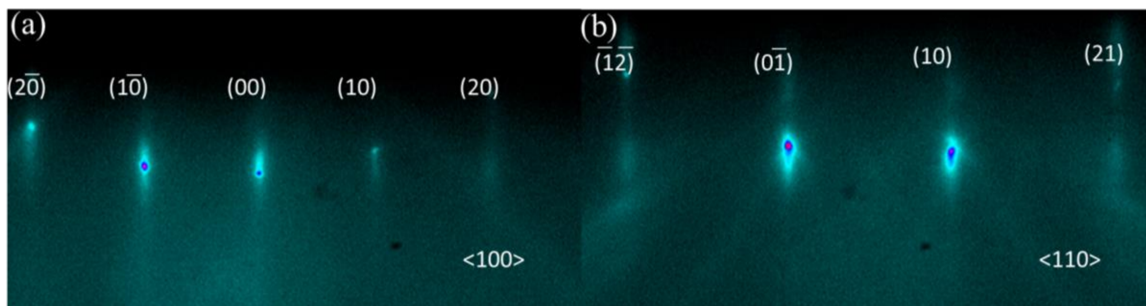

Figure 9.2 The RHEED patterns of 7 uc LAO/10 uc STO on LAO along (a) <100>, and (b) <110> directions.

Figure 9.3 shows the XPS spectra from the same structure. The compositions of the LAO and STO layers were determined by *in situ* XPS. The survey scan in Figure 9.4(a) was performed to investigate the elemental composition and carbon contamination. There is no detectable carbon from the survey scan. High resolution spectra of the Sr 3d, Ti 2p, La 3d, and Al 2p were measured for each sample and typical set of spectra is shown in Figure 9.4(b-e). Because the film is thin, intensity from the LAO substrate interferes with the La 3d and Al 2p spectra from the LAO overlayer. Therefore, we first grew thick single layer LAO films on STO substrate and confirmed the stoichiometry using *in situ* XPS prior to growing the quantum well structure. Due to the energy

dependence of the electron escape depth, the measured integrated intensity was modified using the appropriate energy exponent with the CasaXPS program[119].

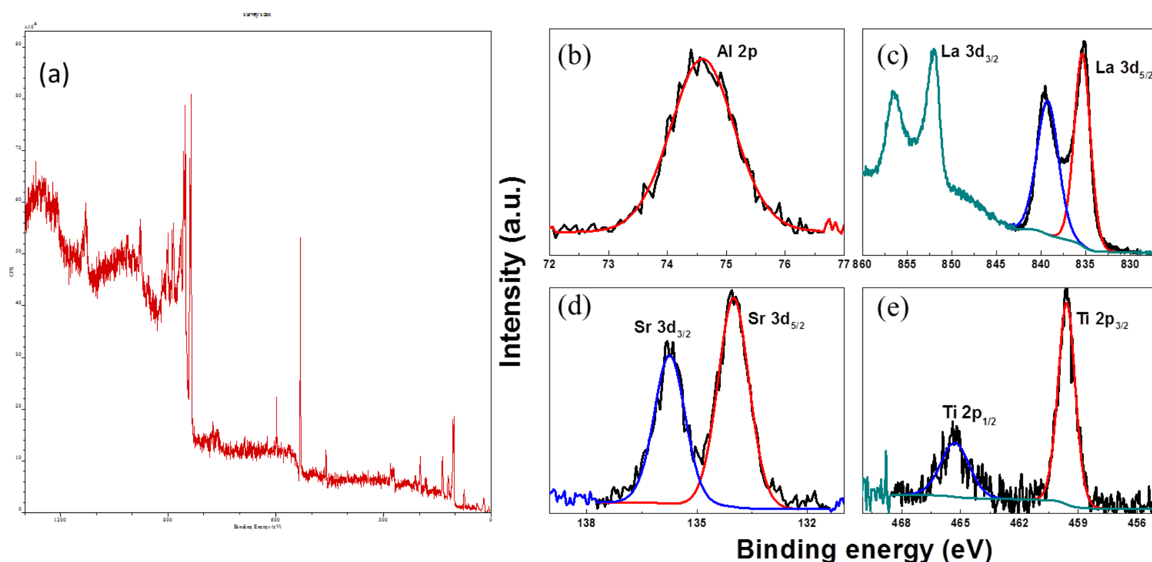

Figure 9.3 (a) Survey scan and representative core level spectra of (b) Al 2p, (c) La 3d, (d) Sr 3d, and (e) Ti 2p from 7 uc LAO/10 uc STO on LAO using *in situ* XPS.

The high angle annular dark field (HAADF) image, obtained in the STEM mode (Z-contrast), of a 7 uc LAO/10 uc STO on LAO is shown in Figure 9.4(a,b). This image confirms that the LAO/STO structure was grown epitaxially and commensurate on the LAO substrate. Because the STO film is very thin, it is clamped to the LAO substrate and the in-plane lattice constant of the STO film is the same as that of the LAO substrate. The STO film on LAO substrate experiences compressive strain due to the lattice mismatch of -2.9 %. Using the Poisson's ratio of bulk STO[304], the out-of-plane lattice constant is expected to be 3.968 Å. However, the out-of-plane lattice constant measured from the STEM image is 4.09 Å (Figure 9.4(c)), indicating an anomalous out of plane expansion in the STO layer. Figure 9.4(d) shows the Z-contrast STEM image of the 7 uc LAO/5 uc

STO on LAO. This STEM image shows less surface grooves than in the 7 uc LAO/10 uc STO on LAO. A possible explanation is that the 10 uc thick STO QW is partially relaxed and the LAO capping layer, being under some tensile strain, is trying to form islands (a Stranski-Kranstanov growth mode). However, the 5 uc thick STO QW is thin enough to be fully strained to the LAO substrate and the LAO capping layer is not under any strain and as a result has a smooth surface.

Figure 9.5 shows the AFM image of a 7 uc LAO/5 uc STO structure on LAO. The film surface has a root mean square (RMS) roughness of 0.13 nm, as determined from a 5 μm×5 μm scan area (Figure 9.5(a)). The LAO/STO film is shown to grow conformally to the substrate as the terraces and the steps of the LAO substrate are clearly observed in the AFM image in Figure 9.5(a). Surface grooves are not observed in AFM. Because the LAO substrate itself has twinning domains, we also observe twinning domains from the sample when we measured the film surface using a larger 10 μm×10 μm scan area as shown in Figure 9.5(b). The surface roughness determined from the 10 μm×10 μm scan area is 0.44 nm. The surface roughness from the larger scan area is used for the modeling and analysis of the ellipsometry data.

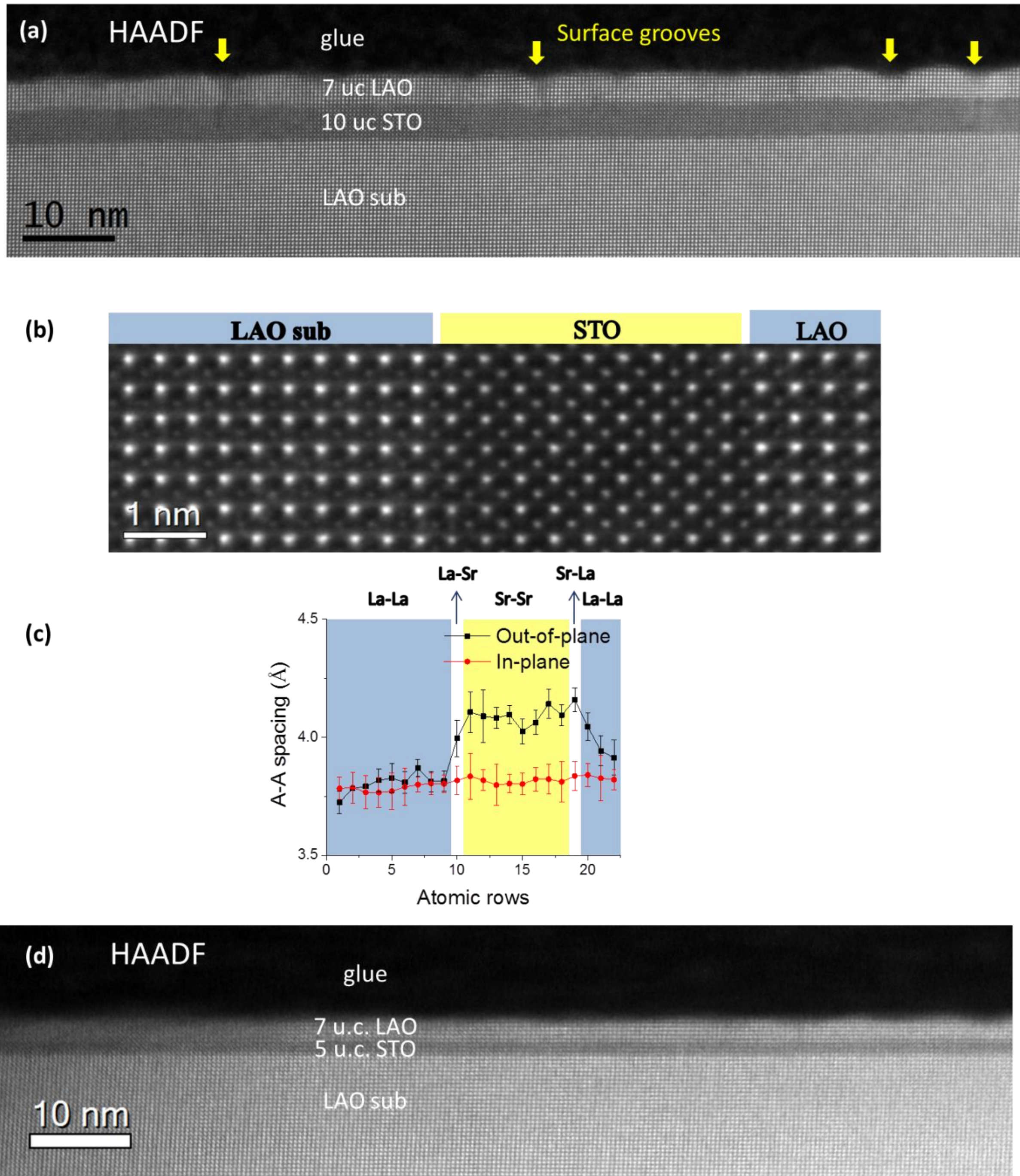

Figure 9.4 (a-b) Z-contrast STEM image of a 7 uc LAO/10 uc STO structure on LAO, (c) the spacing of the A-site atoms (Sr or La) and (d) Z-contrast STEM image of a 7 uc LAO/5 uc STO structure on LAO

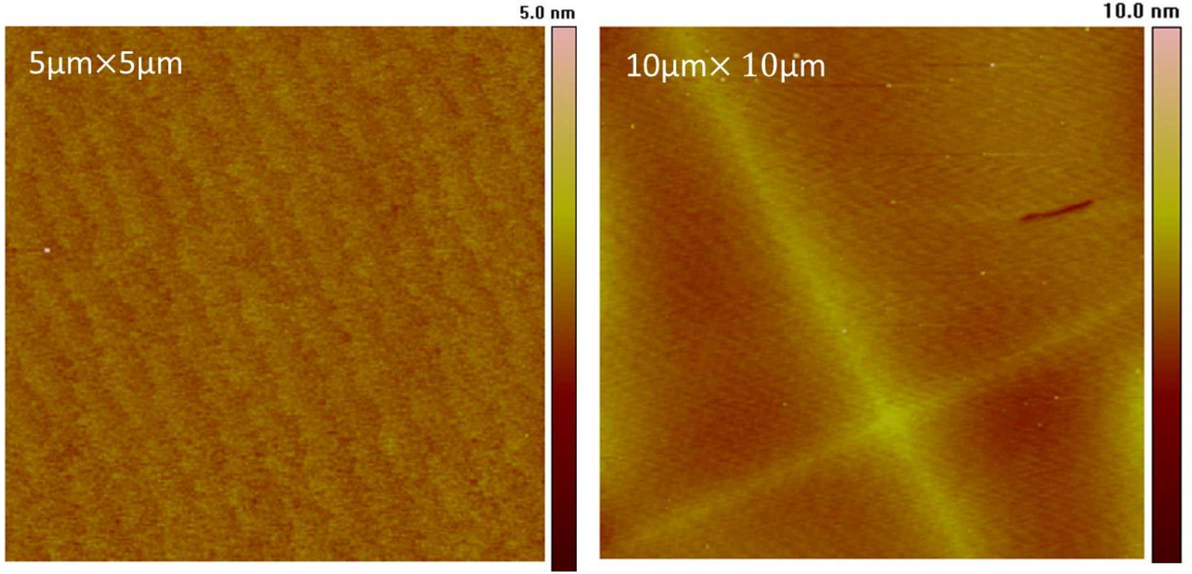

Figure 9.5 AFM images of 7 uc LAO/5 uc STO on LAO (a) 5 μm × 5 μm, and (b) 10 μm × 10 μm

9.3.2 Band alignment of the STO QW

Figure 9.6(a) shows the energy band alignment of the STO/LAO system. To determine the valence band offset (VBO, ΔE_{VBO}) and conduction band offset (CBO, ΔE_{CBO}) of the STO/LAO system, core-level (CL) X-ray photoemission was performed[334]. The equations to calculate the VBO and CBO are as follows:

$$\Delta E_{VBO} = (E_{Sr\ 3d} - E_{VBM})_{STO} - (E_{La\ 4d} - E_{VBM})_{LAO} - (E_{Sr\ 3d} - E_{La\ 4d})_{\text{LAO film on STO}}$$

$$\Delta E_{CBO} = E_{g,LAO} - E_{g,STO} - \Delta E_{VBO},$$

where $(E_{Sr\ 3d} - E_{VBM})_{STO}$ is the energy difference between the Sr 3d CL and valence band maximum (VBM) of the STO substrate; $(E_{La\ 4d} - E_{VBM})_{LAO}$ is the energy difference between the La 4d CL and VBM of the LAO substrate; $(E_{Sr\ 3d} - E_{La\ 4d})_{\text{LAO film on STO}}$ is the

energy difference between the Sr 3d and La 4d CLs measured in the thin LAO film on STO substrate; and $E_{g,LAO}$ and $E_{g,STO}$ are the band gaps of LAO and STO, respectively.

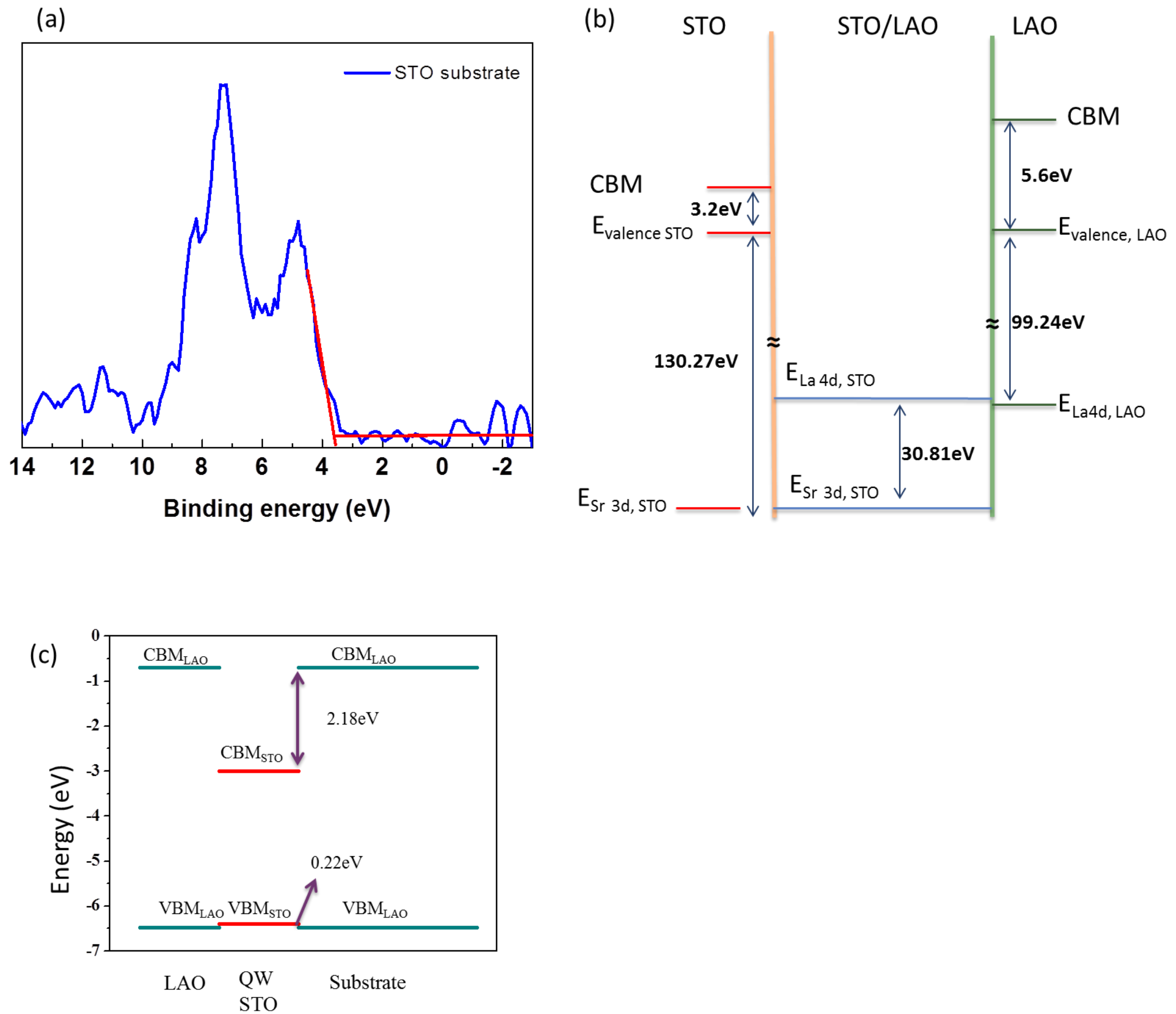

Figure 9.6 (a) XPS valance band spectrum of the STO substrate. The red line indicates the linear extrapolation to determine the VBM energy. (b) The energy band diagram of bulk STO and bulk LAO, and a thin LAO film on Nb-STO, as determined using XPS. (c) The calculated energy band alignment across the LAO/STO/LAO quantum structure.

To determine the VBO, we used STO, and LAO substrates, and a thin (4 uc) LAO film grown on Nb-doped STO substrate. Each valence band maximum (VBM) was determined by linear extrapolation of the leading edge of the valence band spectra in Figure 9.6(a). From the STO substrate, the Sr $3d_{5/2}$ peak and VBM of STO substrate were measured to be at 134.0 eV and 3.73 eV, respectively. The energy difference between the Sr $3d_{5/2}$ and VBM was 130.27 eV. The La $4d_{5/2}$ peak and VBM of LAO substrate were measured to be at 102.68 eV and 3.44 eV, leading to an energy difference of 99.24 eV. For the last term of the VBO equation, we used a 4 uc LAO film on the Nb-STO substrate (0.5 wt.%, CrysTec GmbH, Germany, the carrier concentration is 1.6×10^{20} cm^{-3}) to determine the CL energy difference between Sr $3d_{5/2}$ and La $4d_{5/2}$. We determined the energy difference to be 30.81 eV between Sr $3d_{5/2}$ and La $4d_{5/2}$ from LAO thin film on Nb-STO. From these measured energy positions (see Figure 9.6(b)), we calculate the VBO to be 0.22 eV. This value is in good agreement with theory[332]. The CBO is determined to be 2.18 eV by using the experimental band gaps of 5.6 eV for LAO ($E_{g, LAO}$)[335] and 3.2 eV for STO ($E_{g, STO}$)[16,336]. The band alignment across the LAO/STO/LAO QW structure is shown in Figure 9.6(c).

9.3.3 Optical properties of STO QW

After we checked the film roughness and the crystallinity of the films, the optical properties of the STO QW structure were measured using spectroscopic ellipsometry (SE). The complex dielectric functions were measured as a function of energy from 1.0 eV to 6.0 eV at room temperature.

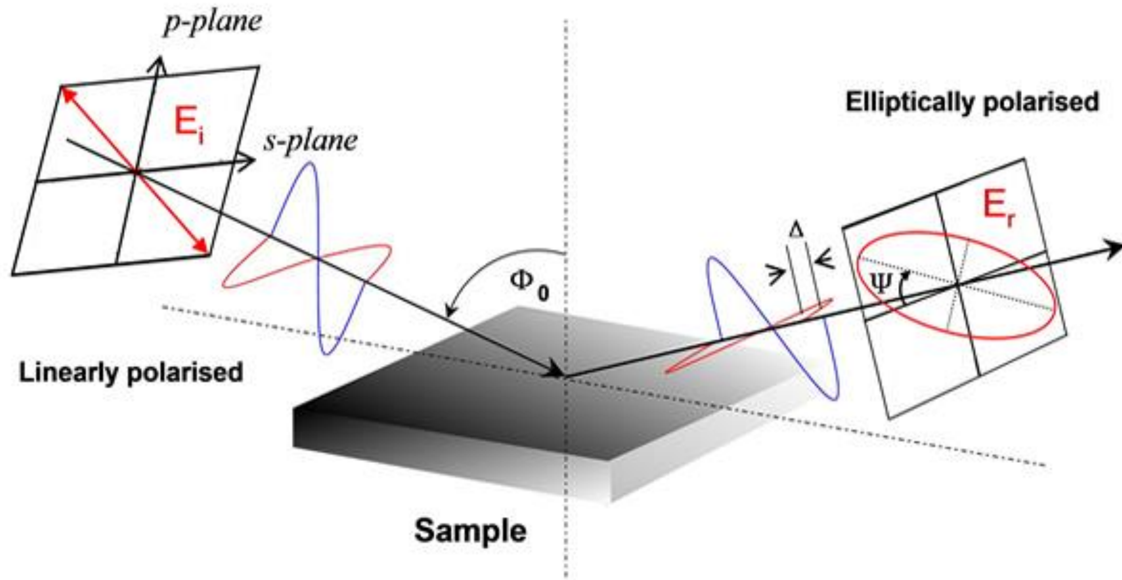

Figure 9.7 Schematic diagram of the principle of ellpsometry[337]

Spectroscopic ellipsometry measures the complex Fresnel ratio

$$\rho = \frac{r_p}{r_s} = \tan\psi e^{i\Delta}, \tag{9.1}$$

which is the ratio of the p-polarized reflectance r_p to the s-polarized reflectance r_s. ρ is usually expressed in terms of the ellipsometric angles ψ and Δ(see Figure 9.7). For a bulk sample with complex refractive index n, ρ is given by[299,338]

$$\rho = \frac{(n\cos\phi_0 - \cos\phi_1)(\cos\phi_0 + n\cos\phi_1)}{(n\cos\phi_0 + \cos\phi_1)(\cos\phi_0 - n\cos\phi_1)} \tag{9.2}$$

where ϕ_0 is the angle of incidence and ϕ_1 the angle of refraction as given by Snell's Law. The imaginary part of the dielectric function $\varepsilon = n^2$ is related to absorption in the sample by elementary excitations. For example, the absorption in the infrared (IR) spectral region is given by lattice absorption of infrared-active phonons or the free-carrier

response in a metal. In the visible and UV spectral region, the absorption is due to interband electronic transitions.

In the case of a thin film on a substrate, we can still invert Equation (9.2) to calculate $\langle n \rangle$ and $\langle \varepsilon \rangle = \langle n \rangle^2$, but these quantities are no longer related to the optical constants of a specific material. Instead, $\langle n \rangle$ and $\langle \varepsilon \rangle$ are determined by the optical constants of the film and the substrate along with the film thickness and surface and interface roughness. Therefore, $\langle n \rangle$ and $\langle \varepsilon \rangle$ are called the pseudo-refractive index and the pseudo-dielectric function. If the dielectric function ε_s of the substrate and the film thickness are known, then the dielectric function ε_f of the film can be determined by fitting the experimental data using well-established procedures[299,338] and commercial software (J.A. Woollam Co., Inc., WVASE32). Surface roughness can also be considered within this approach.

The absorption coefficient α can be expressed as $\alpha = 4\pi k/\lambda$ where k is the extinction coefficient and λ is the wavelength. The extinction coefficient k can be calculated using the dielectric indices (ε_1 and ε_2) with the equation, $k = \{\frac{1}{2}\left[(\varepsilon_1^2 + \varepsilon_2^2)^{\frac{1}{2}} - \varepsilon_1\right]\}^{1/2}$. Therefore, we can extract the absorption coefficient α from SE data and then plot α^2 versus photon energy for bulk STO and the QW STO structure (Figure 9.8). The direct band gap was determined by extrapolation of the plot near 3.8 eV to zero intensity. The intercept at the x-axis corresponds to the direct band gap (see Figure 9.8(a)). The onset of the absorption in bulk STO was found to be 3.78 eV. From the fitting of $\sqrt{\alpha}$ versus photon energy, the intercept of a straight line fit from the extrapolation near 3.2 eV gives a value of 3.26 eV, which is the indirect band gap of bulk STO. These values are similar to standard reference values[339]. For the data obtained from the QW structures, we applied the same plotting method to find the direct band gap. As the STO QW thickness was decreased from 10 to 5, and finally to 2 uc, the onset of direct absorption was blue-shifted

by 0.19 eV for 10 uc, 0.26 eV for 5 uc and 0.39 eV for 2 uc, compared to that of STO bulk.

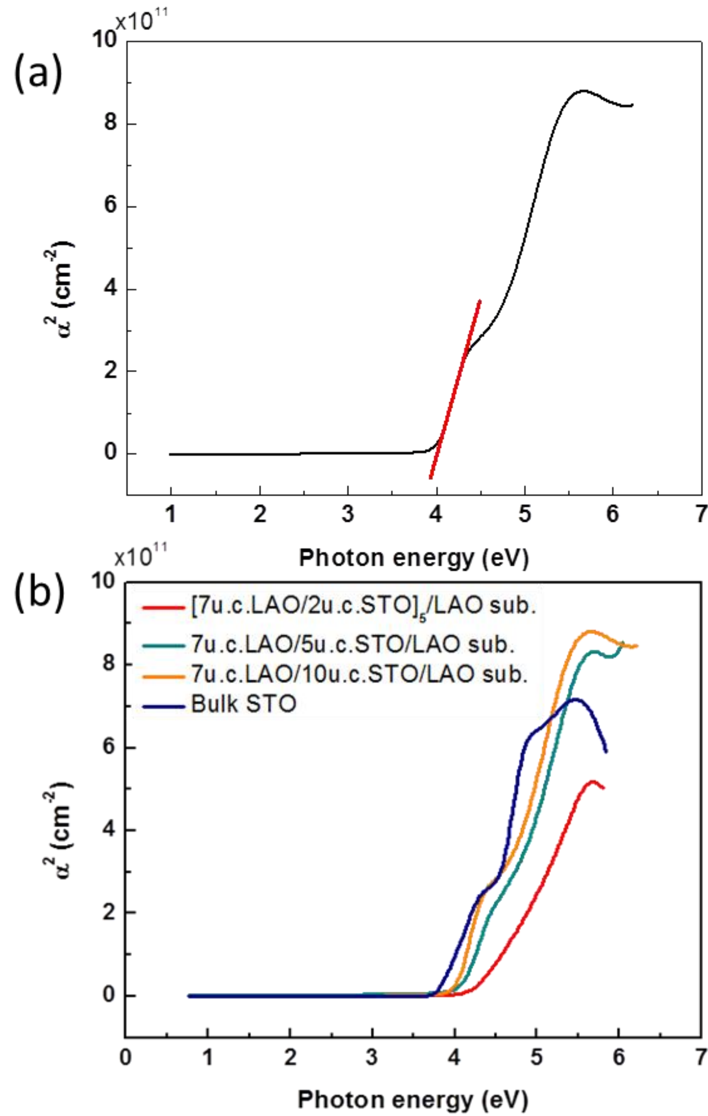

Figure 9.8 (a) Square of the absorption coefficient of 10 uc QW STO plotted as a function of photon energy. The red line is the linear extrapolation to determine the onset of the absorption coefficient. (b)Square of the absorption coefficient of STO vs photon energy for bulk STO and for STO QW structures.

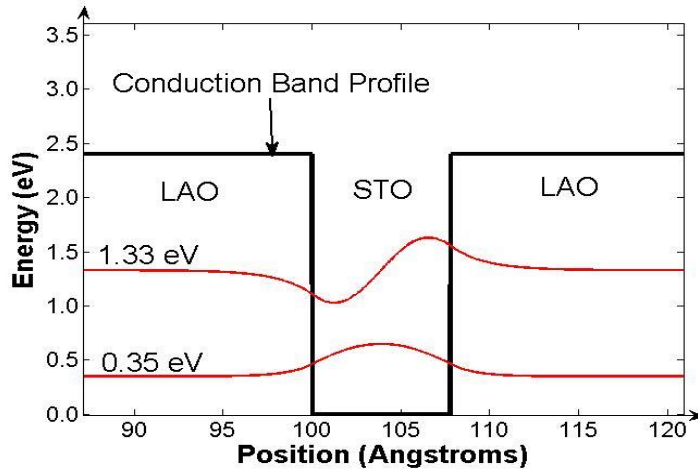

Figure 9.9 Quantized states of a two unit cell thick STO QW (Poisson-Schrödinger modeling by Matthew Bucher in the Demkov group).

As shown in Figure 9.9 the first two quantized states of the STO QW are shifted up when the QW size is reduced. Reducing the thickness to two unit cells, the first quantized state is shifted up by 0.35 eV. α^2, which corresponds to inter-band transitions in Figure 9.6 shows a similar shift. S. A. Chamber[340] reported that the intermixing of cations (La↔Sr for A site and Al↔Ti for B-site) leads to n-type doping of the STO. The conductivity of n-type doped STO can be confirmed by the presence of a Drude tail from spectroscopic ellipsometry. However, as there was no Drude tail in the quantum well samples, the blue shift we observe is derived from the quantum confinement effect, not from the Burstein-Moss shift[311].

9.4 Conclusions

In summary, we have investigated LAO/STO quantum wells grown by MBE. The film quality was confirmed by *in situ* RHEED, and *ex situ* STEM and AFM. Using *in situ* XPS, the band alignment of this quantum well system, was found to have a VBO of 0.22 eV and a CBO of 2.18 eV. Thus, a deep potential well is formed across the conduction

band. As the width of the quantum well is reduced from 10 uc to 2 uc, optical measurements confirm that the absorption edge is blue-shifted by 0.39 eV.

Chapter 10. Conclusions and outlook

10.1 Zintl templates on Si (001)

In Chapters 4 and 5, I investigated the evolution of the atomic and electronic structures of the surface of Si (001) induced by submonolayer Sr and Ba using RHEED and XPS/UPS. I observed various surface reconstructions from 2×3 to 2×1 when Sr or Ba were deposited on Si (001) up to 0.5 ML. I also observed the bulk core level of Si 2p to shift toward higher binding energies by 0.39 eV and 0.49 eV as 1/2 ML Ba and Sr, respectively, is deposited. This shift was also observed in the valence band spectra indicating a charge transfer effect. According to the DFT calculation, this shift comes from the electronic structure changes in Si induced by Sr 4d or Ba 5d electrons. The surface gap of Si (001) is related to a covalent interaction between the Si dangling bonds and Sr or Ba orbitals. Because Ba has less interaction with Si compared to that of Sr with Si, the surface gap is different between Sr on Si and Ba on Si, resulting in different shifts of the Si core level.

The study of this template is very important because the template enables the growth of epitaxial oxides on Si and prevents the oxidation of Si during the initial stages of growth. The template addresses the fundamental problem of how to protect the Si surface from oxidation while maintaining the Si surface crystal structure. The detailed mechanism of how the template does this is still unclear. A possible extension of this work would be the study of the mechanism of how Zintl templates inhibit the oxidation of Si and what the limits of this oxidation protection are with regard to the substrate temperature and oxygen partial pressure. The understanding of the Zintl template would help to better control the growth process for oxide growth on Si and allow for more types of oxides to be epitaxially grown directly on silicon.

10.2 Epitaxial growth and the relaxation behavior of $SrTiO_3$ films on Si (001)

In Chapter 6, I studied how epitaxial $SrTiO_3$ films relax on Si (001) as they are annealed in oxygen. I grew $SrTiO_3$ films on Si (001) using the Sr template. After $SrTiO_3$ film growth, the annealing was performed under different annealing temperatures and oxygen partial pressures. As the annealing temperature and oxygen partial pressure are increased, the interfacial SiO_2 thickness was observed to increase as well. Correspondingly, the in-plane lattice constant of the $SrTiO_3$ film was observed to decrease. I concluded that the increased SiO_2 thickness facilitates the decoupling of the $SrTiO_3$ film from Si and the $SrTiO_3$ films on Si (001) progressively relaxes to its unstrained bulk structure. Understanding the relaxation mechanism and behavior are important because $SrTiO_3$ on Si is a useful pseudo-substrate for the deposition of other functional oxides and this relaxation effect could be used for strain engineering. In the case of very high annealing temperature and high oxygen partial pressures, however, we find that the interface between $SrTiO_3$ and Si is ultimately destroyed. As mentioned in Chapter 6, the RHEED pattern becomes worse for longer annealing times. An open question is how fast Sr or Ti diffuses down through the SiO_2 layer and what by-products are produced under extreme annealing conditions. This understanding would be helpful for device fabrication processing in order to find the oxygen partial pressure and/or annealing time window necessary to get high quality layers without compromising the interface.

10.3 Structural, optical and electrical properties of strained La-doped $SrTiO_3$ films

I have grown La-doped $SrTiO_3$ films with 5, 15 and 25 % dopant concentrations by molecular beam epitaxy. By utilizing four different substrates, $LaAlO_3$, LSAT,

$SrTiO_3$, $DyScO_3$, La-doped $SrTiO_3$ films with various degrees of compressive and tensile strain were fabricated. I expected to observe improvements in the electrical properties due to strain but it turns out that the strain in La-doped $SrTiO_3$ for the very high doping concentrations I considered may not be beneficial for enhancing the mobility. I have attempted to obtain the number of electrons in the material from the measured La concentrations. However, "fully activated" La-doped $SrTiO_3$ films at high doping concentrations (up to 25 %) were not achieved. Therefore, for future study, it would be necessary to understand why La is not "fully activated" and what would cause this phenomenon. Even if not "fully activated", this La-doped $SrTiO_3$ conductive layer is an excellent candidate for the quantum metal layer in a quantum metal field effect transistor (QMFET). This work can be extended by actually making the device for the QMFET application.

10.4 Optical properties of transition metal oxide quantum wells

In quantum well (QW) systems, one can manipulate the degree of confinement of electronic states by adjusting the layer thicknesses to the level of a single atomic layer. By reducing the thickness of oxide layers in heterostructures, new electronic and optical properties can emerge. My work is related to the study of oxide quantum well systems (STO/LAO) using spectroscopic ellipsometry. By controlling the thickness of the STO quantum well layer, I observed modulation of the optical transition energies from ellipsometric measurements of the absorption of light between empty quantized states as well as changes in the real $\varepsilon 1$ and imaginary ε_2 parts of the complex dielectric function spectra. This work is an extension of monolithic integration of oxides on Si. Based on the novel properties of QW systems, an all-oxide quantum well laser, with a much wider degree of tunability, could be a possible application. For further study, by doping the

STO quantum well layer with Nb or La, band filling and dispersion of partially occupied quantized states could be observed using ARPES. In the LTO/LAO system the effect of quantum confinement on the Mott insulator nature of the LTO layer could also be studied.

Throughout this thesis, I explored how to approach the monolithic integration of perovskite oxides on Si and its possible applications. In summary, I described four main subjects: (1) the Zintl template for the growth of perovskite oxids on Si, (2) $SrTiO_3$ growth and relaxation behavior after annealing in oxygen environment at different annealing temperature, (3) electrical and structural properties of strained La-doped $SrTiO_3$, and (4) the optical properties of QW $SrTiO_3$ on $LaAlO_3$. Through these studies, many of the fundamental questions are addressed for future applications. For further development, it would be necessary to obtain a better understanding of the fundamental questions addressed in this thesis and to be able to fabricate the various layers of functional perovskites on Si without degrading their unique properties.

References

[1] S. Datta, Electrochem. Soc. Interface **22,** 41 (2013).

[2] A. I. Kingon, J.-P. Maria, and S. Streiffer, Nature **406,** 1032 (2000).

[3] W. Eerenstein, N. Mathur, and J. Scott, Nature **442,** 759 (2006).

[4] A. Bokov and Z.-G. Ye, in *Frontiers of Ferroelectricity* (Springer, 2007), p. 31.

[5] C. Zener, Phys. Rev. **82,** 403 (1951).

[6] D. Murphy, S. Sunshine, R. Van Dover, R. Cava, B. Batlogg, S. Zahurak, and L. Schneemeyer, Phys. Rev. Lett. **58,** 1888 (1987).

[7] A. P. Ramirez, Journal of Physics-Condensed Matter **9,** 8171 (1997).

[8] Y. Tokura, Y. Taguchi, Y. Okada, Y. Fujishima, T. Arima, K. Kumagai, and Y. Iye, Phys. Rev. Lett. **70,** 2126 (1993).

[9] D. B. Fenner, A. M. Viano, D. K. Fork, G. A. N. Connell, J. B. Boyce, F. A. Ponce, and J. C. Tramontana, J. Appl. Phys. **69,** 2176 (1991).

[10] C. Ziegler, F. Baudenbacher, H. Karl, H. Kinder, and W. Göpel, Anal. Bioanal. Chem. **341,** 308 (1991).

[11] K. J. Hubbard and D. G. Schlom, Journal of Materials Research **11,** 2757 (1996).

[12] T. Tambo, T. Nakamura, K. Maeda, H. Ueba, and C. Tatsuyama, Jpn. J. Appl. Phys. **37,** 4454 (1998).

[13] H. Mori and H. Ishiwara, Jpn. J. Appl. Phys. **30,** L1415 (1991).

[14] R. A. McKee, F. J. Walker, and M. F. Chisholm, Phys. Rev. Lett. **81,** 3014 (1998).

[15] S. A. Chambers, Y. Liang, Z. Yu, R. Droopad, J. Ramdani, and K. Eisenbeiser, Appl. Phys. Lett. **77,** 1662 (2000).

[16] S. Zollner, A. A. Demkov, R. Liu, P. L. Fejes, R. B. Gregory, P. Alluri, J. A. Curless, Z. Yu, J. Ramdani, R. Droopad, T. E. Tiwald, J. N. Hilfiker, and J. A. Woollam, J. Vac. Sci. Technol., B **18,** 2242 (2000).

[17] G. Niu, G. Saint-Girons, B. Vilquin, G. Delhaye, J.-L. Maurice, C. Botella, Y. Robach, and G. Hollinger, Appl. Phys. Lett. **95,** 062902 (2009).

[18] K. Zhao, Y. Huang, Q. Zhou, K.-J. Jin, H. Lu, M. He, B. Cheng, Y. Zhou, Z. Chen, and G. Yang, Appl. Phys. Lett. **86,** 221917 (2005).

[19] A. Posadas, M. Berg, H. Seo, A. de Lozanne, A. A. Demkov, D. J. Smith, A. P. Kirk, D. Zhernokletov, and R. M. Wallace, Appl. Phys. Lett. **98,** 053104 (2011).

[20] A. Lin, X. Hong, V. Wood, A. Verevkin, C. Ahn, R. McKee, F. Walker, and E. Specht, Appl. Phys. Lett. **78,** 2034 (2001).

[21] B. Qu, M. Evstigneev, D. Johnson, and R. Prince, Appl. Phys. Lett. **72,** 1394 (1998).

[22] L. Largeau, G. Patriarche, G. Saint-Girons, G. Delhaye, and G. Hollinger, Appl. Phys. Lett. **92,** 031904 (2008).

[23] C. Dubourdieu, J. Bruley, T. M. Arruda, A. Posadas, J. Jordan-Sweet, M. M. Frank, E. Cartier, D. J. Frank, S. V. Kalinin, and A. A. Demkov, Nat. Nanotechnol. **8,** 748 (2013).

[24] Z. Trajanovic, C. Kwon, M. Robson, K. C. Kim, M. Rajeswari, R. Ramesh, T. Venkatesan, S. Lofland, S. Bhagat, and D. Fork, Appl. Phys. Lett. **69,** 1005 (1996).

[25] R. J. Hamers, R. M. Tromp, and J. E. Demuth, Phys. Rev. B **34,** 5343 (1986).

[26] R. A. Wolkow, Phy. Rev. Lett. **68,** 2636 (1992).

[27] A. Vailionis, H. Boschker, W. Siemons, E. P. Houwman, D. H. A. Blank, G. Rijnders, and G. Koster, Phys. Rev. B **83,** 064101 (2011).

[28] D. G. Schlom, L.-Q. Chen, C. J. Fennie, V. Gopalan, D. A. Muller, X. Pan, R. Ramesh, and R. Uecker, MRS Bulletin **39,** 118 (2014).

[29] V. Gopalan and D. B. Litvin, Nat Mater **10,** 376 (2011).

[30] H. Seo, A. Posadas, and A. A. Demkov, Phys. Rev. B **86,** 014430 (2012).

[31] J. H. Lee, L. Fang, E. Vlahos, X. Ke, Y. W. Jung, L. F. Kourkoutis, J.-W. Kim, P. J. Ryan, T. Heeg, M. Roeckerath, V. Goian, M. Bernhagen, R. Uecker, P. C. Hammel, K. M. Rabe, S. Kamba, J. Schubert, J. W. Freeland, D. A. Muller, C. J. Fennie, P. Schiffer, V. Gopalan, E. Johnston-Halperin, and D. G. Schlom, Nature **466,** 954 (2010).

[32] P. Zubko, S. Gariglio, M. Gabay, P. Ghosez, and J.-M. Triscone, in *Annu. Rev. Condens. Matter Phys.*; *Vol. 2*, edited by J. S. Langer (2011), p. 141.

[33] K. G. Günther, Z. Naturforschg. **13a,** 1081 (1958).

[34] K. R. Arthur Jr, J. Appl. Phys. **39,** 4032 (1968).

[35] W. P. McCray, Nat. Nanotechnol. **2,** 259 (2007).

[36] A. Y. Cho, M. B. Panish, and I. Hayashi, Proc. Symp. GaAs and Related Compounds **2,** 18 (1970).

[37] J. H. Singleton, American Institute of Physics, on behalf of the American Vacuum Society (1984).

[38] M. K. Wu, J. R. Ashburn, C. J. Torng, P. H. Hor, R. L. Meng, L. Gao, Z. J. Huang, Y. Q. Wang, and C. W. Chu, Phys. Rev. Lett. **58,** 908 (1987).

[39] M. Dawber, K. M. Rabe, and J. F. Scott, Rev. Mod. Phys. **77,** 1083 (2005).

[40] K. F. Wang, J. M. Liu, and Z. F. Ren, Adv. Phys. **58,** 321 (2009).

[41] P. M. Boffey, in *New York Times* (1982).

[42] K. S. Harsha, *Principles of vapor deposition of thin films* (Elsevier, 2005).

[43] H. Hertz, Ann. Phys. **17,** 177 (1882).

[44] M. Knudsen, Annalen Der Physik **47,** 697 (1915).

[45] M. A. Herman and H. Sitter, *Molecular beam epitaxy : Fundamentals and current status* (Springer, 1996).

[46] J. E. Mahan, *Physical vapor deposition of thin film* (John Wiley and Sons, New York, 2000).

[47] http://www.ph.utexas.edu/~aadg/lab/index.html

[48] G. Sauerbrey, Zeitschrift Fur Physik **155,** 206 (1959).

[49] C. K. O'Sullivan and G. G. Guilbault, Biosens. Bioelectron. **14,** 663 (1999).

[50] C. S. Lu and O. Lewis, J. Appl. Phys. **43,** 4385 (1972).

[51] X. J. Dai, Austr. J. Phys **49,** 1169 (1996).

[52] A. Ichimiya and P. I. Cohen, *Reflection high energy electron diffraction* (Cambridge, 2004).

[53] E. Bauer, in *Techniques of Metals Research Vol. 2* (Wiley-interscience, New York 1969).

[54] K.Oura, Victor G. Lifshits, Alexander A. Saranin, Andrey V. Zotov, and M. katayama, *Surface science: an introduction* (Springer, 2003).

[55] J. H. Neave, B. A. Joyce, P. J. Dobson, and N. Norton, Appl. Phys. A-Mater **31,** 1 (1983).

[56] B. A. Joyce, Rep. Prog. Phys. **48,** 1637 (1985).

[57] M. Ohring, *Materials science of thin films* (Academic press, 2001).

[58] B. D. Cullity and S. R. Stock, *Elments of x-ray diffraction*, 3rd ed. (Prentice Hall, 2001).

[59] H. Ibach and H. Lüth, *Solid-state physics: an introduction to principles of materials science* (Springer-Verlag, 1995).

[60] C. Kittel, *Introduction to solid state physics*, 8th ed. ed. (Wiley, 2005).

[61] H. Kiessig, Annalen Der Physik **10,** 769 (1931).

62 *X-ray and neutron reflectivity : Principles and applications*; *Vol.* Springer, 2009).

63 http://www-llb.cea.fr/prism/programs/simulreflec/simulreflec.html

64 S. Hufner, *Photoelectron Spectroscopy;Principles and Applications*, 3rd ed. (Berlin: Springer).

65 H. Hertz, Annalen Der Physik **31,** 983 (1887).

66 A. Einstein, Annalen Der Physik **17,** 132 (1905).

67 Electron Spectroscopy for Atoms, Molecules and Condensed Matter; http://www.nobelprize.org/nobel_prizes/physics/laureates/1981/siegbahn-lecture.html

68 H. H. Johann, Zeitschrift Fur Physik **69,** 185 (1931).

69 S. Tanuma, C. J. Powell, and D. R. Penn, Surface and Interface Analysis **20,** 77 (1993).

70 M. Seah and W. Dench, Surf. Interface Anal. **1,** 2 (1979).

71 A. Jablonski, Surf. Interface Anal. **20,** 317 (1993).

72 S. Tanuma, C. J. Powell, and D. R. Penn, Surf. Interface Anal. **21,** 165 (1994).

73 W. H. Gries, Surf. Interface Anal. **24,** 38 (1996).

74 S. Hofmann, *Auger-and X-ray Photoelectron Spectroscopy in Materials Science: A User-oriented Guide*, Vol. 49 (Springer, 2012).

75 C. D. Wagner, L. E. Davis, M. V. Zeller, J. A. Taylor, R. H. Raymond, and L. H. Gale, Surf. Interface Anal. **3,** 211 (1981).

76 J. C. Rivière and S. Myhra, *Handbook of surface and interface analysis: Methods for problem-solving* (CRC Press, 2009).

77 D. A. Shirley, Phys. Rev. B **5,** 4709 (1972).

78 H. Ibach and H. Lüth, *Solid-State Physics: An Introduction to Principles of Materials Science, 2010* (Springer-Verlag, New York).

79 G. Binnig, C. F. Quate, and C. Gerber, Phys. Rev. Lett. **56,** 930 (1986).

80 G. Meyer and N. M. Amer, Appl. Phys. Lett. **53,** 1045 (1988).

81 http://blog.brukerafmprobes.com/guide-to-spm-and-afm-modes/tapping-mode-afm/

82 X. Zhang, A. A. Demkov, H. Li, X. Hu, Y. Wei, and J. Kulik, Phys. Rev. B **68,** 125323 (2003).

83 C. R. Ashman, C. J. Forst, K. Schwarz, and P. E. Blochl, Phys. Rev. B **69,** 075309 (2004).

[84] Z. Yu, Y. Liang, C. Overgaard, X. Hu, J. Curless, H. Li, Y. Wei, B. Craigo, D. Jordan, R. Droopad, J. Finder, K. Eisenbeiser, D. Marshall, K. Moore, J. Kulik, and P. Fejes, Thin Solid Films **462,** 51 (2004).

[85] Y. Liang, S. Gan, Y. Wei, and R. Gregory, Phys. Status. Solidi. B **243,** 2098 (2006).

[86] C. Rossel, B. Mereu, C. Marchiori, D. Caimi, M. Sousa, A. Guiller, H. Siegwart, R. Germann, J. P. Locquet, J. Fompeyrine, D. J. Webb, C. Dieker, and J. W. Seo, Appl. Phys. Lett. **89,** 053506 (2006).

[87] J. W. Reiner, A. Posadas, M. Wang, M. Sidorov, Z. Krivokapic, F. J. Walker, T. P. Ma, and C. H. Ahn, J. Appl. Phys. **105,** 124501 (2009).

[88] V. Vaithyanathan, J. Lettieri, W. Tian, A. Sharan, A. Vasudevarao, Y. L. Li, A. Kochhar, H. Ma, J. Levy, P. Zschack, J. C. Woicik, L. Q. Chen, V. Gopalan, and D. G. Schlom, J. Appl. Phys. **100,** 024108 (2006).

[89] G. Niu, S. Yin, G. Saint-Girons, B. Gautier, P. Lecoeur, V. Pillard, G. Hollinger, and B. Vilquin, Microelectron. Eng. **88,** 1232 (2011).

[90] A. K. Pradhan, J. B. Dadson, D. Hunter, K. Zhang, S. Mohanty, E. M. Jackson, B. Lasley-Hunter, K. Lord, T. M. Williams, R. R. Rakhimov, J. Zhang, D. J. Sellmyer, K. Inaba, T. Hasegawa, S. Mathews, B. Joseph, B. R. Sekhar, U. N. Roy, Y. Cui, and A. Burger, J. Appl. Phys. **100,** 033903 (2006).

[91] J. Wang, H. Zheng, Z. Ma, S. Prasertchoung, M. Wuttig, R. Droopad, J. Yu, K. Eisenbeiser, and R. Ramesh, Appl. Phys. Lett. **85,** 2574 (2004).

[92] H. Seo, A. B. Posadas, C. Mitra, A. V. Kvit, J. Ramdani, and A. A. Demkov, Phys. Rev. B **86,** 075301 (2012).

[93] M. D. McDaniel, A. Posadas, T. Wang, A. A. Demkov, and J. G. Ekerdt, Thin Solid Films **520,** 6525 (2012).

[94] K. Eisenbeiser, R. Emrick, R. Droopad, Z. Yu, J. Finder, S. Rockwell, J. Holmes, C. Overgaard, and W. Ooms, Ieee Electron Device Lett. **23,** 300 (2002).

[95] L. Largeau, J. Cheng, P. Regreny, G. Patriarche, A. Benamrouche, Y. Robach, M. Gendry, G. Hollinger, and G. Saint-Girons, Appl. Phys. Lett. **95,** 011907 (2009).

[96] J. Cheng, A. Chettaoui, J. Penuelas, B. Gobaut, P. Regreny, A. Benamrouche, Y. Robach, G. Hollinger, and G. Saint-Girons, J. Appl. Phys. **107,** 094902 (2010).

[97] A. A. Demkov, H. Seo, X. Zhang, and J. Ramdani, Appl. Phys. Lett. **100,** 071602 (2012).

[98] A. Slepko and A. A. Demkov, Phys. Rev. B **85,** 195462 (2012).

[99] O. V. Yazyev and A. Pasquarello, Phys. Rev. Lett. **96,** 157601 (2006).

[100] M. P. J. Punkkinen, K. Kokko, L. Vitos, P. Laukkanen, E. Airiskallio, M. Ropo, M. Ahola-Tuomi, M. Kuzmin, I. J. Vayrynen, and B. Johansson, Phys. Rev. B **77,** 245302 (2008).

[101] P. E. J. Eriksson and R. I. G. Uhrberg, Phys. Rev. B **81,** 125443 (2010).

[102] E. Landemark, C. J. Karlsson, Y. C. Chao, and R. I. G. Uhrberg, Phys. Rev. Lett. **69,** 1588 (1992).

[103] T. W. Pi, C. P. Cheng, and I. H. Hong, Surf. Sci. **418,** 113 (1998).

[104] P. De Padova, R. Larciprete, C. Quaresima, C. Ottaviani, B. Ressel, and P. Perfetti, Phys. Rev. Lett. **81,** 2320 (1998).

[105] G. Le Lay, A. Cricenti, C. Ottaviani, P. Perfetti, T. Tanikawa, I. Matsuda, and S. Hasegawa, Phys. Rev. B **66,** 153317 (2002).

[106] H. Koh, J. W. Kim, W. H. Choi, and H. W. Yeom, Phys. Rev. B **67,** 073306 (2003).

[107] E. Pehlke and M. Scheffler, Phys. Rev. Lett. **71,** 2338 (1993).

[108] J. A. Kubby, J. E. Griffith, R. S. Becker, and J. S. Vickers, Phys. Rev. B **36,** 6079 (1987).

[109] R. I. G. Uhrberg, J. Phys. : Condens. Matter **13,** 11181 (2001).

[110] C. P. Cheng, I. H. Hong, and T. W. Pi, Phys. Rev. B **58,** 4066 (1998).

[111] M. Kuzmin, R. E. Perala, P. Laukkanen, and I. J. Vayrynen, Phys. Rev. B **72,** 085343 (2005).

[112] T. W. Pi, C. P. Cheng, and G. K. Wertheim, J. Appl. Phys. **109,** 043701 (2011).

[113] A. A. Demkov and X. Zhang, J. Appl. Phys. **103,** 103710 (2008).

[114] D. M. Goodner, D. L. Marasco, A. A. Escuadro, L. Cao, and M. J. Bedzyk, Phys. Rev. B **71,** 165426 (2005).

[115] A. Mesarwi, W. C. Fan, and A. Ignatiev, J. Appl. Phys. **68,** 3609 (1990).

[116] A. Herrera-Gomez, F. S. Aguirre-Tostado, Y. Sun, P. Pianetta, Z. Yu, D. Marshall, R. Droopad, and W. E. Spicer, J. Appl. Phys. **90,** 6070 (2001).

[117] G. Kresse and J. Furthmuller, Phys. Rev. B **54,** 11169 (1996).

[118] P. E. Blochl, Phys. Rev. B **50,** 17953 (1994).

[119] www.casaxps.com

[120] A. D. Katnani and G. Margaritondo, Phys. Rev. B **28,** 1944 (1983).

[121] L. Kohler and G. Kresse, Phys. Rev. B **70,** 165405 (2004).

[122] M. Choi, A. B. Posadas, H. Seo, R. C. Hatch, and A. A. Demkov, Appl. Phys. Lett. **102,** 031604 (2013).

[123] M. Imai and T. Kikegawa, Chem. Mater. **15,** 2543 (2003).

[124] Y. Enta, T. Kinoshita, S. Suzuki, and S. Kono, Phys. Rev. B **36,** 9801 (1987).

[125] K. Shudo and T. Munakata, Phys. Rev. B **63,** 125324 (2001).

[126] A. Crispin, X. Crispin, M. Fahlman, M. Berggren, and W. R. Salaneck, Appl. Phys. Lett. **89,** 213503 (2006).

[127] P. C. Rusu, G. Giovannetti, C. Weijtens, R. Coehoorn, and G. Brocks, J. Phys. Chem. C **113,** 9974 (2009).

[128] J. Wang, J. A. Hallmark, D. S. Marshall, W. J. Ooms, P. Ordejon, J. Junquera, D. Sanchez-Portal, E. Artacho, and J. M. Soler, Phys. Rev. B **60,** 4968 (1999).

[129] A. J. Ciani, P. Sen, and I. P. Batra, Phys. Rev. B **69,** 245308 (2004).

[130] A. Herrera-Gómez, P. Pianetta, D. Marshall, E. Nelson, and W. E. Spicer, Phys. Rev. B **61,** 12988 (2000).

[131] R. Droopad, Z. Yu, J. Ramdani, L. Hilt, J. Curless, C. Overgaard, J. L. Edwards, J. Finder, K. Eisenbeiser, J. Wang, V. Kaushik, B. Y. Ngyuen, and B. Ooms, J. Cryst. Growth **227–228,** 936 (2001).

[132] J. Lettieri, J. H. Haeni, and D. G. Schlom, J. Vac. Sci. Technol. A **20,** 1332 (2002).

[133] W. C. Fan and A. Ignatiev, Phys. Rev. B **44,** 3110 (1991).

[134] F. De Groot and A. Kotani, *Core level spectroscopy of solids* (CRC press, 2008).

[135] T. Koopmans, Physica **1,** 104 (1934).

[136] B. Johansson and N. Mårtensson, Phys. Rev. B **21,** 4427 (1980).

[137] M. Weinert and R. E. Watson, Phys. Rev. B **51,** 17168 (1995).

[138] M. Alden, H. L. Skriver, and B. Johansson, Phys. Rev. Lett. **71,** 2449 (1993).

[139] J. R. Smith, F. J. Arlinghaus, and J. G. Gay, Phys. Rev. B **26,** 1071 (1982).

[140] H. Gronbeck, S. Klacar, N. M. Martin, A. Hellman, E. Lundgren, and J. N. Andersen, Phys. Rev. B **85,** 115445 (2012).

[141] M. V. Gomoyunova and Pronin, II, Tech. Phys. **49,** 1249 (2004).

[142] H. Seo, M. Choi, A. B. Posadas, R. C. Hatch, and A. A. Demkov, J. Vac. Sci. Technol. B **31,** 04d107 (2013).

[143] P. E. J. Eriksson, K. Sakamoto, and R. I. G. Uhrberg, Phys. Rev. B **75,** 205416 (2007).

[144] C. Y. Kim, H. W. Kim, J. W. Chung, K. S. An, C. Y. Park, A. Kimura, and A. Kakizaki, Appl. Phys. A **64,** 597 (1997).

[145] J. P. Perdew, K. Burke, and M. Ernzerhof, Phys. Rev. Lett. **77,** 3865 (1996).

[146] Landolt-Börnstein, *Semiconductors*, Vol. 41, edited by O. Madelung, U. Rössler, and M. Schulz ed. (Springer-Verlag, Berlin, Heidelberg, New York, 2002).

[147] L. J. Sham and M. Schlüter, Phys. Rev. Lett. **51,** 1888 (1983).

[148] H. Seo, R. C. Hatch, P. Ponath, M. Choi, A. B. Posadas, and A. A. Demkov, Phys. Rev. B **89,** 115318 (2014).

[149] Frank Albert Cotton and G. Wilkinson, *Advanced Inorganic Chemistry* (Wiley, 1962).

[150] M. Weinelt, M. Kutschera, T. Fauster, and M. Rohlfing, Phys. Rev. Lett. **92,** 126801 (2004).

[151] N. Buecking, P. Kratzer, M. Scheffler, and A. Knorr, Phys. Rev. B **77,** 233305 (2008).

[152] K. Garrity and S. Ismail-Beigi, Phys. Rev. B **80,** 085306 (2009).

[153] J. He, G. Zhang, J. Guo, Q. Guo, and K. Wu, J. Appl. Phys. **109,** 083522 (2011).

[154] W. Du, B. Wang, L. Xu, Z. Hu, X. Cui, B. C. Pan, J. Yang, and J. G. Hou, J. Chem. Phys. **129,** 164707 (2008).

[155] J. Ramdani, R. Droopad, Z. Yu, J. A. Curless, C. D. Overgaard, J. Finder, K. Eisenbeiser, J. A. Hallmark, W. J. Ooms, V. Kaushik, P. Alluri, and S. Pietambaram, Appl. Surf. Sci. **159,** 127 (2000).

[156] R. A. McKee, F. J. Walker, and M. F. Chisholm, Science **293,** 468 (2001).

[157] X. M. Hu, H. Li, Y. Liang, Y. Wei, Z. Yu, D. Marshall, J. Edwards, R. Droopad, X. Zhang, A. A. Demkov, K. Moore, and J. Kulik, Appl. Phys. Lett. **82,** 203 (2003).

[158] C. J. Forst, C. R. Ashman, K. Schwarz, and P. E. Blochl, Nature **427,** 53 (2004).

[159] X. F. Wang, J. Wang, Q. Li, M. S. Moreno, X. Y. Zhou, J. Y. Dai, Y. Wang, and D. Tang, Phys. D: Appl. Phys. **42,** 085409 (2009).

[160] A. M. Kolpak, F. J. Walker, J. W. Reiner, Y. Segal, D. Su, M. S. Sawicki, C. C. Broadbridge, Z. Zhang, Y. Zhu, C. H. Ahn, and S. Ismail-Beigi, Phys. Rev. Lett. **105,** 217601 (2010).

[161] F. Amy, A. S. Wan, A. Kahn, F. J. Walker, and R. A. McKee, J. Appl. Phys. **96,** 1635 (2004).

[162] H. Li, X. Hu, Y. Wei, Z. Yu, X. Zhang, R. Droopad, A. A. Demkov, J. Edwards, K. Moore, W. Ooms, J. Kulik, and P. Fejes, J. Appl. Phys. **93,** 4521 (2003).

[163] D. P. Kumah, J. W. Reiner, Y. Segal, A. M. Kolpak, Z. Zhang, D. Su, Y. Zhu, M. S. Sawicki, C. C. Broadbridge, C. H. Ahn, and F. J. Walker, Appl. Phys. Lett. **97,** 251902 (2010).

[164] M. P. Warusawithana, C. Cen, C. R. Sleasman, J. C. Woicik, Y. Li, L. F. Kourkoutis, J. A. Klug, H. Li, P. Ryan, L.-P. Wang, M. Bedzyk, D. A. Muller, L.-Q. Chen, J. Levy, and D. G. Schlom, Science **324,** 367 (2009).

[165] F. Niu and B. W. Wessels, J. Cryst. Growth **300,** 509 (2007).

[166] G. Delhaye, C. Merckling, M. El-Kazzi, G. Saint-Girons, M. Gendry, Y. Robach, G. Hollinger, L. Largeau, and G. Patriarche, J. Appl. Phys. **100,** 124109 (2006).

[167] Y. Wei, X. M. Hu, Y. Liang, D. C. Jordan, B. Craigo, R. Droopad, Z. Yu, A. Demkov, J. L. Edwards, and W. J. Ooms, J. Vac. Sci. Technol. B **20,** 1402 (2002).

[168] One monolayer refers to the atomic surface density of an ideal unreconstructed Si(001) surface. This is equivalent to 6.78×10^{14} atoms/cm^2

[169] H. Ledbetter, M. Lei, and S. D. Kim, Phase Transitions **23,** 61 (1990).

[170] G. J. Yong, R. M. Kolagani, S. Adhikari, W. Vanderlinde, Y. Liang, K. Muramatsu, and S. Friedrich, J. Appl. Phys. **108,** 033502 (2010).

[171] A. Posadas, R. Dargis, M. R. Choi, A. Slepko, A. A. Demkov, J. J. Kim, and D. J. Smith, J. Vac. Sci. Technol. B **29,** 03c131 (2011).

[172] The possibility of the presence of a silicate layer was not explicitly taken into account in the x-ray reflectivity simulations although the density of the SiO_2 layer was adjusted as a fitting parameter.

[173] R. Ramesh and D. G. Schlom, Mrs Bulletin **33,** 1006 (2008).

[174] P. Zubko, S. Gariglio, M. Gabay, P. Ghosez, and J.-M. Triscone, Annual Review of Condensed Matter Physics, Vol 2 **2,** 141 (2011).

[175] J. Chakhalian, A. J. Millis, and J. Rondinelli, Nat. Mater. **11,** 92 (2012).

[176] H.-U. Habermeier, Materials Today **10,** 34 (2007).

[177] R. Konta, T. Ishii, H. Kato, and A. Kudo, J. Phys. Chem. B **108,** 8992 (2004).

[178] N. Zhou, K. Zhao, H. Liu, Z. Lu, H. Zhao, L. Tian, W. Liu, and S. Zhao, Journal of Applied Physics **105** (2009).

[179] D. Kan, T. Terashima, R. Kanda, A. Masuno, K. Tanaka, S. Chu, H. Kan, A. Ishizumi, Y. Kanemitsu, Y. Shimakawa, and M. Takano, Nature Materials **4,** 816 (2005).

[180] K. Ueno, S. Nakamura, H. Shimotani, A. Ohtomo, N. Kimura, T. Nojima, H. Aoki, Y. Iwasa, and M. Kawasaki, Nat. Mater. **7,** 855 (2008).

[181] A. Ohtomo and H. Y. Hwang, Nature **427,** 423 (2004).

[182] A. Kalabukhov, R. Gunnarsson, J. Borjesson, E. Olsson, T. Claeson, and D. Winkler, Phys. Rev. B **75,** 121404 (2007).

[183] W. Siemons, G. Koster, H. Yamamoto, W. A. Harrison, G. Lucovsky, T. H. Geballe, D. H. A. Blank, and M. R. Beasley, Phys. Rev. Lett. **98,** 196802 (2007).

[184] G. Herranz, M. Basletic, M. Bibes, C. Carretero, E. Tafra, E. Jacquet, K. Bouzehouane, C. Deranlot, A. Hamzic, J. M. Broto, A. Barthelemy, and A. Fert, Phys. Rev. Lett. **98,** 216803 (2007).

[185] A. Brinkman, M. Huijben, M. Van Zalk, J. Huijben, U. Zeitler, J. C. Maan, W. G. Van der Wiel, G. Rijnders, D. H. A. Blank, and H. Hilgenkamp, Nat. Mater. **6,** 493 (2007).

[186] N. Reyren, S. Thiel, A. D. Caviglia, L. F. Kourkoutis, G. Hammerl, C. Richter, C. W. Schneider, T. Kopp, A. S. Ruetschi, D. Jaccard, M. Gabay, D. A. Muller, J. M. Triscone, and J. Mannhart, Science **317,** 1196 (2007).

[187] J. A. Bert, B. Kalisky, C. Bell, M. Kim, Y. Hikita, H. Y. Hwang, and K. A. Moler, Nature Phys. **7,** 767 (2011).

[188] D. A. Dikin, M. Mehta, C. W. Bark, C. M. Folkman, C. B. Eom, and V. Chandrasekhar, Phys. Rev. Lett. **107,** 056802 (2011).

[189] W. S. Choi, D. W. Jeong, S. S. A. Seo, Y. S. Lee, T. H. Kim, S. Y. Jang, H. N. Lee, and K. Myung-Whun, Phys. Rev. B **83,** 195113 (2011).

[190] A. Posadas, M. Berg, H. Seo, A. de Lozanne, A. A. Demkov, D. J. Smith, A. P. Kirk, D. Zhernokletov, and R. M. Wallace, Appl. Phys. Lett. **98,** 053104 (2011).

[191] H. Seo, A. Posadas, and A. A. Demkov, Phys. Rev. B **86,** 014430 (2012).

[192] A. Ohtomo, D. A. Muller, J. L. Grazul, and H. Y. Hwang, Nature **419,** 378 (2002).

[193] Y. Hotta, T. Susaki, and H. Y. Hwang, Phys. Rev. Lett. **99,** 236805 (2007).

[194] J. Biscaras, N. Bergeal, A. Kushwaha, T. Wolf, A. Rastogi, R. C. Budhani, and J. Lesueur, Nat. Commun. **1,** 89 (2010).

[195] J. S. Kim, S. S. A. Seo, M. F. Chisholm, R. K. Kremer, H. U. Habermeier, B. Keimer, and H. N. Lee, Phys. Rev. B **82,** 201407 (2010).

[196] S. S. A. Seo, W. S. Choi, H. N. Lee, L. Yu, K. W. Kim, C. Bernhard, and T. W. Noh, Phys. Rev. Lett. **99,** 266801 (2007).

[197] M. Kawasaki, K. Takahashi, T. Maeda, R. Tsuchiya, M. Shinohara, O. Ishiyama, T. Yonezawa, M. Yoshimoto, and H. Koinuma, Science **266,** 1540 (1994).

[198] G. Koster, B. L. Kropman, G. Rijnders, D. H. A. Blank, and H. Rogalla, Appl. Phys. Lett. **73,** 2920 (1998).

[199] T. Ohnishi, K. Shibuya, M. Lippmaa, D. Kobayashi, H. Kumigashira, M. Oshima, and H. Koinuma, Appl. Phys. Lett. **85,** 272 (2004).

[200] K. Szot and W. Speier, Phys. Rev. B **60,** 5909 (1999).

[201] M. Kareev, S. Prosandeev, J. Liu, C. Gan, A. Kareev, J. W. Freeland, M. Xiao, and J. Chakhalian, Appl. Phys. Lett. **93,** 061909 (2008).

[202] J. Zhang, D. Doutt, T. Merz, J. Chakhalian, M. Kareev, J. Liu, and L. J. Brillson, Appl. Phys. Lett. **94,** 092904 (2009).

[203] A. Biswas, P. B. Rossen, C. H. Yang, W. Siemons, M. H. Jung, I. K. Yang, R. Ramesh, and Y. H. Jeong, Appl. Phys. Lett. **98,** 051904 (2011).

[204] R. Gunnarsson, A. S. Kalabukhov, and D. Winkler, Surf. Sci. **603,** 151 (2009).

[205] J. E. Boschker and T. Tybell, Appl. Phys. Lett. **100,** 151604 (2012).

[206] S. A. Chambers, T. C. Droubay, C. Capan, and G. Y. Sun, Surf. Sci. **606,** 554 (2012).

[207] J. G. Connell, B. J. Isaac, G. B. Ekanayake, D. R. Strachan, and S. S. A. Seo, Appl. Phys. Lett. **101,** 251607 (2012).

[208] Y. Haruyama, S. Kodaira, Y. Aiura, H. Bando, Y. Nishihara, T. Maruyama, Y. Sakisaka, and H. Kato, Phys. Rev. B **53,** 8032 (1996).

[209] Y. Aiura, I. Hase, H. Bando, T. Yasue, T. Saitoh, and D. S. Dessau, Surf. Sci. **515,** 61 (2002).

[210] W. Meevasana, X. J. Zhou, B. Moritz, C. C. Chen, R. H. He, S. I. Fujimori, D. H. Lu, S. K. Mo, R. G. Moore, F. Baumberger, T. P. Devereaux, D. van der Marel, N. Nagaosa, J. Zaanen, and Z. X. Shen, New J. Phys. **12,** 023004 (2010).

[211] W. Meevasana, P. D. C. King, R. H. He, S. K. Mo, M. Hashimoto, A. Tamai, P. Songsiriritthigul, F. Baumberger, and Z. X. Shen, Nat. Mater. **10,** 114 (2011).

[212] A. F. Santander-Syro, O. Copie, T. Kondo, F. Fortuna, S. Pailhes, R. Weht, X. G. Qiu, F. Bertran, A. Nicolaou, A. Taleb-Ibrahimi, P. Le Fevre, G. Herranz, M. Bibes, N. Reyren, Y. Apertet, P. Lecoeur, A. Barthelemy, and M. J. Rozenberg, Nature **469,** 189 (2011).

[213] E. Frantzeskakis, J. Avila, and M. C. Asensio, Phys. Rev. B **85,** 125115 (2012).

[214] Y. Ishida, R. Eguchi, M. Matsunami, K. Horiba, M. Taguchi, A. Chainani, Y. Senba, H. Ohashi, H. Ohta, and S. Shin, Phys. Rev. Lett. **100,** 056401 (2008).

[215] M. Takizawa, K. Maekawa, H. Wadati, T. Yoshida, A. Fujimori, H. Kumigashira, and M. Oshima, Phys. Rev. B **79,** 113103 (2009).

[216] Y. J. Chang, A. Bostwick, Y. S. Kim, K. Horn, and E. Rotenberg, Phys. Rev. B **81,** 235109 (2010).

[217] M. D'Angelo, R. Yukawa, K. Ozawa, S. Yamamoto, T. Hirahara, S. Hasegawa, M. G. Silly, F. Sirotti, and I. Matsuda, Phys. Rev. Lett. **108,** 116802 (2012).

[218] R. Yukawa, S. Yamamoto, K. Ozawa, M. D’Angelo, M. Ogawa, M. G. Silly, F. Sirotti, and I. Matsuda, Phys. Rev. B **87,** 115314 (2013).

[219] L. Qiao, T. C. Droubay, T. Varga, M. E. Bowden, V. Shutthanandan, Z. Zhu, T. C. Kaspar, and S. A. Chambers, Phys. Rev. B **83,** 085408 (2011).

[220] F. F. Y. Wang and K. P. Gupta, Metallurgical and Materials Transactions B **4,** 2767 (1973).

[221] F. W. Lytle, J. Appl. Phys. **35,** 2212 (1964).

[222] T. C. Chiang, J. A. Knapp, M. Aono, and D. E. Eastman, Phys. Rev. B **21,** 3513 (1980).

[223] F. J. Himpsel, Applied Optics **19,** 3964 (1980).

[224] G. Kresse and J. Hafner, Phys. Rev. B **47,** 558 (1993).

[225] G. Kresse and J. Hafner, Phys. Rev. B **49,** 14251 (1994).

[226] G. Kresse and J. Furthmuller, Comput. Mater. Sci. **6,** 15 (1996).

[227] G. Kresse and D. Joubert, Phys. Rev. B **59,** 1758 (1999).

[228] J. P. Perdew and A. Zunger, Phys. Rev. B **23,** 5048 (1981).

[229] H. J. Monkhorst and J. D. Pack, Phys. Rev. B **13,** 5188 (1976).

[230] E. A. Giess, R. L. Sandstrom, W. J. Gallagher, A. Gupta, S. L. Shinde, R. F. Cook, E. I. Cooper, E. J. M. Osullivan, J. M. Roldan, A. P. Segmuller, and J. Angilello, Ibm Journal of Research and Development **34,** 916 (1990).

[231] H. Seo, A. B. Posadas, and A. A. Demkov, J. Vac. Sci. Technol. B **30,** 04e108 (2012).

[232] K. M. Shen, F. Ronning, D. H. Lu, W. S. Lee, N. J. C. Ingle, W. Meevasana, F. Baumberger, A. Damascelli, N. P. Armitage, L. L. Miller, Y. Kohsaka, M. Azuma, M. Takano, H. Takagi, and Z. X. Shen, Phys. Rev. Lett. **93,** 267002 (2004).

[233] Our TB model includes 14 orbitals: five Ti 3d (grouped into eg and t2g) and three 2p orbitals from three oxygen. The O 2p orbitals are split into eg (σ-type) and t2g (π-type) according to their orbital orientations to the adjacent Ti sites. We keep nine parameters: $E_{d,eg} - E_{p,eg} = 6.5$ eV, $E_{d,t2g} - E_{p,t2g} = 4.3$ eV, $E_{p,t2g} - E_{p,eg} = 0.5$ eV, $t_{pd,\sigma} = 2.0$ eV, $t_{pd,\pi} = 1.3$ eV, $t_{pp,\sigma} = 0.4$eV (2nd neighbor p-p hopping), $t_{pp,\pi} = 0.15$ eV (2nd neighbor p-p hopping), $t'_{pp,\sigma,2} = 0.3$eV (3rd neighbor p-p hopping across a Ti), and $t_{pp,\sigma,2} = 0.15$ eV (3rd neighbor p-p hopping).

[234] K. Szot, W. Speier, U. Breuer, R. Meyer, J. Szade, and R. Waser, Surf. Sci. **460,** 112 (2000).

[235] D. Kobayashi, H. Kumigashira, M. Oshima, T. Ohnishi, M. Lippmaa, K. Ono, M. Kawasaki, and H. Koinuma, J. Appl. Phys. **96,** 7183 (2004).

[236] Y. Aiura, H. Bando, Y. Nishihara, Y. Haruyama, T. Komeda, S. Kodaira, Y. Sakisaka, T. Maruyama, and H. Kato, *Advances in Superconductivity VI* (Springer, Tokyo, 1994).

[237] Y. Aiura, Y. Nishihara, Y. Haruyama, T. Komeda, S. Kodaira, Y. Sakisaka, T. Maruyama, and H. Kato, Physica B **194,** 1215 (1994).

[238] D. Ricci, G. Bano, G. Pacchioni, and F. Illas, Phys. Rev. B **68,** 224105 (2003).

[239] J. P. Buban, H. Iddir, and S. Ogut, Phys. Rev. B **69,** 180102 (2004).

[240] W. D. Luo, W. H. Duan, S. G. Louie, and M. L. Cohen, Phys. Rev. B **70,** 214109 (2004).

[241] J. Carrasco, F. Illas, N. Lopez, E. A. Kotomin, Y. F. Zhukovskii, R. A. Evarestov, Y. A. Mastrikov, S. Piskunov, and J. Maier, Phys. Rev. B **73,** 064106 (2006).

[242] C. Lin, C. Mitra, and A. A. Demkov, Phys. Rev. B **86,** 161102 (2012).

[243] C. Mitra, C. Lin, J. Robertson, and A. A. Demkov, Phys. Rev. B **86,** 155105 (2012).

[244] V. E. Alexandrov, E. A. Kotomin, J. Maier, and R. A. Evarestov, Eur. Phys. J. B **72,** 53 (2009).

[245] D. D. Cuong, B. Lee, K. M. Choi, H.-S. Ahn, S. Han, and J. Lee, Phys. Rev. Lett. **98,** 115503 (2007).

[246] M. Choi, F. Oba, Y. Kumagai, and I. Tanaka, Adv. Mater. **25,** 86 (2013).

[247] Y. Tokura, Y. Taguchi, Y. Okada, Y. Fujishima, T. Arima, K. Kumagai, and Y. Iye, Phys. Rev. Lett. **70,** 2126 (1993).

[248] D. D. Sarma, S. R. Barman, H. Kajueter, and G. Kotliar, Europhys. Lett. **36,** 307 (1996).

[249] R. Yukawa, S. Yamamoto, K. Ozawa, M. D'Angelo, M. Ogawa, M. G. Silly, F. Sirotti, and I. Matsuda, Phys. Rev. B **87,** 115314 (2013).

[250] A. Bussmann-Holder, A. R. Bishop, and A. Simon, Ferroelectrics **400,** 19 (2010).

[251] J. Szade, K. Szot, M. Kulpa, J. Kubacki, C. Lenser, R. Dittmann, and R. Waser, Phase Transitions **84,** 489 (2011).

[252] K. Iwaya, R. Shimizu, T. Ohsawa, T. Hashizume, and T. Hitosugi, Phy. Rev. B **83,** 125117 (2011).

[253] S. A. Chambers, T. Ohsawa, C. M. Wang, I. Lyubinetsky, and J. E. Jaffe, Surf. Sci. **603,** 771 (2009).

[254] M. L. Knotek, Surf. Sci. **101,** 334 (1980).

[255] N. Erdman, K. R. Poeppelmeier, M. Asta, O. Warschkow, D. E. Ellis, and L. D. Marks, Nature **419,** 55 (2002).

[256] M. R. Castell, Surf. Sci. **505,** 1 (2002).

[257] T. Kubo and H. Nozoye, Surf. Sci. **542,** 177 (2003).

[258] O. Warschkow, M. Asta, N. Erdman, K. R. Poeppelmeier, D. E. Ellis, and L. D. Marks, Surf. Sci. **573,** 446 (2004).

[259] K. Johnston, M. R. Castell, A. T. Paxton, and M. W. Finnis, Phys. Rev. B **70,** 085415 (2004).

[260] R. Herger, P. R. Willmott, O. Bunk, C. M. Schlepuetz, B. D. Patterson, B. Delley, V. L. Shneerson, P. F. Lyman, and D. K. Saldin, Phys. Rev. B **76,** 195435 (2007).

[261] F. Lin, S. Wang, F. Zheng, G. Zhou, J. Wu, B.-L. Gu, and W. Duan, Phys. Rev. B **79,** 035311 (2009).

[262] G. W. Trucks, K. Raghavachari, G. S. Higashi, and Y. J. Chabal, Phys. Rev. Lett. **65,** 504 (1990).

[263] M. C. Flowers, N. B. H. Jonathan, Y. Liu, and A. Morris, J. Chem. Phys. **99,** 7038 (1993).

[264] R. C. Hatch, K. D. Fredrickson, M. Choi, C. Lin, H. Seo, A. B. Posadas, and A. A. Demkov, J. Appl. Phys. **114,** 103710 (2013).

[265] M. A. Saifi and L. E. Cross, Phys. Rev. B **2,** 677 (1970).

[266] T. Sakudo and H. Unoki, Phys. Rev. Lett. **26,** 851 (1971).

[267] K. Ueno, S. Nakamura, H. Shimotani, A. Ohtomo, N. Kimura, T. Nojima, H. Aoki, Y. Iwasa, and M. Kawasaki, Nature Mater. **7,** 855 (2008).

[268] K. C. Chiang, C. C. Huang, G. L. Chen, W. J. Chen, H. L. Kao, Y. H. Wu, A. Chin, and S. P. McAlister, IEEE Trans. Electron Devices **53,** 2312 (2006).

[269] M. Kahn, C. Vallee, E. Defay, C. Dubourdieu, M. Bonvalot, S. Blonkowski, J.-R. Plaussu, P. Garrec, and T. Baron, Microelectron. Reliab. **47,** 773 (2007).

[270] A. Eriksson, A. Deleniv, and S. Gevorgian, J. Appl. Phys. **93,** 2848 (2003).

[271] D. Fuchs, C. W. Schneider, R. Schneider, and H. Rietschel, J. Appl. Phys. **85,** 7362 (1999).

[272] Y. Hu, O. K. Tan, J. S. Pan, and X. Yao, J. Phys. Chem. B **108,** 11214 (2004).

[273] A. Ohtomo and H. Y. Hwang, Appl. Phys. Lett. **84,** 1716 (2004).

[274] L. Li, C. Richter, J. Mannhart, and R. C. Ashoori, Nat. Phys. **7,** 762 (2011).

[275] P. Moetakef, C. A. Jackson, J. Hwang, L. Balents, S. J. Allen, and S. Stemmer, Phys. Rev. B **86,** 201102 (2012).

[276] K. Yoshimatsu, K. Horiba, H. Kumigashira, T. Yoshida, A. Fujimori, and M. Oshima, Science **333,** 319 (2011).

[277] O. N. Tufte and P. W. Chapman, Phys. Rev. B **155,** 796 (1967).

[278] H. P. R. Frederikse and W. R. Hosler, Phys. Rev. **161,** 822 (1967).

[279] S. Ohta, T. Nomura, H. Ohta, M. Hirano, H. Hosono, and K. Koumoto, in *Proceedings of the ICT 2005. 24th International Conference on Thermoelectrics, Clemson, South Carolina, p183*, 2005, p. 168.

[280] W. H. Gong, H. Yun, Y. B. Ning, J. E. Greedan, W. R. Datars, and C. V. Stager, J. Solid State Chem. **90,** 320 (1991).

[281] J. Ravichandran, W. Siemons, M. L. Scullin, S. Mukerjee, M. Huijben, J. E. Moore, A. Majumdar, and R. Ramesh, Phys. Rev. B **83,** 035101 (2011).

[282] J. D. Baniecki, M. Ishii, H. Aso, K. Kurihara, and D. Ricinschi, J. Appl. Phys. **113,** 049901 (2013).

[283] J. Son, P. Moetakef, B. Jalan, O. Bierwagen, N. J. Wright, R. Engel-Herbert, and S. Stemmer, Nat. Mater. **9,** 482 (2010).

[284] T. A. Cain, A. P. Kajdos, and S. Stemmer, Appl. Phys. Lett. **102,** 182101 (2013).

[285] S. R. S. Kumar, A. I. Abutaha, M. N. Hedhili, and H. N. Alshareef, J. Appl. Phys. **112,** 114104 (2012).

[286] J. Ravichandran, W. Siemons, H. Heijmerikx, M. Huijben, A. Majumdar, and R. Ramesh, Chem. Mater. **22,** 3983 (2010).

[287] J. E. Sunstrom, S. M. Kauzlarich, and P. Klavins, Chem. Mater. **4,** 346 (1992).

[288] A. Biswas, N. Li, M. H. Jung, Y. W. Lee, J. S. Kim, and Y. H. Jeong, J. Appl. Phys. **113,** 183711 (2013).

[289] B. T. Liu, K. Maki, Y. So, V. Nagarajan, R. Ramesh, J. Lettieri, J. H. Haeni, D. G. Schlom, W. Tian, X. Q. Pan, F. J. Walker, and R. A. McKee, Appl. Phys. Lett. **80,** 4801 (2002).

[290] F. Pan, D. Olaya, J. C. Price, and C. T. Rogers, Appl. Phys. Lett. **84,** 1573 (2004).

[291] D. J. Frank, P. M. Solomon, C. Dubourdieu, M. M. Frank, V. Narayanan, and T. N. Theis, IEEE Trans. Electron Deivices **61,** 2145 (2014).

[292] S. Salahuddin and S. Dattat, Nano Letters **8,** 405 (2008).

[293] R. Oberhuber, G. Zandler, and P. Vogl, Phys. Rev. B **58,** 9941 (1998).

[294] A. Janotti, D. Steiauf, and C. G. Van de Walle, Phys. Rev. B **84,** 201304 (2011).

[295] B. Jalan, S. J. Allen, G. E. Beltz, P. Moetakef, and S. Stemmer, Appl. Phys. Lett. **98,** 132102 (2011).

[296] Y. J. Chang, G. Khalsa, L. Moreschini, A. L. Walter, A. Bostwick, K. Horn, A. H. MacDonald, and E. Rotenberg, Phys. Rev. B **87,** 115212 (2013).

[297] L. J. v. d. Pauw, Philips research reports **13,** 1 (1958).

[298] S. Zollner, A. A. Demkov, R. Liu, J. A. Curless, Z. Yu, J. Ramdani, and R. Droopad, in *Recent Developments in Oxide and Metal Epitaxy-Theory and Experiment*; *Vol. 619*, edited by M. Yeadon, S. Chiang, R. F. C. Farrow, J. W. Evans, and O. Auciello (Materials Research Society, Warrendale, 2000), p. 167.

[299] H. G. Tompkins and W. A. McGahan, *Spectroscopic ellipsometry and reflectometry: a user's guide* (Wiley New York, 1999).

[300] H. Tompkins and E. A. Irene, *Handbook of ellipsometry* (William Andrew, 2005).

[301] T. Willett-Gies, E. DeLong, and S. Zollner, Thin Solid Films (2014, in print).

[302] R. Moos and K. H. Hardtl, J. Am. Ceram. Soc. **80,** 2549 (1997).

[303] A. Janotti, B. Jalan, S. Stemmer, and C. G. Van de Walle, Appl. Phys. Lett. **100,** 262104 (2012).

[304] S. Piskunov, E. Heifets, R. I. Eglitis, and G. Borstel, Comput. Mater. Sci. **29,** 165 (2004).

[305] A. M. Kaiser, A. X. Gray, G. Conti, B. Jalan, A. P. Kajdos, A. Gloskovskii, S. Ueda, Y. Yamashita, K. Kobayashi, W. Drube, S. Stemmer, and C. S. Fadley, Appl. Phys. Lett. **100,** 261603 (2012).

[306] N. G. Eror and U. Balachandran, J. Solid State Chem. **40,** 85 (1981).

[307] J. S. Jeong, P. Ambwani, B. Jalan, C. Leighton, and K. A. Mkhoyan, ACS Nano **7,** 4487 (2013).

[308] Martin D. McDaniel, Agham Posadas, Thong Q. Ngo, Christine M. Karako, John Bruley, Martin M. Frank, Vijay Narayanan, Alexander A. Demkov, and J. G. Ekerdt, J. Appl. Phys. **115,** 224108 (2014).

[309] W. Siemons, G. Koster, H. Yamamoto, T. H. Geballe, D. H. A. Blank, and M. R. Beasley, Phys. Rev. B **76,** 155111 (2007).

[310] J. Humlicek, R. Henn, and M. Cardona, Appl. Phys. Lett. **69,** 2581 (1996).

[311] A. Walsh, J. L. F. Da Silva, and S. H. Wei, Phys. Rev. B **78,** 075211 (2008).

[312] S. Ohta, T. Nomura, H. Ohta, and K. Koumoto, J. Appl. Phys. **97,** 034106 (2005).

[313] W. Wunderlich, H. Ohta, and K. Koumoto, Phys. B **404,** 2202 (2009).

[314] M. L. Scullin, C. Yu, M. Huijben, S. Mukerjee, J. Seidel, Q. Zhan, J. Moore, A. Majumdar, and R. Ramesh, Appl. Phys. Lett. **92,** 202113 (2008).

[315] P. E. Blochl, O. Jepsen, and O. K. Andersen, Phys. Rev. B **49,** 16223 (1994).

[316] C. B. Vining, J. Appl. Phys. **69,** 331 (1991).

[317] V. I. Fistul′, *Heavily doped semiconductors* (Plenum Press, 1969).

[318] X. Sun, M. Lundstrom, and R. Kim, "FD integral calculator," Available: http://nanohub.org/tools/fdical. (2011).

[319] R. Kim and M. Lundstrom, arXiv preprint arXiv:0811.0116 (2008).

[320] G. K. H. Madsen and D. J. Singh, Comput. Phys. Commun **175,** 67 (2006).

[321] S. Thiel, G. Hammerl, A. Schmehl, C. W. Schneider, and J. Mannhart, Science **313,** 1942 (2006).

[322] J. Biscaras, N. Bergeal, S. Hurand, C. Grossetete, A. Rastogi, R. C. Budhani, D. LeBoeuf, C. Proust, and J. Lesueur, Phys. Rev. Lett. **108,** 247004 (2012).

[323] J. Son, J. M. LeBeau, S. J. Allen, and S. Stemmer, Appl. Phys. Lett. **97,** 202109 (2010).

[324] X. F. Zhai, C. S. Mohapatra, A. B. Shah, J. M. Zuo, and J. N. Eckstein, Adv. Mater. **22,** 1136 (2010).

[325] J. Faist, F. Capasso, D. L. Sivco, C. Sirtori, A. L. Hutchinson, and A. Y. Cho, Science **264,** 553 (1994).

[326] S. Nakamura, M. Senoh, S. Nagahama, N. Iwasa, T. Yamada, T. Matsushita, H. Kiyoku, and Y. Sugimoto, Jpn. J. Appl. Phys. **35,** L74 (1996).

[327] S. Datta, G. Dewey, J. Fastenau, M. Hudait, D. Loubychev, W. Liu, M. Radosavljevic, W. Rachmady, and R. Chau, Electron Device Letters, IEEE **28,** 685 (2007).

[328] J. Lee and A. A. Demkov, Phys. Rev. B **78,** 193104 (2008).

[329] K. Yoshimatsu, T. Okabe, H. Kumigashira, S. Okamoto, S. Aizaki, A. Fujimori, and M. Oshima, Phys. Rev. Lett. **104,** 147601 (2010).

[330] S. S. A. Seo, M. J. Han, G. W. J. Hassink, W. S. Choi, S. J. Moon, J. S. Kim, T. Susaki, Y. S. Lee, J. Yu, C. Bernhard, H. Y. Hwang, G. Rijnders, D. H. A. Blank, B. Keimer, and T. W. Noh, Phys. Rev. Lett. **104,** 036401 (2010).

[331] C. A. Jackson and S. Stemmer, Phys. Rev. B **88,** 180403 (2013).

[332] J. Lee and A. A. Demkov, Mater. Res. Soc. Symp. Proc. **966** (2006).

[333] T. H. Shieh and S. C. Lee, Appl. Phys. Lett. **63,** 3350 (1993).

[334] E. A. Kraut, R. W. Grant, J. R. Waldrop, and S. P. Kowalczyk, Phys. Rev. Lett. **44,** 1620 (1980).

[335] S.-G. Lim, S. Kriventsov, T. N. Jackson, J. H. Haeni, D. G. Schlom, A. M. Balbashov, R. Uecker, P. Reiche, J. L. Freeouf, and G. Lucovsky, J. Appl. Phys. **91,** 4500 (2002).

[336] M. Cardona, Phy. Rev. **140,** A651 (1965).

[337] https://www.tcd.ie/Physics/Surfaces/ellipsometry2.php

[338] H. Fujiwara, *Spectroscopic ellipsometry: principles and applications* (John Wiley & Sons, 2007).

[339] K. van Benthem, C. Elsasser, and R. H. French, J. Appl. Phys. **90,** 6156 (2001).

[340] S. A. Chambers, M. H. Engelhard, V. Shutthanandan, Z. Zhu, T. C. Droubay, L. Qiao, P. V. Sushko, T. Feng, H. D. Lee, T. Gustafsson, E. Garfunkel, A. B. Shah, J. M. Zuo, and Q. M. Ramasse, Surface Science Reports **65,** 317 (2010).